ISTANBUL TECHNICAL UNIVERSITY ★ GRADUATE SCHOOL

ORIGIN, AGE AND DEFORMATION HISTORY OF THE ÇATALDAĞ METAMORPHIC CORE COMPLEX

Ph.D. THESIS

Ömer KAMACI

Department of Geological Engineering

Geological Engineering Programme

AUGUST 2021

ISTANBUL TECHNICAL UNIVERSITY ★ GRADUATE SCHOOL

ORIGIN, AGE AND DEFORMATION HISTORY OF THE ÇATALDAĞ METAMORPHIC CORE COMPLEX

Ph.D. THESIS

ÖmerKAMACI
(505082301)

Department of Geological Engineering

Geological Engineering Programme

Thesis Advisor: Prof. Dr. Şafak ALTUNKAYNAK

AUGUST 2021

İSTANBUL TEKNİK ÜNİVERSİTESİ ★ LİSANSÜSTÜ EĞİTİM ENSTİTÜSÜ

ÇATALDAĞ METAMORFİK ÇEKİRDEK KARMAŞIĞI'NIN KÖKENİ, YAŞI VE DEFORMASYON TARİHÇESİ

DOKTORA TEZİ

Ömer KAMACI
(505082301)

Jeoloji Mühendisliği Anabilim Dalı

Jeoloji Mühendisliği Programı

Tez Danışmanı: Prof. Dr. Şafak ALTUNKAYNAK

AĞUSTOS 2021

Ömer KAMACI, a Ph.D. student of İTU Graduate School student ID 505082301, successfully defended the thesis/dissertation entitled "ORIGIN, AGE AND DEFORMATION HISTORY OF THE ÇATALDAĞ METAMORPHIC CORE COMPLEX", which he prepared after fulfilling the requirements specified in the associated legislations, before the jury whose signatures are below.

Thesis Advisor : **Prof. Dr. Şafak ALTUNKAYNAK** ....
İstanbul Technical University

Jury Members : **Prof. Dr. Ş. Can GENÇ** ....
Istanbul Technical University

Prof. Dr. Ercan ALDANMAZ ....
Kocaeli University

Prof. Dr. Orhan KARSLI ....
Recep Tayyip Erdoğan University

Assoc. Prof. Dr. Gürsel SUNAL ....
Istanbul Technical University

Date of Submission : 10 July 2021
Date of Defense : 09 Aug 2021

To my late grandparents and beloved family,

FOREWORD

First of all, I would like to thank my advisor, Prof. Dr. Şafak ALTUNKAYNAK. Throughout this long journey, we had numerous scientific debates on geochemistry, structural geology and petrology of the study area. My academic background was largely shaped by her unwavering encouragement and support. She also went above and beyond in assisting me with my obsessive-compulsive disorder and perfectionism. Without her understanding, this thesis could not be completed. She will always be a member of my family.

My special thanks belong to another family member, Dr. Alp ÜNAL, also known as “Alpittin reis”, who are not any different from my brother which I do not have in my non-academic life. Without his support, this thesis would not be successful. He will always stay an important part of my life. At this time, I must acknowledge the numerous contributions of Ph.D. student Işıl Nur Güraslan, a.k.a. Isildur Güraslan.

A lot of people have contributed to this thesis that I am grateful to. Especially, I would like to thank my thesis committee Prof. Dr. Ş. Can GENÇ and Prof. Dr. Ercan ALDANMAZ for their kind and helpful suggestions for my Ph.D. study. Prof. Dr. Yucel YILMAZ, Prof. Dr. Serdar AKYÜZ, and Assoc. Prof. Dr. Gürsel SUNAL have also made significant contributions. I would also like to thank Prof. Dr. Attila KILINÇ for his instructive and enjoyable discussions on computational thermodynamics and crystal size distribution throughout my time at the University of Cincinnati.

Gün AKINCI and Serhat YARAR did an excellent job with the field study. We worked well together in the scorching heat of the Aegean region. I would like to acknowledge the contributions of geologists Elif KARADAĞ and Zeynep ÇALIŞKANOĞLU during the sampling period.

Salih ÇEBİ, Tekin KÜÇÜKALİ and Mustafa KAMACI deserve special thanks for their financial and logistical support during the study. TUBİTAK (Scientific and Technological Research Council of Turkey) also provided me with a scholarship to study at the University of Cincinnati as a visiting scholar, which I greatly appreciated.

Finally, not only throughout this thesis but throughout my life, my entire family, particularly my beloved wife Öznur, has been incredibly supportive. I couldn't have managed without them, and I love you so much.

JULY 2021 Ömer KAMACI
(Geologist)

TABLE OF CONTENTS

Page

FOREWORD .... **ix**
TABLE OF CONTENTS .... **xi**
LIST OF TABLES .... **xiii**
LIST OF FIGURES .... **xiii**
SUMMARY .... **xix**
ÖZET .... **xxi**
1. INTRODUCTION **1**
1.1 Scope of Thesis 4
1.2 Structure of the Thesis 4
2. THE ÇATALDAĞ PLUTONIC COMPLEX IN WESTERN ANATOLIA; ROLES OF DIFFERENT GRANITES ON THE CRUSTAL BUILD-UP IN CONNECTION WITH THE CORE COMPLEX DEVELOPMENT **7**
2.1 Introduction 7
2.2 Çataldag Plutonic Complex (ÇPC) 10
2.2.1 The Granite-Gneiss-Migmatite Complex (GGMC) 11
2.2.2 The Çataldağ Granodiorite (ÇG) 14
2.3 Structural Data 16
2.3.1 Çataldağ Detachment Fault Zone (ÇDFZ) 16
2.3.2 Deformation of the Granite-Gneiss-Migmatite Complex (GGMC) 19
2.3.3 Deformation of the Çataldağ Granodiorite (ÇG) 22
2.4 LA–ICP–MS Geochronology 23
2.4.1 Analytical methods 23
2.4.2 Results 24
2.5 Ar/Ar Geochronology 25
2.5.1 Analytical methods 25
2.5.2 Results 27
2.6 Discussion 30
2.6.1 Emplacement of the Granite-Gneiss- Migmatite Complex (GGMC) 30
2.6.2 Emplacement of Çataldağ Granodiorite (ÇG) 31
2.6.3 The timing of ductile to brittle deformation and uplift of ÇPC 32
2.6.4 Roles of different granites on the Cenozoic crustal build-up in connection with the core complex development 33
2.7 Conclusions 36
3. COOLING AND DEFORMATION HISTORY OF THE ÇATALDAĞ METAMORPHIC CORE COMPLEX (NW TURKEY) **39**
3.1 Introduction 39
3.2 Lithologies and Kinematics 42
3.3 Analytical Methods: Two-feldspar Thermometry 45
3.4 Microstructures and Two-feldspar Thermometry 47
3.4.1 The submagmatic-to-solid state ductile deformation zone (DZ) 47
3.4.1.1 The ductile zone of the ÇSP 47
3.4.1.2 The ductile zone of the TGMC 48

3.4.1.3 Deformation temperatures of DZ 48
3.4.2 Mylonitic zone (MZ) 49
3.4.2.1 The mylonitic deformation zone of ÇSP 49
3.4.2.2 The mylonitic deformation zone of the TGMC................................. 51
3.4.2.3 Deformation temperatures of the MZ.. 53
3.5 Discussion.. 54
3.5.1 Exhumation history and the Early Miocene deformation of the TGMC... 54
3.5.2 Cooling and deformation history of the ÇSP along the ÇDFZ 55
3.5.3 Emplacement, deformation and cooling of Oligo-Miocene syn-extensional granitoids in Western Anatolia 58
3.6 Conclusions 63
4. THE ROLE OF ACCRETED CONTINENTAL CRUST IN THE FORMATION OF GRANITES WITHIN THE ALPINE STYLE CONTINENTAL COLLISION ZONE: GEOCHEMICAL AND GEOCHRONOLOGICAL CONSTRAINS FROM LEUCOGRANITES IN THE ÇATALDAĞ METAMORPHIC CORE COMPLEX (NW TURKEY) 65
4.1 Introduction 65
4.2 Geological Background 67
4.3 Morphology and Petrography... 69
4.4 Analytic Methods 75
4.4.1 Major, trace and isotope geochemistry... 75
4.4.2 In-situ Ti-in-zircon analysis 76
4.5 Geochemistry.. 76
4.5.1 Major and trace element characteristics 76
4.5.2 Sr, Nd, Pb isotopes 82
4.6 Petrogenesis of Leucogranites 84
4.6.1 Source characteristics and melt evolution 84
4.6.2 P-T conditions and melting mechanism 86
4.7 Evidences for the Role of Accreted Continental Crust in the Formation of Çataldağ Leucogranites 92
4.8 Conclusions 96
5. CONCLUSIONS... 97
REFERENCES 99
APPENDICES 119
CURRICULUM VITAE 141

LIST OF TABLES

Page

Table 3.1 : Chemical composition of feldspars and two-feldspar thermometer results of ÇCC based on the equations of Putirka 2008. .... **50**
Table 3.2 : Detailed microstructures of the ÇCC **52**
Table 3.3 : Geochronology of GGMC and ÇSP and deformation zones **56**
Table 3.4 : Correlation of deformed granitoids of Anatolian Core Complexes........ **61**
Table 4.1 : Major oxides and trace element analyses of GGMC in Çataldağ Core Complex **78**
Table 4.2 : Sr, Nd, Pb isotope geochemistry analyses of GGMC in Çataldağ Metamorphic Core Complex **83**
Table 4.3 : Ti-in-zircon thermometry results of leucogranites in Çataldağ Metamorphic Core Complex **87**
Table A.1 : U/Pb LAICPMS age data of the CPC.……………………………….**120**
Table A.2 : $^{40}Ar/^{39}Ar$ ages obtained from the CPC………………………………..**126**

LIST OF FIGURES

Page

Figure 2. 1: Simplified tectonic map of the Aegean region showing major tectonic units, metamorphic massifs, Eocene and Oligo-Miocene granitoids. Red box shows the study area. (Modified from Bonev el al., 2006; Cavazza et al 2009; Erkül, 2010). Extension-related Early Miocene plutons: 1-6, 1-Salihli, 2-Turgutlu, 3-Eğrigöz, 4-Koyunoba, 5-Yenice, 6-Eybek granite……………………………….. ..**9**
Figure 2. 2: a) Geological map of the Çataldağ Plutonic Complex. b) NW-SE cross-section of CPC (A-A'); c) N-S cross-section showing the GGMC (B-B'); d) N-S cross-section of the ÇG (C-C'). Map coordinates: Universal Transverse Mercator (UTM) projection, zone 35. .... **10**
Figure 2. 3: GGMC units: a, b) Two-mica granite; c, d) Gneiss; e) Schollen type of migmatites (after Mehnert, 1968): including melanosome and leucosomes (UTM coordinate 35S 612620/4421440); Ms: muscovite, Kf: K-feldspar, Bi: biotite, Q: quartz, Pl: plagioclase, Gr: garnet. Magnification for b and d is 4X, crossed plane. **12**
Figure 2. 4: Mafic syn-plutonic dyke within the GGMC (UTM coordinate 35S 618185/4417585). **13**
Figure 2. 5: a, b) Typical K-feldspar megacrystals forming porphyritic texture of ÇG (UTM coordinate 35S 607975/4414830); c) intrusive contact between ÇG and metamorphic country rock in western boundary (UTM coordinate 35S 601249/4403663). Kf: K-feldspar, Magnification for b is 4X, crossed plane. **14**
Figure 2. 6: Augen-gneiss in the ÇDFZ with top-to-the north sense of feldspar-fish and step-over structures in northern border of ÇG, C: shear plane, S: schistosity plane. **15**
Figure 2. 7: The fault plane structures of the ÇDFZ a) low angle fault plane and undulation; b) slickenline and rake (UTM coordinate 35S 616580/4422555). **16**
Figure 2.8: a) Hanging wall and footwall of the ÇDFZ in the eastern border of GGMC (UTM coordinate 35S 629500/4418835); b) mylonites (UTM coordinate 35S 618730/4419565); c) microphotograph of top-to-the north sense muscovite-fish from the outer zone of the GGMC, crossed plane, 10X magnification; d) boudinage of the leucosomes in migmatite of the GGMC (UTM coordinate 35S 612345/4419795); **17**
Figure 2. 9: a) Google Earth image of the low angle fault plane of the ÇDFZ and b) turtle-back structure in south of the ÇG. (UTM coordinate 35S 612574/4409832). **18**
Figure 2.10: Structural reconstruction of ÇPC and ÇDFZ; a) the initial shape of the ÇDFZ before oblique dextral-normal faulting; b) Recent shape of ÇDFZ after the oblique dextral-normal faulting. **19**
Figure 2. 11: Strike and dip of foliations and plunge and azimuth of stretching lineations in structural map of ÇPC. **20**

Figure 2. 12: Lower hemisphere equal-area projections of foliation (a, b, c, d) and lineation (e) from the ÇPC: a) foliations for inner zone of the GGMC; b) foliation for the eastern outer zone of the GGMC; c) foliations for the northern outer zone of the GGMC; d) foliations for the northern border of the ÇG; e) lineation for the GGMC. **21**
Figure 2. 13: Movement direction of hanging-wall **23**
Figure 2. 14: Cathodoluminiscence (CL), back-scattered (BSE) images and U/Pb LA–ICP–MS Zircon and monazite ages of GGMC. **26**
Figure 2. 15: Results of $^{40}Ar/^{39}Ar$ geochronology of porphyritic granodiorite of ÇG **28**
Figure 2. 16: Results of $^{40}Ar/^{39}Ar$ geochronology of gneiss and two-mica granite of GMMC **29**
Figure 2. 17: Graphical abstract showing contact relationships and deformational structures in ÇPC. **31**
Figure 3.1: Simplified tectonic map of the Aegean region showing the major tectonic units, metamorphic massifs and the western Anatolian deformed granites/leucogranites (shown by stars) in Çataldağ, Menderes and Kazdağ Core Complex. **41**
Figure 3.2: Simplified geological and structural map of the Çataldağ Metamorphic Core Complex (ÇMCC). Colour index of geothermocronological data is as following: U-Pb Zircon (red) and monazite (orange), $^{40}Ar/^{39}Ar$ muscovite (green), biotite (blue) and K-feldspar (black) ages with mineral closure temperature in same colour. **42**
Figure 3.3: Progressive deformation of the ÇSP from sub-magmatic to solid-state deformed granodiorite (DZ) to solid-state to brittle mylonitic gneiss (MZ) that shows top-to-the-north sense of shear and a model of the synkinematic nature of the ÇSP. Deformation temperatures are obtained from two-feldspar thermometer. **43**
Figure 3.4: DZ and MZ deformations in the TGMC under ÇDFZ. Deformation temperatures are obtained from two-feldspar thermometer. **44**
Figure 3.5: Shear sense indicators of the ÇMCC along the mylonitic zone (MZ): a) σ-type muscovite-fish structures, b) biotite-fish, c) truncated K-feldspar-fish, d) domino-type feldspar microfracture, e) asymmetric poly-mineralic (quartz-feldspar) shear fold with C-S structures, f) σ-type feldspar-fish structures following brittle deformation, g and h) δ-type and σ-type winged mantled feldspar by quartz in metatexite, respectively. **46**
Figure 3. 6: Microstructures of the ÇSP and evolution of temperature-deformation path: a) rock-chip of granodiorite, b) chessboard extinction (CBE) of quartz, c) myrmekite replacement in margin of K-feldspar megacryst, d) rock-chip of deformed granodiorite, e) quartz grain boundary migration (GBM), f) flame-shaped perthite (FSP), g) rock-chip of mylonitic (augen) gneiss, h) Feldspar-fish, and i) the quartz subgrain rotation recrystallisation (ÇSPR), quartz-ribbons, bulging recrystallisation (BLG), and late stage fracturing of K-feldspar. Q: quartz, Kf: K-feldspar, P: Plagioclase. **49**
Figure 3. 7: Microstructures of the TGMC and evolution of temperature-deformation path: a) rock-chip of gneiss, b) quartz subgrain rotation recrystallization (ÇSPR); c) bulging recrystallization (BLG) of K-feldspar, d) rock-chip of mylonite, e) domino-type microfracture of brittle K-feldspar, f) quartz ribbon structures, g) rock-chip of ultramylonite, h) elongated biotites in

cataclastic flow and i) maximum grain-size reduction in cataclastic flow. Q: quartz, Kf: K-feldspar, M: mica (muscovite). **51**
Figure 3. 8: a) Evolution of temperature and strain intensity on the microstructures of the ÇMCC. b) Comparison diagram of temperature estimation of deformation zones from microstructures and two-feldspar thermometry. Quartz microstructures, GBM: Grain boundary migration, SGR: Subgrain rotation recrystallisation, BLG: Bulging recrystallisation, ÇDFZ: Çataldağ Detachment Fault Zone, FDBTZ: Feldspar ductile-to-brittle transition zone, QDBTZ: Quartz ductile-to-brittle transition zone **53**
Figure 3.9: a) Two-stage cooling of the TGMC and rapid cooling of ÇSP based on microstructures, two-feldspar geothermometer and geothermochronology. b) Evolution of cooling rates from the Latest Eocene to the Early Miocene of the deformed plutons of western Anatolia. D/B transition: ductile-brittle deformation. **57**
Figure 4. 1: Simplified map of the main tectonic units and plutonic rocks of Western Anatolia in the study area. **68**
Figure 4. 2: a) Geological map of the Çataldağ Plutonic Complex. b) NW-SE cross-section of CPC (A-A'); c) N-S cross-section showing the GGMC (B-B'); d) N-S cross-section of the ÇG (C-C'). Map coordinates: Universal Transverse Mercator (UTM) projection, zone 35................................ **70**
Figure 4. 3: Migmatites in field and microphotographs. Leucosome pockets in metatexite (a), syn-migmatitic bands (b), leucogranitic veins in metatexite (c); schlieren in diatexite (d); diatexite (dirty granite) (e); microphotographs under cross-polarized light (f) and plane-polarized light (g) of melanosome. Magnification of thin section photographs: 4X. **71**
Figure 4. 4: Field photograph and microphotographs under plane-polarized light (b) and cross-polarized light (c) of garnet-bearing leucogranite. Gr: garnet, Pl: plagioclase, Kf: K-feldspar and Q: quartz. Magnification of thin section photographs: 4X. **73**
Figure 4. 5: Two-mica granite in field and microphotographs under cross-polarized light (b) and plane-polarized light (c). Magnification of thin section photographs: 4X. **74**
Figure 4. 6: Field photographs of the mafic syn-plutonic dyke typically showing irregular and fragmented margins with leucogranite........................... **75**
Figure 4. 7: Classification and chemical variation diagrams of GGMC samples. A) Total alkalis (Na2O + K2O) versus silica diagram; alkali and sub-alkali line is labelled according to Miyashiro (1978); B) K2O versus SiO2 diagram distinguishing tholeiitic, calc-alkaline, high-K calc-alkaline and shoshonitic series, after Peccerillo and Taylor (1976); C) ASI (aluminium saturation index) diagram of the GGMC (Maniar and Piccoli, 1989); D) Peraluminous classification of leucogranite (Villaseca et al, 1998). **80**
Figure 4. 8: Harker variation diagrams for the leucogranite samples, illustrating correlations between MgO, FeOt, CaO, Al2O3, Th and Sr with SiO2. **81**
Figure 4. 9: Primitive mantle-normalized (Sun and McDonough, 1989) and chondrite-normalized (Boynton, 1984) trace element diagrams for the GGMC. . **82**
Figure 4. 10: A) $\varepsilon Nd_{(33)}$ vs. $^{87}Sr/^{86}Sr_{(33)}$ diagram for GGMC samples. Bulk mixing line between syn-plutonic gabbro-dioritic dyke with mica-schist (Sample OS-

77) from Western Anatolian Orogenic Crust (WAOC); and enriched mantle melts (Deschamps et al, 2017) with micaschist. Data sources: Altunkaynak et al. (2012a and b); Erkül and Erkül (2012). B) εNd(i) vs. TDM (Nd-model ages) diagram of leucogranite and mafic dyke samples. Dashed line shows the possible mixing trend between the two rock types. C) $^{87}Sr/^{86}Sr_{(33)}$ vs $^{206}Pb/^{204}Pb$ isotopes diagram. D) $^{143}Nd/^{144}Nd_{(33)}$ vs $^{206}Pb/^{204}Pb$ isotopes diagram. Data sources: Asthenosphere, SC, ATP granites (Altunkaynak et al, 2012 and the references therein). **85**

Figure 4. 11: In-situ Ti-in-zircon thermometry of leucogranite samples. A) BSE images of different zircon generations, ages and temperatures. B) 206Pb/238U ages versus temperatures obtained from Ti-in-zircon thermometry. **88**

Figure 4. 12: Partial melting signatures of leucogranites. A) La vs LaN/YbN diagram; B) crustal source characteristics of leucogranites (Patino Douce and Harris, 1998); Average Al-Ti temperatures versus Rb/Zr (C) and Th (D) as partial melting index. **89**

Figure 4. 13: Melting mechanisms of leucogranite. A) Na_2O/K_2O vs FeO diagram of melt compositions for different melting reactions. B and C) Correlation of Ms-dehydration, Bt-dehydration and water-present mica dehydration melting mechanisms. **90**

Figure 4. 14: P-T conditions of water-absent dehydration melting of mica-schist from the study area (OS-77). GBL: Garnet-bearing leucogranite; TMG: Two-mica leucogranite. **92**

Figure 4. 15: Eocene magmatic thickening and thermal weakening of Western Anatolian orogenic crust. Partial removal of young orogenic crust triggered by slab retreat beneath the Hellenic arc caused upwelling of the hot asthenosphere, migmatization, partial melting of subducted continental crust and metasomatized lithospheric mantle to form leucogranitic melts. **95**

ORIGIN, AGE AND DEFORMATION HISTORY OF THE ÇATALDAĞ METAMORPHIC CORE COMPLEX

SUMMARY

In this thesis, a new metamorphic core complex was identified in NW Anatolia, located between Balıkesir and Bursa cities, and named as Çataldağ Metamorphic Core Complex (ÇMCC) based on thorough field observations, meso-microstructural features, geochronology and geochemistry data. The ÇMCC is divided into three parts with different structural characteristics: (1) footwall rocks; (2) the hanging wall rocks and (3) a mylonitic shear zone separating the footwall rocks from the hanging wall rocks. The footwall rocks are made up of a granite-gneiss-migmatite complex (GGMC) in which migmatitic rocks experienced HT/LP metamorphism in amphibolite (upper amphibolite?) facies; and a synkinematic granitic intrusion (Çataldağ syn-kinematic pluton: ÇSP). The hanging wall rocks are composed of basement rocks of the Sakarya continent, supra-detachment sediments and Neogene lacustrine sediments. The mylonitic shear zone, on the other hand, consists of footwall rocks that underwent continuous ductile to brittle deformation below the Çataldağ detachment fault zone (ÇDFZ), which separates the footwall and hanging wall rocks.

U-Pb zircon and monazite ages of anatectic leucogranites range from 33.8 ±0.14 Ma. to 30.1 ±0.23 Ma (Late Eocene-Early Oligocene). $^{40}Ar/^{39}Ar$ ages obtained from biotite, muscovite, and feldspar minerals of the footwall rocks and the mylonitic rocks vary from 20.7±0.1 Ma to 21.3±0.3 Ma (Early Miocene). The $^{40}Ar/^{39}Ar$ biotite ages of the ÇSP range from 20.8±0.1 Ma to 21.1±0.02 Ma. These age data clearly indicate that GGMC and ÇSP were formed in different periods (Eo-Oligocene and Early Miocene, respectively), but they uplifted together during the Early Miocene (21.3–20.7 Ma).

Microstructural studies on quartz, feldspar and mica minerals show that GGMC and ÇSP underwent continuous deformation from ductile to brittle conditions during their cooling and exhumation with top-to-north and top-to-northeast sense of shear. Two main deformation zones were determined within the ÇMCC, based on the temperature and the intensity of the strain: The ductile deformation zone at the central parts of GGMC and ÇSP; and the mylonitic zone at the peripheral zones of the GGMC and ÇSP, through the ÇDFZ. Within the ductile zone, microcline twinning, myrmekite development along the K-feldspar megacrysts, flame-shaped perthite, chessboard extinction, grain boundary migration and sub-grain rotation recrystallization of quartz are observed. These microstructures indicate that dynamic recrystallization processes at high temperatures (>600^{o}C–450^{o}C) were dominant in the ductile zone. In the mylonitic zone, mylonitic gneiss and schists show distinct foliation which is accompanied by C-S structures in K-feldspar and micas, and ribbon structures in quartz. In addition, feldspars show bulging recrystallization, feldspar-fishes and domino-type microfractures. These microstructures indicate that the dynamic deformation within the mylonitic zone was continuous from the mid-temperature (500^{o}C–<250^{o}C) to brittle conditions.

Two-feldspar thermometer calculations estimated that the deformation temperatures for the ductile and mylonitic zone were 501–588°C (avg. 544°C for ÇSP and avg. 517°C for GGMC) and 430–557°C (avg. 484°C for ÇSP and avg.436°C for GGMC), respectively. Microstructures, two-feldspar geothermometry and thermochronology data show that the GGMC cooled slowly (<50 °C/my) during the Eo-Oligocene and then rapidly (> 500 °C/my) during the Early Miocene (21 Ma) along the ÇDFZ. The ÇSP, on the other hand, was gradually deformed from sub-magmatic to brittle conditions and cooled rapidly (> 500 °C/my) in the Early Miocene (21 Ma).). The Early Miocene granodioritic intrusion was considered as a "synkinematic" pluton (Çataldağ Syn-kinematic pluton: ÇSP) which was emplaced at shallow depths along the ÇDFZ due to its progressive sub-solidus deformation, C-S fabrics, and spatiotemporal link with the ÇDFZ,

The Eo-Oligocene granites within the GGMC are represented by peraluminous garnet-bearing leucogranite and two-mica leucogranite. Garnet-bearing leucogranites consist of quartz (30-35%) + plagioclase (25-30%) + K-Feldspar (25-30%) + muscovite (5%) + garnet (2%) ± biotite, while two-mica leucogranites is formed from quartz (30-35%) + plagioclase (25-30%) + K-Feldspar (20-22%) + biotite (5-8%) + muscovite (3%) ± garnet. Both leucogranite types are enriched in LREE (Rb, U, K, Pb) and depleted in HFSE (Nb, Ta, Zr, Ti). Their $^{87}Sr/^{86}Sr$, $^{206}Pb/^{204}Pb$ and $^{207}Pb/^{204}Pb$ initial isotope values range from 0.7094 to 0.7113, 18.79 to 18.91, and 15.71 to 15.73, respectively, and $\varepsilon Nd_{(33)}$ values vary between -5.13 and -7.79. On the other hand, gabbroic syn-plutonic dykes show similar isotopic characteristics ($^{87}Sr/^{86}Sr_{(33)}$ = 0.7055, $\varepsilon Nd_{(33)}$ = -1.8 and $^{206}Pb/^{204}Pb$ = 18.8) to enriched mantle melts. Trace element and isotope models show that the leucogranites have a dominant crustal melt component (85-70%) and a minor mantle component (<30%). Partial melting modeling (via PhasePlot/MELTS) and Ti-in-zircon thermometer calculations indicate that the leucogranitic melt was formed by water-absent muscovite dehydration melting of a mica-schist source (a melt fraction of max. 35%) at ≥ 7–10 kb and 739–840 °C. The inherited zircon core ages of the leucogranites change between Precambrian and Cambrian. T_{DM} model ages of the leucogranites are relatively high (> 1.2 Ga). Whole-rock geochemistry, isotopic features, T_{DM} ages, and inherited zircon chronology combined with the geology of the region indicate that leucogranitic melts were formed by the partial melting of the Anatolide-Tauride continental crust which was underthrusted below the Sakarya Continent along the İzmir-Ankara Suture Zone. The source of the syn-plutonic mafic (gabbro-diorite) dykes within the core of the ÇMCC, on the other hand, is inferred to be derived from the enriched mantle (EMII) beneath western Anatolia.

It is inferred that the migmatization and melt generation which produced leucogranites were most likely caused by thermal weakening and partial removal of the western Anatolian young orogenic lithosphere during the transitional phase between the latest phase of collision and the earliest phase of extension, in the Eo-Oligocene. The exhumation of GGMC and ÇSP as a domal-shaped core complex at the footwall of the Çataldag detachment fault was developed under the back-arc extension driven by slab rollback beneath the Hellenic arc during the Early Miocene.

ÇATALDAĞ METAMORFİK ÇEKİRDEK KARMAŞIĞI'NIN KÖKENİ, YAŞI VE DEFORMASYON TARİHÇESİ

ÖZET

Bu tez çalışmasında, kapsamlı saha gözlemleri, mezo-mikro yapısal özellikler, jeokronoloji ve jeokimya verilerine dayandırılarak KB Anadolu'da, Balıkesir ve Bursa şehirleri arasında, yeni bir metamorfik çekirdek kompleksi tanımlanmış ve Çataldağ Metamorfik Çekirdek Kompleksi olarak adlandırılmıştır. ÇMCC üç kısımdan oluşur: (1) taban bloğu kayaları; (2) tavan bloğu kayaları ve (3) taban bloğu kayalarını tavan bloğu kayalarından ayıran milonitik bir makaslama zonu. Taban bloğu kayaları, amfibolit fasiyesinde (Üst Amfibolit?) HT/LP metamorfizmasına uğramış migmatit, gnays ve anatektik lökogranitlerden (granit-gnays-migmatit kompleksi: GGMC) ve sinkinematik nitelikli bir granitik sokulumdan oluşur (ÇSP). Tavan bloğu kayaları Sakarya kıtasına ait yeşil şist fasiyesinde metamorfizmaya uğramış temel kayaları, supra-detachment çökelleri ve Neojen yaşlı göl çökelleri ile temsil edilmektedir. Makaslama zonu ise, varlığı bu çalışmada ortaya konan Çataldağ sıyrılma fay zonu (ÇDFZ) altında sünekten kırılgana değişen sürekli deformasyona uğramış taban bloğu kayalarını içerir.

Lökogranitlerden elde edilen U-Pb zirkon ve monazit yaşları, 33,8 ± 0,14 My ile 30,1 ± 0,23 My (Geç Eosen-Erken Oligosen) arasında değişir. Taban bloğu ve milonitik zon içerisindeki örneklerden alınan $^{40}Ar/^{39}Ar$ (muskovit, biyotit ve K-Feldispat) yaşları 20,7 ± 0,1 ile 21,3 My ± 0,3 My (Erken Miyosen) arasında, ÇSP'nin $^{40}Ar/^{39}Ar$ biyotit yaşları ise 20,8 My ± 0,1 ile 21,1 ± 0,02 My arasında değişir. Bu veriler, GGMC (Eo-Oligosen) ve ÇSP (Erken Miyosen)'nin farklı dönemlerde oluştuğunu, ancak Erken Miyosen'de (21,3–20,7 My) birlikte yükseldiklerini ortaya koyar.

Mikroyapısal özellikleri GGMC ve ÇSP'nin yükselme ve soğuma sürecinde, kuzeye ve kuzeydoğuya yönlü, sünekten kırılgana değişen sürekli bir deformasyona maruz kaldıklarını göstermektedir. Deformasyonun şekli, şiddeti ve sıcaklığına göre ÇMCC içerisinde sünek deformasyon zonu ve milonitik zon olmak üzere iki ana deformasyon zonu tanımlanmıştır. Sünek deformasyon zonu GGMC ve ÇSP'nin merkezi zonlarında gözlenir. Bu zonda, mikroklin ikizlenmesi, K-feldspar megakristalleri çevresinde mirmekit oluşumları, ateş-şekilli pertit; satranç tahtası sönmesi, tane sınırı göçü ve tanecik rotasyonu yapıları görülür. Sünek zonda gözlenen mikro yapılar yüksek sıcaklık koşullarında (>600°C–450°C) dinamik rekristalizasyon süreçlerinin etkin olduğuna işaret eder. Milonitik zon ise ÇDFZ'ye yakın alanlarda izlenen sünek ve üzerleyen kırılgan deformasyon zonudur. Bu zonda milonitik gnays ve şistler içindeki K-feldspat ve mikalarda C-S yapıları gözlenir, kuvarslar ise kurdele yapıları sergiler. Ayrıca, K-feldispatlarda şişme rekristalizasyonu, feldspat balıkları ve domino tipi mikro çatlaklar gözlenir. Tüm bu mikro yapılar, milonitik zondaki dinamik deformasyon koşullarının orta-düşük sıcaklardan (500°C–<250°C) kırılgan koşullara kadar devam ettiğini göstermektedir.

İki-feldispat termometresi hesaplamaları ile, sünek zon için deformasyon sıcaklığı 501–580°C (ÇSP için ort. 544°C; için ort. 517°C), milonitik zon için ise 430–557°C (ÇSP için ort. 484°C; GMMC için ort. 436°C) olarak saptanmıştır. Mikrotektonik, iki-feldispat jeotermometresi ve termokronoloji verileri birlikte değerlendirildiğinde, GGMC'nin Eo-Oligosen boyunca yavaş (<50 °C/my) ve Erken Miyosen'de (21 My) ÇDFZ boyunca hızlı (>500 °C/my) soğuduğu söylenebilir. ÇSP ise ÇDFZ etkisi altında sub-magmatikten kırılgana kademeli olarak deforme olmuş ve Erken Miyosen'de (21 My) hızla soğumuştur (>500 °C/my). Çevre kayaçlarla olan dokanak ilişkileri, submagmatikten kırılgana değişen deformasyonu ve ÇDFZ ile zamansal ve mekansal ilişkisi ÇSP'nin kabukta sığ derinliklere sinkinematik olarak yerleşmiş bir magmatik gövde olduğunun göstergeleridir.

GGMC içinde bulunan granitler peralüminyumlu garnet-lökogranit ve iki-mikalı lökogranit ile temsil edilir. Garnet-lökogranit, kuvars (% 30-35) + plajiyoklaz (% 25-30) + K-feldispat (% 25-30) + muskovit (% 5) + granat (% 2) ± biyotitten oluşmaktadır. İki mikalı lökogranitler ise kuvars (% 30-35) + plajiyoklaz (% 25-30) + K-feldispat (% 20-22) + biyotit (% 5-8) + muskovit (% 3) ± granattan oluşur. Her iki lökogranit türü de hafif nadir toprak elementlerince (Rb, U, K, Pb) zenginleşmiş ve HFS elementleri (Nb, Ta, Zr, Ti) bakımından tüketilmiştir. ^{87}Sr / ^{86}Sr, ^{206}Pb / ^{204}Pb ve ^{207}Pb / ^{204}Pb ilksel izotop değerleri sırasıyla 0.7094 ile 0.7113, 18.79 ile 18.91 ve 15.71 ile 15.73 arasında ve $\varepsilon Nd_{(33)}$ ise değerleri -5.13 ile -7.79 arasında değişir. Öte yandan, yine GGMC içinde bulunan gabro-diyorit bileşimli sinplutonik dayklar, zenginleşmiş manto eriyiklerine benzer izotop özellikleri sergiler ($^{87}Sr/^{86}Sr_{(33)} = 0.7055$, $\varepsilon Nd_{(33)}=-1.8$ ve $^{206}Pb/^{204}Pb=18.8$).

İz element ve izotop jeokimya modellemeleri, lökogranitlerin baskın bir kabuk bileşenine (% 85-70) ve az oranda manto bileşenine (<% 30) sahip olduğunu gösterir. Kısmi ergime modellemesi (PhasePlot/MELTS kullanılarak) ve Ti-in-Zirkon termometresi, lökogranitleri oluşturan magmanın, mikaşist benzeri bir kaynak kayanın ergimesi ile oluştuğuna işaret eder (maksimum %35'lik bir ergime derecesi). Bu ergiyikler maksimum 7–10 kb basınç ve 739–840°C sıcaklık koşullarında, susuz muskovit dehidrasyon ergimesiyle oluşmuştur. Lökogranitlerin kalıntı zirkon çekirdek yaşları Prekambriyen'den Kambriyen'e değişir. TDM model yaşları ise > 1.2 Ga gibi yüksek değerler vermektedir. Tüm kayaç jeokimyası, izotopik özellikler, TDM yaşları ve kalıntı zirkon kronolojisi, bölgenin jeolojisi ile birlikte, lökogranitik ergiyiklerin, İzmir-Ankara Kenet Zonu boyunca Sakarya Kıtası'nın altına dalan Anatolid-Torid kıtasal kabuğunun kısmi ergimesiyle türediğine işaret etmektedir.

Bu çalışmadan elde edilen veriler bölge jeolojisi ile birlikte değerlendirildiğinde, migmatitleşme ve lökogranitleri üreten kabuksal eriyikler ve ilişkili mafik sinplütonik daykları oluşturan manto eriyikleri büyük olasılıkla, kıta-kıta çarpışmasının son aşaması ile Ege genişleme sisteminin erken dönemi arasındaki geçiş sürecinde, Eo-Oligosen'de gelişmiştir. Söz konusu ergiyiklerin gelişimi için gerekli ısı kaynağı, Batı Anadolu genç orojenik litosferinin (Eosen magmatizmasının etkisiyle) termal olarak zayıflaması ve litosferin tabanının kısmen giderilmesi sonucunda manto yükselimi ile karşılanmış olması muhtemeldir.

Erken Miyosen'de GGMC ve ÇSP'nin Çataldağ sıyrılma fayının taban bloğunda kubbe şeklinde bir çekirdek kompleksi olarak yükselmesi, Kazdağ ve Menderes metamorfik çekirdek kompleksleri ile uzay-zamansal olarak benzerdir. Bu dönemde geniş yayılım sergileyen ÇSP gibi plutonların, genişleme sistemiyle eşyaşlı (syn-extensional) olarak yerleşip, hızlıca soğurken deforme olması da yoğun üst kabuk deformasyonunun göstergesidir. Tüm bu genişlemeyle ilişkili yapılar K-G yönlü Helen Slabı'nın (diliminin) yay-ardı genişleme sistemi içinde gerçekleşmiş olmalıdır.

1. INTRODUCTION

“A core complex is a domal or arched geologic structure composed of ductilely deformed rocks and associated intrusions underlying a ductile-to-brittle high-strain zone that experienced tens of kilometers of normal-sense displacement in response to lithospheric extension”.

Teyssier & Whitney, 2002; Whitney et al. 2013.

Continental metamorphic core complexes (MCCs) have attracted great interest in the geoscience community since their discovery in the North American Cordillera and Aegean regions in the 1970s (e.g. Coney, 1973; Davis & Coney 1979; Davis et al. 1980; Crittenden 1980; Wernicke 1981; Coney, 1980; Lister and Davis, 1989; Bozkurt and Park, 1994). It is widely accepted that MCCs occur in response to lithospheric extension driven by plate divergence (rifted continental margins) or by plate convergence (slab roll-back, orogenic collapse) (Armstrong, 1972; Coney, 1980; Flecher and Hallet, 1983; Wernicke, 1985; Yin, 1991). However, the formation of some MMCs, such as Karakoram and Pamir domes in Himalayan MCC, have been attributed to compressional tectonics (Burg et al., 1984; Lee et al., 2004; Cottle et al. 2009). Therefore, their origin and development mechanisms have been explained by different models. The four most popular of these models are: (a) Extension models: simple shear extension with a component of an isostatic rebound during crustal thinning (Wernicke, 1981; Davis, 1983; Lister et al. 1984; Wernicke & Axen, 1988) or transtension (McFadden et al. 2010; Erkül et al., 2017), (b) diapirism models: diapirism as a result of Rayleigh–Taylor instability, partial melting and density inversion (Ramberg, 1981; Rey et al. 2001; Vanderhaege & Teyssier, 2001; Teyssier & Whitney, 2002); (c) Compression models: doming above a thrust ramp (Burg et al. 1984), partial melt-induced channel flow (e.g. Godin et al. 2006; Searle et al. 2006; Cottle et al. 2009; Searle and Lamont 2020) or transpressional uplift (e.g. Matte, 2007); and (d) transitional models including partial melting in a compressional setting, and exhumation due to extension (Whitney et al., 2007; Lamont et. al, 2020).

Regardless of their origin, MCCs are a significant geological phenomenon, because they allow researchers to investigate the mid-to-lower continental crust and pattern of crustal flow that marks the continents' deep structure. They are also important locations for heat and material transfer from deep to shallow crustal levels and provide opportunities to monitor the thermal and mechanical processes in the lithosphere during the differentiation of continental crust (Rey et al., 2009; Whitney et al., 2013).

Another matter of debate regarding MMCs is the causal link among the metamorphic core complex formation/detachment faulting, the crustal melting and granitic magmatism. Numerical and analog modelings suggest that the geothermal gradient, the thickness of the continental crust, composition of the deep crust, the strain rate during extension, and the presence or absence of a hot lower crust are all crucial parameters that affect the interrelationship between MMCs, melting and plutonic activity (Brun, 1999; Tirel et al., 2008; Rey et al., 2009). The presence of hot lower crust, in particular, may cause a local thermal anomaly, resulting in crustal melting of the deep crust and granitic magmatism (Charles et al., 2012 and references therein). The exhumation velocity is another important factor in controlling the degree of partial melting in the core zone of MMCs. Slow exhumation rates lead to a low degree of partial melting and thus the formation of migmatite and gneiss cored MCCs whereas fast exhumation rates result in a significant degree of partial melting and granitic intrusions (Rey et al., 2009) and thus the formation of granite-cored MMCs. Type of granitoids (I- or S-Types) in the footwall of MCCs are influenced not only by the exhumation velocity but also the intensity of regional extension. However, in many continental extensional domains, it has not been conclusively demonstrated whether granitic magmatism was a driving force or a passive consequence of extension that also leads to MCC development. Because MCC development is commonly accompanied by partial melting of the deep crust and/or lithospheric mantle and also heat and mass transfer towards the shallow levels of crust, leading to the complicated interplay between granitic magmatism and detachment faulting/MCC formation. Testing these interrelations require integrated field, structural, geochronological and petrological studies to constrain the relative timing between magmatism, strain localization and metamorphism, the geometrical relationship between granitoids and detachment faulting and characterization of magmatism (Foster and Fanning, 1997;

Vanderhaeghe, 2009; Vanderhaeghe and Teyssier, 2001; Whitney et al., 2004; Rabillard et al., 2018 and references therein).

The Aegean region and its eastern part, western Anatolia contains several extensional elements such as extensional basins, high-angle normal faults, detachment faults, and MCCs (Rhodope, Kazdağ, Menderes, and Cycladic MCC). MCCs are represented by Cordilleran-type MCC which are bounded by major detachment faults and contain high-grade metamorphic rocks, migmatites, and many granitic plutons emplaced into the footwall of detachment faults (Buick, 1991; Faure et al., 1991; Dinter and Royden, 1993; Gautier and Brun, 1994; Vandenberg and Lister, 1996; Gautier et al., 1999; Gessner et al., 2001; Altunkaynak and Dilek 2006; Pe-Piper and Piper, 2007; Altunkaynak and Genç, 2008; Denèle et al., 2011). Although the extensional origin has been widely considered for these MMCs, (Menderes: Bozkurt and Park, 1994; van Hinsbergen, 2010; Bozkurt et al., 2011; Cenki-Tok et al., 2016; Baran et al., 2017; Kazdağ: Okay and Satır, 2000; Bonev et al 2009; Cavazza et al 2009; Cyclades: Buick, 1991; Gautier and Brun 1994; Vandenberg and Lister 1996; Rey et al. 2011; Rhodope: Dinter and Royden 1993), the compressional and/or transitional origin is also argued for the Cycladic MCCs (Pourteau et al., 2010; Lamont et al 2020; Searle and Lamont 2020 and the references therein).

The studies on western Anatolian MMCs (Menderes and Kazdağ) mainly focus on their internal structure, thermochronology, metamorphism, and their relations to regional tectonics (Bozkurt and Park, 1994; Işık et al., 2004; Thomson and Ring, 2006; van Hinsbergen, 2010; Dilek et al., 2010; Bozkurt et al., 2011; Cenki-Tok et al., 2016; Okay and Satır, 2000; Bonev et al 2009; Cavazza et al 2009; Erkül et al., 2017; Altunkaynak et al, 2021). Although there are also some studies investigating the connection between MCCs and granitic magmatism in western Anatolia (Dilek et al, 2009; Catlos et al 2012; Erkül and Erkül, 2012; Erkül et al 2017), this issue remains poorly understood. For instance, partial melting and leucogranite generation in the core zones of the western Anatolian MMCs has received very little attention. The melting conditions, mechanisms, and deep-crustal source components of anatectic melts (leucogranites) in MCCs are almost completely unknown in the literature. Nature (temperatures and strain intensity) of microscale deformations of footwall rocks has received scant attention even in structural-oriented studies.

The aim of this thesis is to contribute to the above-mentioned discussions and the deficiencies in the literature, and more importantly, to introduce the Çataldağ metamorphic core complex (ÇMCC), which is described in this study for the first time, to the geology literature and to provide a framework for future studies on it.

1.1 Scope of Thesis

This study focuses on the origin, age, and deformation history of the Çataldağ metamorphic core complex (ÇMCC). It includes field and laboratory studies mainly from granitic rocks within the footwall of the ÇMCC. The main goals of the field studies (geological mapping, meso-structural mapping and sampling) were i) to discover the key field relationships between migmatites, gneiss and granites and Çataldağ detachment fault zone (ÇDFZ) ii) to collect critical structural data from the footwall and hanging wall rocks to understand their emplacement mechanisms and deformation history.

The scope and purpose of lab studies may be summarized as follows. 1) new major-trace element geochemistry, Sr-Nd-Pb isotope data, geochronology (U/Pb zircon and monazite) and Ti-in-zircon thermometry data from leucogranites to examine the origin and age of core rocks of ÇMCC. 2) detailed microstructural data, mineral chemistry (K-feldspar and plagioclase) combined with two-feldspar geothermometry calculations and Ar/Ar geochronology (muscovite, biotite and feldspar) from the footwall rocks to understand the deformation and cooling history of footwall rocks and also the relationship between detachment faulting and granitic magma emplacement at various depths.

Finally, all data and findings obtained from this study were evaluated together with the geology and tectonics of western Anatolia and a model was proposed for the formation of ÇMCC.

1.2 Structure of the Thesis

This thesis was organized into 5 chapters. Chapter I includes the introduction, chapters II to IV present the papers that were published during the preparation of this thesis and chapter V is the conclusions.

Chapter I is divided into two sections, the scope of the thesis and the structure of the thesis. The key objectives of the study and the importance of the findings are briefly clarified in this chapter.

Chapter II covers Kamacı et al, 2017, which is the first publication produced within the scope of this thesis. In this study, Çataldağ Metamorphic Core Complex and associated detachment fault zone (ÇDFZ) were defined for the first time, and the roles of different granites on the crustal build-up in connection with the core complex development were discussed based on field observations, petrographical and geochronological data. The footwall of ÇDFZ is formed from a deep-seated granite-gneiss-migmatite complex (GGMC) and a shallow level granitic intrusion (Çataldağ granodiorite: ÇG). U-Pb zircon (LA-ICPMS) and monazite ages of GGMC yielded ages of 33.8 and 30.1 Ma (Latest Eocene-Early Oligocene). $^{40}Ar/^{39}Ar$ (muscovite, biotite and K-feldspar) ages obtained from the GGMC yielded the deformation age span 21.38±0,05 Ma and 20.81±0.04 Ma, which is similar to the emplacement age (20.84±0.13 Ma and 21.6±0.04 Ma) of ÇG. The ÇG-GGMC pair represents a core complex (ÇMCC) that was exhumed as a dome structure in the footwall of a ring-shaped low-angle detachment (ÇDFZ) surface in the Early Miocene. Micro and mesoscale shear sense indicators show that the footwall rocks underwent ductile deformation which was superimposed by semi-brittle to brittle deformation, and also indicate top-to-N and top-to-NE sense of movement. It was concluded that the exhumation of ÇMCC occurred as a result of the combined effects of the thermal weakening of crust and roll-back of the Aegean subducted slab during the Oligocene-Early Miocene.

Chapter III is based on Kamacı and Altunkaynak, 2019 which presents the cooling and deformation history of the Çataldağ Metamorphic Core Complex (ÇMCC) based on detailed microstructural analyses and the two-feldspar thermometer (combined with previously published geochronology data in Kamacı et al., 2017). Two main deformation zones were determined according to temperature and strain intensity: a ductile deformation zone (DZ) within the central zones, and a mylonitic zone (MZ) within the peripheral zones of the ÇMCC. The DZ underwent high temperature (> 600-500 °C; sub-magmatic conditions) and low intensity of deformation while MZ experienced a temperature ranging from >500°C to <250 °C with a higher intensity of strain and ductile to brittle deformation. Consistent with the temperatures estimated from microstructural analyses, two feldspar geothermometry yields deformation temperatures of (501–588 °C) in DZ and of 430–557 °C in MZ. Integrated microstructure, two feldspar thermochronology and geochronology data reveal that Granite-Gneiss-Migmatite Complex (here referred to as TGMC) was cooled slowly (<50 °C/my) throughout the Eo-Oligocene and rapidly (>500 °C/my) along the ÇDFZ in the Early Miocene. The Early Miocene Çataldağ granodiorite (was referred to as ÇG in chapter I) was considered as a “synkinematic” pluton (Çataldağ Syn-kinematic Pluton, ÇSP) because of its progressive sub-solidus deformation, C-S fabrics and spatiotemporal relationship with the ÇDFZ. ÇSP was emplaced into shallow levels along ÇDFZ and cooled rapidly (>500 °C/my) in the Early Miocene (21 Ma). All these findings support that the Eo-Oligocene aged TGMC and Early Miocene aged ÇSP, which were emplaced into different levels in the crust, suffered continuous ductile-to-brittle deformation and were exhumed together along the ÇDFZ during the Early Miocene under the N-S extensional regime in western Anatolia.

Kamacı and Altunkaynak, 2020 forms the base for Chapter IV, which presents new major-trace element geochemistry, Sr-Nd-Pb isotope and Ti-in-zircon thermometry data from leucogranites and syn-plutonic mafic dykes connected to the gneiss-migmatite dome within ÇMCC. Here, researchers discuss granitic melt evolution within the context of the western Anatolian orogenic crust's syn-to post-collisional evolution. According to whole-rock geochemistry, isotopic characteristics, leucogranites have a dominant crustal melt component (85-70%) and a minor mantle component (<30%). Ti-in-Zircon thermometer calculations and geochemical modelings indicate that leucogranites melts were produced by water-absent muscovite dehydration melting of a micaschist source at ≥ 7–10 kb and 739–840 °C. Inherited zircon chronology and TDM ages reveal that source was Anatolide-Tauride crustal units that were underthrusted beneath the Sakarya Continent along the İzmir-Ankara suture zone. It is concluded that partial melting and melt migration to produce leucogranites were most likely linked to thermal weakening and partial removal of the western Anatolian young orogenic lithosphere during the Eo-Oligocene, the transitional phase between the late phase of collision and the early phase of extension.

In chapter V, the general conclusions of the thesis are summarized and presented.

2. THE ÇATALDAĞ PLUTONIC COMPLEX IN WESTERN ANATOLIA; ROLES OF DIFFERENT GRANITES ON THE CRUSTAL BUILD-UP IN CONNECTION WITH THE CORE COMPLEX DEVELOPMENT

2.1 Introduction

Studies on the extensional tectonics and the low-angle normal faults facilitated our understanding of the connection between granite ascent and emplacement mechanisms. Such insights have been contributed greatly to the "space problem" or "room problem", which were discussed since 1835 by Charles Lyell (Hutton et al., 1990). These processes are now believed to operate in many places including the Basin and Range (Gans et al., 1989), Sierra Nevada (Tobish et al., 1993), the Cyclades (Gautier et al., 1993), Papua New Guinea (Hill et al., 1995), Yemen (Geoffrey et al., 1998), the Tyrrhenian Sea (Jolivet et al., 1998), Greenland (Strachan et al., 2001) and the Menderes Massif (Çemen et al., 2006; Dilek et al, 2009; Erkül, 2010; Erkül and Erkül, 2012; Işık et al., 2004; Catlos et al., 2012; Okay and Satır 2000), where granite intrusions into extensional shear zones have been conclusively demonstrated.

The Aegean Province is a well-known region of extension (McKenzie, 1978; Lister et al., 1984; Taymaz et al., 1991; Jackson, 1994; Gautier and Brun, 1994; Dinter, 1998; McClusky et al., 2000; Jolivet and Faccenna, 2000; Jolivet et al., 2013). As a part of the Aegean Extensional Province, western Anatolia experienced intense extensional deformation and magmatism in the late Oligocene-Early Miocene, as manifested by the development of extensional basins, metamorphic core complexes, and widespread magmatism.

This chapter is based on the paper, Kamaci, Ö., Ünal, A., Altunkaynak, S., Georgiev, S., Billor, P., The Çataldağ Plutonic complex in western Anatolia; roles of different granites on the crustal build-up in connection with the core complex development, in "Active Global Seismology: Neotectonics and Earthquake Potential of the Eastern Mediterranean Region, 189-222, 2017.

Exhumation of lower to middle crustal rocks and the development of extensional metamorphic domes (Menderes and Kazdağ Metamorphic Core Complexes: Bozkurt and Park, 1994; Hetzel et al., 1995; Isik and Tekeli, 2001; Gessner et al., 2001; Ring et al., 2003; Bozkurt, 2007; van Hinsberg, 2010; Okay and Satir, 2000; Bonev et al., 2009; Cycladic Core Complex: Buick, 1991; Gautier and Brun, 1994; Vandenberg and Lister, 1996; Rhodope Core Complex: Dinter and Royden, 1993, Crete Core Complex: Jolivet et al., 1994; Kilias et al., 1994) occurred during the extension in western Anatolia and the adjacent regions.

Granitic plutonism and extension are broadly contemporaneous in many core complexes. There are many studies which display the detachment faults and the related normal faults played an important role in the exhumation of these granites in an extensional regime. Examples from the Menderes Core complex include the Salihli, Turgutlu, Egrigöz, Koyunoba, Baklan and Alasehir granites (Işık et al., 2003; Çemen et al., 2006; Dilek et al., 2009; Catlos et al., 2010; Erkül and Erkül 2012, Altunkaynak et al., 2012a) and from the Kazdağ core complex include the Evciler and Eybek plutons (Okay and Satir, 2000; Beccaletto et al., 2005; Bonev et al., 2009). However, there are some other studies on the granites of western Anatolia, suggesting that granite generation and emplacement of the coeval intrusions are not linked directly to any core complex development (the Eğrigöz and Koyunoba granites; Hasözbek et al., 2010). Other granitic bodies straddling on both sides of the Izmir-Ankara-Erzincan Suture Zone (IAESZ) and around the core complexes were uplifted also, when the overlying rocks were exhumed in the same period. Therefore, western Anatolia is among the best places to study interplay between extension and granite emplacement.

We have studied on Çataldağ plutonic complex (ÇPC) that is exposed to the immediate north of the IAESZ (Figure 2.1). The Çataldağ plutonic complex shows close spatial and temporal relationship to a detachment fault zone (Çataldağ detachment fault zone: ÇDFZ) and consists of two contrasting granitic bodies displaying different textural, structural and lithological features. Our geochronological data suggests these granitic bodies have also different emplacement ages corresponding to the Eo-Oligocene and the Early Miocene and thus represent magmatic phases shortly preceding and during the extension. This is the first detailed structural study that was conducted on Çataldağ plutonic complex and the ÇDFZ. Therefore, main purposes of this paper are: (1) to introduce structural (micro- and macro-structures) and geochronological (LA-ICP-MS ages on zircon and monazite and $^{40}Ar/^{39}Ar$ ages) data sets obtained from these two diverse granitic body, (2) to compare and correlate these data with Çataldağ Detachment fault zone (ÇDFZ) and the related deformations. The broader goal is to better define emplacement mechanisms of the Çataldağ Plutonic Complex and its role in the Cenozoic crustal build-up of western Anatolia, which can serve as a model for other regions of the world.

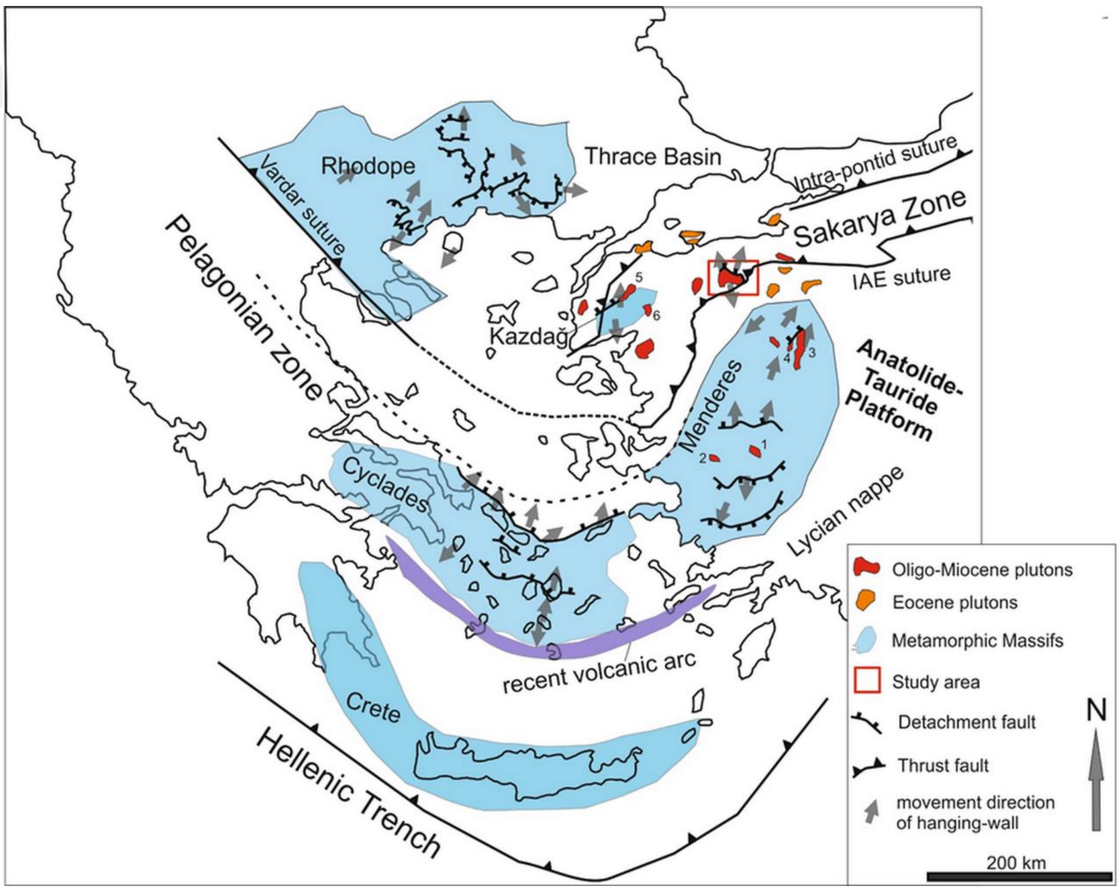

Figure 2.1 : Simplified tectonic map of the Aegean region showing major tectonic units, metamorphic massifs, Eocene and Oligo-Miocene granitoids. Red box shows the study area. (Modified from Bonev el al., 2006; Cavazza et al 2009; Erkül, 2010). Extension-related Early Miocene plutons: 1-6, 1-Salihli, 2-Turgutlu, 3-Eğrigöz, 4-Koyunoba, 5-Yenice, 6-Eybek granite.

2.2 Çataldag Plutonic Complex (ÇPC)

An older granite-gneiss-migmatite complex (GGMC) constitutes the eastern half of the ÇPC, whereas a younger granodioritic body (ÇG: Çataldağ granodiorite) and associated sills and dykes form in the western half.

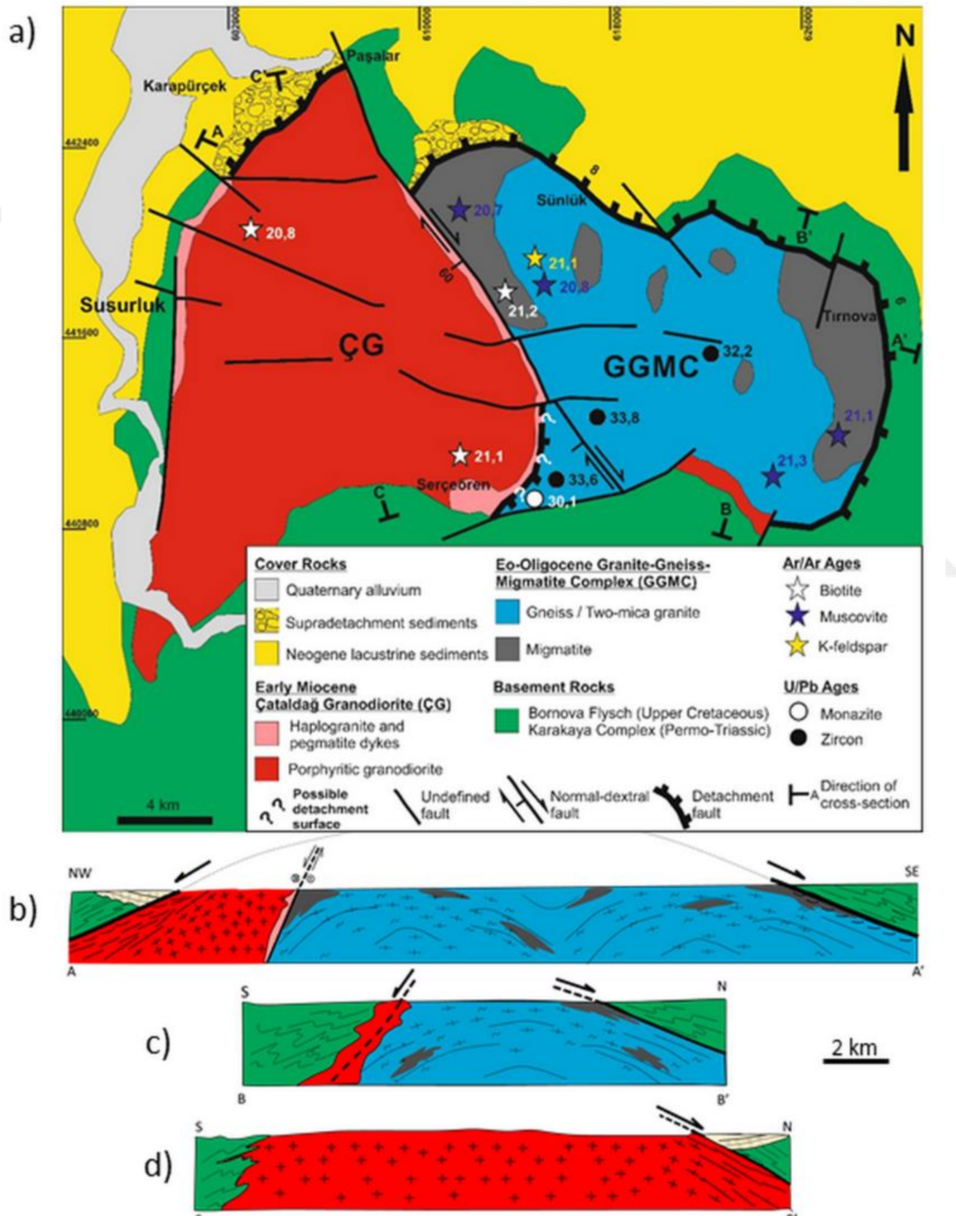

Figure 2.2 : a) Geological map of the Çataldağ Plutonic Complex. b) NW-SE cross-section of CPC (A-A’); c) N-S cross-section showing the GGMC (B-B’); d) N-S cross-section of the ÇG (C-C’). Map coordinates: Universal Transverse Mercator (UTM) projection, zone 35.

2.2.1 The Granite-Gneiss-Migmatite Complex (GGMC)

The GGMC of the ÇPC is located around Turfaldag Mountain (Figure 2.2a). The GGMC is an internally heterogeneous igneous body. It consists mainly of two-mica granite, uartz-feldspar gneiss, and migmatite. All of the members gradually pass into one another. Two-mica granite is common in the central zone of GGMC. It is variably deformed but has preserved magmatic textures. Locally preserved magmatic textures indicate that they are equigranular and weakly porphyritic medium-grained granite. Two-mica granite contains quartz, orthoclase, oligoclase, muscovite and reddish-brown biotite with occasional garnet (Figures 2.3a and 2.3b). Apatite, titanite, zircon and monazite are common accessories. Muscovite is seen as both primary and secondary phases. The latter as the alteration product, formed particularly along cleavage planes of feldspars. Cataclastic deformation is a common feature in the GGMC, which overprints the magmatic textures. In deformed two-mica granites, quartz is surrounded by recrystallized small subgrains. Ellipsoidal K-feldspar and plagioclase are aligned along the main foliation. Garnet is generally present as shattered porphyroclasts in the rock.

Gneiss is a quartzo-feldspatic, leucocratic rock represented by an assemblage that consist mainly of quartz, plagioclase, K-feldspar and muscovite (Figures 2.3c and 2.3d). It has also garnet, biotite and zircon. Gneiss gradually passes into two-mica granite, which also contains quartz, plagioclase, K-feldspar and muscovite as the major minerals suggesting its granitic origin. Foliation and lineation are defined by muscovite, biotite and quartz. In the field, gneiss and migmatite are observed to be intricately intermixed (Figure 2.3e).

Common mineral composition of the migmatite is biotite + quartz + K-feldspar + plagioclase + garnet ± cordierite ± sillimanite. This mineral paragenesis indicates that the migmatite underwent amphibolite facies (upper amphibolite?) metamorphism. Leucosome and melanosome (restite) rich migmatites (Sawyer, 2008) can be distinguished within the GGMC (Figure 2.2a). Melanosome rich migmatite is a common rock particularly in the northwestern and in the eastern borders of the GGMC and towards the center, passing into leucosome rich migmatite. The mineral assemblage of the leucosome is similar to that of gneiss and granite. Boundaries between leucosome and melanosome are marked by an anomalously biotite-rich zone. It shows schlieren and fold type structures, where the migmatisation reached an advanced stage (Figure 3e).

Mafic syn-plutonic dykes were identified within the migmatite close to northern border of GGMC (Figure 2.4). Structures and contact relations of mafic dykes and the host rock indicate that the host was totally molten or mush, when the dyke was intruded. It is gabbroic diorite in composition and consists of plagioclase, hornblende, clinopyroxene, biotite and quartz (as rounded xenocryst). Microgranular texture is predominant in the rock.

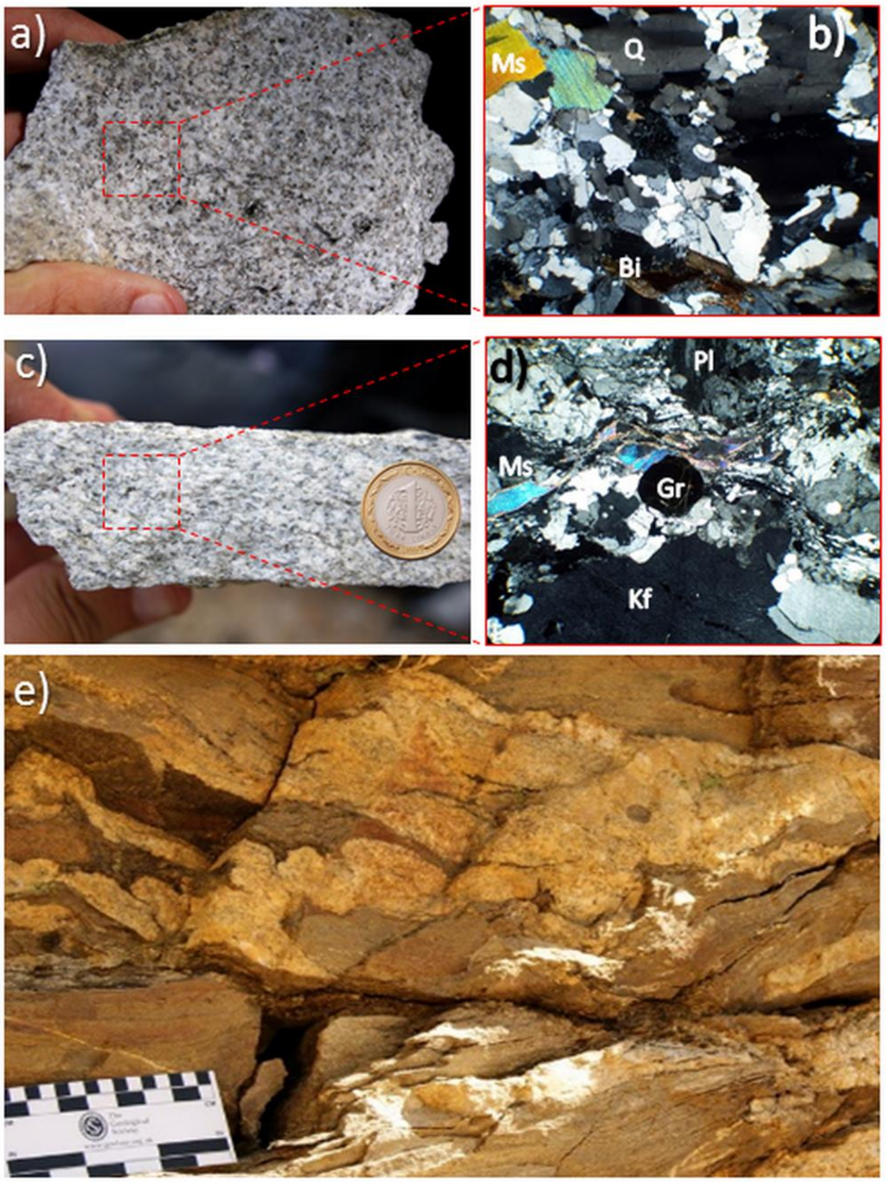

Figure 2.3 : GGMC units: a, b) Two-mica granite; c, d) Gneiss; e) Schollen type of migmatites (after Mehnert, 1968): including melanosome and leucosomes (UTM coordinate 35S 612620/4421440); Ms: muscovite, Kf: K-feldspar, Bi: biotite, Q: quartz, Pl: plagioclase, Gr: garnet. Magnification for b and d is 4X, crossed plane.

During the continuous ductile deformation, the dykes were pinched out to form a number of separate small dykes aligned along same direction surrounded by migmatite (Figure 2.4).

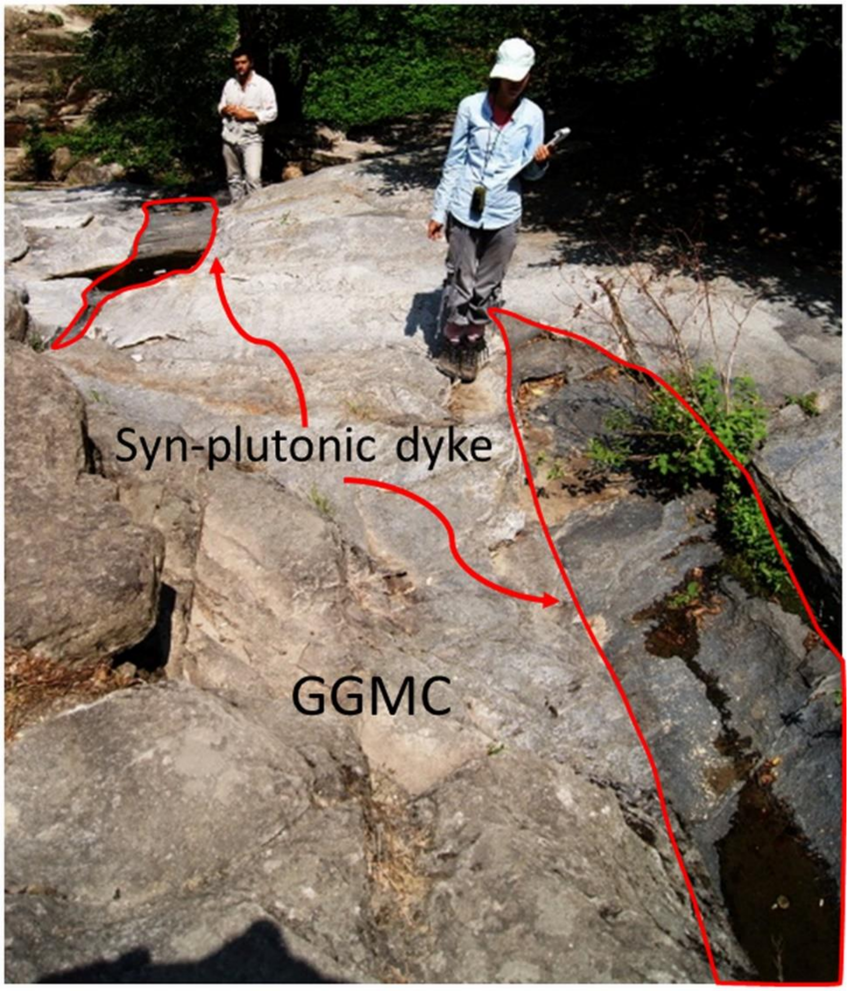

Figure 2.4 : Mafic syn-plutonic dyke within the GGMC (UTM coordinate 35S 618185/4417585).

Along the northern and eastern borders, the GGMC is bounded by a low angle normal fault zone (ÇDFZ) that juxtapose granite-migmatite complex with the greenschist facies metamorphic rock of the basement rocks (Karakaya complex and Bornova Flysch; Okay, 1984, Okay et al., 2001) (see “structural data” section for detailed data on the ÇDFZ). Haplogranitic sheets and pegmatitic dikes of ÇG were emplaced through this fault and cut the GGMC along its western contact.

2.2.2 The Çataldağ Granodiorite (ÇG)

The Çataldağ granodiorite consists mainly of homogeneous granodiorite with haplogranitic peripheral rocks. The main granodiorite body is dominated by biotite granodiorite and subordinate hornblende-epidote granodiorite in the south. From N to S they gradationally pass into one another. The granodiorite is easily identified in the field by its distinctive porphyritic texture consisting of large megacrysts of K-feldspar reaching up to 5 cm (Figures 2.5a and 2.5b). It is made up of plagioclase (oligoclase-andesine), quartz, K-feldspar (orthoclase+ perthite) and biotite. Minor hornblende and epidote are observed where the granite is in contact with calc-silicate rocks along southern contact zone. Titanite, zircon, apatite and opaques occur as accessory minerals. Chlorite, sericite and epidote form the secondary minerals.

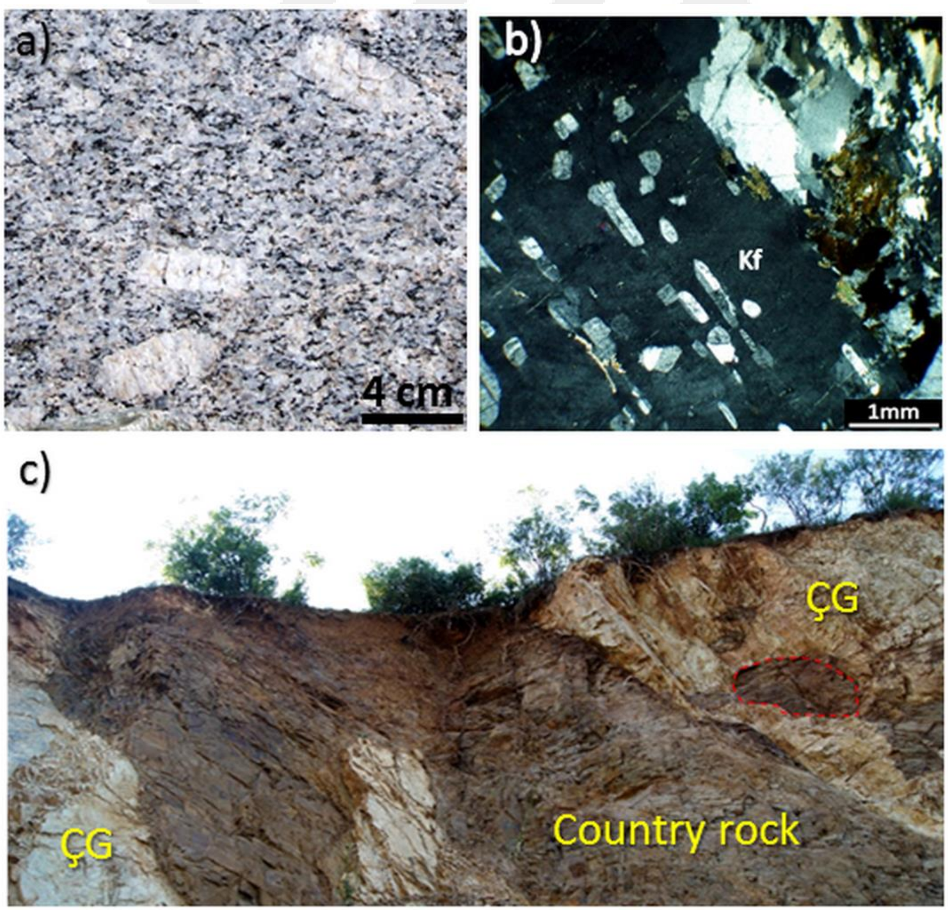

Figure 2.5 : a, b) Typical K-feldspar megacrystals forming porphyritic texture of ÇG (UTM coordinate 35S 607975/4414830); c) intrusive contact between ÇG and metamorphic country rock in western boundary (UTM coordinate 35S 601249/4403663). Kf: K-feldspar, Magnification for b is 4X, crossed plane.

Haplogranitic sheets crop out along the western and eastern borders of the main granodiorite body. It is a leucocratic and fine grained rock displaying aplitic or graphic-granopyhric texture. It consists mainly of quartz, K-feldspar, plagioclase (oligoclase) and minor biotite and garnet. The haplogranite contact with the main body of the granodiorite is sharp. It displays a chilled margin against the metapelitic-metabasic basement rocks of the Karakaya Complex and Bornova Flysch; Okay, 1984, Okay et al., 2001) in the west.

The ÇG intruded into metapelitic-metabasic basement rocks of the Karakaya Complex (Figure 2.5c). A primary igneous contact zone is observed along the southern border. The ÇG was intruded into calc-silicate country rocks and formed a well-developed contact aureole where mineral paragenesis of calcite + diopside + garnet + wollastonite ± vesuvianite indicate that the contact metamorphism reached pyroxene-hornfels facies in the inner aureole. Within the host granodiorite, euhedral hornblende and epidote were also locally developed as a result of Ca metasomatism. Aplite sills and dykes, pegmatite dykes and enclaves of the country rocks are common along the southern margin of the ÇG.

The ÇG is bounded along the northern and eastern contact by a low angle normal fault (the Çataldağ Fault Zone). In the northern part of ÇG, the granite laterally pass into augen-gneiss (Figure 2.6). Syngenetical haplogranite and pegmatite dykes of ÇG were intruded in this fault zone and formed a narrow dyke belt between the ÇG and GGMC (Figures 2.2a and 2.2b). Younger (oblique) normal-dextral and normal faults cut and concealed the primary contact of the ÇG in western margin.

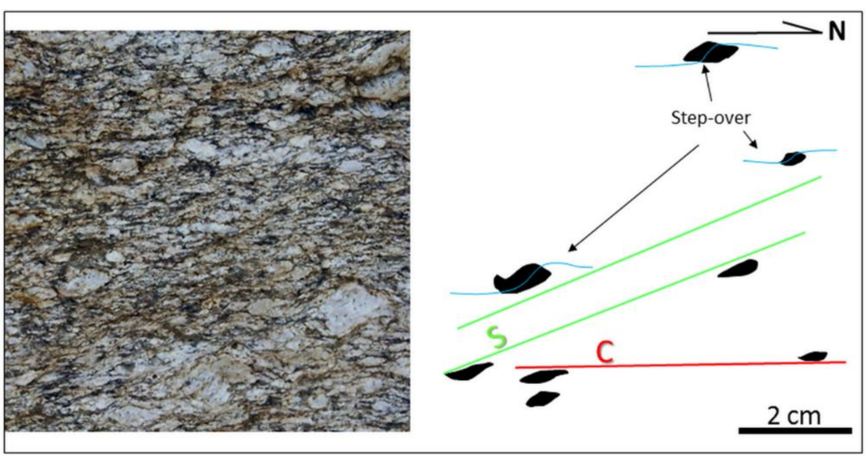

Figure 2.6 : Augen-gneiss in the ÇDFZ with top-to-the north sense of feldspar-fish and step-over structures in northern border of ÇG, C: shear plane, S: schistosity plane.

2.3 Structural Data

2.3.1 Çataldağ Detachment Fault Zone (ÇDFZ)

GGMC and ÇG are bounded along northern and eastern contacts by a low angle normal fault we named herein as the Çataldağ Detachment Fault zone (Figure 2.2). All the structural features (e.g. slickenlines, undulation, turtle-back) that are observed within the fault zone and fault plane collectively display normal fault character of ÇDFZ (Figures 2.7a and 2.7b). ÇDFZ separates GGMC and ÇG which represents the footwall, from the basement rocks (Karakaya Complex and Bornova Flysch of Okay 1984; Okay et al., 2001) and the sedimentary cover rocks, located on the hanging wall. Attitude of the fault plane of the detachment fault is N85E 8NW along the northern border (Figure 2.7a). It turns to N5W 6NE toward the eastern border (Figure 2.8a). Slickenlines are clearly observed around the Sunluk area (northern border of GGMC) and trend N5W (Figure 2.7b). This is also the same as the dip of the fault plane. Rake measurement for fault plane is calculated as (-90), which indicates a normal fault characteristic (Figure 2.7b).

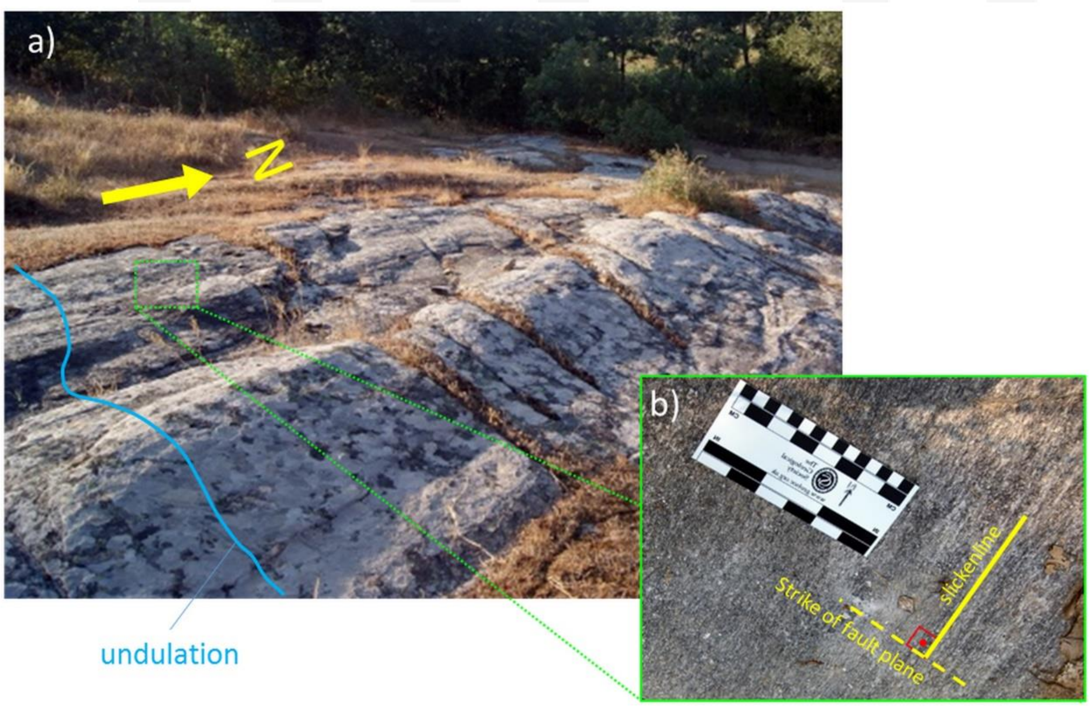

Figure 2.7 : The fault plane structures of the ÇDFZ a) low angle fault plane and undulation; b) slickenline and rake (UTM coordinate 35S 616580/4422555).

The mylonitic texture exhibits progressive changes from ductile to brittle deformation in the footwall rocks. A top-to-the N sense of motion is determined from the structures of the mylonitic shear zone (Figures 2.8b, 2.8c and 2.8d). On the fault plane some undulations, sub-parallel to direction of the shear foliation is observed (Figure 2.7a). The fault planes undulate and thus, one of the typical indicators of low angle normal faults, local turtle back structures are observed in the eastern border of ÇG, as exemplified from the east of Serçeören area (Figure 2.9).

Within the ÇG, the fault and related deformation are not clearly seen everywhere due to weathering and erosion. In some places the fault plane is commonly eroded and/or truncated, and therefore displaced (hidden) by younger (oblique) dextral normal and normal faults. Attitude of the dextral normal fault plane is N20W 60SW. To show the original shape and geometry of this dome and the associated detachment fault, the ~3.5-4 km right-slip displacement along the NW-SE-oriented dextral normal fault that cuts across the dome has been restored. Further retro-deforming the dome by restoring the right-oblique displacements along the E-W-striking faults in its southern half, produces an E-W-oriented elliptical body of crystalline rocks bounded in its northern, eastern and southern parts by ÇDFZ (Figure 2.10).

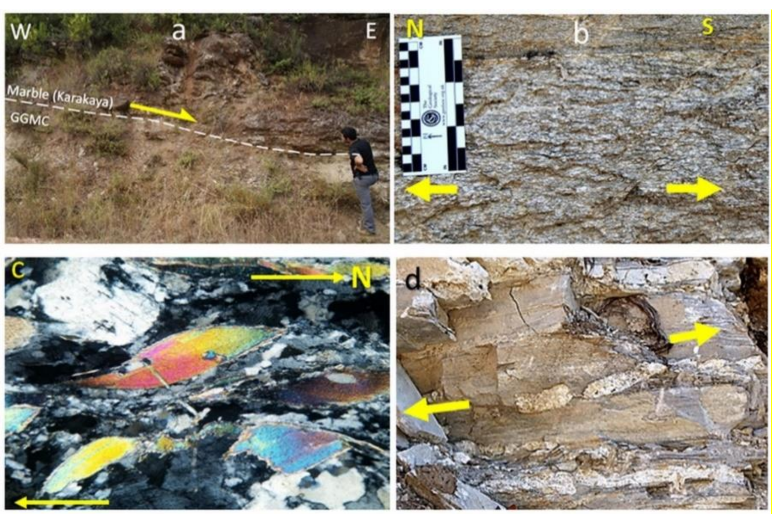

Figure 2.8 : a) Hanging wall and footwall of the ÇDFZ in the eastern border of GGMC (UTM coordinate 35S 629500/4418835); b) mylonites (UTM coordinate 35S 618730/4419565); c) microphotograph of top-to-the north sense muscovite-fish from the outer zone of the GGMC, crossed plane, 10X magnification; d) boudinage of the leucosomes in migmatite of the GGMC (UTM coordinate 35S 612345/4419795).

Supra-detachment sediments are clearly seen above the northern contact of the ÇDFZ. These sedimentary rocks are represented by poorly lithified conglomerate in immediate contact, and comprised of clasts of granodiorite and granite-gneiss derived from the ÇG and GGMC, and onlap the detachment surface. Bedding planes tilted into the detachment surface, and bedding thickness increase toward the detachment surface. This indicates syn-extensional deposition of these rocks, which is reminiscent of supradetachment basin sequences (Oner and Dilek 2011, 2013).

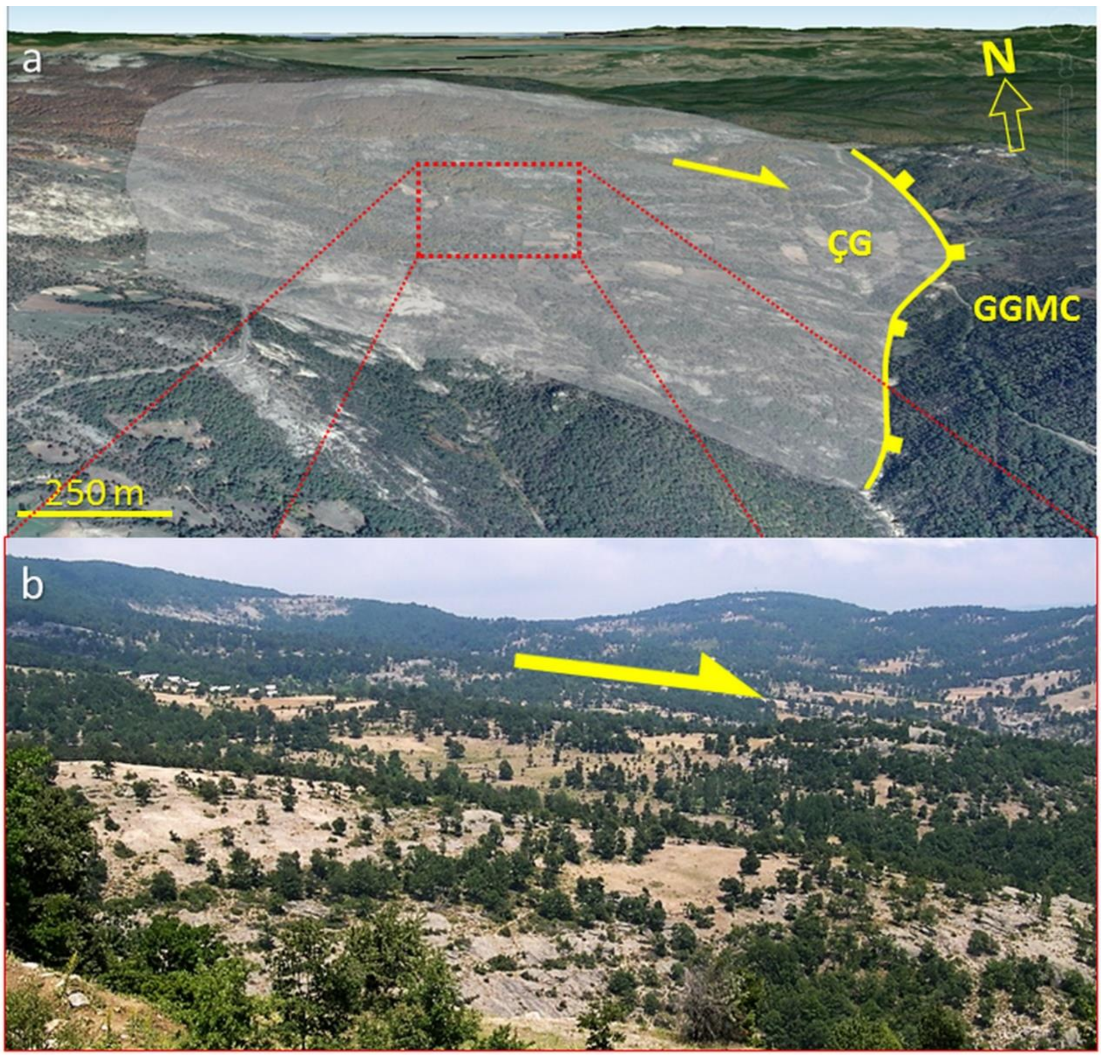

Figure 2.9 : a) Google Earth image of the low angle fault plane of the ÇDFZ and b) turtle-back structure in south of the ÇG. (UTM coordinate 35S 612574/4409832).

2.3.2 Deformation of the Granite-Gneiss-Migmatite Complex (GGMC)

Structures indicate that the GGMC underwent both ductile and brittle deformation. A total of 315 foliations were measured from the GGMC (Figure 2.11). The lower hemisphere steographic plots of the foliations and lineations are shown in Figure 2.12. Deformation style is different in the inner zone (IZ on Figure 2.11) and the outer zone (OZ in Figure 2.11) of GCMC which are described separately below. In the inner zone, the rock was ductilily deformed, and the foliation of the rock is defined by the orientation of elongated feldspar and mica minerals, whereas in outer zone, the GGMC commonly displays semi-brittle to brittle deformation.

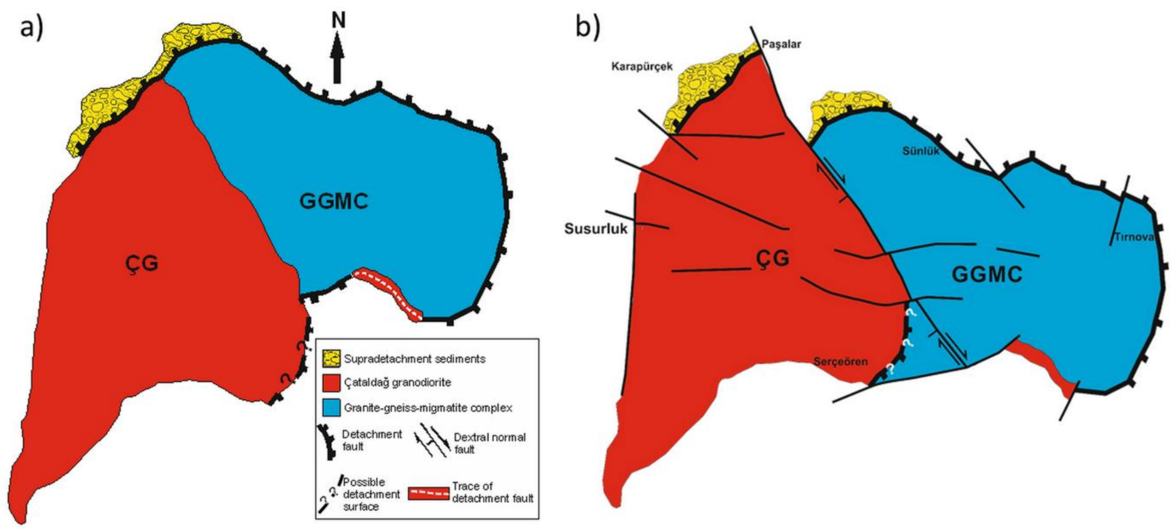

Figure 2.10 : Structural reconstruction of ÇPC and ÇDFZ; a) the initial shape of the ÇDFZ before oblique dextral-normal faulting; b) Recent shape of ÇDFZ after the oblique dextral-normal faulting.

Steographic plots of the foliations of inner zone are shown in Figure 2.12a. Dips of the foliations are clustered mainly in NW and SE in directions. Strike and dips of foliations demonstrate two NE-SW trending smaller scale subdomes within a larger dome recognized on the whole body of GGMC (Fig 2.11).

In the inner zone, micro scale deformation is characterized by an incipient mylonitisation that is evidenced by the beginning of grain size reduction and softening reactions generated by quartz recrystallization processes, such as grain boundary migration and subgrain rotations. Feldspars are commonly represented by porphyroclasts. K-feldspar frequently displays semi-ductile features such as bulging recrystallization. Micas are in plastic forms commonly around feldspars. The whole microstructural data suggest that the temperature ranged approximately from 450 to 250 °C (Passchier and Trouw, 1996) in the inner zone during the syn-kinematic deformation.

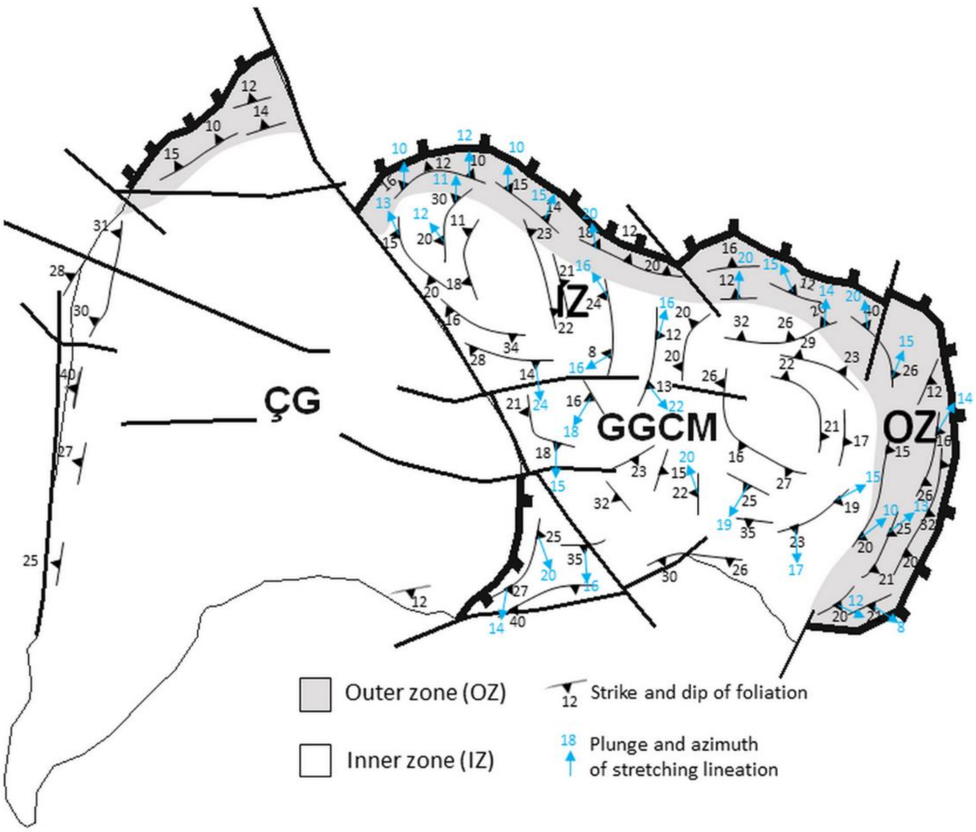

Figure 2.11 : Strike and dip of foliations and plunge and azimuth of stretching lineations in structural map of ÇPC.

Outer zone is represented by a mylonitic zone that has been variably overprinted by late brittle deformation along the borders of GGMC. Mylonitization increases towards outer zone indicating the ÇDFZ is responsible from the deformation (Figure 2.11). Trend of foliations is parallel - sub-parallel to the trend of the ÇDFZ (Figure 2.11).

The plunges of lineations of GGMC are roughly parallel with the dip directions of ÇDFZ (Figure 2.11 and Figure 2.12e) regardless attitude of the foliation measured all over the region. However, movement direction of hanging-wall is top-to-N and top-to-NE (Figure 2.13).

Overprinting brittle deformation represented by microstructures such as microfaults and cracks that are seen in quartz and feldspar. The brittle deformational behavior of quartz is stated as to be below 250°C by Passchier and Trouw (1996).

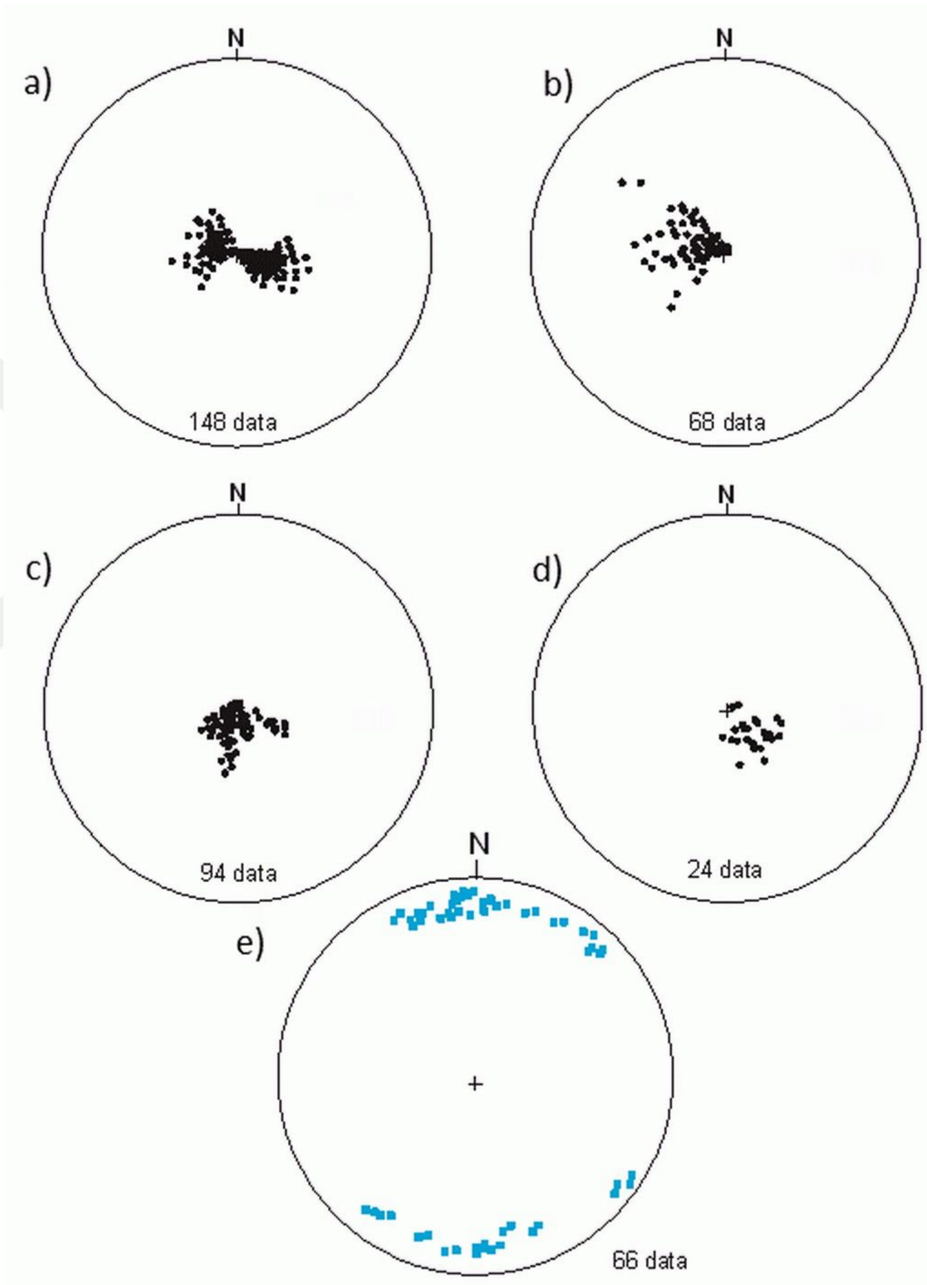

Figure 2.12 : Lower hemisphere equal-area projections of foliation (a, b, c, d) and lineation (e) from the ÇPC: a) foliations for inner zone of the GGMC; b) foliation for the eastern outer zone of the GGMC; c) foliations for the northern outer zone of the GGMC; d) foliations for the northern border of the ÇG; e) lineation for the GGMC.

Shear direction is determined from the small scale faults. All of the microfaults display dip slip displacement and the motion is “top to north and northeast” from north to east, respectively. The same shear sense can also be determined from mica-fish texture (Figure 2.8c), which suggests that the rocks underwent different stages of a progressive deformation. They passed through ductile deformation at an early stage. Later a brittle deformation superimposed on the ductile deformation.

In summary, GGMC displays effects of a progressive deformation. The inner zone of GGMC (Figure 2.11) displays ductile deformation, whereas the outer zone exhibits both ductile and brittle deformation. The data collectively suggest that, GGMC underwent continuous deformation starting from about a temperature interval of 450°C-250°C and it continued in the lower temperatures (Passchier and Trouw, 1996).

2.3.3 Deformation of the Çataldağ Granodiorite (ÇG)

Similar to the outer zone of the GGMC, north-northwest border of ÇG displays evidence for both ductile and brittle deformation in every scale. Along the north boundary of ÇG, the structural evidence indicate a regional top-to-N shear sense of semi-plastic mylonitic deformation. This is reflected by the orientation and elongation of biotite and feldspar defining foliation that are locally observed (Figure 2.6). Their dips commonly trend to N-NW (Figure 2.12d).

The grain boundary migrations (GBR), subgrain rotations (SGR) and feldspar-fish structures are common in the northern border (Figure 2.6). According to Passchier and Trouw (1996), the structures such as feldspar-fish and mica-fish are formed at the temperatures of 600°C and 300°C respectively.

Towards to the northern border of the ÇG the CDFZ separates the basement rocks that are exposed on the hanging wall from the ÇG on the footwall. Cataclasis increases towards the fault plane. The shear sense indicators, e.g. feldspar-fish structure (Figure 2.6), in the northern part of the ÇG are consistently define top-to-the north movement. The microfaults observed in the fault zone share the same top-to-the north and northwest sense of shear.

In contrast to northern and western borders, other contacts of ÇG with the metamorphic country rock is primary intrusive in character. The structures that resulted in the exhumation of the plutonic bodies do not cut southern border.

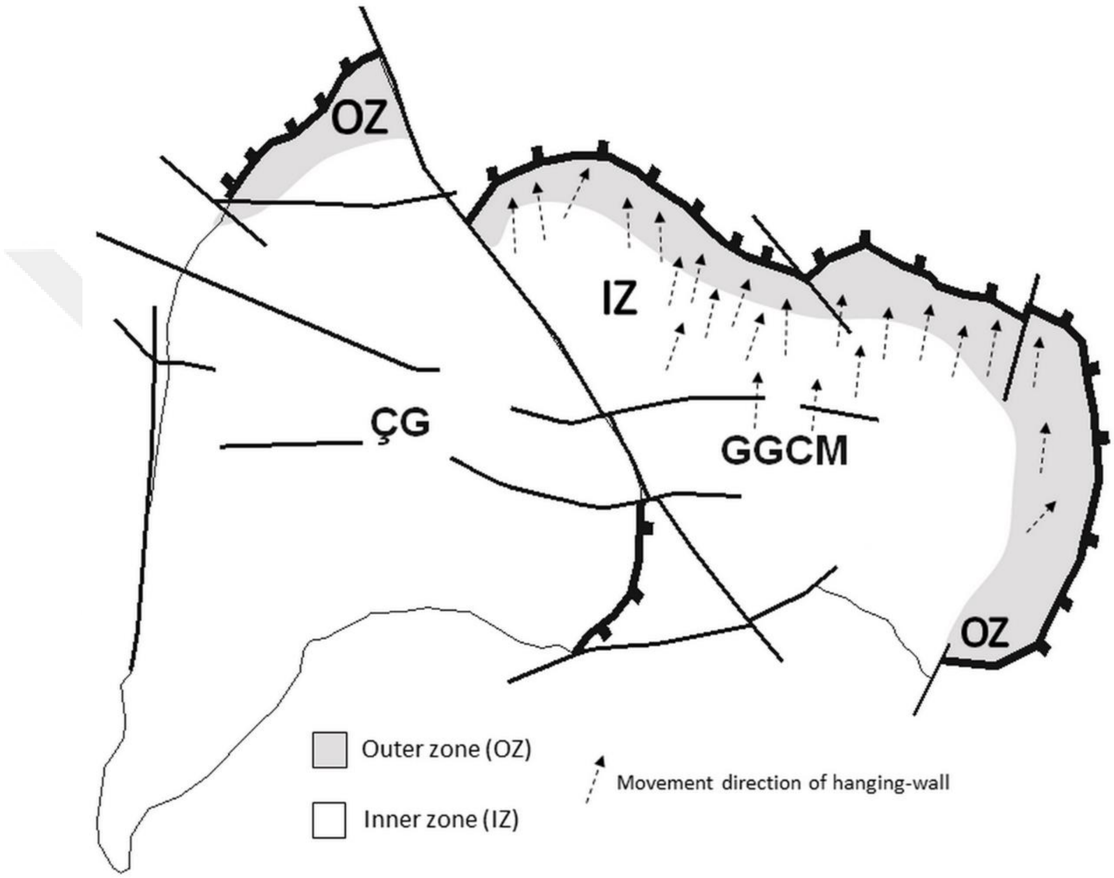

Figure 2.13 : Movement direction of hanging-wall.

2.4 LA–ICP–MS Geochronology

2.4.1 Analytical methods

Cathodoluminiscence (CL) and back-scattered (BSE) images were collected prior to zircon analyses to identify inherited cores, cracks and inclusions using the scanning electron microscope JSM- 6610 LV at the University of Belgrade.

U–Pb isotope analyses were carried out using a New Wave Research (NWR) Excimer 193 nm laser-ablation system UP-193FX attached to a Perkin-Elmer ELAN DRC-e inductively coupled plasma mass spectrometer (LA–ICP–MS) at the Geological institute, Bulgarian Academy of Science in Sofia, Bulgaria. Spatial resolution was about 35 µm (rarely 20-25 µm) for the thinner zones and frequency of 8 Hz. The well characterized zircon standard (GEMOC GJ-1; 608 Ma with near-concordant Pb) was used as external standard. Ablation of the standard and samples in He was employed to increase sample transport efficiency, decrease ablation product deposition and to stabilize and increase the signals. During the analyses the SuperCell of NWR allowed the use of low carrier gas flow. The measurement protocol included the isotopes ^{206}Pb, ^{207}Pb, ^{208}Pb, ^{204}Pb, ^{232}Th, ^{238}U and ^{201}Hg. In nearly all cases, ^{204}Pb content was below the level of detection and no correction was applied. Operating conditions for the laser were kept stable to ensure constant U/Pb fractionation. Measurement procedure involved calibration against the standard zircon GJ-1 at the beginning of the ‘‘block’’ with a run of two analyses, followed by eight zircon analyses, one standard GJ-1, next seven unknowns and finishing the ‘‘block’’ with two further analyses of the GJ-1 standard. This technique allows a suitable correction for instrumental drift along with the minimization of elemental fractionation effects. Raw data were processed using GLITTER, a data reduction program of the GEMOC, Macquarie University, Australia (http://www.gemoc.mq.edu.au/). $^{207}Pb/^{206}Pb$, $^{208}Pb/^{232}Th$, $^{206}Pb/^{238}U$ and $^{207}Pb/^{235}U$ ratios were calculated and the time-resolved ratios for each analysis were then carefully examined. Optimal signal intervals for the background and ablation data were selected for each sample and automatically matched with the standard zircon analyses, thus correcting for the effects of ablation/ transport-related U/Pb fractionation and the mass bias of the mass spectrometer. Net background-corrected count rates for each isotope were used for calculation of sample ages. U–Pb Concordia ages are calculated and plotted using ISOPLOT (Ludwig, 2003. Rho value is taken as 0.5 for the U–Pb Concordia diagrams.

2.4.2 Results

LA-ICP-MS ages were achieved from zircon and monazite from GGMC (Table A.1). Most of the zircon grains in the samples of GGMC reveal the complex internal structure and inherited cores and autocrystic magmatic rims (Figure 2.14). Most of the cores have endured magmatic corrosion which is represented by rounding and some of the newly grown zircon zones penetrate in them. Some of the margins between the cores and the rims are cracked probably due to thermal effect. The newly grown magmatic zircons are presented most often as outer zones with well-developed oscillatory zoning with inclusion oriented along them (Figure 2.14).

Gneiss: A total of 45 spot analyses from 27 grains of zoned zircons were done (Table A.1). 45 spot analyses of distinct zircon zones of 27 grains are made (Table A.1). The concordia age of 33.80 ± 0.14 Ma represents the magmatic crystallization age. LA-ICP-MS age data for the xenocrystic zircons and cores define several clusters of the inherited component (Figure 2.14).

Garnet-bearing two-mica granite: 45 spot analyses of distinct zircon zones of 30 grains were made (Table A.1). The concordia age of 32.15 ± 0.13 Ma is accepted as magmatic crystallization age. LA-ICP-MS age data for the xenocrystic zircons and cores define several clusters of the inherited component (Figure 2.14).

Two-mica Granite: 22 spot analyses of distinct zircon zones of 14 grains are made (Table A.1). The concordia age of 33.36 ± 0.69 Ma represents the magmatic crystallization age. LA-ICP-MS age data for the xenocrystic zircons and cores define several clusters of the inherited component.

Additionally, in the sample are dated monazite crystals revealing $^{206}Pb/^{238}U$ weighted average age of 30.13 ± 0.23 that can be interpreted as the age of hydrothermal alteration or reheating by new magmatic impulse (Figure 2.14). It can be preferred as magmatic age because of being compatible with zircon ages. Some zircons $^{206}Pb/^{238}U$ gives younger age which is due to Pb loss.

2.5 Ar/Ar Geochronology

2.5.1 Analytical methods

$^{40}Ar/^{39}Ar$ geochronology was carried out on biotite, muscovite and K-Feldspar samples from the ÇPC at the Auburn University Noble Isotope Mass Analysis Laboratory (ANIMAL). The rock samples were selected after petrographic analysis of thin sections from each sample. The selected samples were crushed and sieved for whole rock and biotite grains.

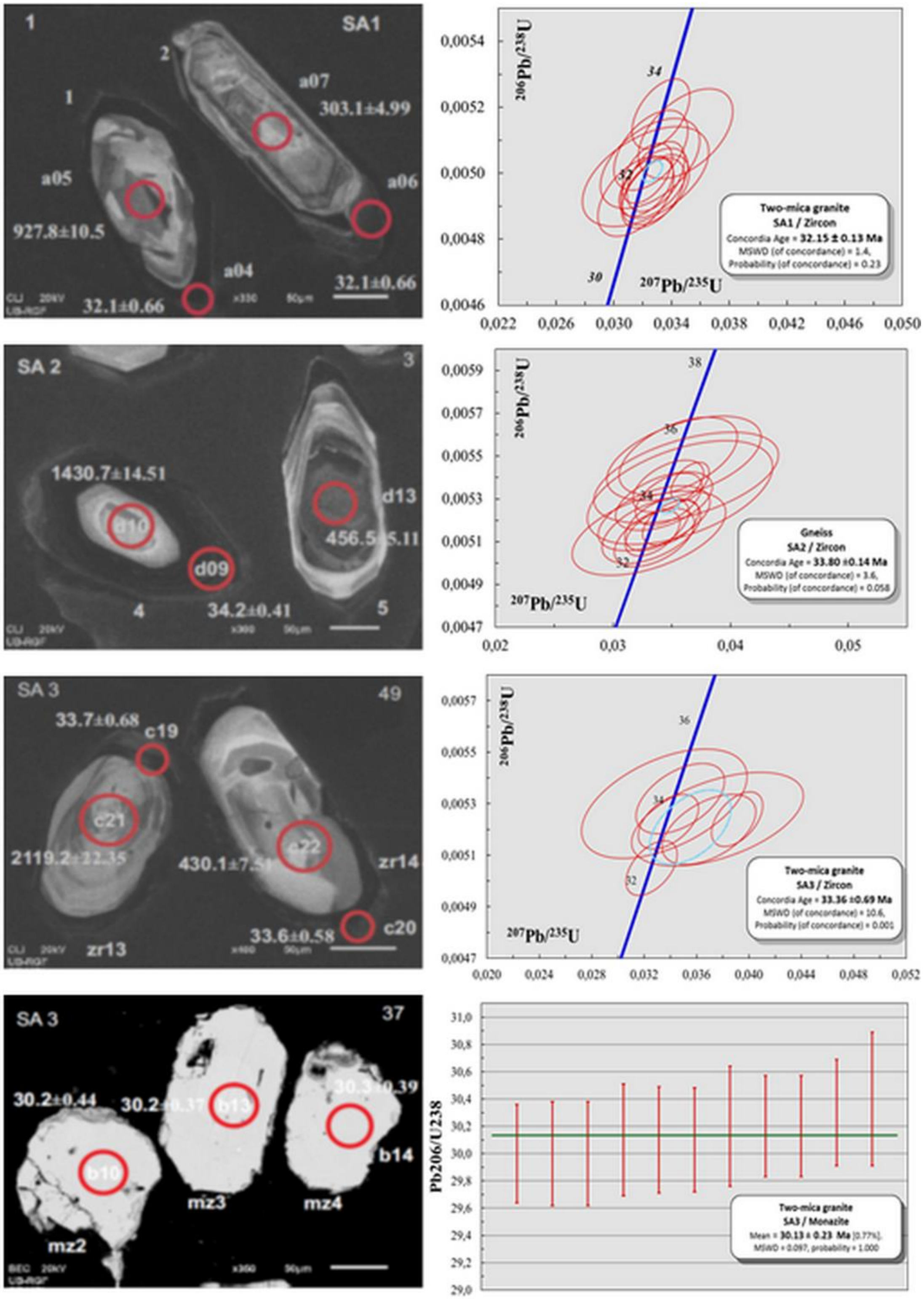

Figure 2.14 : Cathodoluminiscence (CL), back-scattered (BSE) images and U/Pb LA–ICP–MS Zircon and monazite ages of GGMC.

The individual biotite (850–600 μm), muscovite and K-feldspar grains were hand-picked under a binocular microscope to be generally free from visible inclusion of other phases and free from visible alterations. The selected samples were washed with de-ionized water in ultrasonic cleaner. Samples were located in aluminum disk with monitor FC-2 (age = 28.02 Ma, Renne et al., 1998) along with CaF_2 flux monitor. All samples and standards were irradiated in the USGS TRIGA reactor located at the Denver Federal Center, USA. The ANIMAL analytical lab is equipped with a low-volume, high sensitivity 10 cm radius sector mass spectrometer and automated sample extraction system (50 W Syndrad CO_2 laser). The analyses of these samples were conducted by laser incremental heating analysis (LIH) of approximately 100 grains of whole rock. The biotite, muscovite and K-feldspar samples were dated from single crystal total fusion (SCTF) and single crystal incremental heating method (SCIH).

All statistical $^{40}Ar/^{39}Ar$ ages in this study (weighted means, plateau, or isochron) are quoted at the standard deviation in precision of measurement, whereas errors in individual measurements are quoted at one standard deviation. Data reduction was calculated through use of custom Microsoft Excel application. The plateau and correlation ages were calculated by isoplot (Ludwig, 2003). Plateau in this study was defined as at least three or more contiguous increments containing more than 50% of the ^{39}ArK in three or more contiguous steps with no resolvable slope among ages.

2.5.2 Results

Single grain plateau ages were obtained by laser controlled incremental heating to provide more detail on the outgassing behaviors of the samples. SCTF and SCIH ages were achieved from biotite, muscovite, K-feldspar samples of ÇG and GGMC. The results are given in Table A.2, Figures 2.15 and 2.16.

The Çataldağ granodiorite (ÇG): SCTF and SCIH biotite ages of biotite-granodiorite samples (OS-55 and OS-72) of ÇG yielded well-developed plateau ages of 20.84 ± 0.13 Ma (MSWD = 0.4) and 21.16 ± 0.04 Ma (MSWD = 0.26), respectively; by total of 36 biotite grains (Figure 2.15).

The granite-gneiss-migmatite complex (GGMC): Muscovite of two-mica granite (OS-75 and OS-105), gneiss (OS-150), mylonitic granite (OS-77) and biotite in migmatite (OS-

111) of GGMC have been dated. SCIH and SCTF muscovite age of two-mica granite (OS-75) has a plateau age of 21.38 ± 0.05 Ma (MSWD = 0.84). SCTF muscovite age of other two-mica granite (OS-105) yields 20.81 ± 0.04 Ma with the highest MSWD of 1.4 (Figure 2.16). Gneiss (OS-150) has been dated on biotite and K-feldspar. SCIH biotite and K-feldspar ages of 20.80 ± 0.08 Ma (MSWD = 0.35) and 21.12 ± 0.06 Ma (MSWD = 0.60), respectively. Mylonitic granite (OS-77) of ÇDFZ, has a well-developed plateau age of 21.28 ± 0.09 Ma (MSWD = 0.34) which is very close to age of two-mica granite (OS-75). Migmatite, sample OS-111 has SCIH and SCTF biotite ages of 21.18 ± 0.07 Ma (MSWD = 0.58) and 21.11 ± 0.21 Ma, respectively.

As a summary, $^{40}Ar/^{39}Ar$ mica ages of ÇG and GGMC are similar which ranges from 21.3 to 20.8 Ma.

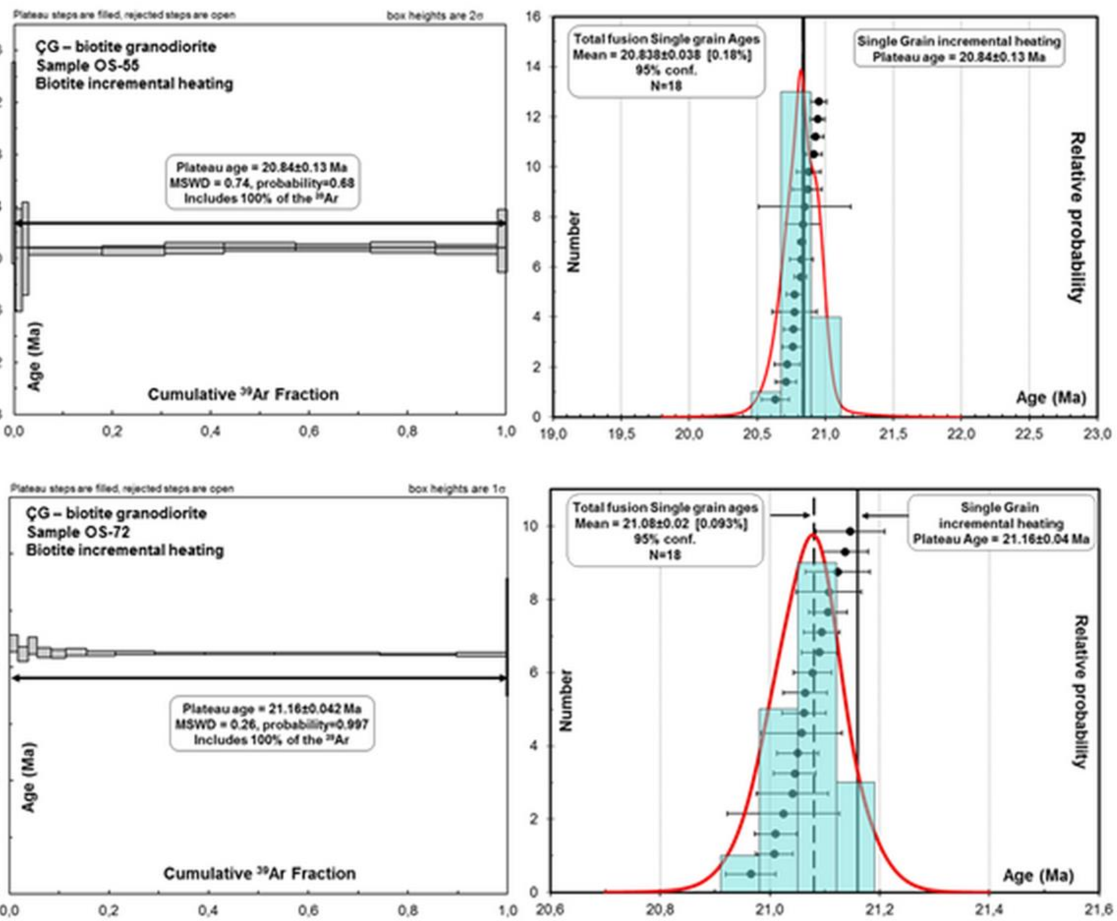

Figure 2.15 : Results of $^{40}Ar/^{39}Ar$ geochronology of porphyritic granodiorite of ÇG.

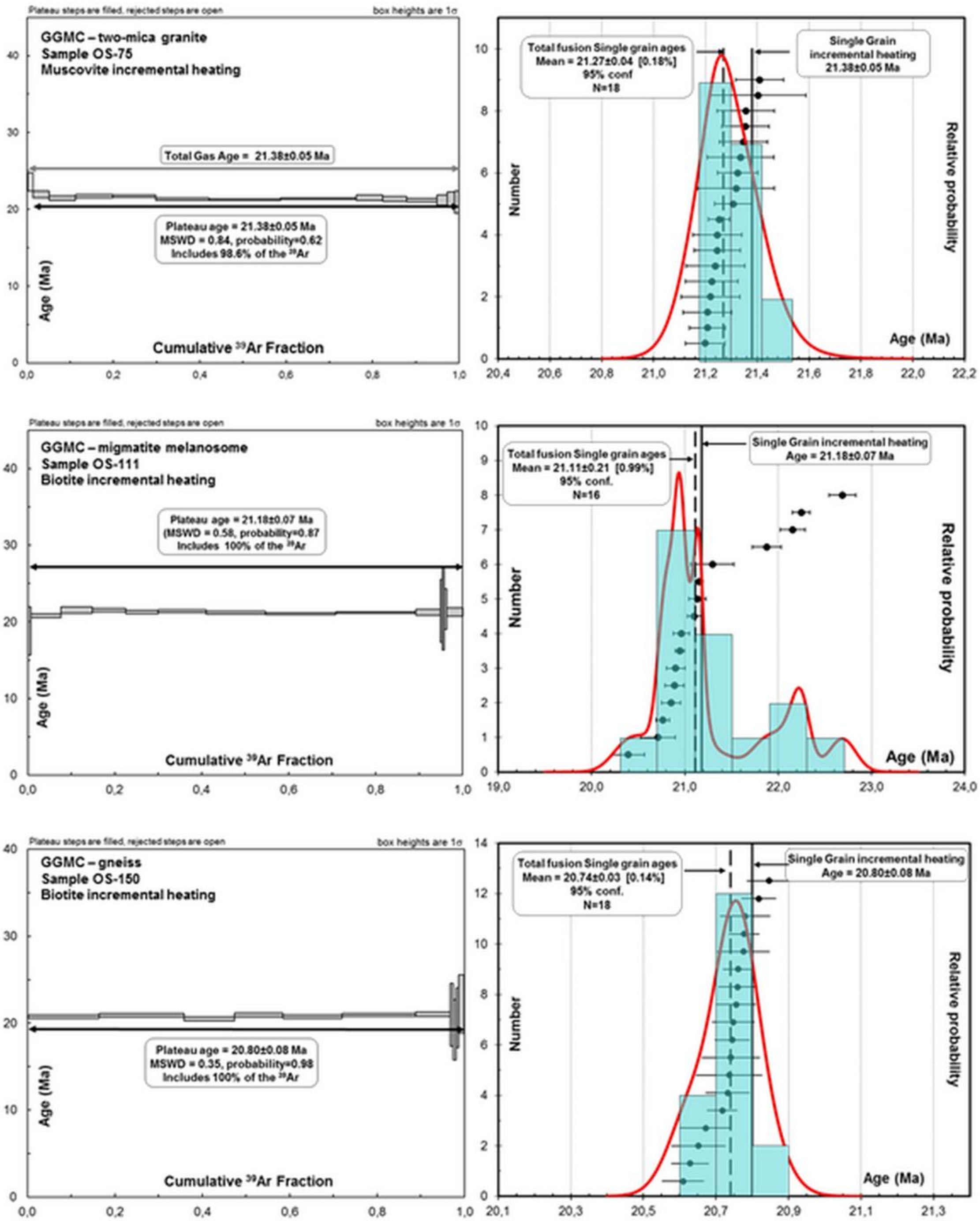

Figure 2.16 : Results of $^{40}Ar/^{39}Ar$ geochronology of gneiss and two-mica granite of GMMC.

2.6 Discussion

2.6.1 Emplacement of the Granite-Gneiss-Migmatite Complex (GGMC)

The granite-gneiss–migmatite complex exhibits a domal structure, at the core of dome, granitic gneiss and S-type two-mica granites are dominant and both are concordant with migmatite of amphibolite facies. Within the migmatitic zones, discrete parts of melanosome, rich in biotite, sillimanite, cordierite and garnet represent restites from partial melting. This data suggest that high grade metamorphic rocks (amphibolite to upper amphibolite P/T conditions) of metasediments of pelitic – psammitic composition may be viewed as precursor of GGMC. The igneous textures and some micro scale features, presence of primary garnet and muscovite, and also inherited zircon cores are the supporting evidence for an anatectic melt of crustal origin (Figure 2.14).

Granite with a typical igneous texture passing into the migmatite of amphibolite facies toward the peripheral zone and absence of contact metamorphism around the GGMC are regarded as supporting evidence for the granitic rocks of deep-seated origin. The granitic magma that formed GGMC was possibly emplaced in middle crustal depths.

The intrusion age of the S-type two-mica granites, and the precursor of the migmatite, dates the migmatization and partial melting processes beneath western Anatolia. The zircon and monazite ages for the GGMC are 33.8-32.1 Ma and 30.1 Ma, respectively. The age obtained from the S-type two-mica granite, gneiss and the migmatite falls into the same range, indicating that all the rock groups of GGMC were formed during the Eo-Oligocene. This period may thus be evaluated as the age of the partial melting, migmatization and deformation.

Along the northern, eastern and southeastern borders, the GGMC is bounded by a low angle normal fault zone (ÇDFZ) that juxtaposes deep-seated granite-migmatite complex with the greenschist facies metamorphic rocks of Karakaya complex (Figures. 2.2a, 2.2b, 2.2c, and Figure 2.17). Along the western border, it was intruded by ÇG and associated haplogranite and pegmatite dykes of Early Miocene. These two plutons forming the ÇPC were uplifted together along ÇDFZ during the Early Miocene (see section 2.6.3).

2.6.2 Emplacement of Çataldağ Granodiorite (ÇG)

In contrast to GGMC, ÇG is an I-type granodiorite (Kamacı and Altunkaynak 2011A, 2011B; Kamacı et al., 2013), and represents a discordant, shallow level intrusive body that intruded into the neighboring GGMC and metamorphic basement rocks of Sakarya continent. It is formed mainly from K-feldspar megacryst biotite-granodiorites, haplogranitic peripheral zone and associated dykes and sills. It commonly displays porphyritic texture. Granonophyric-graphic textures are also rarely observed. These textural features and discordant nature of the ÇG indicate that the granitic magma reached shallow levels in the crust, most probably in the epizone.

Figure 2.17 : Graphical abstract showing contact relationships and deformational structures in ÇPC.

Along the northern and eastern contacts, the ÇG is also bounded by the ÇDFZ. The Cataldağ granodiorite is relatively undeformed in its center, but shows discrete mylonitic bands and cataclastic textures in the footwall of the detachment fault in its northern edge (Figures 2.2 and 2.17). The reason for not showing very extensive deformation fabric is due possibly to the significant amount of exhumation and uplift had already taken place.

Hot granodioritic melt was syn-kinematically emplaced into an already partly exhumed GGMC located in the footwall of the detachment. High temperature ductile deformation products e.g. grain boundary migration and chess-board twins of quartz, have occurred in rapidly cooling ÇG as syn-kinematic textures (Kamaci and Altunkaynak, in prep.). Cooling and ductile deformation appears to be coeval. The T-time history of some detachment zones reveals rapid cooling (>50 °C/my) of the footwall rocks, followed by a more protracted cooling history (<20 °C/my) (Whitney et al., 2013). Deformation of ÇG appears to have started from high temperature ductile to semi-ductile rheology.

The ÇG related haplogranite and dykes cross cut the mylonitic GGMC and ÇG and form a narrow dyke belt between the ÇG and GGMC. They are weakly deformed, therefore, it is inferred that haplogranite and pegmatitic dykes were synchronous with the final stage of shearing deformation.

This interpretation is supported by geochronological data. Zircon SHRIMP age of the sample collected from the western pluton is 21,91 Ma ± 0,33 (Altunkaynak et al., 2012a). $^{39}Ar/^{40}Ar$ and zircon SHRIMP ages obtained from ÇG yield cooling and emplacement ages between 21.3 and 20.8 Ma, respectively. This indicates rapid cooling of the ÇG that followed its emplacement. This thermochronological data also supports syn-extensional emplacement and rapid uplift of ÇG along ÇDFZ.

2.6.3 The timing of ductile to brittle deformation and uplift of ÇPC

Using Ar/Ar method on the biotite, muscovite and feldspar, we determined mica and feldspar ages from the mylonitic rocks of ÇPC, varying from 20,8 Ma (±0,1) to 21,3 Ma (±0,3). The ages are consistent with the K/Ar ages of Boztuğ et al. (2009) from the Çataldağ pluton. Previously Altunkaynak et al. (2012a) also produced zircon SHRIMP age data of 21.9±0.3 Ma from the ÇG. All of the age data are consistent and correspond to the Early Miocene period. In contrast, zircon and monazite LA-ICPMS ages from the GGMC vary between 33.8 and 30.1 Ma (Latest Eocene-Early Oligocene). Therefore, the magmatic crystallization ages of the GGMC (Latest Eocene-Early Oligocene) and the ÇG (Early Miocene) differ significantly. Uplift ages obtained from the ÇG and GGMC are almost the same corresponding to a narrow range of 21.3 and 20.7 Ma. The data indicates clearly that GGMC and ÇG were formed in different periods, but they ascended together during the Early Miocene, when the first major period of N-S extension began in the western Anatolia. Similar ages come from Menderes and Kazdağ Massifs, both of which are the well-known core complexes that formed during the Early Miocene (Bozkurt and Satır, 2000; Tekeli et al., 2001; Cavazza et al., 2009).

Boztuğ et al (2009) asserted that the ÇG elevated rapidly. This view, in the light of the age data summarized above may be regarded acceptable for ÇG, but not for the GGMC. Because correlation of the zircon (21.9 Ma) and mica ages (20.8 Ma) reveals that the uplift of the ÇG to the shallow levels in the crust took place only in a 1 Ma period. The GGMC, on the other hand, which has a deeper crustal origin, was elevated to the final location in at least 8-13 Ma period according to the monazite and zircon (30-34 Ma) and mica (~21 Ma) ages obtained from the same rocks. This data indicates that, at least between the ~34 Ma and 30 Ma interval, the elevation rate of GGMC was relatively slow and then between 21.3 Ma and 20.7 Ma it was elevated rapidly to the higher levels in the crust.

The small and medium scale features that formed within a shear zone (e.g. mica-fish, feldspar-fish) are observed extensively within the ÇDFZ. The ÇG and the mylonitic GGMC have the same, Early Miocene, deformation (mica) ages. This suggests that ÇDFZ is solely responsible from the main stage of elevation of the whole body ÇPC (Figure 2.2). The younger and smaller faults have played relatively subsidiary roles.

2.6.4 Roles of different granites on the Cenozoic crustal build-up in connection with the core complex development

Within the Cenozoic evolution of western Anatolia, two major magmatic episodes producing granitoid plutons occurred following the closure of the Neo-Tethys Ocean. The first developed during the Early-Late Eocene, and produced mainly medium to high-K calc-alkaline, I-type granitoid plutons that are restricted to NW Anatolia. The Eocene volcanic rocks are rare and also limited to NW Anatolia. The second magmatic phase occurred during the Late Oligocene-Middle Miocene and is marked mostly by medium- to high-K calc-alkaline to shoshonitic I-type granitic plutons emplaced into the continental blocks on both side of the IAESZ (Altunkaynak and Yilmaz, 1998; 1999). Extrusive counterparts of Late Oligocene-Middle Miocene granitoid plutons are widespread in the entire west Anatolia (Yılmaz, 1989, 1990; Altunkaynak and Dilek, 2006; Dilek and

Altunkaynak, 2010; Altunkaynak et al. 2010; Ünal et al., 2012; Altunkaynak et al., 2012a, Helvacı et al. 2009; Erkül et al., 2013; Ersoy et al., 2012). Between these two major phases, during the Eo-Oligocene S-type, two-mica granites associated with gneiss and migmatite domes, e.g. Uludağ and Gördes domes occurred in western Anatolia (Catlos and Çemen, 2005; Okay et al., 2008; Bozkurt et al., 2010; Yurdagül, 2004). The Granite-Gneiss-Migmatite complex of ÇPC is a typical product of this transitional phase between two major long lived magmatic episodes.

Eo-Oligocene is a critical period for the Cenozoic Western Anatolian geodynamics. Prior to this, the Sakarya continent collided with the Anatolide-Tauride Platform along the İzmir-Ankara suture during the late Cretaceous-pre-Eocene period (Şengör and Yılmaz 1981; Yılmaz 1997a; Okay and Tüysüz, 1999; Okay and Satır, 2000) and the post-late orogenic N-S compressional deformation was still continuing across the orogenic belt (Yılmaz et al 2000; Altunkaynak and Dilek, 2006). As a consequence of this the western Anatolian crust is estimated to have excessively thickened. Possibly it exceeded 50 km (McKenzie, 1972; Şengör et al., 1984; Seyitoğlu and Scott, 1996; Dilek and Whitney, 2000). The granitic magma of GGMC resulted from anatectic melting in the middle crust and was emplaced in a zone that was not far above from where the melt was originated during the Eo-Oligocene. However, existence of mafic syn-plutonic dykes of gabbroic-diorite in composition within the migmatites of GGMC indicating the partly contemporaneous basic dyke emplacement with the migmatization can be attributed to heat and material transfer from upwelling mantle. In fact, syn-convergent extension that would require mantle upwelling and progressively increasing contribution of mantle material during the late-post orogenic N-S compressional deformation is widely recognized within the interiors of the Tethys orogen of NW Turkey (Aldanmaz et al., 2000; Köprübaşı and Aldanmaz, 2004; Altunkaynak and Dilek 2006; Altunkaynak, 2007; Dilek and Altunkaynak 2007; Keskin et al. 2008; Altunkaynak et al 2012b; Ersoy et al., 2011, 2012; Altunkaynak and Dilek 2013). From Early Eocene to Late Eocene, addition of voluminous magmatic products of plutonic and volcanic activities into the crust may have led to magmatic thickening and thermal weakening of orogenic crust by the end of the Eocene. Perhaps, migmatization and partial melting created a ductile middle crust that accommodated or drove the initiation of ductile low angle normal faults similar to ÇDFZ during the transitional phase, the Eo-Oligocene. Therefore in the light of thermochronology, structure and geology of GGMC combined with the regional tectonics of western Anatolia, we infer the partial melting and the migmatization period of GGMC corresponds to the transitional phase between the latest phase of orogeny when the crust was still thick and the incipient phase of extension. This period partly overlaps with the retreat of the subducted slab beneath the Hellenic arc that triggered extension on the upper plate during the Oligocene (~30 Ma; see Jolivet and Facenna, 2000; Bozkurt 2000; Bozkurt and Mittwede 2005 and Catlos and Çemen 2005 and the references therein) - Early Miocene period. Extension has continued possibly interruptedly to the present. Thus, we infer that combination of thermal weakening and syn-convergent extension (see, Altunkaynak and Dilek 2006; Altunkaynak et al 2010; 2012b for the detailed discussion on Syn-convergent extension) and the slab rollback at the Hellenic trench played significant role for the extension and, in turn intensive Oligocene-Early Miocene magmatic activity.

When the crustal extension and associated exhumation reached a certain threshold, the lithospheric mantle responded to the isostatic rebound and started to experience partial melting that produced the ÇG during the Early Miocene. The reason for not showing very extensive but relatively higher temperature deformation fabric in the ÇG is possibly because: (1) the significant amount of exhumation and uplift of GGMC had already taken place along the ÇDFZ. (2) Syn-kinematically, ÇG was intruded into partly exhumed GGMC within the footwall of the detachment surface and (3) the ÇG got caught up the ÇDFZ and these two plutons forming ÇPC were uplifted together along ÇDFZ during the Early Miocene.

Extensional deformation in western Anatolia is manifested mainly by a series of north-dipping detachment faults and shear zones. The Kazdag Massif in NW Anatolia (Okay and Satir, 2000, Işık et al. 2004; Thomson and Ring, 2006; Bozkurt 2007; Dilek and Altunkaynak 2007), the Menderes core complex in Central Western Anatolia (Cavazza et al., 2009; Isik et al., 2003; Çemen et al., 2006; Dilek et al., 2009; Catlos et al., 2010; Erkül, 2010; Erkül and Erkül 2012), Cyclades core complex in the southern Aegean region all began its initial exhumation in the Late Oligocene–Early Miocene (Jolivet et al., 2009 and references therein). During the exhumation of the deeply seated metamorphic rocks and syn-tectonic granitic plutons were formed commonly in the footwalls of major detachment faults. They display evidence of a ductile deformation in an earlier stage, which was superimposed later by a semi-brittle and brittle deformation similar to the Çataldağ Plutonic Complex.

In harmony with these extensionally induced major events that are recorded in the region, in our study area we identified the following coeval events; 1) Development of roughly N-S trending stretching lineations formed in association with the detachment fault (ÇDFZ) along the northern and eastern edge of ÇPC. 2) Exhumation of Eo-Oligocene granite-gneiss-migmatite complex (GGMC) of middle crustal levels to higher elevations along a detachment fault. 3) The emplacement of syn-extensional I-type granodiorite (ÇG) during the Early Miocene.

Accordingly, we conclude that the ÇG – GGMC massif duo is a core complex, which was exhumed in the Early Miocene as a dome structure in the footwall of a ring-shaped low-angle detachment surface.

2.7 Conclusions

This study has reached the following conclusions:

- Çataldağ plutonic complex consists of two completely different granitic bodies. That are named herein as the Granite-gneiss-migmatite complex (GGMC) and the Çataldağ granodiorite (ÇG). GGMC is a heterogeneous body consisting of migmatite, gneiss and two-mica granite, and represents a deep–seated pluton. By contrast, ÇG represents a discordant, shallow level intrusive body. The GGMC is Latest Eocene-Early Oligocene and ÇG is Early Miocene in age. The age data when evaluated together with the contact relationships, internal petrological and primary structural textural features indicate that the two plutons were formed at different times, and were emplaced at different levels in the crust.

- ÇDFZ is a low-angle detachment fault zone that bounds the northern and eastern margins of GGMC and ÇG. Both GGMC and ÇG occur in the footwall of this detachment fault as a dome-shaped core complex, whereas Neogene sedimentary rocks and the metamorphic basement rocks are exposed in its hanging wall. A number of micro and meso scale shear sense structural indicators are observed in the fault zone. They display evidence of a ductile deformation in an earlier stage, which was superimposed later by a semi-brittle and brittle deformation. Among those are small scale asymmetrical folds, mica-fish, feldspar-fish and micro faults. They indicate top-to-north top-to-NE sense of movement that occurred in the early Miocene. This exhumation was partly contemporaneous with the development of the major core complexes of the region e.g. The Menderes Massif and The Kazdağ Massif.

3. COOLING AND DEFORMATION HISTORY OF THE ÇATALDAĞ METAMORPHIC CORE COMPLEX (NW TURKEY)

3.1 Introduction

Spatial and temporal link between Metamorphic Core Complex (MCC) formation and magmatism is well known after pioneering studies in the Basin and Range Province, the Canadian Cordillera, the Variscan belt and Aegean Region which provided a better understanding of how the continental crust evolves in response to extensional tectonics (Crittenden et al., 1980; Lister and Baldwin, 1993; Daniel and Jolivet, 1995; Vanderhaeghe et al., 1999). The history of metamorphic core-complex evolution involves rapid cooling and exhumation of middle crustal or deeper rocks and associated granitoids in the footwall of the detachment faults and coeval sedimentation of continental clastic rocks in the hanging wall. Extension is characterised by progressive deformation from ductile to brittle, which is well expressed by footwall rocks that are composed of protomylonites, mylonites, ultramylonites, cataclastic rocks and late brittle faults (e.g. Coney, 1980; Lister and Davis, 1989; Bozkurt and Park, 1994; Işık et al., 2003). In particular, syn-extensional and shear zone-controlled synkinematic plutons are significant markers of ductile-to-brittle deformation in an extending crust (Lister and Baldwin, 1993; Vanderhaeghe, 2001; de Saint Blanquat et al., 2011; Charles et al., 2011). Western Anatolia, which is part of the Aegean extensional province, is one of the best places to study extensional deformation and magmatism. In the Late Oligocene-Early Miocene, exhumation of deep crustal rocks bounded by detachment faults and syn-extensional granites emplaced into the footwall of these faults and mylonitic granitic rocks occurred (Bozkurt and Mittwede, 2005; Figure 3.1).

This chapter is based on the paper, Kamacı, Ö., Altunkaynak, Ş., Cooling and deformation history of the Çataldağ Metamorphic Core Complex (NW Turkey). J. Asian Earth Sciences, 172, 279-291, 2019.

The Menderes Core Complex (MCC) granites (Eğrigöz, Koyunoba, Alaçamdağ, Baklan, Salihli, Turgutlu: Gessner et al., 2001; Işık et al., 2003; Çemen et al., 2006; Dilek et al., 2009; Catlos et al., 2010; Oner and Dilek, 2011; Erkül and Erkül 2012, Altunkaynak et al., 2012; Erkül et al, 2017), the Kazdağ core complex (KCC) granites (Evciler and Eybek: Okay and Satir, 2000; Genç and Altunkaynak, 2007, Bonev et al., 2009) and the Çataldağ granodiorite (Kamacı et al., 2017) are good examples of syn-extensional granitic plutons that were emplaced into shear zones in the footwall of detachment faults in Western Anatolia. The Cycladic Core Complex (Buick, 1991; Gautier and Brun, 1994; Vandenberg and Lister, 1996) and the Rhodope Core Complex (Dinter and Royden, 1993) also contain syn-extensional granites. These deformed plutons were emplaced into shallow crustal levels and underwent ductile-to-brittle deformation under shear zones in which mylonitic equivalents of the granitic rocks were exposed.

Detailed studies including the usage of modern geothermometry methods, geochronology and microtectonics to better understand the deformation and cooling histories of metamorphic core complexes and associated granite intrusions in western Anatolia are limited. In order to fill this gap, we conducted a detailed and integrated study of petrography, microstructural analyses and two feldspar geothermometry together with our previously published geochronological data to better understand the time-progressive deformation and cooling history of the Çataldağ Metamorphic Core Complex, and synkinematic granite emplacement associated with the crustal extension in NW Anatolia (Turkey).

Through the deformations and the mineral closure temperatures obtained via geochronology of the TGMC, the ÇSP and other deformed plutons intruded into the Anatolian metamorphic core complexes provide an overall picture of the Oligo-Miocene extension history of Western Anatolia.

To understand the history of deformation, we conducted a detailed analysis of microstructures. Quartz, feldspar, and mica, the dominant minerals of the TGMC and ÇSP, were used to study the variation in microstructures, the processes, and the conditions of deformation.

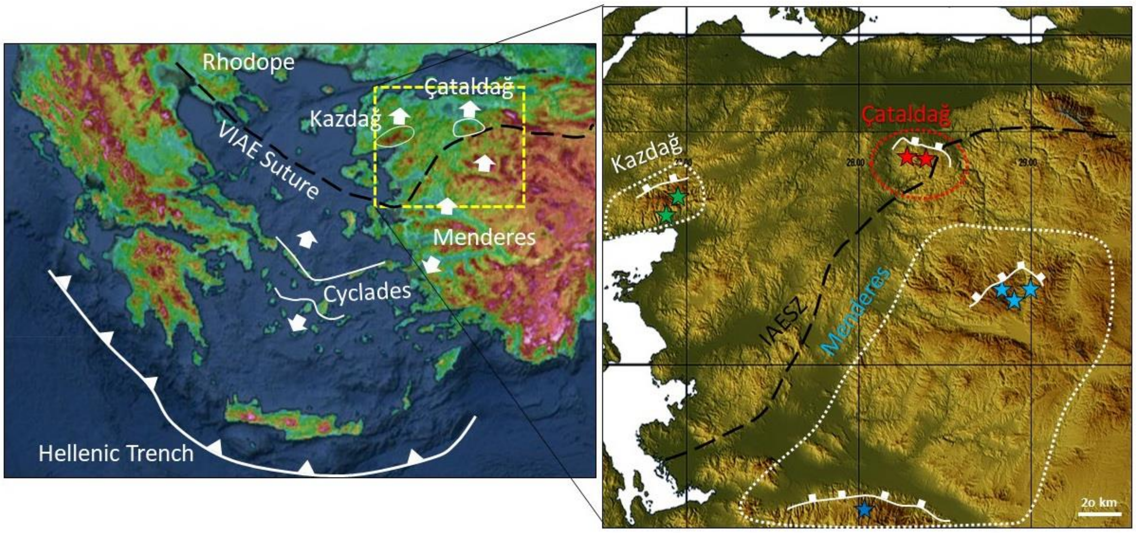

Figure 3.1 : Simplified tectonic map of the Aegean region showing the major tectonic units, metamorphic massifs and the western Anatolian deformed granites/leucogranites (shown by stars) in Çataldağ, Menderes and Kazdağ Core Complex.

Furthermore, the temperature for recrystallisation of feldspars due to tectonothermal processes provided by two-feldspar thermometry was compared with the deformation temperatures obtained from analysis of microstructures (after Langille et al., 2010; Bikramaditya Singh and Gururajan, 2011).

This study presents the first detailed microstructural data, K-feldspar and plagioclase chemistry and two-feldspar geothermometry data from the TGMC and ÇSP. Together with the geochronology and mineral closure temperatures, these data provide new constraints on shear zone development associated with extension and implicate exhumation mechanism. This study also allows a better understanding of the emplacement, deformation, and cooling of synkinematic plutons, and shows the connection among the extension-detachment faulting and granitic magma emplacement at different depths in the western Anatolian extending crust.

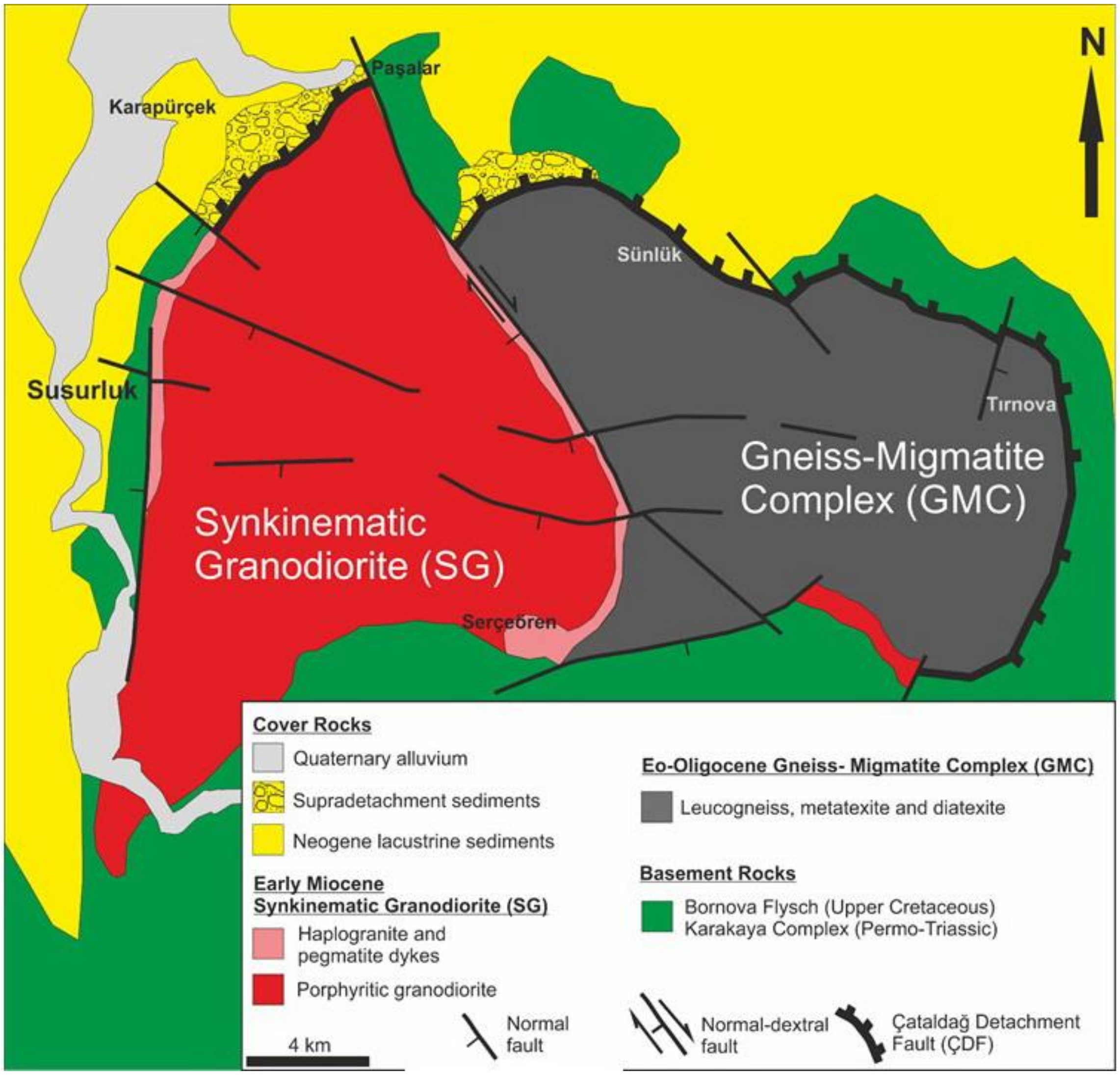

Figure 3.2 : Simplified geological and structural map of the Çataldağ Metamorphic Core Complex (ÇMCC). Colour index of geothermocronological data is as following: U-Pb Zircon (red) and monazite (orange), $^{40}Ar/^{39}Ar$ muscovite (green), biotite (blue) and K-feldspar (black) ages with mineral closure temperature in same colour.

3.2 Lithologies and Kinematics

Çataldağ core complex is a domal uplift of metamorphic and plutonic rocks bounded by shear zone (ÇDFZ). The domal uplift is represented by TGMC which is a diatexitic cored migmatite dome. The deformed plutonic rocks bounded by shear zones (Çataldağ Detachment Fault Zone; ÇDFZ) are represented by ÇSP.

The Latest Eocene-Early Oligocene TGMC forms the eastern part, whereas the Early Miocene ÇSP and associated sills and dykes constitute the western part of the ÇMCC.

The TGMC (Figure 3.4) consists mainly of two-mica granite, quartz-feldspar leucogneiss, and migmatites, with no abrupt transitions between rock types. Two-mica granite is rare and seen only in the central zone of the TGMC. It is variably deformed but has locally preserved magmatic textures, indicating equigranular and weakly porphyritic medium-grained granite containing quartz + orthoclase + oligoclase + muscovite + reddish-brown biotite ± garnet Apatite, titanite, zircon, and monazite are also present as accessory minerals. Leucogneiss is represented by highly deformed quartzo-feldspatic rocks consisting of quartz + K-feldspar + plagioclase + muscovite + garnet ± biotite ± zircon. The major minerals of the gneiss suggest its granitic origin. In the field, the gneiss and the migmatites are observed to be intricately intermixed.

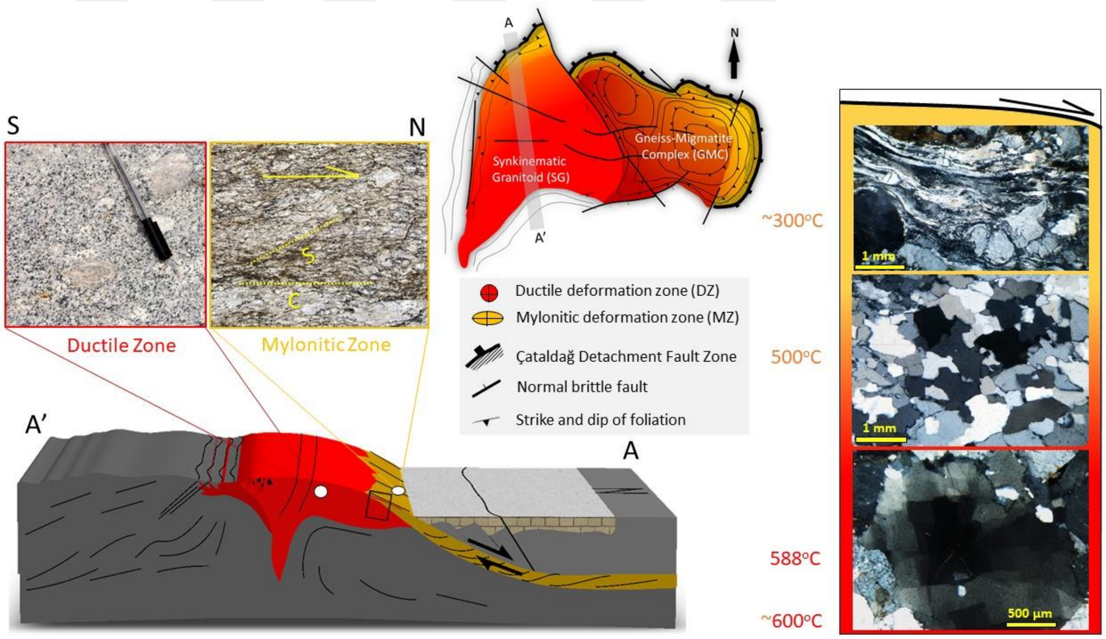

Figure 3.3 : Progressive deformation of the ÇSP from sub-magmatic to solid-state deformed granodiorite (DZ) to solid-state to brittle mylonitic gneiss (MZ) that shows top-to-the-north sense of shear and a model of the synkinematic nature of the ÇSP. Deformation temperatures are obtained from two-feldspar thermometer.

Migmatites are commonly represented by the metatexites (formerly partially-molten rocks; Menhert, 1968; Brown, 1973; Vanderheaghe, 2009) which display limited magmatic fabric and highly deformed rocks in solid-state. They result from small extents and low temperatures of partial melting (Sawyer, 2008). The mineral composition of the melanosome is biotite + quartz + K-feldspar + plagioclase + garnet ± cordierite ± sillimanite while the leucosome is made of quartz and feldspar. Metatexite is particularly common on the northwestern and eastern borders of the TGMC. Towards the centre of the TGMC, metatexite passes into diatexite (former magma), which is a migmatite member represented by generally a magmatic fabric with limited solid-state deformation and more extensive partial melting. Garnet-bearing two-mica granites are representative of diaxites in the TGMC.

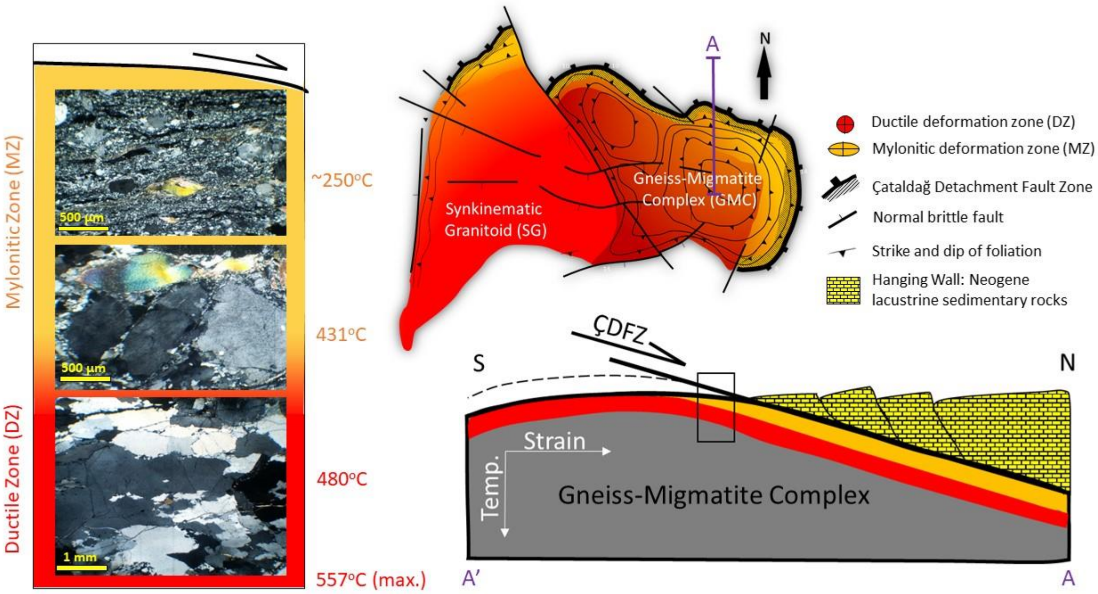

Figure 3.4 : DZ and MZ deformations in the TGMC under ÇDFZ. Deformation temperatures are obtained from two-feldspar thermometer.

The ÇSP mainly consists of granodiorite, with haplogranite and pegmatite dykes. The granodiorite is identified in the field by its porphyritic texture consisting of large megacrysts of K-feldspar. It is formed from plagioclase, quartz, K-feldspar (orthoclase, perthite, and microcline), and biotite. Titanite, zircon, apatite, and opaque minerals occur as accessory minerals. The haplogranite contact with the main body of the granodiorite is sharp, displaying a chilled margin against the metapelitic-metabasic basement rocks of the Karakaya Complex and Bornova Flysch in the west (Okay, 1984; Okay et al., 2001).

The ÇSP was emplaced into the metapelitic-metabasic and calc-silicate basement rocks of the Karakaya Complex. A well-developed contact aureole is observed along the southern border with a mineral paragenesis of calcite+diopside+garnet+wollastonite±vesuvianite indicating pyroxene-hornfels facies conditions.

TGMC and ÇSP are bounded along their northern contacts by the Çataldağ Detachment Fault Zone (ÇDFZ; Kamaci et al., 2017). Slickenlines, undulation, and turtle-back surfaces which are observed within the fault zones and fault planes display the normal fault characteristics of the ÇDFZ (for further information, see Kamaci et al., 2017). The TGMC and ÇSP form the footwall, while the hanging wall is represented by the basement rocks, supra-detachment colluvium sediments and Neogene lacustrine sediments (Figures 3.3 and 3.4).

The shear sense indicators are used to determine the spatial distribution of the shear sense at the microscale. The oriented samples were cut parallel to the lineation and perpendicular to the foliation (XZ section). The shear sense structures of ÇDFZ were as follows: σ-type mica-fish structures (muscovite, biotite; Figure 3.5a and Figure 3.5b, respectively), truncated K-feldspar-fish (Figure 3.5c), domino-type feldspar microfracture (Figure 3.5d), asymmetric poly-mineralic (quartz-feldspar) shear fold (Figure 3.5e), σ-type feldspar-fish structures following brittle deformation (Figure 3.5f), δ-type (Figure 3.5g) and σ-type winged mantled feldspar by quartz in metatexite (Figure 3.5h). The samples consistently record a top-to-the-north shear sense.

3.3 Analytical methods: Two-feldspar Thermometry

Two-feldspar thermometry (Barth 1951, 1968; Stormer 1975; Whitney and Stormer 1977; Powell and Powell 1977; Fuhrman and Lindsley 1988; Elkins and Grove 1990; Benisek et al. 2004; Putirka 2008) was applied to the rocks of the ÇSP to determine deformation temperatures.

The chemical composition of the plagioclase and K-feldspar from the DZ was analysed, and the perthitic K-feldspar and plagioclase compositions at the contact between the feldspar porphyroclast pairs from the MZ were selected for thermometry. The two-feldspar thermometer uses the distribution of the albitic composition between the coexisting plagioclase and K-feldspar to provide the temperature of chemical re-equilibrium/recrystallisation of feldspars during tectonothermal events (Langille et al., 2010; Bikramaditya Singh and Gururajan, 2011).

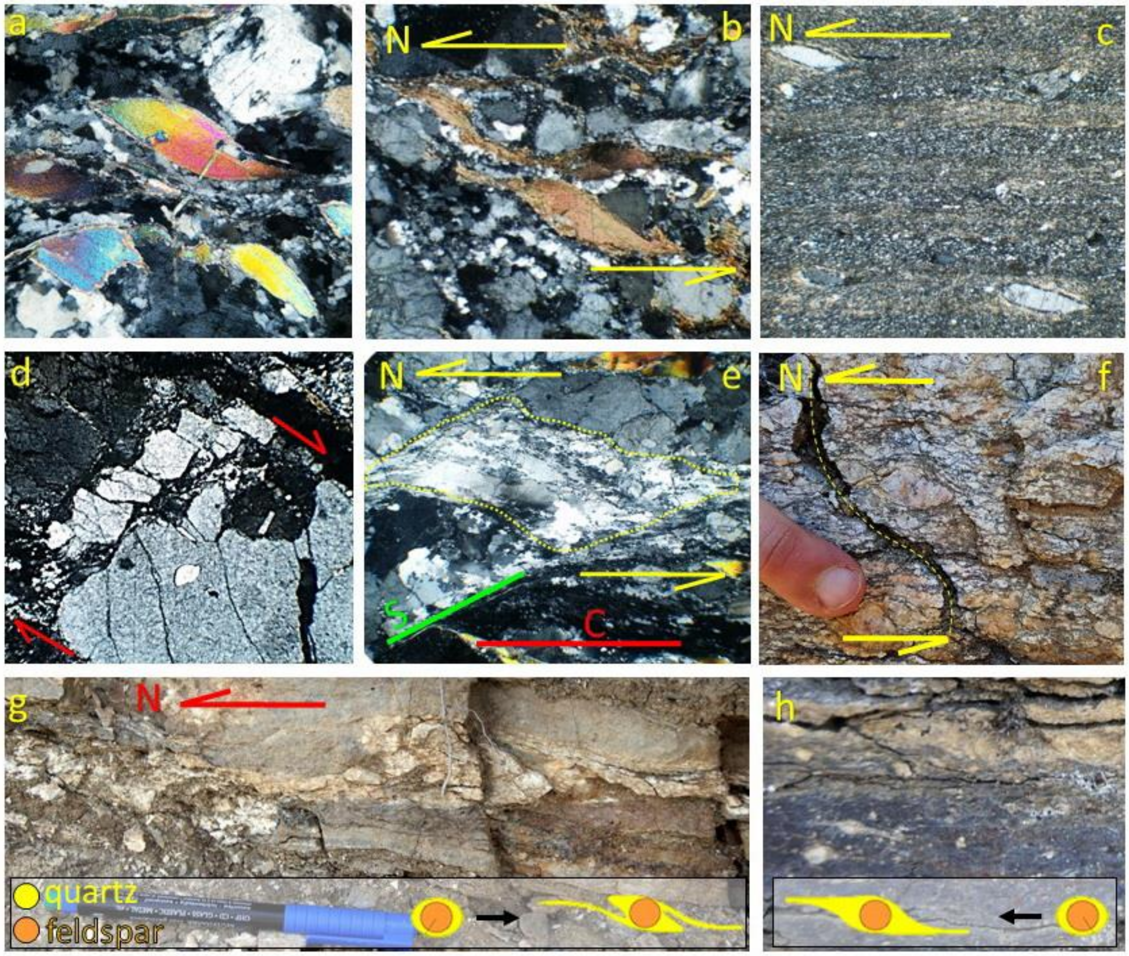

Figure 3.5 : Shear sense indicators of the ÇMCC along the mylonitic zone (MZ): a) σ-type muscovite-fish structures, b) biotite-fish, c) truncated K-feldspar-fish, d) domino-type feldspar microfracture, e) asymmetric poly-mineralic (quartz-feldspar) shear fold with C-S structures, f) σ-type feldspar-fish structures following brittle deformation, g and h) δ-type and σ-type winged mantled feldspar by quartz in metatexite, respectively.

Electron microprobe analyses of representative samples were carried out on the CAMECA-SX50 Electron Probe Micro Analyzer (EPMA) at the University of Kentucky. Thin sections of the representative samples were made and carbon coated prior to use in the EPMA. The analyses were run with a probe current of 10 nA, an acceleration voltage of 15 kV and a beam diameter of 0.5 lm. Point analyses were conducted across plagioclase and K-feldspar. The equations (Eqn 3.1 and Eqn 3.2) of Putirka (2008) are used to estimate the temperatures presented in Table 1.

$$T = \frac{-442 - 3.72P}{0.11 + 0.1\ln\left(\frac{X_{Ab}^{afs}}{X_{Ab}^{pl}}\right) - 3.27\left(X_{An}^{afs}\right) + 0.0098\ln\left(X_{An}^{afs}\right) + 0.52\left(X_{An}^{pl}X_{Ab}^{pl}\right)} \tag{3.1}$$

$$\frac{10^4}{T} = 9.8 - 0.098P - 2.46\ln\left(\frac{X_{Ab}^{afs}}{X_{Ab}^{pl}}\right) - 1.42\left(X_{Si}^{afs}\right) + 423\left(X_{Ca}^{afs}\right) - 2.42\ln\left(X_{An}^{afs}\right) - 11.4\left(X_{An}^{pl}X_{Ab}^{pl}\right) \tag{3.2}$$

3.4 Microstructures and Two-feldspar Thermometry

Microstructural analysis of the ÇMCC revealed that both the TGMC and the ÇSP were affected by solid-state deformation. Microstructures were classified as submagmatic-to-solid state ductile deformation zone (DZ) and ductile-to-brittle mylonitic deformation zone (MZ) based on the estimated deformation temperature and intensity of the strain. The microstructures (DZ and MZ) are summarised below (Table 3.2; Figures 3.6 and 3.7).

3.4.1 The submagmatic-to-solid state ductile deformation zone (DZ)

3.4.1.1 The ductile zone of the ÇSP

The DZ corresponds to a high temperature deformation zone of the ÇSP. The DZ is characterised by the coexistence of (preserved) magmatic texture as a result of weak strain intensity and high temperature of deformation (Figures 3.6a, 3.6b and 3.6c). The plagioclase of the granodiorite is mostly euhedral in shape and shows oscillatory zoning. The K-feldspar display microcline (tartan) twinning and its megacrsyts present marginal replacement by myrmekite (Figure 3.6c). The quartz exhibits chessboard extinction (Figure 3.6b) and Grain-Boundary Migration (GBM; Figure 3.6e). The rocks of the DZ display weak foliations which are difficult to observe macroscopically (Figure 3.6a). Toward the MZ, the DZ shows a narrow zone where the magmatic textures are overprinted by intracrystalline deformation (Figures 3.6d, 3.6e, and 3.6f). The transition from the DZ to the MZ is associated with the development of a foliation indicating more intense deformation. The K-feldspar is represented by flame perthites (Figure 3.6f). The micas form anastomosing folia around feldspars.

3.4.1.2 The ductile zone of the TGMC

The DZ is characterised by microstructures indicating medium temperature solid-state deformation and significant intensity of strain, evidenced by grain size reduction and softening reactions of quartz and K-feldspar recrystallisation processes such as subgrain rotation recrystallisation (ÇSPR) and the development of core-and-mantle structures (Figures 3.7a, 3.7b, and 3.7c). Feldspars are seen as porphyroclasts. Bulging recrystallisation (BLG) is common on K-feldspars (Figure 3.7c). Quartz shows grain size reduction and suffers from GBM to ÇSP (Figure 3.7b). The DZ clearly displays macroscale foliation (Figure 3.5a).

3.4.1.3 Deformation temperatures of DZ

Chessboard extinction and GBM in quartz and myrmekite formation in feldspars are important indicators of high temperature (HT) deformation. At temperatures >600°C, quartz exhibits chessboard extinction (Lister and Dornsiepen, 1982). GBM is the most common quartz recrystallisation process (>500°C; Stipp et al., 2002) in the DZ.

HT deformation is also indicated by myrmekites replacing the K-feldspar megacrysts along grain boundaries that are mostly parallel to the foliation (500-600°C; Simpson and Wintsch 1989). The solid-state myrmekite around the K-feldspars can also cause grain size reduction, which commonly occurs under HT conditions (Vernon et al., 1983; Simpson, 1985; Pryer, 1993). Microcline twinning is common in feldspars, but does not occur in the absence of stress (Gerald and McLaren, 1982). The presence of flame-shaped perthite (FSP) indicates that the deformation of feldspar was continuous from HT to lower temperature conditions (Vernon, 1991). BLG of feldspars is common in the DZ.

The lowest temperature limit of the DZ is about 450°C, which is related to the ductile-brittle transition temperature in feldspar (Passchier and Trouw, 2005). Micas display ductile deformation, especially around feldspars. In light of the microstructures, DZ can be concluded to have deformed ductilely from >600 to >450°C (Figure 3.8a).

Two-feldspar geothermometry provides deformation temperatures in the DZ of 501-588°C (average 544°C for the ÇSP and average 483°C for the TGMC). This range of temperatures is consistent with the temperature range estimated from microstructures (Figure 3.8b).

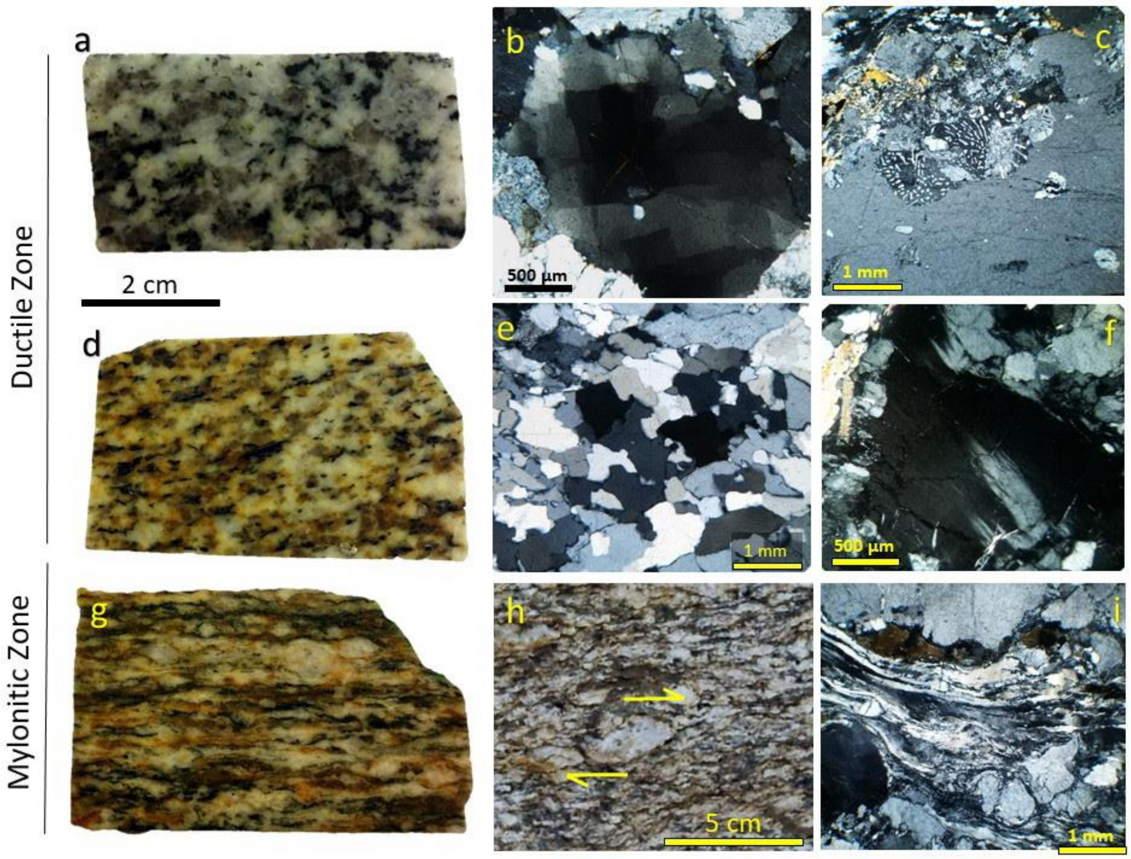

Figure 3.6 : Microstructures of the ÇSP and evolution of temperature-deformation path: a) rock-chip of granodiorite, b) chessboard extinction (CBE) of quartz, c) myrmekite replacement in margin of K-feldspar megacryst, d) rock-chip of deformed granodiorite, e) quartz grain boundary migration (GBM), f) flame-shaped perthite (FSP), g) rock-chip of mylonitic (augen) gneiss, h) Feldspar-fish, and i) the quartz subgrain rotation recrystallisation (ÇSPR), quartz-ribbons, bulging recrystallisation (BLG), and late stage fracturing of K-feldspar. Q: quartz, Kf: K-feldspar, P: Plagioclase.

3.4.2 Mylonitic zone (MZ)

3.4.2.1 The mylonitic deformation zone of ÇSP

The MZ shows distinct foliation and kinematic C-S structures. The MZ is distinguished from the DZ by the higher intensity of strain at relatively lower temperature conditions (Figures 3.6g, 3.6h, and 3.6i). The granodiorite of the DZ evolves into protomylonitic-to-mylonitic augen gneiss toward the ÇDFZ (Figure 3.3). The plagioclase of the mylonitic gneiss shows a grain size reduction. The K-feldspar porphyroclasts are represented by sigmoidal shapes as a shear sense indicator (Figure 3.6h).

Table 3.1 : Chemical composition of feldspars and two-feldspar thermometer results of ÇCC based on the equations of Putirka 2008.

	K- Feldspar Composition							Plagioclase Composition							Eqn 3.1	Eqn 3.2	Global regression	Average	Total Average
	SiO_2	Al_2O_3	FeOt	CaO	Na_2O	K_2O	TOTAL	SiO_2	Al_2O_3	FeOt	CaO	Na_2O	K_2O	TOTAL	T(C)	T(C)	T(C) (±30)	T(C)	T(C)
Ductile Zone	63.67	19.12	0.02	0.02	1.17	14.49	98.49	59.99	26.24	0.00	6.64	7.25	0.22	100.34	542.58	502.50	527.99	524.35	544.48
	64.36	19.00	0.08	0.02	1.35	14.82	99.62	62.22	25.19	0.13	5.77	7.98	0.19	101.49	550.89	510.30	526.92	529.37	
	64.94	19.15	0.09	0.02	0.98	15.11	100.29	62.58	24.92	0.00	5.64	8.20	0.21	101.54	540.05	500.10	543.57	527.91	
	62.98	18.90	0.00	0.03	1.04	15.08	98.03	62.68	24.47	0.13	5.30	8.08	0.25	100.91	555.73	514.44	560.14	543.44	
	65.80	19.15	0.11	0.05	1.08	14.95	101.15	62.01	24.18	0.14	5.14	8.20	0.25	99.93	608.52	552.63	603.33	588.16	
	65.67	19.45	0.01	0.04	0.93	15.26	101.36	61.82	24.71	0.15	5.32	8.19	0.27	100.46	573.42	525.69	587.63	562.25	
	64.99	19.27	0.13	0.03	0.70	15.72	100.84	62.51	24.57	0.15	5.18	8.21	0.22	100.85	530.39	493.13	584.10	535.87	
Mylonitic Zone	64.53	19.25	0.05	0.02	0.82	14.88	99.55	61.86	24.65	0.06	5.42	7.98	0.16	100.13	525.65	487.29	546.76	519.90	516.72
	64.67	18.97	0.05	0.03	0.90	15.68	100.29	62.36	24.91	0.08	5.23	8.40	0.19	101.17	530.75	494.34	549.56	524.88	
	64.99	19.27	0.13	0.03	0.70	15.72	100.84	62.72	24.32	0.00	4.89	8.33	0.13	100.40	527.29	490.53	581.09	532.97	
	64.53	19.25	0.05	0.02	0.82	14.88	99.55	63.87	23.69	0.12	4.26	8.78	0.28	101.00	509.95	473.88	529.46	504.43	
	64.57	19.45	0.01	0.02	0.93	15.26	100.24	64.23	23.70	0.00	3.95	8.94	0.14	100.96	508.43	474.21	521.63	501.42	
Representative electron microprobe analyses of feldspars and two-feldspar thermometry results (Putirka 2008) of GGMC																			
Ductile Zone	62.70	18.87	0.07	0.03	1.99	14.46	98.12	62.49	21.57	0.10	2.48	10.76	0.40	97.79	559.28	518.60	497.93	525.27	483.73
	62.10	19.21	0.04	0.01	1.29	14.89	97.54	63.11	21.91	0.16	2.46	10.60	0.32	98.56	460.61	436.94	436.65	444.73	
	64.52	18.87	0.00	0.01	1.67	14.76	99.82	63.32	21.85	0.07	2.29	10.71	0.30	98.53	449.05	426.61	413.04	429.57	
	62.29	19.30	0.00	0.01	1.89	14.20	97.70	63.51	22.09	0.00	2.27	10.68	0.31	98.85	467.91	443.23	425.57	445.57	
	63.98	18.80	0.00	0.04	1.76	14.68	99.27	63.63	21.81	0.00	2.36	10.74	0.37	98.91	565.76	521.66	512.27	533.23	
	63.08	18.76	0.00	0.05	2.03	14.25	98.16	65.16	22.16	0.00	2.22	10.47	0.34	100.35	591.51	542.86	536.05	556.81	
	62.62	18.77	0.00	0.01	1.49	15.07	97.96	65.57	22.14	0.05	2.25	11.11	0.29	101.41	469.26	444.73	438.72	450.90	
Mylonitic Zone	63.21	18.81	0.01	0.01	0.80	16.13	99.00	65.93	21.85	0.00	2.17	10.44	0.31	100.70	430.67	412.32	452.68	431.89	436.29
	62.43	19.36	0.00	0.01	1.03	15.79	98.62	64.26	22.14	0.05	2.25	11.11	0.29	100.11	446.03	425.70	439.72	437.15	
	62.09	18.95	0.00	0.01	1.07	15.35	97.48	64.03	21.89	0.09	1.67	9.27	1.89	98.84	445.19	423.71	450.58	439.83	

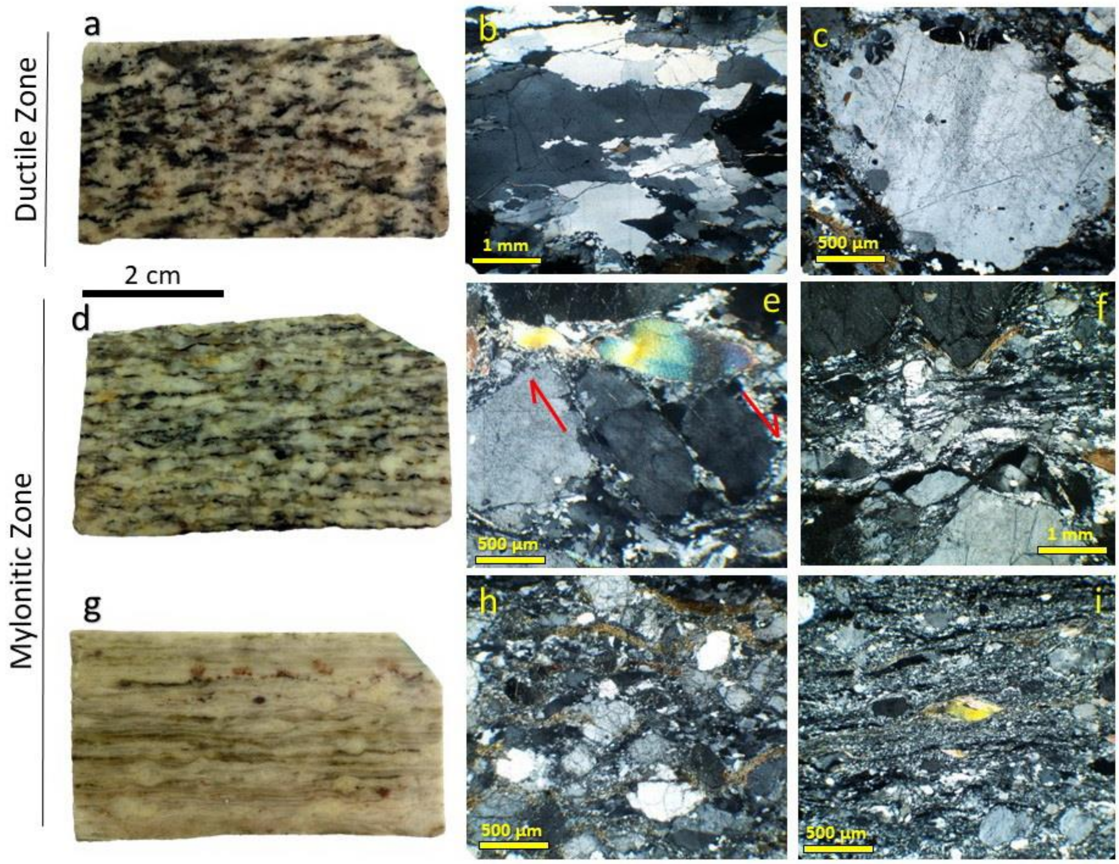

Figure 3.7 : Microstructures of the TGMC and evolution of temperature-deformation path: a) rock-chip of gneiss, b) quartz subgrain rotation recrystallization (ÇSPR); c) bulging recrystallization (BLG) of K-feldspar, d) rock-chip of mylonite, e) domino-type microfracture of brittle K-feldspar, f) quartz ribbon structures, g) rock-chip of ultramylonite, h) elongated biotites in cataclastic flow and i) maximum grain-size reduction in cataclastic flow. Q: quartz, Kf: K-feldspar, M: mica (muscovite).

The quartz recrystallisation type is mostly ÇSPR and less BLG. Quartz ribbon structures are common. As an elongation indicator, the aspect ratio of ribbons is 1/5-10 (shorter side/longer side) (Figure 3.6i). Biotite minerals are represented by mineral-fish structures.

3.4.2.2 The mylonitic deformation zone of the TGMC

The mylonitic/ultramylonitic rocks in this group show low temperature solid-state deformation (Figures 3.7d, 3.7e and 3.7f). Feldspars exhibit brittle deformation. Some feldspars show domino-type displacements (Figure 3.7e).

Table 3.2 : Detailed microstructures of the ÇCC.

Unit	Grade	State/Rheology	Plagioclase	K-Feldspar	Quartz	Mica	Temperature	Intensity of strain
Synkinematic Granitoid (SG)	Ductile Zone (DZ)	Sub-magmatic to solid-state / ductile	Mostly euhedral, oscillatory zoning	Microcline twinning (1), replaced marginally by myrmekite (2), local GBM (3), flame perthites (6)	GBM recrystallisations (4), chessboard extinction/subgrains (5)	Static transformation in chlorite	500 to 700	weak
	Mylonitic Zone (MZ)	Solid-state / ductile	Porphyroclast	Feldspar-fish	SGR, ribbon (aspect ratio: 1:2-5)	Biotite-fish (C-S fabrics), Grain size reduction by shearing	400 to 500	High
Gneiss-Migmatite Complex (GMC)	Ductile Zone (DZ)	Solid-state / ductile	Porphyroclast	Porphyroclast, myrmekite along microcline fractures (7), undulose extinction, BLG recrystallisation	GBM to SGR recrystallization, beginning of grain size reduction	Anastomosing folia around feldspar	400 to 500	Significant
	Mylonitic Zone (MZ)	Solid-state / semi-ductile	Porphyroclast, brittle fracturing	Brtitle fracturing, cataclastic flow, domino-type microfractures	BLG, ribbon (aspect ratio: 1:>10)	Mica-fish (C-S fabrics), Grain size reduction by shearing	300 to 400	High
	(1) Eggleton 1979; Eggleton and Buseck, 1980; Fitz Gerald and McLaren, 1982; Bell and Johnson, 1989 (2) Simpson and Wintsch 1989; Vernon 1991a (3) Passchier and Trouw, 2005 (4) Jessel, 1997; Stipp et al., 2002, (5) Blumenfeld et al., 1986; Mainprice et al., 1986; Kruhl, 1996); Stipp et al. 2002), (6) (Pryer and Robin, 1996), (7) Vernon, 1983							

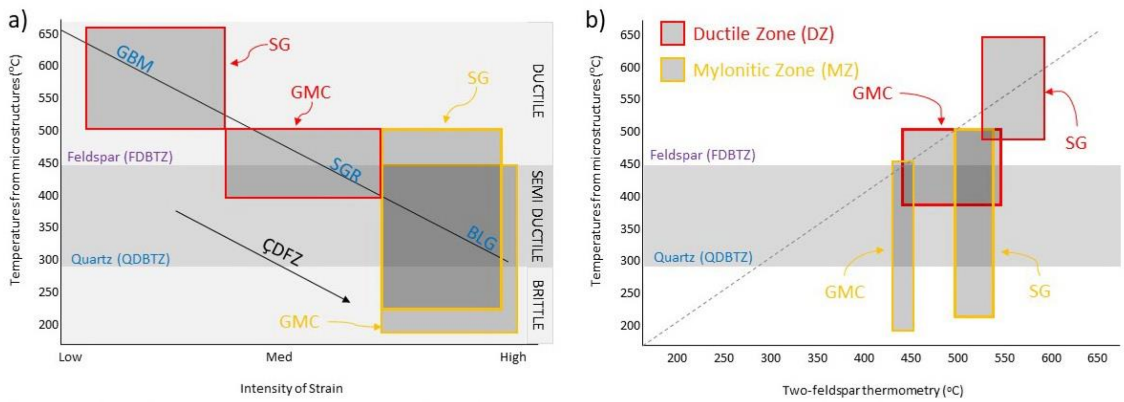

Figure 3.8 : a) Evolution of temperature and strain intensity on the microstructures of the ÇMCC. b) Comparison diagram of temperature estimation of deformation zones from microstructures and two-feldspar thermometry. Quartz microstructures, GBM: Grain boundary migration, SGR: Subgrain rotation recrystallisation, BLG: Bulging recrystallisation, ÇDFZ: Çataldağ Detachment Fault Zone, FDBTZ: Feldspar ductile-to-brittle transition zone, QDBTZ: Quartz ductile-to-brittle transition zone.

Quartz is mostly recrystallised as ribbon stuctures (Figure 3.7f). Most of the biotite and muscovite minerals present mica-fish structures. Ultramylonites developed in the TGMC show more grain size reduction and more cataclastic flow than the ones of the ÇSP (Figures 3.7g, 3.7h, and 3.7i). The MZ clearly exhibits C-S structures and mica-quartz bands at a macroscopic scale (Figure 3.7d) and is located at the northern and eastern boundaries of TGMC (Figure 3.4).

3.4.2.3 Deformation temperatures of the MZ

Grain size reduction and mineral fish structures indicate high strain intensity in the MZ. Feldspar-fish is present at a higher temperature grade, possibly indicating conditions of a temperature of >450°C. Fine-grained recrystallised K-feldspar at the rim probably indicates BLG recrystallisation accommodated by dislocation creep, which indicates temperatures of 450-550°C (Passchier and Trouw, 2005). Quartz shows ÇSPR, ribbon structures, and undulation extinction in the ÇSP, indicating medium temperature (MT) conditions (400-500°C; Stipp et al., 2002). Quartz shows BLG recrystallisation (280-400°C; Stipp et al., 2002), undulation extinction and cataclasis (<250°C; Stipp et al., 2002) in the TGMC. The ribbon structure is predominant in the mylonites and ultramylonites of the TGMC. Some quartz aggregates are elongated and form discontinuous layers, probably due to elongation and recrystallisation of former single quartz grains (Vernon, 2004). Feldspars are mainly represented by brittle deformed porphyroclasts. Strain shadows are also present in intersection zones of quartz and feldspar porphyroclasts. In the same rocks, feldspars, quartz, and biotite show evidence of brittle deformation, which indicates that continuous deformation was active from medium to lower temperature conditions (cataclasis: <250°C). These microstructures require a temperature range of 500-450°C to <250°C (Figure 3.8a).

Two-feldspar geothermometry provides mylonitic deformation temperatures of around 432-533°C (average 517°C for the ÇSP and average 436°C for the TGMC), which are in agreement with the assumed deformation temperature range from microstructures (Figure 3.8b).

These temperature ranges reflect a dynamic metamorphic episode during the emplacement of ÇSP that resulted in the recrystallisation of feldspars. The deformation temperature range of the DZ is smaller than that of the MZ. Therefore, the MZ represents a shallower level of shear zone of the ÇDFZ than the DZ.

Superimposed cataclastic deformation progressively increases toward the ÇDFZ. Cataclasites display angular to sub-rounded quartz, feldspar, and biotite, which exhibit fractures, microfaults, and undulose extinction.

3.5 Discussion

3.5.1 Exhumation history and the Early Miocene deformation of the TGMC

The temperature of deformation is determined based on microstructures and two-feldspar geothermometry decreases from the DZ to the MZ along the ÇDFZ. This observation indicates that the ÇDFZ is responsible for the ductile-to-brittle deformation and exhumation of ÇMCC (Figure 3.4).

The geochronological zircon and monazite LA-ICPMS ages from the DZ of the TGMC vary between 33.8 and 30.1 Ma (the Latest Eocene-Early Oligocene; Kamacı et al., 2017). $^{40}Ar/^{39}Ar$ ages obtained from biotite, muscovite, and feldspar minerals in the mylonitic rocks (MZ) of the TGMC vary from 20.8 Ma (±0.1) to 21.3 Ma (±0.3) (Kamaci et al., 2017). Therefore, the magmatic crystallisation ages (the Latest Eocene-Early Oligocene) and deformation ages (Early Miocene) of the TGMC are quite different from each other (Table 3.3).

In order to evaluate the thermochronological evolution of the TGMC, the following closure temperatures of minerals are used: zircon at about 750°C (TGMC; Kamaci et al., 2017) and monazite at about 700°C for LA-ICPMS method (Kamaci and Altunkaynak, unpublished geochemical data), white mica at about 425°C for $^{40}Ar/^{39}Ar$ (Harrison et al., 2009), biotite at about 275-300°C for $^{40}Ar/^{39}Ar$ (Harrison et al., 1985), and K-feldspar at about 160-250°C for 40Ar/39Ar method (Lovera et al., 1989) (Table 3.3).

According to zircon and monazite (33.4-30.1 Ma, respectively) and mica (~21 Ma) ages obtained from the same rock type reveals that the TGMC had been exhumed to its final location in at least a 8-13 Ma period. With reference to the closure temperatures of zircon, monazite, muscovite, biotite, and K-feldspar, the history of deformation temperatures of the TGMC is about 750°C at 33-34 Ma, 700°C at 30 Ma, 350-400°C at 21.3 Ma, 250°C at 21 Ma, and 160-250°C at 20.7 Ma. This data indicates that the cooling history of TGMC has two stages: between at least the ~34 Ma and 30 Ma intervals, the cooling rate of TGMC was relatively slow (stage 1), and then between 21.3 Ma and 20.7 Ma, it cooled rapidly at higher levels in the crust (stage 2).

3.5.2 Cooling and deformation history of the ÇSP along the ÇDFZ

Based on the microstructures and two-feldspar geothermometry, the temperature of deformation decreases from the DZ to the MZ towards the ÇDFZ, and accordance of dip directions of foliation in the MZ indicate that the ÇDFZ was responsible for the ductile-to-brittle deformation of the ÇSP (Figure 3.3).

Combined geochronology and the mineral closure temperatures allow reconstructing the cooling and thermochronological evolution of the ÇSP. $^{40}Ar/^{39}Ar$ ages yielded from biotite of granodiorite (DZ) and biotite in the mylonitic rocks (MZ) of the ÇSP vary from 20.8 Ma (±0.1) to 21.1 Ma (±0.3) (Kamaci et al., 2017). Altunkaynak et al. (2012) also present zircon SHRIMP age data as 21.9±0.3 Ma from the DZ (Table 3.3). All of the age data obtained from the ÇSP are consistent with each other and correspond to the Early Miocene.

Table 3.3 : Geochronology of GGMC and ÇSP and deformation zones.

				Crystallization age (U-Pb)				Cooling/deformation age (Ar/Ar)					
		Mineral		Zircon		Monazite		Muscovite		Biotite		K-feldspar	
		Closure temperature range (°C)		840-760[1]		713[2]		425-350[3]		300-275[4]		350-150	
		Sample	Rock Type										
GGMC	DZ	OS-345	gneissic granite							20.7	±0,03	21.1	±0,06
GGMC	DZ	OS-351	gneissic granite	32.2	±0,13								
GGMC	DZ	OS-353	gneissic leucogranite	33.8	±0,14								
GGMC	DZ	OS-111	migmatite (restite)							21.2	±0,07		
GGMC	DZ	OS-395	two-mica granite	33.4	±0,69	30.1	±0,23						
GGMC	MZ	OS-75	two-mica granite/mylonite					21.3	±0,04				
GGMC	MZ	OS-105	two-mica granite/mylonite					20.8	±0,04				
		Sample	Rock Type										
ÇSP	DZ	OS-72	biotite granodiorite							21.1	±0,02		
ÇSP	DZ	A2012[5]	biotite granodiorite	21.9	±0,33								
ÇSP	MZ	OS-55	biotite granodiorite /protomylonite							20.8	±0,13		

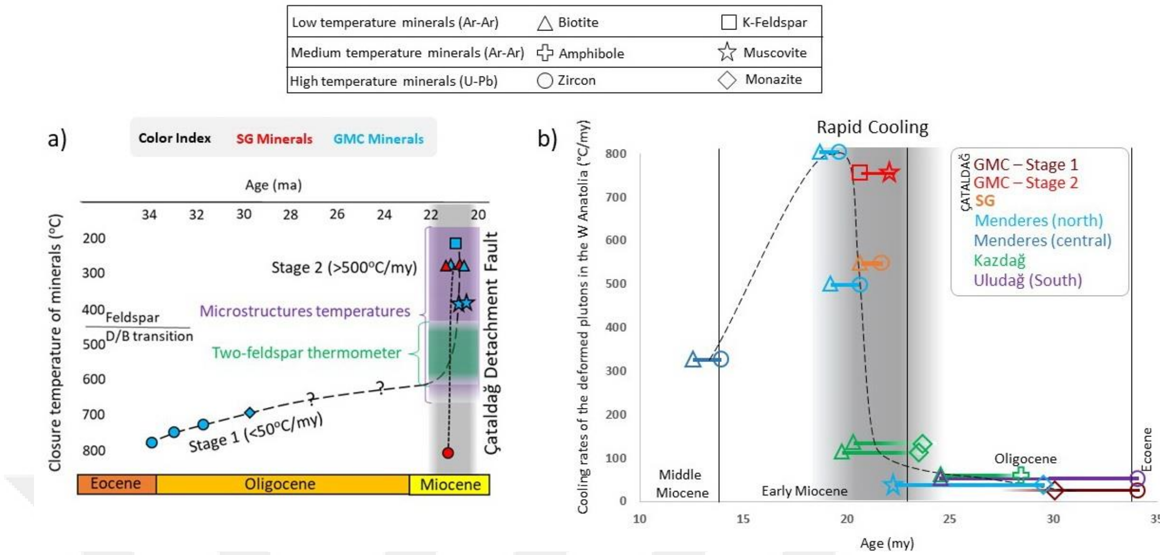

Figure 3.9 : a) Two-stage cooling of the TGMC and rapid cooling of ÇSP based on microstructures, two-feldspar geothermometer and geothermochronology. b) Evolution of cooling rates from the Latest Eocene to the Early Miocene of the deformed plutons of western Anatolia. D/B transition: ductile-brittle deformation.

Closure temperatures of minerals were applied as follows: zircon at about 800°C (ÇSP) for LA-ICPMS method (Kamaci et al., 2017) and biotite at about 275-300°C for $^{40}Ar/^{39}Ar$ geochronology (Harrison et al., 1985) (Table 3.3). Comparing the zircon (21.9 Ma) and biotite (20.8 Ma) ages reveals that cooling of the ÇSP took place over a 1 Ma period with a cooling rate of >500°C/my determined by means of the mineral closure temperature of zircon and biotite, which are 800°C and 275°C, respectively (Kamacı et al., 2017; Harrison et al., 1985).

Furthermore, microstructures show that the ÇSP underwent continuous deformation from high temperature (DZ) and medium temperature to low temperature (brittle deformation) conditions (MZ). Two-feldspar thermometry of the ÇSP demonstrates that the temperature range of the latest recrystallisation and/or re-equilibrium of feldspar was about 400-600°C. The combined microstructure, two-feldspar geothermometry, and geochronological data of the ÇSP are consistent with a rapid cooling rate of >500°C/my.

Rapidly constructed plutons generally have faster cooling rates than more slowly constructed plutons (de Saint Blanquat et al., 2011). Thermal models for rapidly cooled plutons indicate that 30000 years are needed to obtain a temperature decrease from 850°C to 700°C of a 3 km-thick granite at a depth of 3 km (1 kbar) in a crust at 100°C (Clemens, 1998). Temperature decreases from 800°C (zircon closure temperature) to 275°C (biotite closure temperature) require less than 200000 years in a shallow crust. Extensional deformation can play an important role on cooling rates by decreasing temperatures in ductile shear zones (Lister and Baldwin, 1993). Therefore, cooling rates are affected by deformation in syn-kinematic granites. ÇSP suffered from a ductile-to-brittle deformation restricted to about 1 my at shallow depths (Table 3.4; from 21.9 to 20.8 Ma).

The progressive sub-solidus deformation and C-S fabrics in granitic rocks are diagnostic of a synkinematic emplacement of plutons (Berthé et al., 1979; Gapais, 1989; Vanderhaeghe et al., 1999; Charles et al., 2011). Therefore, the emplacement of the ÇSP can be considered as a "synkinematic" pluton which is exhumed along the ÇDFZ.

The deformation ages obtained from the ÇSP and the TGMC are almost the same; corresponding to a narrow range of 21.1 to 20.8 Ma, while the magmatic crystallisation ages of the TGMC (The Latest Eocene-Early Oligocene) and the ÇSP (Early Miocene) differ significantly. In summary, the cooling rate of completely different parts of the ÇMCC (stage 2 of the TGMC and the ÇSP) increased rapidly during the narrow range of 21.3 to 20.7 Ma (Figure 2.9a). Therefore, localized deformation and cooling of the ÇSP suggests that its emplacement is coeval with the development of the ÇMCC.

3.5.3 Emplacement, deformation and cooling of Oligo-Miocene syn-extensional granitoids in Western Anatolia

Many plutons were emplaced as a result of post-collisional magmatism from the Eocene to the Middle Miocene in the Aegean region and western Anatolia (Altunkaynak and Yılmaz 1989; Faure et al., 1991; Gautier et al., 1993; Pe-Piper and Piper, 2000; Altunkaynak, 2006; Dilek and Altunkaynak, 2007; Altunkaynak et al, 2012 a, b). The common features of the Latest Oligocene-Early to Middle Miocene plutons were emplacement into shallow crustal levels, rapid cooling, and deformation in a kinematic boundary near shear zones. These plutons were commonly emplaced into the footwalls of major detachment faults and are represented by the Evciler and Eybek plutons in the Kazdağ Core Complex, the Eğrigöz, Koyunoba, Alaçamdağ, Salihli, and Turgutlu plutons in the Menderes Core Complex and the Çataldağ Synkinematic Pluton (ÇSP) in the Çataldağ Metamorphic Core Complex (Table 3.4).

The predominant crystallisation ages of these syn-extensional granites are 24-19 Ma (Evciler, Eybek, ÇSP, Koyunoba, Alaçamdağ, and Eğrigöz). Toward the south, the crystallisation age reaches 15 Ma (Salihli and Turgutlu granites) in the central Menderes CC (Glodny and Hetzel, 2007; Altunkaynak et al., 2012a, b). The crystallisation ages (via U-Pb zircon geochronology, 24-19 Ma) nearly cover the deformation ages (40Ar/39Ar muscovite, biotite, and feldspar geochronology, 21-19 Ma) of the shallow seated syn-tectonic granites. That is, all of the syn-tectonic plutons cooled rapidly in the shallow crustal levels over the same period (Table 3.4).

All of these syn-tectonic granites were emplaced at shallow levels in the continental crust (e.g. epizone; <7 km) (Okay and Satir, 2000; Cavazza et al., 2009; Erkül et al 2013; Kamacı et al., 2013) (Table 3.4; Figure 3.7). As soon as they had been emplaced at the upper crustal levels, the granites possibly started to deform in high temperature conditions in the footwalls of the detachment faults. The Eğrigöz pluton in the Northern Menderes Core Complex shows HT ductile deformation features (Işık et al., 2004 and references therein) which correspond to DZ. The Alaçamdağ of the MCC (Erkül and Erkül, 2012) and the Evciler pluton of the KCC (Okay and Satir, 2000) present protomylonitic textures near the shear zones of the Simav and Alakeçi detachment faults, respectively, which are similar to the rocks of MZ. Almost all of the plutons display mylonitic deformation along the shear zones. Extensional deformation on the plutons is nearly continuous. Rocks showing ductile deformation were overprinted by brittle deformation consistent with exhumation of the footwalls of the detachment faults through the ductile/brittle transition. Toward the shear zone of the detachment faults, the granites show mylonitic foliation and stretching lineation. The sense of shear of the MCC (the Simav and Alaşehir detachment faults), KCC (Alakeçi detachment fault), ÇMCC (ÇDFZ) and Cycladic Core Complex (Avigad and Garfunkel, 1991; Gautier et al., 1999) are congruent with the N–S- or NE–SW-trending crustal extension of the Aegean region in the Latest Oligocene-Early Miocene.

In order to understand the role of extensional tectonics on the emplacement and cooling processes of the granites, we need to go back further in time, to the Early Oligocene. A simple calculation ([mineral closure temperature of high temperature crystallisation age – mineral closure temperature of low temperature cooling age]/[high temperature crystallisation age – low temperature cooling age]) of the cooling rate of the granites indicates that during the Oligocene, the TGMC and South Uludağ had average cooling rates of 40°C/my (see Table 3.4 and Figure 3.9b). The NE Evciler pluton, which is late Oligocene in age, shows a 65°C/my cooling rate according to 40Ar/39Ar hornblende (ca. 28 Ma) and $^{40}Ar/^{39}Ar$ biotite (ca. 25 Ma) geochronology of the same rock (Altunkaynak et al., 2012). The Oligo-Miocene plutons (S Evciler and Eybek) of the KCC have higher cooling rates than the Oligocene granites at about 130°C/my (Table 3.4). The cooling rates increase dramatically at 22-19 Ma (Figure 3.9b). The highest cooling rates possibly began at ca. 22 Ma. The Eğrigöz, ÇSP, Koyunoba, and Alaçamdağ granites represent a cooling rate of ≥500°C/my (Figure 3.9b). The changing cooling rates are possibly related to the emplacement levels of the plutons. Another possible reason for the increasing cooling rates may be activity of the detachment faults in extending crust.

The extensional regime in western Anatolia played a significant role on crustal build-up and syn-extensional magmatism (Altunkaynak et al. 2012 and references therein). Three models have been proposed to explain the N-S extension and widespread magmatism in western Anatolia: (1) late orogenic collapse of thickened crust following closure of the Tethys ocean along the IAESZ (Seyitoglu and Scott, 1991); (2) "subduction models" positing back arc extension with slab roll-back resulting in southward migration of the Aegean trench (McKenzie, 1978; Le Pichon and Angellier, 1979; Lister et al., 1984; Buick et al., 1990; Okay and Satir, 2000; Jolivet et al., 2013 and references therein); as a "combining model" of retreat of the downgoing slab (model 2) and gravitational collapse of the orogenic crust (model 1) (Gautier et al., 1999 and Vanderhaeghe and Teyssier, 2001);

Table 3.4 : Correlation of deformed granitoids of Anatolian Core Complexes.

		Menderes				Kazdağ			Uludağ	Çataldağ		
Plutons		Gördes	Eğrigöz	Koyunoba/ Alaçamdağ	Central (Salihli, Turgutlu)	Evciler (Northeast)	Evciler (South)	Eybek	South	ÇSP	GMC	
Approximate cooling rate		<100°C/my	800°C/my	500°C/my	330°C/my	65°C/my	140°C/ my	120°C/ my	50°C/my	550°C/my	Stage 1: 35°C/my	Stage 2: 750°C/my
Cooling	Low-temperature geochronology	24,7 my (18)	18,9 my (1)	19,8 my (8)	12-13 my (11)	24,8 my (1)	20,6 my (3)	20,1 my (1) (12)	27,5 my (19)	21 my (4)	21 my (4)	
	Mineral	Muscovite	Biotite	Biotite	Biotite	Biotite	Biotite	Biotite	Muscovite	Biotite	Muscovite	Feldspar
Shear zone	Deformed rocks	Orthogneiss/ leucogranite	mylonite (6) (13)	protomylonite, ultramylonite (8)	mylonite (13)		protomylonite		Metagranite/ Orthogneiss	MZ (protomylonite)	mylonite, ultramylonite	
	(Detachment) faults / sense of shear		Simav (top-to-N)		Alaşehir/ Gediz (top-to-N)		Alakeçi (top-to-N)			Çataldağ Detachment Fault Zone (top-to-N)		
Emplacement	High-med. Temp. Geochronology (U-Pb, Ar/Ar)	30 my (17)	19,5 my (1)	20,7 my (9)	15-16 my (7,10)	27,9 my (500 C) (1)	24 my (2)	23,9 my (1) (750C) (2)	34 my (16)	21,9 my (1) (800C)(4)	34-32 my (750C) (4)	
	Mineral	Monazite	Zircon	Zircon	Zircon	Amphibole	Monazite	Monazite	Monazite	Zircon	Zircon /Monazite	
	Depth (average)	Deep seated	shallow (13)	shallow (13)	7 km (14)	?	7km (3)	2-7 km (15)	Midcrust (16)	Shallow (5)	deep seated (5)	

and (3) “syn-convergent extension models” positing magma generation driven by slab break-off, delamination or convective removal of the lithosphere (Köprübaşı and Aldanmaz, 2004; Altunkaynak and Dilek, 2006; Boztug et al., 2009). Overall, the models address the fundamental problem: what is the main mechanism, extension-driven magmatism or magmatism-driven extension?

A physically heterogeneous crust may be important for developing of MCC. Pre-existing faults in the brittle upper crust can initiate to formation of MCC (Buck, 1993; Koyi and Skelton, 2001; Lavier et al., 1999; Rey et al., 2009). Like all orogenic crusts, the WA crust is physically heterogeneous due to the presence of pre-existing faults. As a post-collisional environment, Western Anatolia had many pre-existing faults which were available for reactivation and may have caused strain localisation, especially near IAESZ where the Eğrigöz, ÇSP, Koyunoba, and Alaçamdağ granites were emplaced. However, pre-existing faults or presence of detachment faults may not be the main cause for the formation of MCC. Detailed analysis in Hellenides shows that the nappe pile and the contacts between nappes have been folded during syn-orogenic exhumation and then transposed during late-orogenic extension (Scheffer et al., 2016).

One of the pioneering studies on the chicken and egg relationship between magmatism and tectonics show that granite emplacement triggers continental extension (Lister and Baldwin, 1993). Numerical and anologue modeling which indicate the importance of pre-existing viscosity–density anomalies such as granitic or migmatitic bodies below the brittle–ductile transition can initiate formation of MCC (Brun et al., 1994; Vanderhaeghe and Teyssier, 2001; Corti et al., 2003; Tirel et al., 2004; Tirel et al., 2008).

The orogenic Anatolian crust was highly evolved thermally due to Eocene to Oligocene magmatism which may have caused rheological heterogeneity and thermal weakening (Altunkaynak and Dilek 2006; Dilek and Altunkaynak, 2007; Altunkaynak et al., 2012a) (Figure 3.7). This magma emplacement-related high geothermal gradient may have caused strain localisation (normal faulting) in the upper crust (Whitney et al. 2013). Western Anatolian Eocene plutons such as the Orhaneli, Topuk, and Gürgenyayla plutons, and Eo-Oligocene magmatism such as the Gördes (MCC), South Uludağ granite, and the TGMC are located near the ÇSP, Eğrigöz, Koyunoba, and Alaçamdağ granites. Therefore, the WA orogenic crust has been heating up since the Eocene (Altunkaynak et al. 2012b).

Briefly, the WA crust should have been heated from the deep- to mid-crustal level before the Early Miocene. An increasing geothermal gradient (decreasing viscosity) in the crust is a perfect way to create core complexes under regional extension.

Extensional deformation beginning in the upper crust is the key factor, as it provides space and triggers initiation of an isostatic rebound mechanism (Buck et al., 1988; Wernicke and Axen, 1988), which may lead to decompression of exhumed rocks. Although pre-existing faults are not absolutely required for developing of MCC, a thinned upper crust due to brittle extension can create space at shallow crustal levels. This process is controlled by detachment faults. Therefore, the initiation of brittle deformation of the upper crust via low angle normal faults is important for the formation of metamorphic core complexes and the initiation of emplacement of synextensional granites. The presence of shallow-seated, rapidly cooled, and mostly ductile-to-brittlely deformed plutons which were emplaced into the Kazdağ, Çataldağ, and Menderes CC indicates that brittle deformation in the upper crustal level possibly began during the Latest Oligocene-Early Miocene (24-19 My) in Western Anatolia (Figure 9b).

3.6 Conclusions

- The microstructural features of quartz, feldspar, biotite, and muscovite indicate that the TGMC and ÇSP underwent progressive deformation during cooling, passing from sub-magmatic to mylonitisation to brittle conditions. The progressive sub-solidus deformation and C-S fabrics in granitic rocks are clear indicators of a synkinematic emplacement of ÇSP.
- Based on the microstructures, two main deformation zones were identified: a ductile deformation zone (DZ) and a mylonitic zone (MZ). The DZ experienced high temperatures (sub-magmatic condition; a temperature range of >600 to 500°C) and a low intensity of strain deformation. The mylonitic zone (MZ) covers a temperature range from 500°C to <250°C with a higher intensity of strain and ductile-to-brittle deformation.
- Two-feldspar geothermometry yields deformation temperatures in the DZ of 501-588°C (an average of 544°C for the ÇSP and an average of 517°C for the TGMC).

The mylonitic zone has lower deformation temperature values of 430-557°C (an average of 484°C for ÇSP and an average of 436°C for TGMC).

- The TGMC and ÇSP, which were emplaced during different periods, suffered continuous ductile-to-brittle deformation and uplifted together along the ÇDFZ during the Early Miocene.
- Microstructures, two-feldspar geothermometry and thermochronology data indicate that the TGMC was cooled slowly (<50°C/my) throughout the Eo-Oligocene and rapidly (>500°C/my) along the ÇDFZ in the Early Miocene (21 Ma), while the shear zone-controlled ÇSP was emplaced into shallow levels of the Anatolian extending crust, deformed progressively (ductile-to-brittle) along the ÇDFZ and cooled rapidly (>500°C/my) in the Early Miocene (21 Ma) under the N-S extensional regime in the western Anatolia.

4. THE ROLE OF ACCRETED CONTINENTAL CRUST IN THE FORMATION OF GRANITES WITHIN THE ALPINE STYLE CONTINENTAL COLLISION ZONE: GEOCHEMICAL AND GEOCHRONOLOGICAL CONSTRAINS FROM LEUCOGRANITES IN THE ÇATALDAĞ METAMORPHIC CORE COMPLEX (NW TURKEY)

4.1 Introduction

Leucogranites are common in collisional orogens such as Himalaya, Variscan, Hercynides and Caledonides (Chappell and White, 1974; Barbarin, 1999; Harris et al., 1995; Hopkinson et al 2017). They are generally considered to form by partial melting of over-thickened orogenic crust in the final stages of an orogenic event, but they also occur in post-collisional extensional settings (Chappell & White, 1974; Searle & Fryer, 1986; Le Fort et al., 1987; Castelli & Lombardo, 1988; Harris et al., 1995; Inger & Harris, 1993; Sylvester, 1998). Although some geochemical studies on leucogranites suggest that some of these granites are not "pure" crustal melts, and comprise a mantle component (Gray, 1984; Collins, 1996; Healy et al., 2004), they have been mostly defined as crustal melts that derived by partial melting of metasediments (Chappell and White 1974; Deschamps et al, 2017; Hopkinson et al., 2017 and the references therein). However, explanations of their melt production and migration processes and the heat supply required for their genesis remain controversial because they are observed in different tectonic settings. Investigation of leucogranites associated with gneiss-migmatite domes and metamorphic core complexes can provide insight to the relationship between granites and middle-lower crustal source rocks, crustal melting conditions, and the mechanism(s) that are crucial during crustal evolution.

This chapter is based on the paper, Kamacı, Ö., Altunkaynak, Ş., The role of accreted continental crust in the formation of granites within the Alpine-style continental collision zone: Geochemical and geochronological constraints from leucogranites in the Çataldağ Metamorphic Core Complex (NW Turkey), Lithos, 354, 105347, 2020.

In order to better understand the above issues, we have chosen the newly discovered Çataldağ Metamorphic Core complex (Kamacı et al., 2017; Kamacı and Altunkaynak, 2019a) in Western Anatolia as the study area that provide an opportunity to track the connection between leucogranites and migmatites which commonly represent the source region of granites at middle to lower crust, and also the geochronological and isotopic fingerprints of magma generation through accreted crust beneath Sakarya Continent.

Western Anatolia, in the eastern continuation of the Alpine collisional belt, underwent Alpine crustal thickening prior to intense lithospheric extension that has continued since the Oligocene, as evidenced by the development of metamorphic core complexes, extensional basins and syn-extensional magmatism (Gessner et al., 2001; Işık et al., 2003; Çemen et al., 2006; Genç and Altunkaynak, 2007; Bonev et al., 2009; Dilek et al., 2009; Erkül and Erkül, 2012, Altunkaynak et al., 2012a; Erkül et al, 2017; Kamacı et al, 2017; Kamacı and Altunkaynak, 2019a). Two major, long-lived magmatic activities (Altunkaynak and Dilek, 2006; Helvacı et al. 2009; Altunkaynak et al., 2012a; 2012b; Ünal and Altunkaynak, 2018) forming mainly I-type granitic bodies developed in NW Anatolia following the closure of the Neo-Tethys Ocean and continental collision between the Anatolide-Tauride block and the Sakarya Continent (Şengör and Yılmaz, 1981). The first episode of magmatism occurred in the Early-Late Eocene and is marked by the emplacement of granitoid plutons along the suture zone and into the Sakarya Continent in NW Anatolia (Altunkaynak et al 2012b; Güraslan and Altunkaynak, 2019). The volcanic equivalents of these plutons are rare and also limited to NW Anatolia. Second episode developed in the Late Oligocene-Middle Miocene and is represented by widespread volcano-plutonic complexes emplaced into the Sakarya and Anatolide-Tauride continental blocks on both side of the suture zone. Eo-Oligocene granites connected with gneiss- migmatite domes (e.g., Uludağ and Gördes domes; Catlos and Çemen, 2005; Okay et al., 2008; Bozkurt et al., 2010; Topuz and Okay, 2017) and metamorphic core complexes (e.g. ÇMCC; Kamacı et al., 2017; Kamacı and Altunkaynak, 2019a) were developed in the region during the transitional phase between two major episodes corresponding to the late phase of collision and the early phase of extension.

In this paper, for the first time, we present new major-trace element geochemistry, Sr-Nd-Pb isotope characteristics, and Ti-in-zircon thermometry data from leucogranites and syn-plutonic mafic dykes associated with a gneiss-migmatite dome exhumed as the footwall of the Çataldağ Metamorphic Core Complex, in order to provide constraints on their source components, melting conditions/mechanisms, and melt evolution beneath western Anatolia as a case study of the role of accreted continental crust in the formation of granites within the Alpine style continental collision zone.

4.2 Geological Background

The basement rocks of Western Anatolia are composed of the Sakarya continent (SC) units, the Izmir-Ankara suture zone (Akyüz and Okay, 1996), the Anatolide-Tauride platform (ATP) units, metamorphic core complexes (Menderes Metamorphic Core Complexes: Bozkurt and Park, 1994; Hetzel et al., 1995; Gessner et al., 2001; Isik and Tekeli, 2001; Ring et al., 2003; van Hinsberg, 2010; Plunder et al., 2015; Kazdağ Metamorphic Core Complexes: Bonev et al., 2009; Çataldağ Core Complex: Kamacı et al. 2017; Kamacı and Altunkaynak, 2019a). Cover rocks consist of volcanic and sedimentary rocks of different ages starting from the Eocene and continuing until the Quaternary (Yılmaz, 1989; Altunkaynak and Genç 2008; Ersoy et al, 2017; Kamacı and Altunkaynak, 2019b) (Figure 4.1).

Granitic intrusions in Western Anatolia are dated from the Early Eocene to the Mid-Miocene (Altunkaynak et al., 2012a;2012b and references therein). The first granitic products occurred during the Eocene (Orhaneli, Topuk, Tepeldağ, Gürgenyayla, Sivrihisar, Kapıdağ, Karabiga, Fıstıklı and Marmara plutons; Altunkaynak et al, 2012b and references therein) (Figure 4.1). Eocene granitoids are represented mainly by granodiorite, monzodiorite, granite and minor syenite which show an I-type affinity, are metaluminous to slightly peraluminous in nature, and have a medium-K calc-alkaline character. Melts forming Eocene granitoids are thought to be derived mainly from the lithospheric mantle and contaminated by continental crust. Another episode of wide-spread granitic magmatism occurred in the Late Oligocene-Middle Miocene (Figure 4.1).

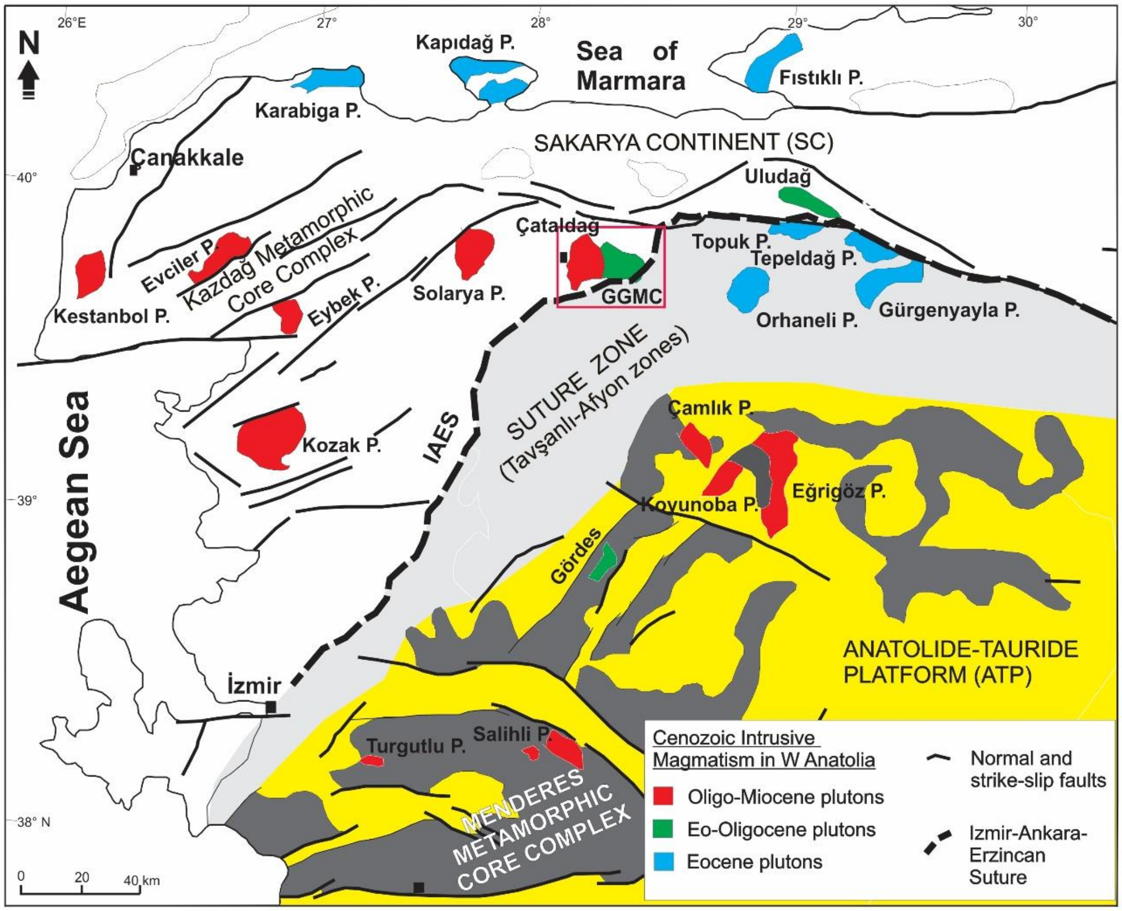

Figure 4.1 : Simplified map of the main tectonic units and plutonic rocks of Western Anatolia in the study area.

These granitoids (Çataldağ, Solarya, Eybek, Kestanbol, Evciler, Kozak, Eğrigöz, Koyunoba, Çamlık, Alaçamdağ) are represented by granodiorite, monzonite, diorite and syenite. They show an I-type affinity, are metaluminous to slightly peraluminous in nature, have a high-K calc-alkaline and shoshonitic character, and hybrid (crust and mantle) sources. Eocene and Oligo-Miocene magmatic activities in western Anatolia are interpreted to have resulted from syn-convergent extension driven by slab break-off or partial removal of the lithosphere (Köprübaşı and Aldanmaz, 2004; Altunkaynak, 2007; Altunkaynak et al, 2012a, 2012b). Between these two magmatic stages, granitic magmatism of a different character occurred in the Latest Eocene-Earliest Oligocene. Uludağ two-mica granites (Yurdagül, 2004; Okay et al., 2008; Topuz and Okay, 2017), Gördes leucogranites (Catlos and Çemen, 2005; Bozkurt et al., 2010) and the Çataldağ leucogranites are typical products of this phase. They display a high-K calc-alkaline character and are peraluminous in nature, indicating stronger crustal signatures than the Eocene and Miocene granitoids. Eo-Oligocene granitoids are rare and closely associated with gneissic domes and metamorphic core complexes (Menderes and Çataldağ) in western Anatolia (Catlos and Çemen, 2005; Okay et al., 2008; Bozkurt et al., 2010; Topuz and Okay, 2017; Kamacı et al., 2017; Kamacı and Altunkaynak, 2019a).

One of the metamorphic core complexes in western Anatolia, Çataldağ core complex (ÇCC), displays a typical domal uplift, and is composed of metamorphic and plutonic rocks bounded by the Çataldağ Detachment Fault Zone (ÇDFZ; Kamacı et al, 2017; Kamacı and Altunkaynak, 2019a) (Figure 4.2). The ÇCC consists of a granite-gneiss-migmatite complex (GGMC) and a synkinematic pluton (SP; Kamacı and Altunkaynak, 2019a). The SP is formed from I-type granodiorite in the inner zone, and haplogranite and pegmatite dykes in the peripheral zone. Both the GGMC and the SP are affected by ductile-to-brittle deformation in the Early Miocene along the ÇDFZ (Kamacı and Altunkaynak, 2019a). The leucogranites associated with the GGMC are the main focus of this paper.

4.3 Morphology and Petrography

The Granite-Gneiss-Migmatite Complex of the ÇCC consists of migmatite, granitic gneiss and leucogranite and mafic syn-plutonic dykes. Migmatites of GGMC are formed typical crustal melting sequence producing metatexite (Figures 4.3a, 4.3b and 4.3c) and diatexite (Figure 4.3e). Metatexite refers to partially molten rock with synmigmatitic deformation (Mehnert, 1968; Brown, 1973; Brown, 2001; Vanderhaeghe 2001; 2009). (Figure 4.3) while diatexite represents heterogeneous magma in which there is no continuous synmigmatitic structures. Metatexite is generally observed along the peripheries of the GGMC (Figure 4.2). It shows synmigmatitic banding, foliation and folding (Figures 4.3a, 4.3b and 4.3d). Migmatitic banding is defined by alternations of melanosome, mesosome and leucosome layers (Figure 4.3b). In some places, metatexites contains granitic vein network (Figure 4.3c). Leucosomes are light-coloured and represented by pockets and veins of leucogranite which are composed of feldspars (65-70%) and quartz (30-35%). Solid, darker coloured melanosome contains biotite, quartz, cordierite and sillimanite (Figures 4.3d, 4.3f and 4.3g). Biotites in the melanosome are represented by elongated crystals, while quartz shows recrystallized subgrains (Figures 4.3f and 4.3g). Yellowish pleochroic haloes around zircon are common in anhedral cordierites. Diatexites are characterized by a significant proportion of leucosome showing igneous texture of the rock (Figure 4.3e). Schlieren structures are common, with wispy, discontinuous biotite-rich layers representing the melanosome.

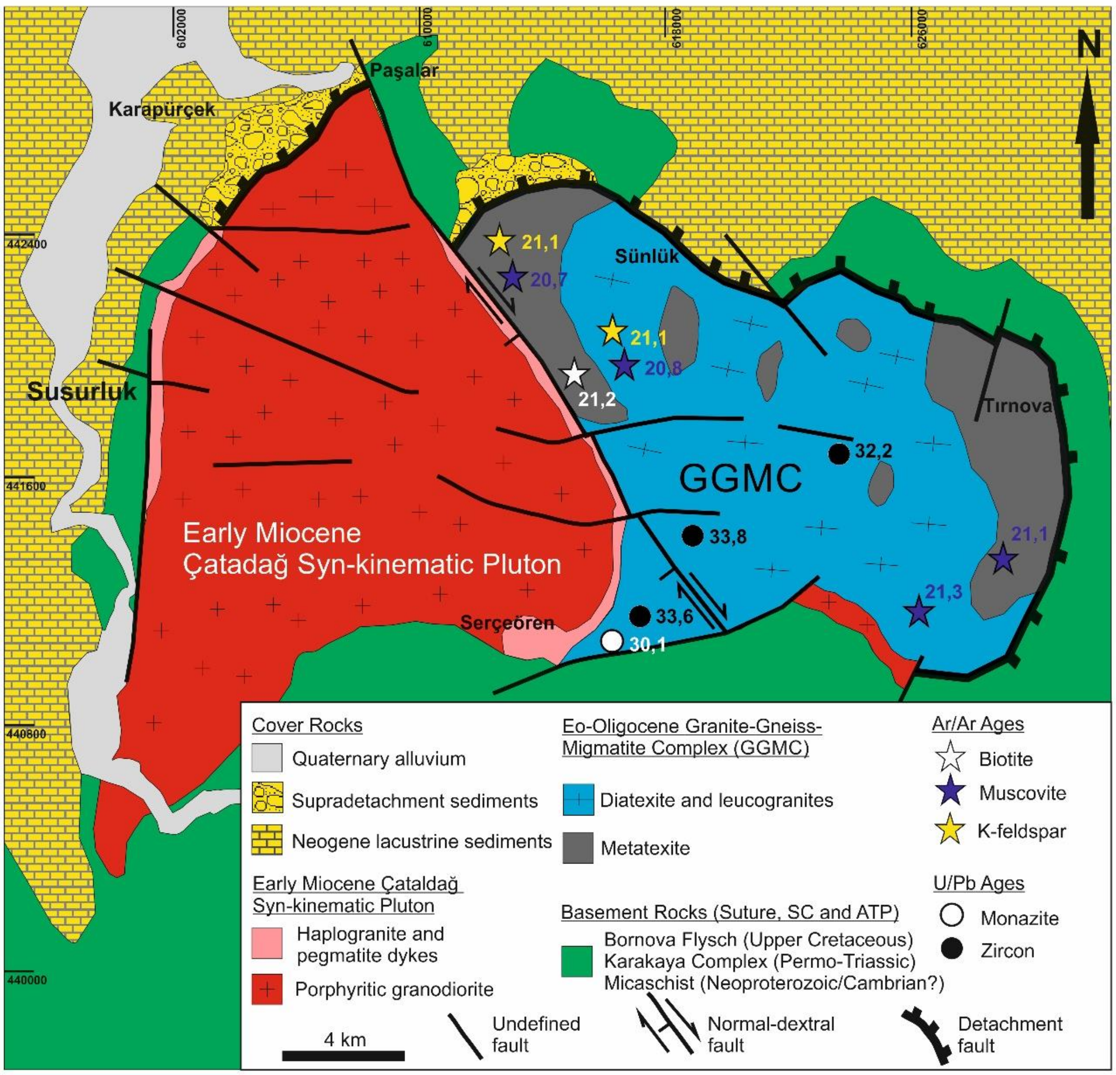

Figure 4.2 : a) Geological map of the Çataldağ Plutonic Complex. b) NW-SE cross-section of CPC (A-A’); c) N-S cross-section showing the GGMC (B-B’); d) N-S cross-section of the ÇG (C-C’). Map coordinates: Universal Transverse Mercator (UTM) projection, zone 35.

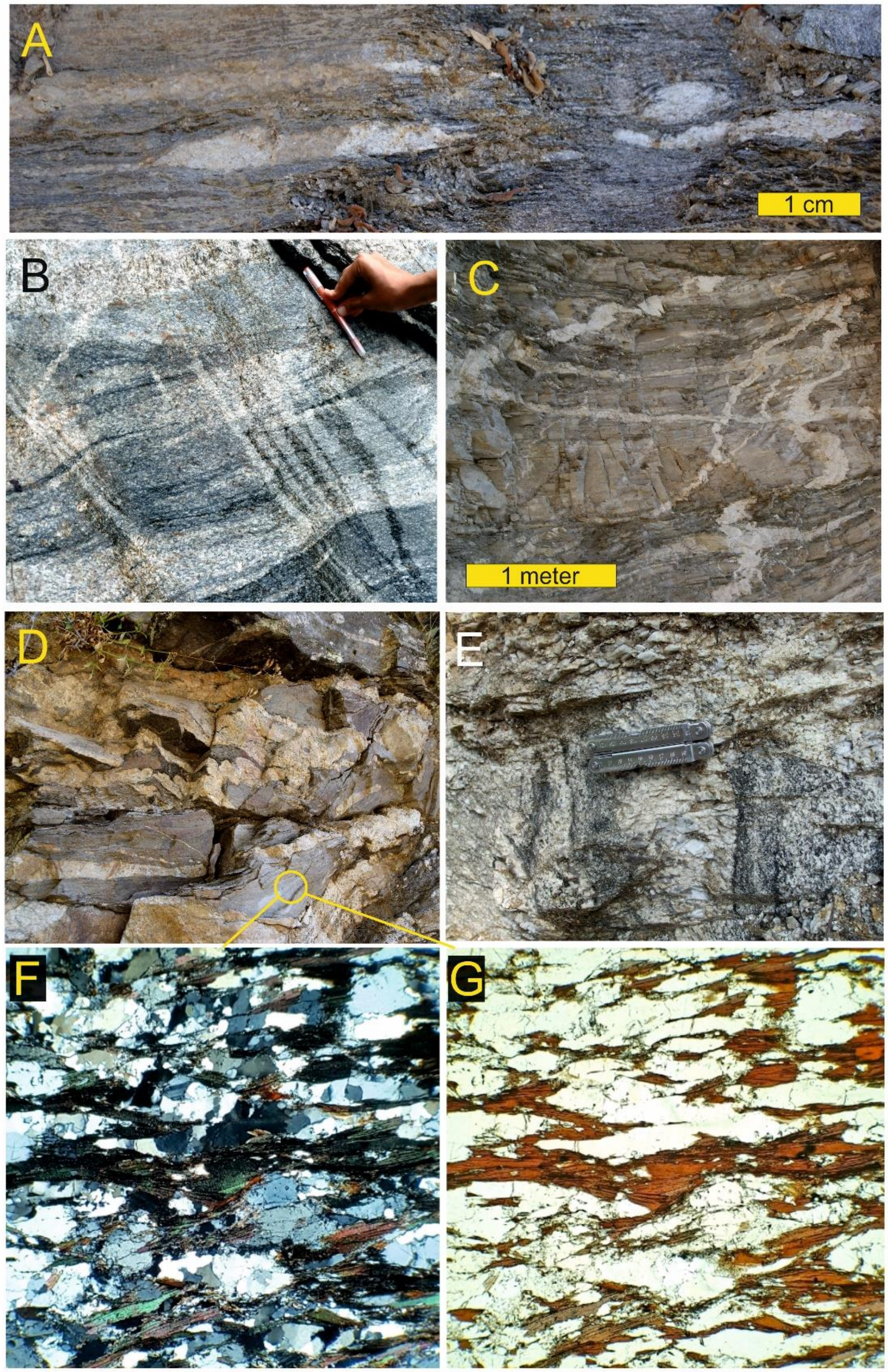

Figure 4.3 : Migmatites in field and microphotographs. Leucosome pockets in metatexite (a), syn-migmatitic bands (b), leucogranitic veins in metatexite (c); schlieren in diatexite (d); diatexite (dirty granite) (e); microphotographs under cross-polarized light (f) and plane-polarized light (g) of melanosome. Magnification of thin section photographs: 4X.

Leucogranites in the GGMC consist of the garnet-bearing leucogranite and two-mica leucogranite which are the focus of this study. The garnet-bearing leucogranite and two-mica leucogranite are spatially associated with each other, and are common at the centre of the GGMC and the periphery of the metatexites (Figures 4.4 and 4.5). Garnet-bearing leucogranite is simply recognised in the field by its white colour and reddish, euhedral garnet crystals which can be seen with the naked eye (Figure 4.4). It is composed of quartz (30-35%) + plagioclase (25-30%) + K-feldspar (25-30%) + muscovite (5%) + garnet (2%) ± biotite. Magmatic textures are rarely preserved because of widespread cataclastic deformation that overprints previous structures. All minerals except quartz show brittle structures. Quartz displays bulging and subgrain rotation recrystallization. Garnets are represented by euhedral porphyroclasts that generally show microfracturing. Zircon and monazite are also present as accessory minerals.

The two-mica leucogranite is variably deformed but displays preserved magmatic textures more commonly than the garnet-bearing leucogranite. The two-mica leucogranite has a holocrystalline granular texture, made up of quartz (30-35%) + plagioclase (25-30%) + K-feldspar (20-22%) + biotite (5-8%) + muscovite (3%) ± garnet (Figure 5). Plagioclase displays polysynthetic twinning while K-feldspar is represented by perthitic crystals (Figure 5). Biotite is subhedral in shape and reddish brown in colour, which is similar to the biotite found in basement rocks (micaschist). Muscovites have a prismatic habit. Accessory minerals are represented by apatite, titanite, zircon and monazite (Figure 4.5).

Mafic syn-plutonic dikes were identified within the leucogranites. (Figure 4.6). Contact relations and structures observed in mafic dikes and the granite indicate that the host granite was still molten or mush, when the mafic dike was intruded into it. Mafic dikes dismembered into boudins and observed as a number of separate small dikes aligned along the same direction surrounded by leucogranite as a consequence of viscous-ductile deformation (Figure 4.6). These dykes are gabbroic-dioritic and dioritic in composition, and contain plagioclase (60%), hornblende (25%), clinopyroxene (10%) and iron oxides (5%). The dykes generally show a holocrystalline microgranular texture, with a rare porphyritic texture defined by the presence of euhedral hornblende phenocrysts also occurring locally. Prismatic plagioclase crystals show albite twinning. Clinopyroxene also displays prismatic shapes.

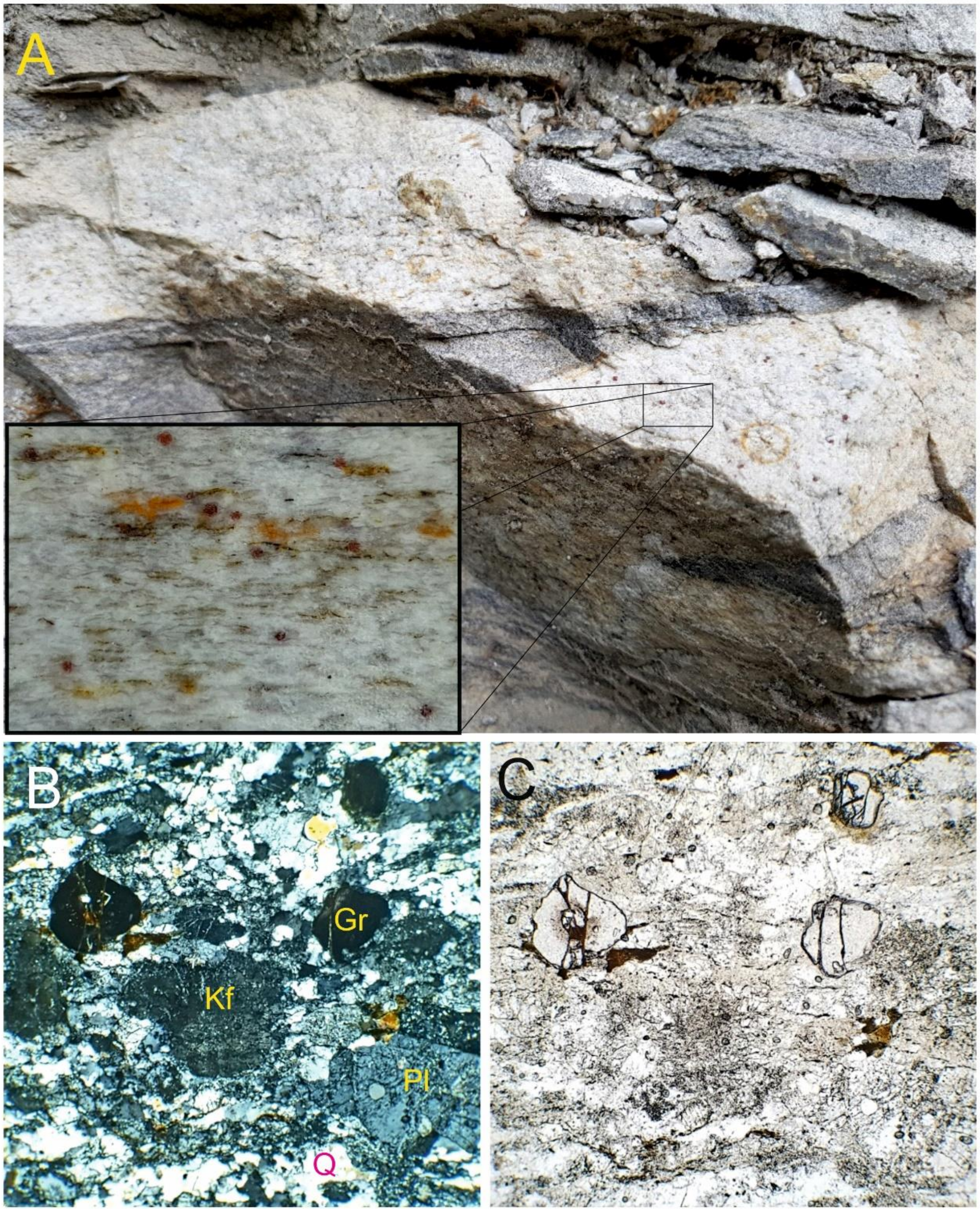

Figure 4.4 : Field photograph and microphotographs under plane-polarized light (b) and cross-polarized light (c) of garnet-bearing leucogranite. Gr: garnet, Pl: plagioclase, Kf: K-feldspar and Q: quartz. Magnification of thin section photographs: 4X.

Figure 4.5 : Two-mica granite in field and microphotographs under cross-polarized light (b) and plane-polarized light (c). Magnification of thin section photographs: 4X.

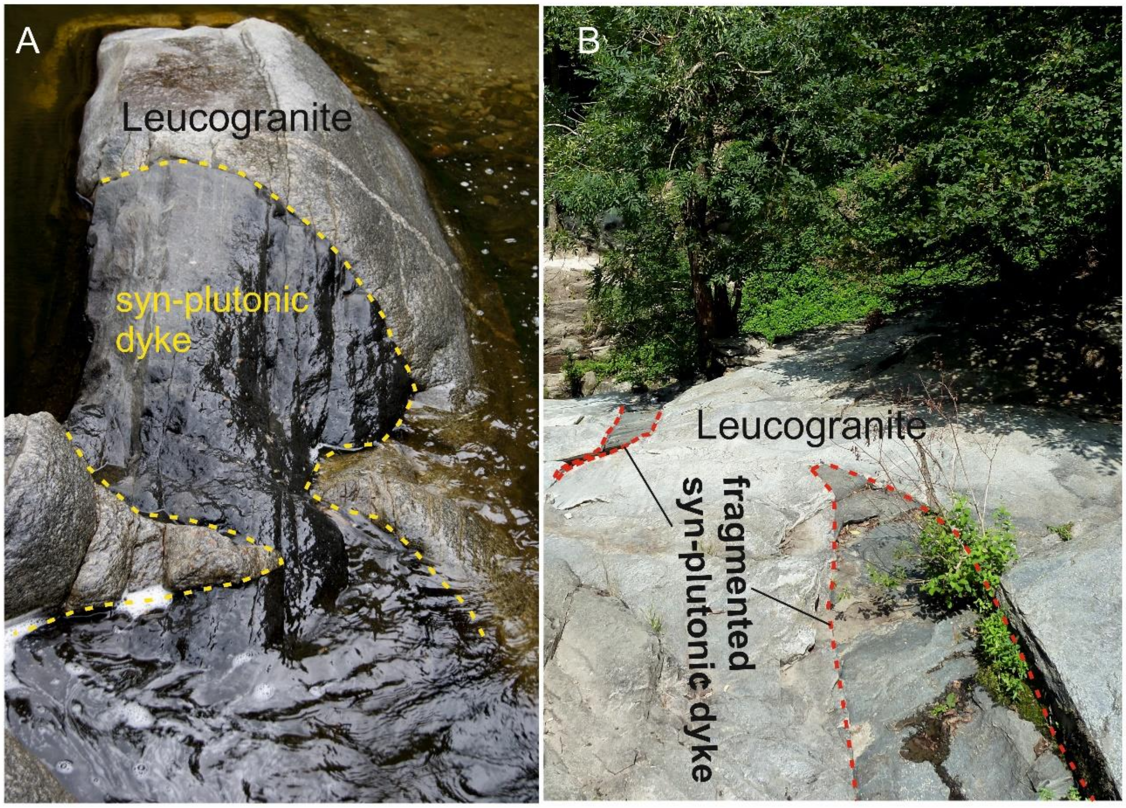

Figure 4.6 : Field photographs of the mafic syn-plutonic dyke typically showing irregular and fragmented margins with leucogranite.

4.4 Analytic Methods

4.4.1 Major, trace and isotope geochemistry

Major and trace elements were analyzed in Actlabs in Ontario, Canada. The samples underwent lithium metaborate/tetraborate fusion followed by measurement using the ICP-optical emission spectrometry. Repeated measurements of known rock standards indicate that the concentrations of the major elements are within 0.2% and are also certified as such by the laboratory. For ICP–MS analyses fused sample is diluted and analyzed by Perkin Elmer Sciex ELAN 6000, 6100 or 9000 ICP/MS. Three blanks and five controls (three before sample group and two after) are analyzed per group of samples. Duplicates are fused and analyzed every fifteen samples. Instrument is recalibrated every forty samples (Table 4.1).

Sr-Nd-Pb isotopes were analyzed in ALS Scandinavia Lab (Sweden). Sr-and Nd- isotope ratio measurements were determined by MC-ICP-MS (NEPTUNE, ThermoScientific, Bremen) according to combination of internal standardization (using $^{86}Sr/^{88}Sr$ and

$^{144}Nd/^{146}Nd$ stable ratios) and external calibration with matrix-matched standards to correct for instrumental mass-bias. Samples were prepared by alkaline (0.1 g sample, 0.3 g Lithium methaborate/tetraborate mixture) fusion method for Sr-Nd isotope measurements. Matrix separation was performed by Sr-Specific resin (disposable 2 ml columns) for Sr-isotope measurements, and by combination of Dowex 50 W ion exchange resin (REE as a group) and LnSpec resin (disposable 2 ml columns) for Nd isotope measurements. Pb-isotope ratio measurements also determined by MC-ICP-MS (NEPTUNE, ThermoScientific, Bremen) using combination of internal standardization (Tl added to all solutions at fixed concentration) and external calibration with matrix-matched standards to correct for instrumental mass-bias. Samples were dissolved in a mixture of HF and HNO_3 (0.5 g sample, 5 ml HNO3+HF). Matrix separation was performed by Sr-Specific resin (disposable 2 ml columns). All isotope measurements were performed at least in duplicate. To calculate the initial values of the Sr-Nd isotopes, we used an average age of 33 Ma. All major, trace and isotope geochemistry diagrams are generated by the GCDkit software (Janousek et al., 2006).

4.4.2 In-situ Ti-in-zircon analysis

Ti-in-Zircon analyses were carried out using a New Wave Research (NWR) Excimer 193 nm laser-ablation system UP-193FX attached to a Perkin-Elmer ELAN DRC-e inductively coupled plasma mass spectrometer (LA-ICP-MS) using external standard NIST 610 at the Geological Institute, Bulgarian Academy of Science in Sofia, Bulgaria. The composition was recalculated using Sills software with an internal standard of SiO_2 (32.8 wt.%) from the stoichiometry of zircon.

4.5 Geochemistry

4.5.1 Major and trace element characteristics

Major oxides and trace elements of 12 leucogranite samples (6 two-mica leucogranite, 6 garnet-bearing leucogranite), 2 gabbroic-diorite dykes, a melanosome, and a mica-schist sample as country basement rock were analysed.

The major oxide-trace element results of the two-mica leucogranite and the garnet-bearing leucogranite present similar geochemical characteristics. Their SiO_2 contents vary across a range of 70.69–77.25 wt.%. The SiO_2 contents of the gabbroic-diorite dykes vary between 52.71 and 53.27 wt.%, and the melanosome contains 58.59 wt.% SiO_2. MgO contents are 0.11–0.74 wt.% for leucogranite, 6.24–6.77 wt.% for gabbroic-diorite dykes, and 3.91 wt.% for the melanosome. On the total alkali silicate diagram (Cox et al., 1979), all leucogranite rocks plot within the granite field (Figure 4.7a). The gabbroic-diorite dykes and the melanosome are classified as gabbroic-diorite and monzonite, respectively (Figure 7a).

All samples are subalkaline in nature except the melanosome which is located in the alkaline field of the total alkali silicate diagram (Figure 4.7a). On the K_2O vs. SiO_2 classification diagram of Peccerillo and Taylor (1976), the majority of samples are classified as high-K calc-alkaline (Figure 4.7b). One leucogranite sample is located in the calc-alkaline field, while another leucogranite sample plots in the shoshonite field.

All leucogranite samples correspond to S-type granite with peraluminous nature (defined by an ASI value of > 1.1; ASI: 1.1–1.2 for leucogranite, 1.45 for mica-schist, Figure 4.7c). The gabbroic-diorite dykes are classified as metaluminous. To better understand the predominantly peraluminous nature of the leucogranite, we also used the peraluminous classification of Villaseca et al. (1998). The garnet-bearing leucogranite is classified as felsic peraluminous, while the two-mica leucogranite plots mostly in the moderately peraluminous region (Figure 4.7d).

In the major oxide and trace element variation diagrams of leucogranite (Figure 4.8), TiO_2 (0.04–0.31 wt.%), FeOt (0.41–1.84 wt.%), MgO (0.11–0.74 wt.% and Mg# 31–45), CaO (0.82–2.21 wt.%), Al_2O_3 (13.58–15.83 wt.%) and Na_2O (3.26–4.55 wt.%) contents slightly decrease with increasing SiO_2 content (70.69–77.25 wt.%). K_2O, Th (6.00–17.76 ppm), Sr (134–437 ppm) and Ba (325–876 ppm) contents are more variable, and do not appear to depend on SiO_2 content.

On primitive mantle-normalized trace element spider diagrams (Figure 4.9a), leucogranites are characterized by enriched large-ion lithophile elements (LILE) and high field strength elements (HFSE) except Nb, P and Ti which display relative depletions with respect to primitive mantle.

Table 4.1 : Major oxides and trace element analyses of GGMC in Çataldağ Core Complex.

Symbol	Two-mica granites (TMG)						Garnet-bearing leucogranite (GBL)						Gabbro-diorite dykes		Melanosome	Mica-schist
Samples	OS-105	OS-150	OS-351	OS-538	OS-539	OS-533	OS-2	OS-74	OS-75	OS-353	OS-395	OS-537	OS-33	OS-89	OS-111	OS-77
Major oxides (%)																
SiO2	73.67	72.52	70.69	72.07	72.35	71.14	72.60	73.57	77.25	72.74	72.64	72.81	52.71	53.27	58.59	75.69
Al2O3	14.03	15.41	15.83	14.74	14.25	15.35	15.05	14.29	13.58	15.29	14.88	14.99	16.08	15.44	16.15	13.83
FeO	1.55	1.84	1.69	1.32	1.61	1.40	0.73	0.60	0.41	0.97	0.73	0.85	8.33	8.17	8.38	0.99
MgO	0.50	0.51	0.57	0.38	0.74	0.55	0.26	0.22	0.11	0.31	0.19	0.31	6.77	6.24	3.91	0.27
CaO	1.13	2.21	1.88	1.59	1.50	1.29	1.54	1.11	0.82	1.03	1.12	1.16	7.39	7.16	1.28	1.36
Na2O	3.26	4.55	4.42	3.68	3.48	4.14	3.85	3.45	3.76	3.80	3.63	3.75	3.51	3.63	2.77	2.78
K2O	4.29	2.31	3.34	4.03	4.38	4.22	4.53	4.06	3.92	4.36	5.37	4.11	1.74	1.85	5.62	2.37
TiO2	0.31	0.25	0.27	0.21	0.20	0.23	0.13	0.04	0.04	0.14	0.09	0.12	1.21	1.24	1.26	0.17
P2O5	0.08	0.09	0.12	0.06	0.23	0.08	0.12	0.08	0.06	0.10	0.09	0.06	0.27	0.27	0.24	0.06
MnO	0.02	0.05	0.03	0.03	0.04	0.04	0.02	0.03	0.02	0.02	0.01	0.03	0.15	0.14	0.09	0.01
LOI	1.14	1.17	0.90	1.03	0.99	0.98	0.67	1.89	0.86	1.10	1.10	1.18	1.77	1.42	1.37	1.83
Total	99.98	100.91	99.74	99.15	99.77	99.41	99.49	99.34	100.84	99.86	99.85	99.36	99.93	98.82	99.66	99.36
Trace elements (ppm)																
Cs	3.9	4.7	8.3	4.1	7.3	9.8	8.0	3.7	4.2	7.1	6.2	6.2	12.8	17.6	14.6	2.0
Rb	150	99	148	151	189	187	185	165	127	201	196	176	77	68	315	73
Ba	775	795	788	876	431	526	711	386	325	433	792	498	540	609	658	732
Sr	270	427	393	280	161	222	268	150	134	188	275	169	439	410	142	236
Pb	42	43	7	47	45	50	50	43	49	3	4	46	6	5	28	53
Th	12.8	17.7	13.6	17.8	12.8	12.5	8.9	6.0	3.0	10.8	6.5	6.8	8.4	8.6	10.4	12.4
U	3.2	5.1	6.4	4.6	8.2	12.2	8.8	2.4	1.7	2.7	4.1	4.8	1.8	1.9	3.5	2.9
Zr	144	170	134	141	81	115	72	57	34	67	52	69	168	170	281	114
Hf	3.2	3.7	4.6	3.9	2.3	3.4	2.4	2.2	1.3	2.4	2.2	2.1	3.4	3.8	6.5	3.3
Ta	0.4	0.8	1.1	1.1	1.8	1.2	2.0	1.3	0.8	1.2	0.9	1.1	1.2	1.3	1.0	0.9
Y	6.0	14.0	8.9	11.5	15.9	7.0	13.0	13.0	13.0	11.4	13.6	10.8	21.0	23.0	37.0	10.0
Nb	4.0	11.0	9.3	10.8	17.1	10.9	14.0	8.0	5.0	9.5	4.8	6.5	16.0	16.0	15.0	7.0

Table 4.1 (continued) : Major oxides and trace element analyses of GGMC in Çataldağ Core Complex.

Symbol	Two-mica granites (TMG)						Garnet-bearing leucogranite (GBL)						Gabbro-diorite dykes		Melanosome	Mica-schist
Samples	OS-105	OS-150	OS-351	OS-538	OS-539	OS-533	OS-2	OS-74	OS-75	OS-353	OS-395	OS-537	OS-33	OS-89	OS-111	OS-77
Sc	3.0	3.0	3.0	6.4	7.6	5.8	3.0	1.0	1.0	2.0	1.0	5.2	22.0	21.0	22.0	3.0
Cr													250	150	120	
Ni													100	90	30	
Co	3.0	2.0	2.6	4.4	3.0	1.7	1.0	1.0	1.0	0.8	1.1	2.3	33.0	29.0	20.0	2.0
V	21	17	12	9	18	13							150	145	165	10
Ga	22	22	20	17	16	20	18	21	14	22	16	16	18	15	24	18
Zn	50	50	40	32	29	42							140	100	110	
Cu														40	20	
La	22.60	41.50	26.70	28.26	18.27	21.67	32.60	13.30	6.80	19.20	13.60	12.05	21.90	26.50	35.30	22.10
Ce	43.00	72.90	48.40	50.96	33.53	41.27	50.80	25.40	12.10	36.30	23.60	22.98	41.80	49.00	74.70	40.60
Pr	4.65	7.08	5.11	5.37	3.90	4.95	5.28	2.69	1.35	4.42	2.74	2.76	4.62	5.57	9.00	4.45
Nd	16.60	24.70	18.20	19.43	13.37	16.70	17.80	9.60	4.70	14.50	9.70	9.18	18.10	21.60	36.30	15.50
Sm	2.90	4.00	3.14	3.62	3.08	3.37	3.10	2.30	1.10	3.20	2.31	2.14	4.00	4.60	7.50	3.00
Eu	0.63	0.90	0.79	0.50	0.36	0.50	0.65	0.34	0.27	0.41	0.64	0.32	1.17	1.26	1.61	0.67
Gd	1.90	3.00	2.30	2.42	2.81	1.89	2.40	2.10	1.00	2.57	2.26	1.98	3.90	4.40	6.90	2.20
Tb	0.20	0.50	0.31	0.43	0.51	0.32	0.40	0.40	0.20	0.37	0.36	0.31	0.70	0.70	1.10	0.30
Dy	1.10	2.50	1.92	2.09	2.65	1.34	2.10	2.20	1.10	2.14	2.27	1.72	3.80	4.00	6.60	1.80
Ho	0.20	0.50	0.27	0.42	0.58	0.26	0.40	0.40	0.20	0.40	0.45	0.36	0.70	0.80	1.30	0.30
Er	0.50	1.40	0.60	1.11	1.38	0.63	1.10	1.00	0.60	0.98	1.32	0.94	2.20	2.20	3.70	0.90
Tm	0.07	0.19	0.11	0.15	0.24	0.09	0.16	0.14	0.11	0.14	0.20	0.14	0.30	0.34	0.53	0.13
Yb	0.50	1.30	0.63	0.93	1.33	0.47	1.10	0.90	0.70	0.65	1.12	0.79	2.10	2.20	3.60	0.80
Lu	0.08	0.23	0.12	0.15	0.23	0.08	0.18	0.14	0.10	0.11	0.16	0.12	0.35	0.35	0.61	0.13

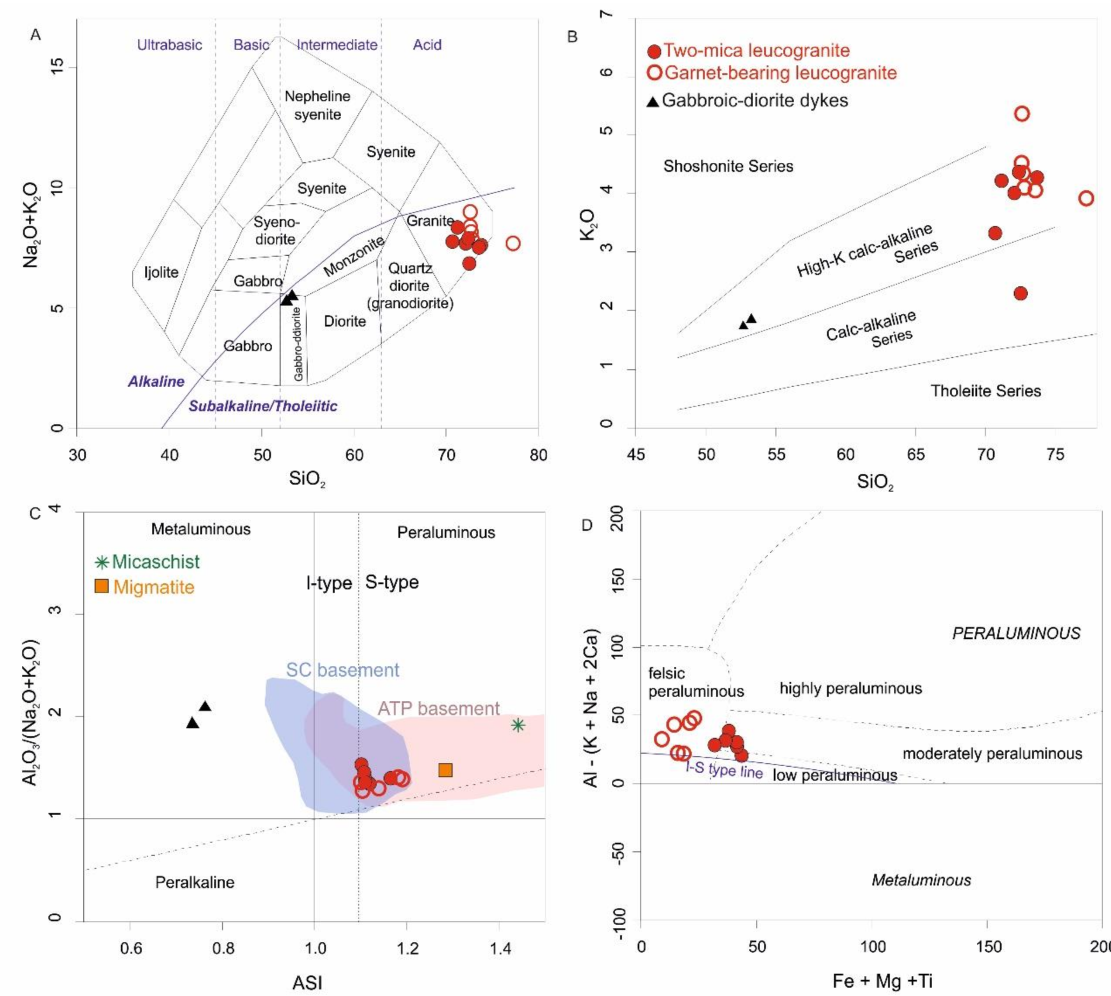

Figure 4.7 : Classification and chemical variation diagrams of GGMC samples. A) Total alkalis (Na2O + K2O) versus silica diagram; alkali and sub-alkali line is labelled according to Miyashiro (1978); B) K2O versus SiO2 diagram distinguishing tholeiitic, calc-alkaline, high-K calc-alkaline and shoshonitic series, after Peccerillo and Taylor (1976); C) ASI (aluminium saturation index) diagram of the GGMC (Maniar and Piccoli, 1989); D) Peraluminous classification of leucogranite (Villaseca et al, 1998).

Leucogranites are enriched in LILE and depleted in heavy rare earth elements (HREE) compared to the average middle crust (Rudnick and Gao, 2003), and display trace element compositions similar to mica-schist (OS-77). Trace element patterns of gabbroic-diorite dykes on the same diagram show similar element enrichment patterns to those of leucogranite, except they are also enriched in Ti, P and HREE with respect to leucogranite (Figure 4.9a). On chondrite-normalized spider diagrams (Figures 4.9b, 4.9c), the REE distributions of the leucogranites show clear light rare earth element (LREE) enrichments relative to HREE

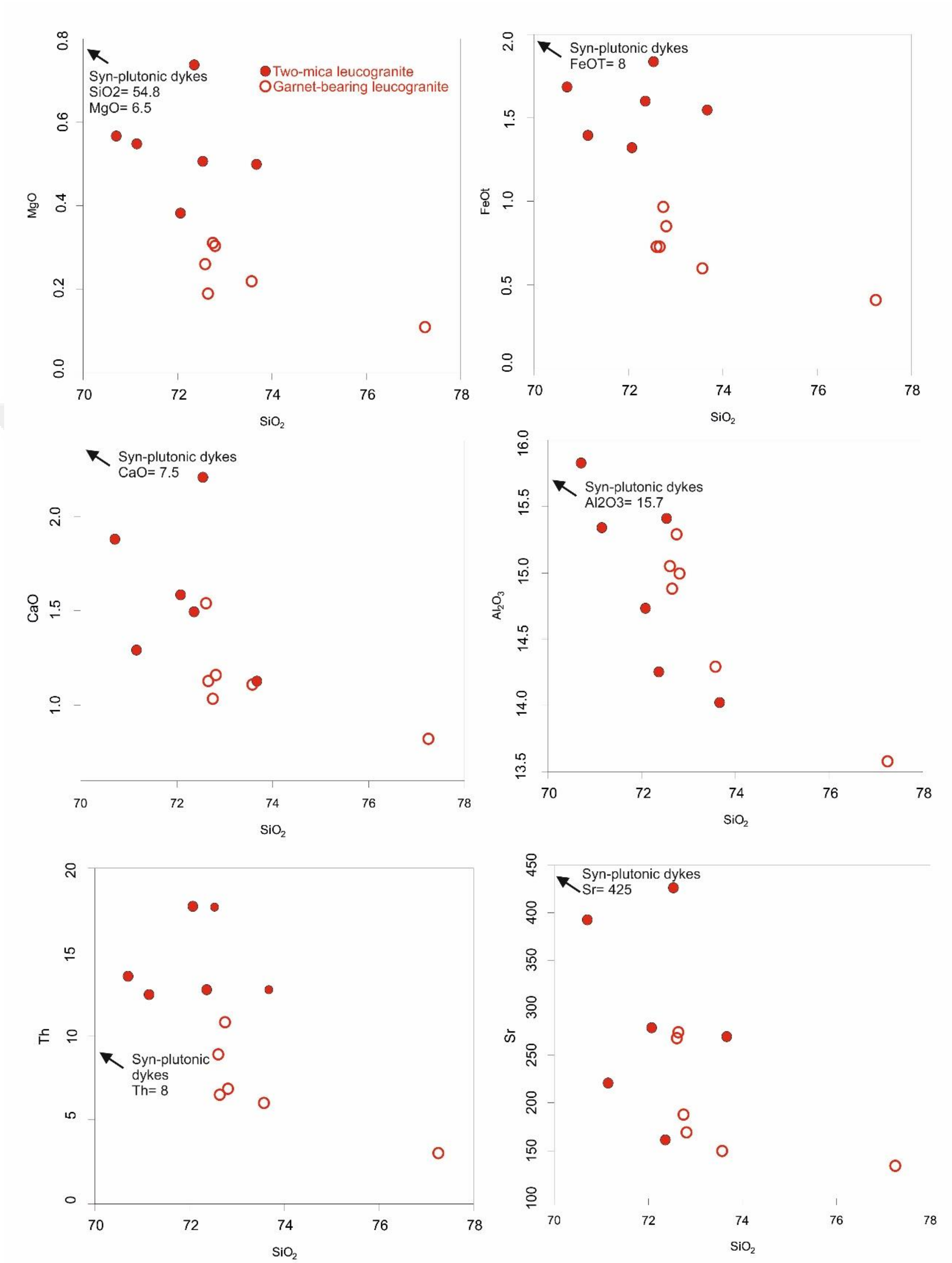

Figure 4.8 : Harker variation diagrams for the leucogranite samples, illustrating correlations between MgO, FeOt, CaO, Al2O3, Th and Sr with SiO2.

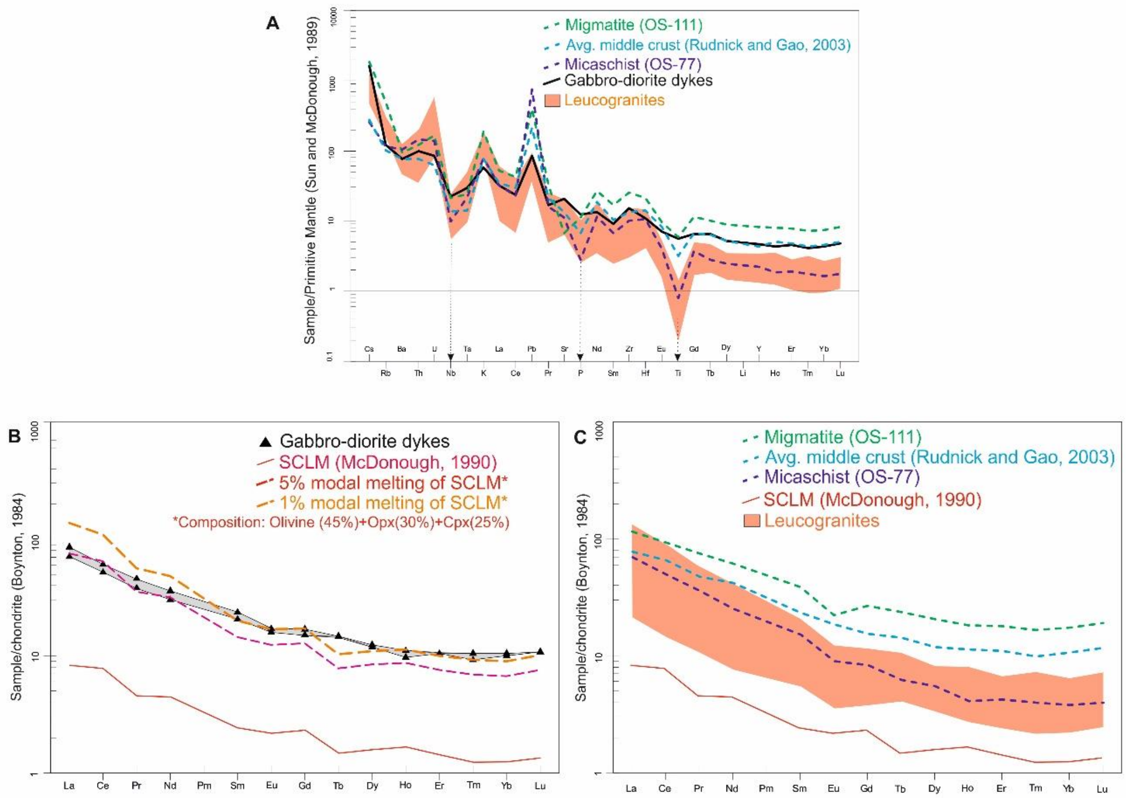

Figure 4.9 : Primitive mantle-normalized (Sun and McDonough, 1989) and chondrite-normalized (Boynton, 1984) trace element diagrams for the GGMC.

La_N/Yb_N = 8.2–31.2). The overall REE concentrations of leucogranite indicate similar trends to the mica-schist sample. Eu is characterized by negative anomalies which are similar for all leucogranite samples (Eu/Eu* = 0.36–0.90). The gabbroic-diorite dykes show similar trends to low degree (1–5%) partial melts of subcontinental lithospheric mantle (SCLM, McDonough, 1990) on the chondrite-normalized spider diagram (Figure 4.9b).

4.5.2 Sr, Nd, Pb isotopes

The Sr, Nd and Pb isotopes of 7 leucogranite (4 garnet-bearing leucogranite and 3 two-mica leucogranite) samples, 2 gabbroic-diorite dykes, and a mica-schist sample were analysed. The initial ratios of Sr and Nd isotopes were calculated using an average zircon (U/Pb) crystallization age of 33 Ma.

Table 4.2 : Sr, Nd, Pb isotope geochemistry analyses of GGMC in Çataldağ Metamorphic Core Complex

	Unit	Sample	$^{87}Sr/^{86}Sr$	$^{87}Sr/^{86}Sr_{(33)}$	$^{143}Nd/^{144}Nd$	$^{143}Nd/^{144}Nd_{(33)}$	EpsNdi	TDM	$^{206}Pb/^{204}Pb$	$^{207}Pb/^{204}Pb$	$^{208}Pb/^{204}Pb$	$^{208}Pb/^{206}Pb$	$^{207}Pb/^{206}Pb$
Leucogranites	Two-mica granites	OS-105	0.71127	0.71052	0.512291	0.5122690	-6.38	1.1	18.816	15.707	38.942	2.070	0.835
		OS-351	0.71044	0.70993	0.512355	0.5123330	-5.13	1.0	18.819	15.709	38.945	2.069	0.835
		OS-533	0.71142	0.71028	0.512290	0.5122640	-6.47	1.4					
	Garnet-bearing leucogranite	OS-74	0.71279	0.71130	0.512227	0.5121960	-7.79	1.9	18.909	15.720	39.021	2.064	0.831
		OS-75	0.71226	0.71097	0.512271	0.5122400	-6.93	1.7	18.893	15.725	38.989	2.064	0.832
		OS-353	0.71169	0.71023	0.512331	0.5123020	-5.72	1.5	18.795	15.713	38.906	2.070	0.836
		OS-395	0.71108	0.71011	0.512287	0.5122560	-6.62	1.8	18.814	15.709	38.929	2.069	0.835
		OS-537	0.71228	0.71087	0.512284	0.5122540	-6.67	1.7					
Mafic dyke		OS-89	0.70570	0.70547	0.512524	0.5124960	-1.93	1.0	18.85	18.850	15.699	39.058	2.072
		OS-33	0.70586	0.70563	0.512629	0.5126010	0.11	0.9	18.79	18.785	15.694	38.984	2.075
Mica-schist		OS-77	0.71373	0.71331	0.512207	0.5121820	-8.06	1.4	18.81	18.806	15.693	38.932	2.070

The $^{87}Sr/^{86}Sr_{(33)}$ ratios range from 0.709387 to 0.711300 for leucogranite, and average 0.705553 for gabbroic-diorite dykes, and 0.713318 for the mica-schist. $^{143}Nd/^{144}Nd_{(33)}$ values vary from 0.512198 to 0.512233 for leucogranites, and average 0.512549 for gabbroic-diorite dykes, and 0.512182 for the mica-schist. The highest Sr $_{(33)}$ and the lowest $\varepsilon Nd_{(33)}$ isotopic values belong to the leucogranite samples, while the gabbroic-diorite dykes show the opposite initial isotope values. $\varepsilon Nd_{(33)}$ values for leucogranite samples vary from −5.13 to −7.79, except one sample with a distinctly low value ($\varepsilon Nd_{(33)}$ = -2.36). Gabbroic-diorite dykes exhibit the highest $\varepsilon Nd_{(33)}$ values ranging between 0.11 and –1.93 (Figure 10a). $^{206}Pb/^{204}Pb$, $^{208}Pb/^{204}Pb$ and $^{208}Pb/^{206}Pb$ isotopes of leucogranite average 18.84, 38.95 and 2.067, respectively. Pb isotopes of gabbroic-diorite dykes are similar to those of leucogranites: 18.82, 39.02 and 2.074, respectively (Table 4.2; Figures 4.10c and 4.10d).

4.6 Petrogenesis of Leucogranites

4.6.1 Source characteristics and melt evolution

The presence of associated migmatitic rocks and the existence of Al-rich minerals (e.g. muscovite and garnet) indicate a crustal origin for the leucogranite samples. The crustal origin of leucogranites is also evidenced by their geochemical features (subalkaline and peraluminous nature, high contents of SiO_2, low concentrations of CaO, MgO, FeO, and TiO_2) and isotope characteristics (high $^{87}Sr/^{86}Sr_{(33)}$ isotope ratios and low $\varepsilon Nd_{(33)}$ average values of 0.7110 and −6.5, respectively).
On the other hand, leucogranites display relatively higher #Mg, higher $\varepsilon Nd_{(33)}$ values and lower initial $Sr^{87}/Sr^{86}{}_{(33)}$ isotopic ratios than those of granitic rocks which are derived from pure crustal melts (e.g. Himalayan leucogranites). These data suggest that mantle components have also contributed to the evolution of the leucogranites. This mantle contribution is also evidenced by the existence of syn-plutonic gabbroic-diorite dykes which display metaluminous characteristics and a high K calc-alkaline character. The dykes are characterized by relatively lower SiO_2 (average 52.9%) and higher MgO (6.5%) and FeO (8.3%) values, and show similar isotopic characteristics ($^{87}Sr/^{86}Sr_{(33)}$ = 0.7055, $\varepsilon Nd_{(33)}$ = -1.8 and $^{206}Pb/^{204}Pb$ = 18.8) to enriched mantle melts (EMM and EM_{II} sources) (Deschamps et al. 2017) (Figure 4.10). The melting model on the chondrite-normalized spider diagram (Figure 4.9b) shows that syn-plutonic

gabbroic-diorite dykes can originate from low degree modal melting (1–5%) of enriched lithospheric mantle (Figures 4.9 and 4.10).

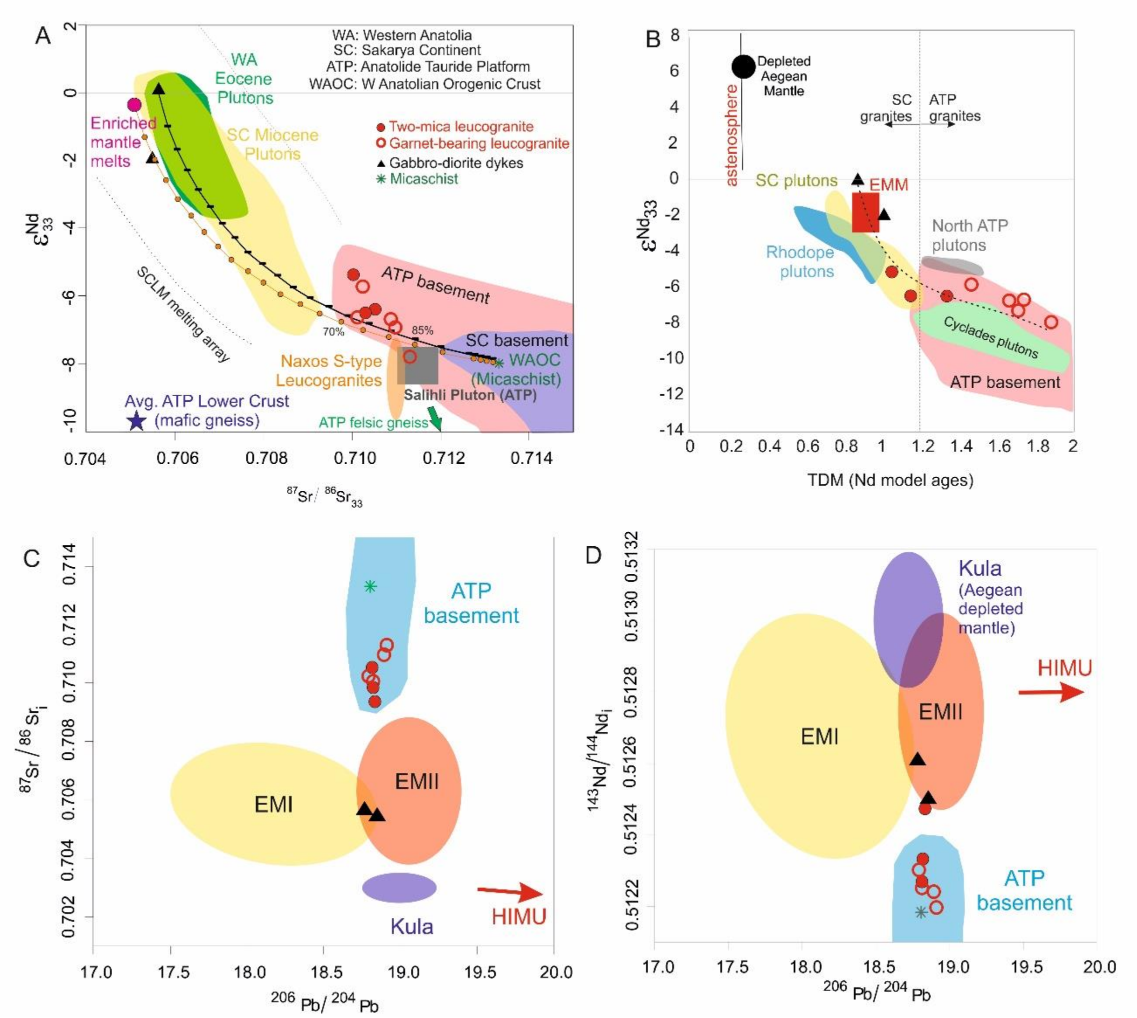

Figure 4.10 : A) εNd(33) vs. $^{87}Sr/^{86}Sr_{(33)}$ diagram for GGMC samples. Bulk mixing line between syn-plutonic gabbro-dioritic dyke with mica-schist (Sample OS-77) from Western Anatolian Orogenic Crust (WAOC); and enriched mantle melts (Deschamps et al, 2017) with micaschist. Data sources: Altunkaynak et al. (2012a and b); Erkül and Erkül (2012). B) εNd(i) vs. TDM (Nd-model ages) diagram of leucogranite and mafic dyke samples. Dashed line shows the possible mixing trend between the two rock types. C) $^{87}Sr/^{86}Sr_{(33)}$ vs $^{206}Pb/^{204}Pb$ isotopes diagram. D) $^{143}Nd/^{144}Nd_{(33)}$ vs $^{206}Pb/^{204}Pb$ isotopes diagram. Data sources: Asthenosphere, SC, ATP granites (Altunkaynak et al, 2012 and the references therein).

Considering the spatial and temporal relationship between granites and gabbro-diorite dykes in the study area, in order to test the possible role of the crust-mantle interactions during the formation of granites, we conducted a bulk mixing model between a mafic end-member of gabbroic-diorite dyke composition and a mica-schist, which represents the crustal end-member on the $^{87}Sr/^{86}Sr$ vs. εNd diagram (Figure 4.10a). The model results show that the gabbroic-diorite dykes display similar initial Sr-Nd isotopic values to enriched mantle melts (EMM), Western Anatolian (WA) Eocene plutons and the Miocene plutons of the SC (Altunkaynak et al., 2012a, 2012b; Deschamps et al., 2017), whereas the mica-schist sample (OS-77) plots in the same field as both the ATP and SC basement rocks (Figure 4.10). The majority of the leucogranite samples plot in the fields of metamorphic basement rocks, leucogranites of the ATP (particularly Salihli granite; Erkül and Erkül, 2012) and Naxos S-type leucogranites in the $Sr_{(33)}$ vs $\varepsilon Nd_{(33)}$ diagram (Figure 4.10a). All samples show a negative trend between these two different end members with a crustal component between 70% and 85% indicating studied granites dominantly originated from crustal melts with a minor contribution of enriched mantle components.

Scattered patterns in the major and trace element discrimination diagrams, negative Th and positive Rb/Zr (LILE/HFSE) trends compared against SiO_2 content, plus the insignificant tetrad effect in REE patterns indicate that fractional crystallization was insignificant during the evolution of leucogranite melts (Figure 4.12a).

4.6.2 P-T conditions and melting mechanism

Zircon thermometers are generally used to calculate crystallization conditions and to calculate the minimum melting temperatures of magmas (Watson and Harrison, 2005). Insitu Ti-in-zircon thermometry can work accurately on the rapidly cooled systems since the slow cooling may result in progressive crystallization of zircon crystals. In our case, Çataldağ Metamorphic Core complex is assumed as a rapidly cooled system according to thermochronological data (Kamacı and Altunkaynak, 2019a) which allows us to model the partial melting conditions of the leucogranites (Table 4.3). Average Ti-in-zircon was calculated from zircon with magmatic cores and rims (35.3 and 31.8 Ma shown by red colours in Figure 4.11a) by the equations of Ferry and Watson, 2007, and Claiborne et al., 2010). Leucogranites display melting temperatures ranging from 738.7 ± 16.7 °C to 844.7 ± 19 °C (Figures 4.11a and 4.11b). Zircons of two-mica leucogranite display slightly higher temperatures (754–845 °C with a mean of 764 ± 17 °C) than zircons of garnet-bearing leucogranite (723–774 C with an average of 738 ± 16 °C) (Figures 4.11a and 4.11b).

Table 4.3 : Ti-in-zircon thermometry results of leucogranites in Çataldağ Metamorphic Core Complex.

Sample	Zircon Spots	Pb206/U238 Age (my)*	Ti (ppm)	Temperatures (°C)			
				FW2007**	CE2010***	Average	±
OS-395	7r	33.4	11.6	754.2	787.4	770.8	16.6
	7c	33.6	24.3	825.6	863.7	844.7	19.0
	11c	33.4	11.8	755.9	789.2	772.5	16.7
	12r	33.4	10.0	741.3	773.7	757.5	16.2
	13r	33.7	10.5	745.0	777.6	761.3	16.3
OS-353	1r	34.6	10.3	743.4	775.9	759.6	16.3
	2r	34.1	13.6	768.6	802.8	785.7	17.1
	4r	35.3	9.5	736.6	768.7	752.6	16.0
	7r	34.4	9.9	740.4	772.7	756.5	16.2
	9r	34.5	19.8	804.7	841.3	823.0	18.3
	14r	33.1	15.2	779.2	814.0	796.6	17.4
	21r	33.1	13.6	768.5	802.7	785.6	17.1
	21c	33.7	16.9	789.2	824.8	807.0	17.8
	23r	32.9	9.9	739.9	772.2	756.1	16.1
OS-351	5r	31.9	8.1	723.1	754.3	738.7	15.6
	8r	32.5	9.3	734.3	766.2	750.3	16.0
	9r	32.8	10.2	743.1	775.6	759.4	16.2
	15r	31.8	8.9	730.5	762.2	746.4	15.8
	15c	32.5	8.1	723.2	754.4	738.8	15.6
	21r	33.3	14.4	774.1	808.6	791.4	17.3
*Kamacı et al., 2017							
**Equation of Ferry and Watson, 2007							
***Equation of Claiborne et al., 2010							

Average temperatures of pelitic and psammitic sources from Figure 12b were used to estimate temperatures by the equation of Jung and Pfander (2007). The results of the Al-Ti thermometer display results mostly consistent with the Ti-in-zircon thermometer; with two-mica leucogranite yielding higher temperatures than garnet-bearing leucogranite. In Figures 4.12c and 4.12d, temperatures show negative trends with increasing Rb/Zr ratio and positive trends with increasing Th. In detail, this shows that the garnet-bearing leucogranite is represented by lower degrees of partial melting with low temperature conditions while the two-mica leucogranite shows a higher degree of partial melting with higher temperatures.

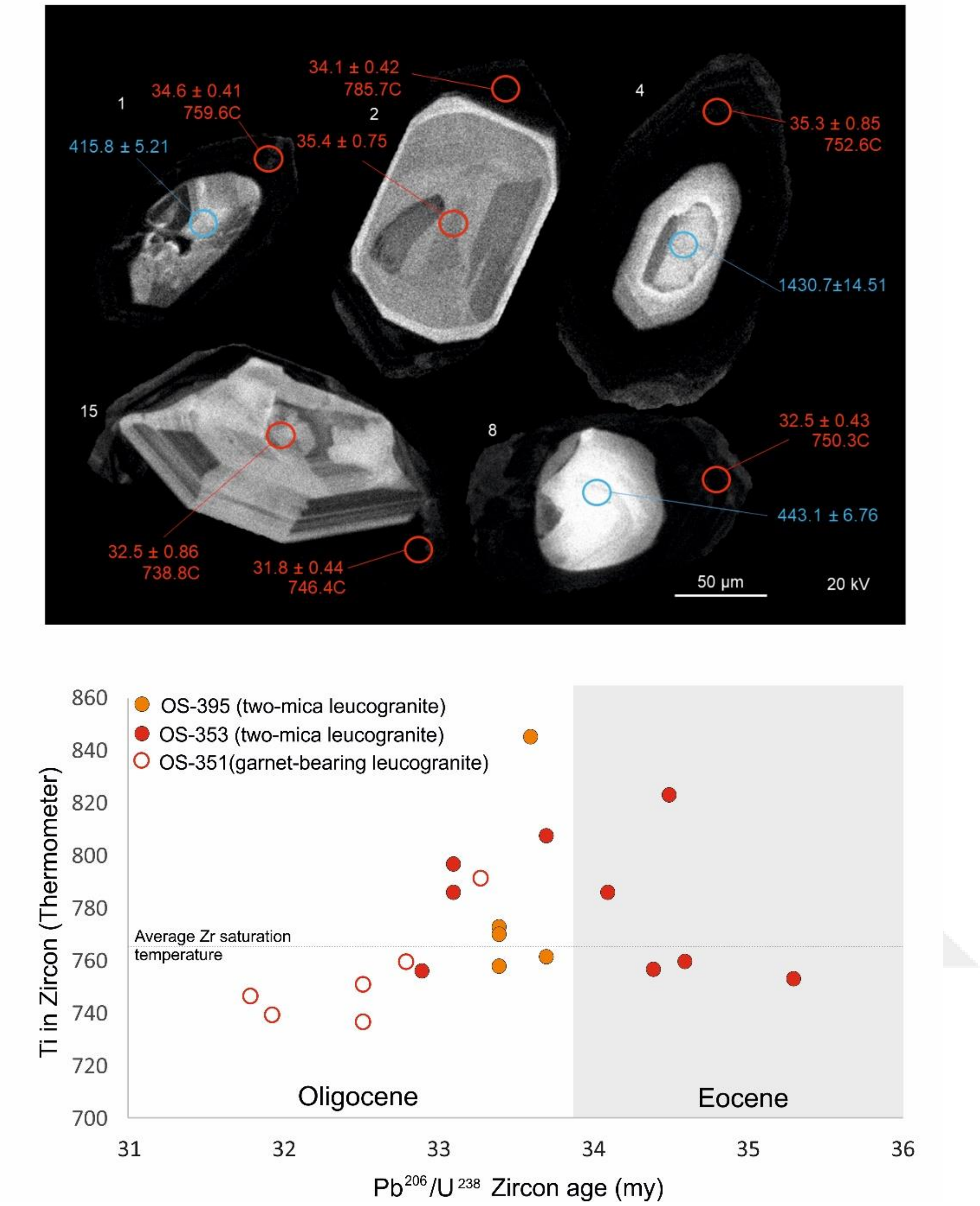

Figure 4.11 : In-situ Ti-in-zircon thermometry of leucogranite samples. A) BSE images of different zircon generations, ages and temperatures. B) 206Pb/238U ages versus temperatures obtained from Ti-in-zircon thermometry.

Therefore, temperature may be the main factor that influences the degree of partial melting and the differentiation of the leucogranite samples.

Several models have been proposed for the melting mechanisms of peraluminous S-type leucogranites, particularly in the Himalayan domain: (1) water-fluxed anatexis (Le Fort et al., 1987); (2) decompression melting under vapour-absent conditions (Harris and Massey, 1994); and (3) melting triggered by shear heating (Zhu and Shi, 1990).

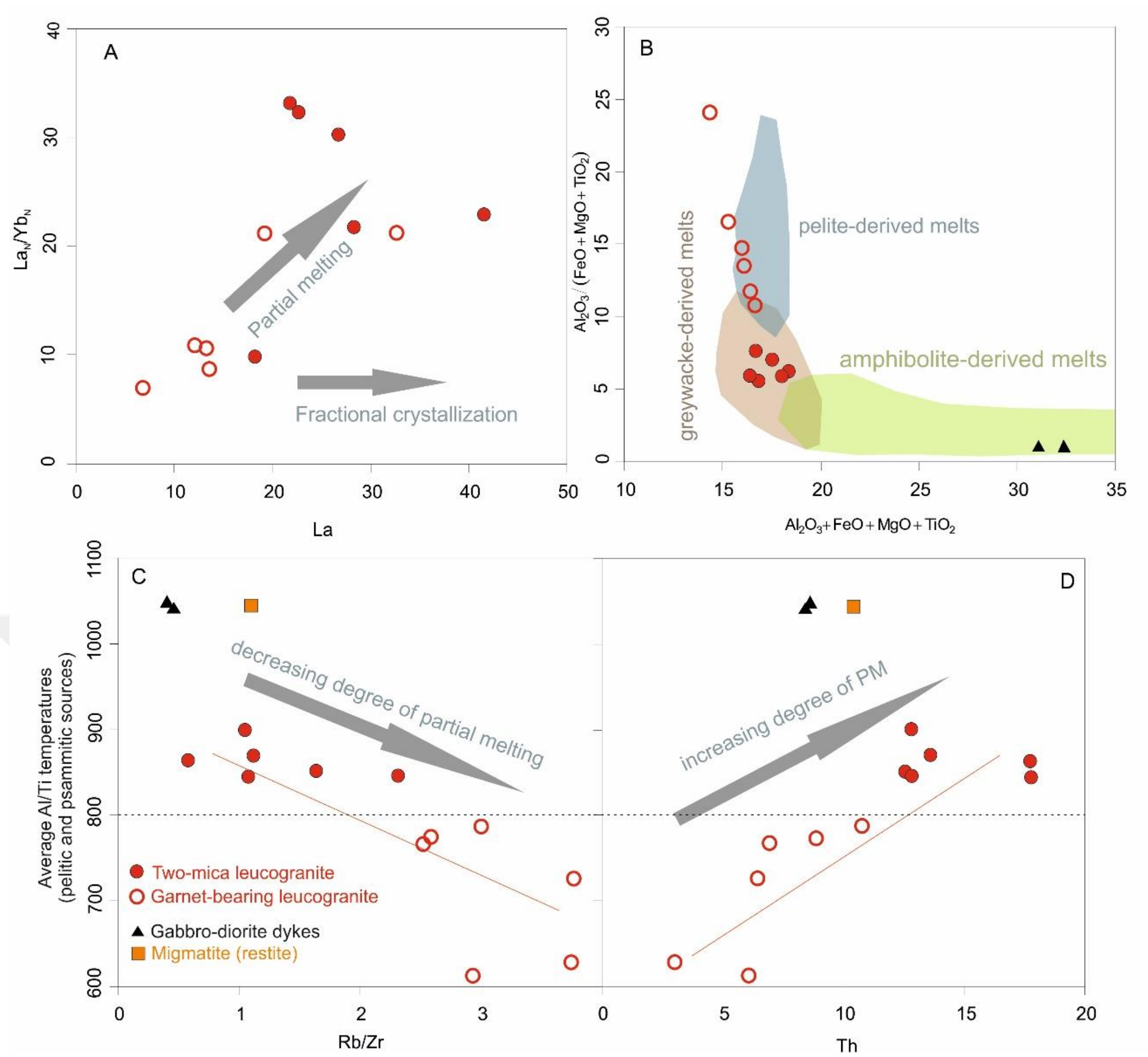

Figure 4.12 : Partial melting signatures of leucogranites. A) La vs LaN/YbN diagram; B) crustal source characteristics of leucogranites (Patino Douce and Harris, 1998); Average Al-Ti temperatures versus Rb/Zr (C) and Th (D) as partial melting index.

The major differences between water-fluxed and dehydration melting are (i) the presence and composition of peritectic minerals and melts, and (ii) melting temperatures (Weinberg & Hasalova, 2015). During water-absent muscovite dehydration melting, K-feldspar in melt increases with time (Figures 4.13a and 4.13b). Dehydration melting generates melts with a lower FeO content and higher Na_2O/Ka_2O ratio than water-fluxed melting (Figure 4.13c; Patino Douce and Harris, 1996; 1998).

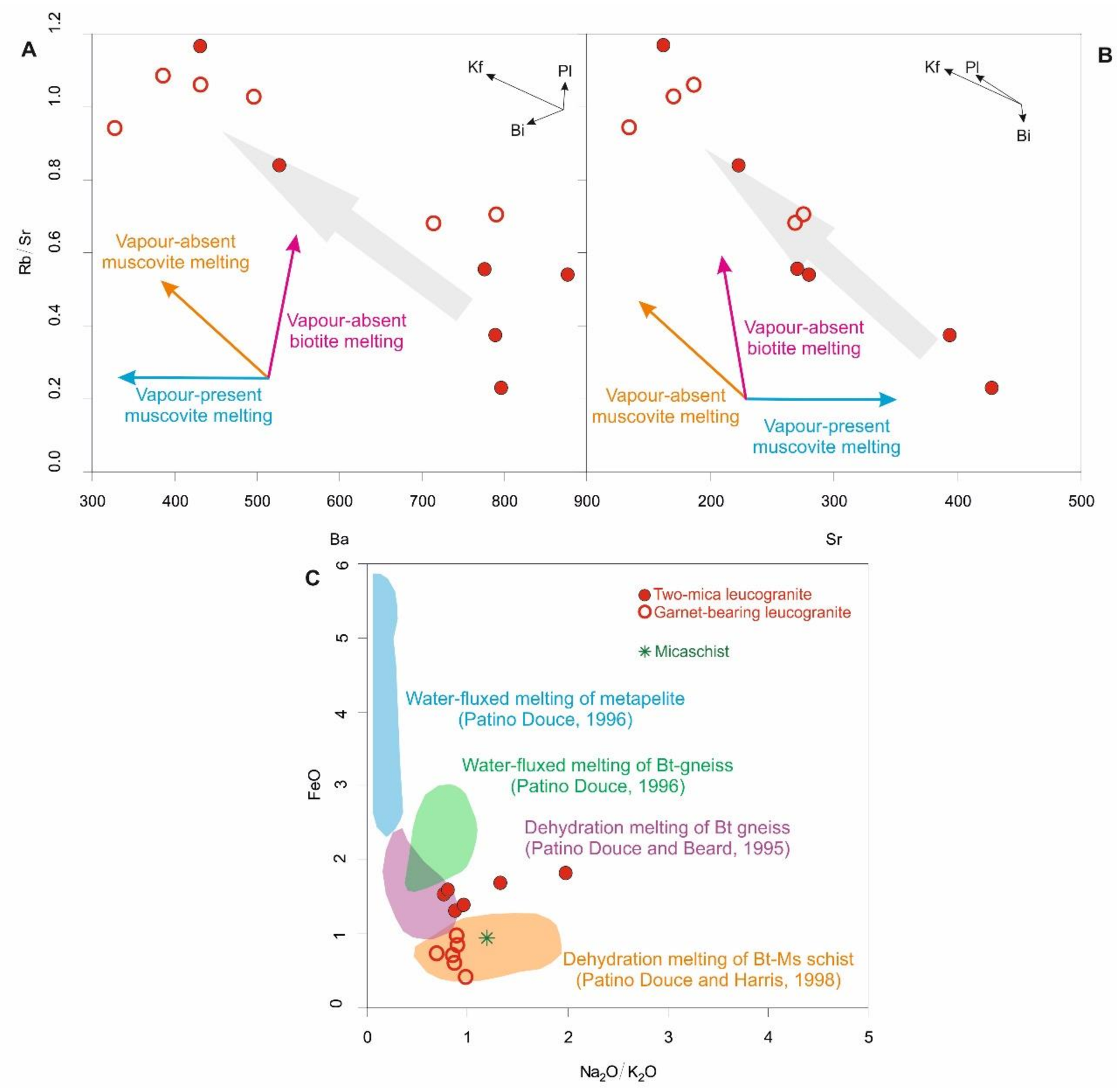

Figure 4.13 : Melting mechanisms of leucogranite. A) Na_2O/K_2O vs FeO diagram of melt compositions for different melting reactions. B and C) Correlation of Ms-dehydration, Bt-dehydration and water-present mica dehydration melting mechanisms.

Both shear heating and water-fluxed melting need relatively lower melting temperatures (~650 C; Sawyer, 2010) than water-absent melting. Melting temperatures of the leucogranite samples (739–840 °C) are significantly higher than the melts produced by water-fluxed melting. The higher melting temperatures of leucogranite and the presence of K-feldspar in the peritectic melt suggest that both water-fluxed melting and melting by shear heating are unlikely for the generation of leucogranite.

The PhasePlot software with the MELTS algorithm (Ghiorso and Sack, 1994) was used to model water-absent (< 1% H2O) partial melting of a selected sample of mid-crustal source in the study area (mica-schist, OS-77) (Figure 4.14). P-T conditions of partial melting combined with temperatures obtained from Ti-in-zircon thermometry indicate a melt fraction of > 30% (max. 35%) at 739–840 °C for leucogranites (Figure 4.14). To determine the muscovite bearing protolith, the dehydration melting curves of both ms-bi schist and ms schist sources (Patino Douce and Harris, 1998) were added to the phase diagram. Modelled muscovite breakdown of the protolith suggests P-T conditions were compatible with the melting of a ms-bi schist source (Figure 4.14). Therefore, the leucogranite samples probably formed by the water-absent melting of a muscovite and biotite-bearing protolith. This protolith composition is similar to the one of the muscovite-biotite schists (OS-77 sample), which has ≥ 15 wt.% muscovite contents that could have acted as a fertile source to increase the melt fraction (two units of melt were produced per melting of 1 wt.%; Harris and Inger, 1992).

The dehydration melting of a pelitic mica-bearing source is commonly associated with the dehydration melting of muscovite, and can be represented by (Kretz, 1983):

$$22Ms + 8Qz + 7Pl \rightarrow 25melt + 5Kfs + 5Als + 2Bi \tag{4.1}$$

where Ms = muscovite, Qz = quartz, Pl = plagioclase, Kfs = K-feldspar, Als = aluminosilicate, and Bi = biotite. This reaction shows that peritectic biotite crystals develop after the breakdown of muscovite (for each 11 moles of muscovite consumed about 1 mole of biotite is formed). Therefore, the biotite content of the melanosome (Sample OS-111) increases with ongoing melting. In addition to the development of new biotite as a result of dehydration melting of muscovite, biotite crystals with high Ti content (with reddish-brown colours) are observed within sample OS-111, and correspond to the restite of the dehydration melting.

To estimate pressure conditions, we combined the intersection points of the reaction curves with the results of Ti-in-zircon thermometry. We also constrained the P-T conditions with the biotite dehydration melting curve, as biotite dehydration is not observed in migmatites. The pressure conditions of water-absent melting of muscovite-biotite-schist (OS-77) and the generation of leucogranite were calculated to be ≥ 7–10 kb, which corresponds to mid-crustal depths in the Western Anatolian Orogenic Crust (WAOC) (Figure 4.14).

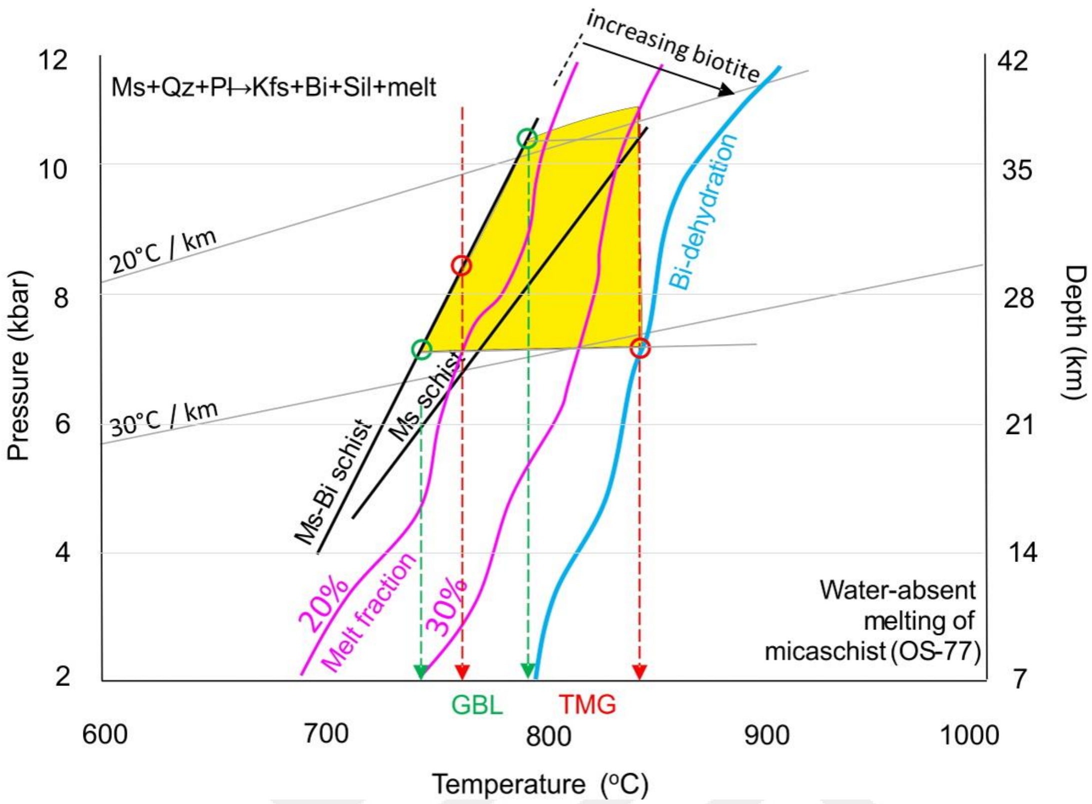

Figure 4.14 : P-T conditions of water-absent dehydration melting of mica-schist from the study area (OS-77). GBL: Garnet-bearing leucogranite; TMG: Two-mica leucogranite.

4.7 Evidences for the Role of Accreted Continental Crust in the Formation of Çataldağ Leucogranites

In western Anatolia, following the closure of the Neo-Tethyan Ocean during pre-Eocene, continental collision between the Sakarya Continent (SC) belonging to Laurasia and the Anatolide-Tauride Platform (ATP) belonging to Gondwana took place. The İzmir-Ankara-Erzincan suture zone (IAESZ) represents this collision zone (Şengör and Yılmaz 1981; Okay and Tüysüz, 1999; Yılmaz, 2017). Cretaceous to Palaeogene subduction–accretion complexes constitute the footwall of the IAESZ, including the Tavşanlı zone, the Bornova Flysch zone, the Afyon zone and the Lycian nappes (Okay and Tüysüz, 1999). The Tavşanlı zone represents the northward subducted passive continental margin of the ATP, which underwent blueschist metamorphism in the Cretaceous (100–80 Ma, Sherlock et al., 1999). The zone contains jadeite-glaucophane-chloritoid-lawsonite-bearing metasedimentary and felsic rocks (Önen and Hall, 1993). The basal tectonic unit in the Tavşanlı Zone is the Orhaneli unit which is made up of metabasite, marble and metaclastic rocks (Okay, 1984). which underwent HP/LT metamorphism in the Late Cretaceous and Palaeocene (24 kbar and 500 °C; Plunder et al., 2015). The HP/LT metamorphic rocks of the Tavşanlı Zone was intruded by granodiorites and underwent a dynamo-contact metamorphism indicating the HP/LT rocks reached their present position by the Eocene (Okay and Satır, 2006). The presence of HP/LT crustal metamorphic rocks is evidence of the continental subduction process, which marks an incipient phase of collisional tectonics forming the orogenic crust.

The most striking components of western Anatolian orogenic crust, Menderes and Kazdağ massifs correspond to Cenozoic Cordilleran-type core complexes. Compressional deformation caused Barrovian-type regional metamorphism which is responsible for the development of metamorphic core rocks of upper amphibolite facies in these massifs (Bozkurt and Park, 1994; Isik and Tekeli, 2001; Gessner et al., 2001; Bonev et al., 2009; van Hinsberg, 2010) and thickening of the crust before the Oligocene (> 50 km, Plunder et al., 2015; Yılmaz, 2017 and references therein). The Çataldağ Metamorphic core complex (ÇMCC), focus of this study, is one of the metamorphic core complexes in Aegean and Western Anatolian region (Kamacı et al, 2017; Kamacı and Altunkaynak, 2019a). Leucogranites in Çataldağ Metamorphic Core Complex provide an opportunity to track the geochronological and isotopic fingerprints of accreted ATP crustal units underneath Sakarya Continent and its role in the formation of the granitic melts.

As presented above, field study, geochemical and thermochronological data obtained from leucogranites such as spatial relations with migmatites, mineral compositions (i.e. muscovite, cordierite and garnet in granites), strongly peraluminous nature (ASI ≥ 1.1), zircons with inherited cores, and isotope ratios similar to the basement rocks of western Anatolia point out to their crustal origin. The ÇMCC and connected leucogranites are located on immediately north of the IAESZ so they are considered as a part of the Sakarya Continent. However, in the T_{DM} versus $\varepsilon Nd_{(33)}$ diagram, the majority of the leucogranite samples plot in the field of ATP granites (Figure 10b). The T_{DM} (The Nd depleted mantle model of Goldstein et al., 1988) ages of leucogranites change between 1.06 to 1.89 Ga, which corresponds to the ages of ATP granites (T_{DM} > 1.2 Ga), while the SC granites present lower T_{DM} ages (T_{DM} ≤ 1.2 Ga; Figure 4.9b). This brings into question whether the crustal source rocks of the leucogranites belong to the ATP or Sakarya Continent.

The oldest magmatic rocks reported in the Sakarya Continent are of Carboniferous age, along the Kazdağ and Uludağ massifs, and were intruded into high-grade gneiss, amphibolite and marble (Topuz et al., 2010). However, ages obtained from the cores of zircon crystals from the leucogranites (blue colours in Figure 4.11a) correspond to the Cambrian–Precambrian (415.8 ± 5.2–1430.7 ± 14.5 Ma; Kamacı et al., 2017), which is older than the oldest magmatism in the SC. This age span is compatible with the reported ages from zircons related to Precambrian magmatism in the ATP. The middle to lower crustal rocks of the ATP are represented by the Çine and Bozdağ units of the Menderes Metamorphic Massif (MMM), which document a Neoproterozoic/Cambrian polyorogenic history (Candan et al., 2001; Gessner et al., 2004; Catlos and Çemen, 2005; Ring and Collins, 2005; Zlatkin et al., 2012). The Çine unit is made up of orthogneiss, largely undeformed metagranite, pelitic gneiss, eclogite and amphibolite. The protolith ages of orthogneiss and metagranite of the Çine unit date to ca. 560–530 Ma (Loos and Reischmann, 1999; Gessner et al., 2004; Zlatkin et al., 2012). The Bozdağ unit consists of metapelites containing amphibolite, eclogite and marble lenses. Protolith ages of the Bozdağ rocks are suggested to be Precambrian by their stratigraphic relations (Candan et al., 2001; Gessner et al., 2004). The overlapping protolith ages of the MMM (Çine and Bozdağ units) and the leucogranite imply the role of partial melting of the ATP crust under the SC during the formation of leucogranite melts.

The ages obtained from the magmatic zircons within the leucogranites (Figure 4.11) indicate that its emplacement age is Eo-Oligocene (35–32 Ma). During the Eocene period, preceding the emplacement of studied leucogranites, slab break-off related magmatism dominated NW Anatolia (Altunkaynak and Dilek., 2006; Altunkaynak et al., 2012b). The addition of voluminous magmatic products to the crust may have contributed to crustal thickening and thermal weakening of the crust by the end of the Eocene (> 50 km; Aldanmaz et al., 2000; Köprübaşı and Aldanmaz, 2004; Altunkaynak and Dilek, 2006; Altunkaynak et al 2012b; Ersoy et al, 2017). P-T calculations of leucogranite melting conditions indicate a mid-crustal depth (> 25 km). Such a depth means the crust was still thick in the Eo-Oligocene (Kamacı et al., 2017 and references therein). Emplacement of Eo-Oligocene granitoids partly overlaps with the retreat of the subducted slab beneath the Hellenic arc that triggered extension (~30 Ma; Bozkurt, 2000; Jolivet and Facenna, 2000; Catlos and Çemen, 2005) in western Anatolia. Concurrent gabbroic-diorite dyke emplacement and migmatization in middle crustal levels of the western Anatolian orogenic crust supports heating and material transfer from upwelling mantle (Figure 4.15).

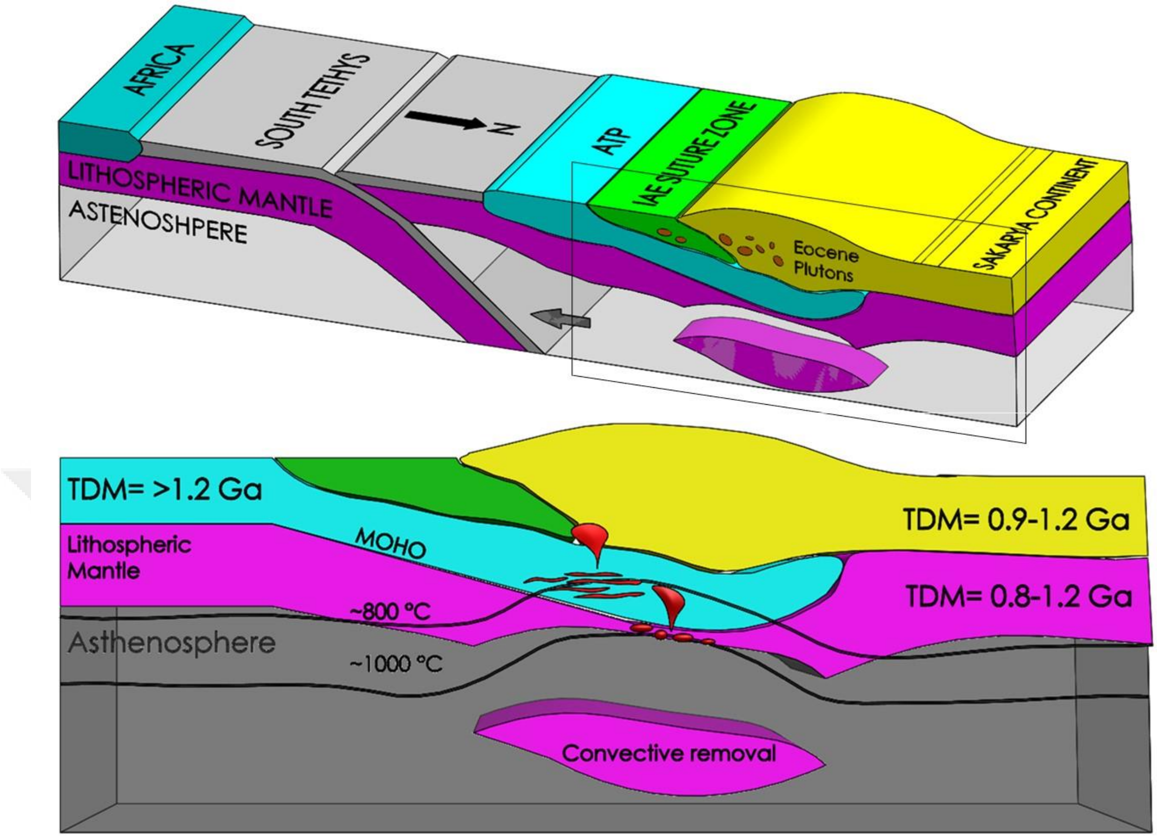

Figure 4.15 : Eocene magmatic thickening and thermal weakening of Western Anatolian orogenic crust. Partial removal of young orogenic crust triggered by slab retreat beneath the Hellenic arc caused upwelling of the hot asthenosphere, migmatization, partial melting of subducted continental crust and metasomatized lithospheric mantle to form leucogranitic melts.

Therefore, on the basis of geochemical and geochronological evidences, we infer that migmatization and melt generation to produce leucogranites is most probably related to thermal weakening, partial removal of western Anatolian young orogenic lithosphere and the retreat of the subducted slab beneath the Hellenic arc in the Eo-Oligocene, which is considered as the transition between the latest phase of orogeny and the earliest phase of extension in Western Anatolia. Future geochemical and geochronological studies on the leucogranites connected to metamorphic core complexes in western Anatolia and the Alpine belt should provide an excellent opportunity to investigate the role of underthrusted/ accreted continental crust (Vanderhaeghe and Duchene, 2010) in the formation of granites within the Alpine style continental collision zones (Figure 4.15).

4.8 Conclusions

- Eo-Oligocene leucogranites from the Çataldağ Core Complex, which located in the Sakarya Continent (SC), include garnet-bearing leucogranite and two-mica leucogranite. Both show similar geochemical and isotopic characteristics that indicate a crustal origin.
- Mixing modelling based on isotopic signatures of granites compared to the ones of the potential crustal and mantle sources shows that leucogranites in the CMCC have crustal source for more than 70% and a mantle contribution of less than 30%.
- Crustal melts that formed the leucogranites were generated by water-absent muscovite dehydration melting of a mica-schist source (a melt fraction of max. 35%), at ≥ 7–10 kb and 739–840 °C.
- Inherited zircon cores ages (Precambrian to Cambrian) and T_{DM} model ages (> 1.2 Ga) of both the garnet-bearing leucogranite and the two-mica leucogranite indicate that granitic melts were derived mainly from a crust equivalent to the one of the Anatolian-Tauride Platform.
- Geochemical properties, isotopic characteristics and inherited zircon chronology, combined with the geology of NW Anatolia, indicate that leucogranite melts were derived mainly from partial melting of rocks from the Anatolian-Tauride platform underthrusted below the Sakarya continent along the Izmir-Ankara-Erzincan Suture Zone with a minor contribution of enriched mantle (EM II) potentially present beneath WAOC.
- We infer that migmatization and melt generation to produce leucogranites are most probably related to thermal weakening and partial removal of western Anatolian young orogenic lithosphere during the transitional phase between the latest phase of collision and the earliest phase of extension, in the Eo-Oligocene.

5. CONCLUSIONS

In this study, a new metamorphic core complex was identified in NW Anatolia based on thorough field observations, meso-and microstructural features, geochronology and geochemical data listed below. This domal structure exposed in and around Çataldağ mountain between Balıkesir and Bursa cities and is named the Çataldağ Metamorphic Core Complex (ÇMCC). The ÇMCC is divided into three different parts which show different structural characteristics: (1) footwall rocks; (2) the hanging wall rocks and (3) the mylonitic shear zone, which consists of footwall rocks that underwent continuous ductile to brittle deformation below the Çataldağ detachment fault zone (ÇDFZ). ÇDFZ separates the footwall rocks from the hanging wall rocks.

The footwall of ÇDFZ comprises a heterogenous core of a granite-gneiss-migmatite complex (GGMC) and a synkinematic granitic intrusion (Çataldağ syn-kinematic pluton: ÇSP). Mineral paragenesis of migmatites within the GGMC reveals that they underwent HT/LP metamorphism in amphibolite (upper amphibolite?) facies. The hanging wall rocks, on the other hand, are represented by metamorphic (greenschist facies) rocks of the Karakaya complex and Bornova flysch, supra-detachment sediments and Neogene lacustrine sediments.

The U-Pb zircon and monazite ages of granite (leucogranite) within GGMC range from 33.8 ±0.14 Ma. to 30.1 ±0.23 Ma (Late Eocene-Early Oligocene). $^{40}Ar/^{39}Ar$ ages obtained from biotite, muscovite, and feldspar minerals of the footwall rocks and the mylonitic rocks vary from 20.7 ±0.1 Ma to 21.3 ±0.3 Ma (Early Miocene). The $^{40}Ar/^{39}Ar$ biotite ages of the ÇSP range from 20.8 ±0.1 Ma to 21.1 ±0.02 Ma. This age data clearly indicates that GGMC and ÇSP were formed in different periods (Eo-Oligocene and Early Miocene, respectively), but they were uplifted together during the Early Miocene (21.3–20.7 Ma).

Microstructural studies reveal that GGMC and ÇSP underwent continuous deformation from ductile to brittle conditions during their cooling and exhumation with a top-to-north and top-to-northeast sense of shear. Microstructures also indicate that dynamic recrystallization processes at high temperatures (>600–450^{o}C) were dominant, whereas dynamic deformation within the mylonitic zone was continuous from the mid-temperature (500ºC–<250ºC) to brittle conditions. Two-feldspar thermometer calculations indicate that the deformation temperatures for the ductile and mylonitic zone are 501–588°C and 430–557°C, respectively. Combined microtectonics, two-feldspar geothermometry and thermochronology data show that the GGMC cooled slowly (<50°C/my) during the Eo-Oligocene and then rapidly (> 500 °C/my) during the Early Miocene (21 Ma) along the ÇDFZ. The ÇSP, on the other hand, was gradually deformed from sub-magmatic to brittle conditions and cooled rapidly (> 500°C/my) in the Early Miocene (21 Ma). Because of its progressive sub-solidus deformation, C-S fabrics, and spatiotemporal link with the DFZ, the Early Miocene granodioritic intrusion was considered as a "synkinematic" pluton that was emplaced at shallow depths along the ÇDFZ.

Eo-Oligocene granites belonging to GGMC include garnet-bearing leucogranite and two-mica leucogranite. Geochemical and isotopic characteristics of leucogranites indicate a dominant crustal origin with a minor contribution of the metasomatized lithospheric mantle. This crustal melting was generated by water-absent muscovite dehydration melting of a mica-schist source (a melt fraction of max. 35%), at ≥ 7–10 kb and 739–840 °C, which corresponds to deep-crustal levels. The inherited zircon ages (Precambrian to Cambrian) with Pan-African crustal signatures and high TDM model ages (> 1.2 Ga) of leucogranites reveal that granitic melts were derived mainly from a crustal source equivalent to one of the Anatolian-Tauride block units that were underthrusted beneath the Sakarya Continent along the İzmir-Ankara suture zone. The source of the syn-plutonic mafic (gabbro-diorite) dykes within the core of the ÇMCC, on the other hand, is inferred to be derived from the enriched mantle (EMII) beneath western Anatolia.

The migmatization and melt production that formed leucogranites were most likely triggered by thermal weakening and partial removal of the western Anatolian young orogenic lithosphere during the Eo-Oligocene transitional phase between the latest phase of collision and the earliest phase of extension. In the Early Miocene, with the advanced back-arc extension, the upper crust was subjected to intense brittle deformation, allowing both the exhumation of metamorphic core complexes, including ÇMCC, as well as the emplacement of syn-extensional/syn-kinematic plutons into the shallow depths of the western Anatolian continental crust.

REFERENCES

Akyüz, H.S., Okay, A.I. (1996). A section across a Tethyan suture in northwestern Turkey. *International Geology Review, 38*(5):405-418

Aldanmaz, E., Pearce, J., Thirlwall, M., Mitchell, J. (2000). Petrogenetic evolution of late Cenozoic, post-collision volcanism in western Anatolia, Turkey. *Journal of Volcanology and Geothermal Research, 102*(1–2), 67–95.

Altunkaynak, Ş. (2007). Collision-Driven Slab Breakoff Magmatism in Northwestern Anatolia, Turkey. *The Journal of Geology, 115*, 63–82.

Altunkaynak, Ş., Dilek, Y. (2006). Timing and nature of post collisional volcanism in Western Anatolia and geodynamic implications. *Geological Society of America Special Paper, 409*, 321–351.

Altunkaynak, Ş., Dilek, Y. (2013). Eocene mafic volcanism in northern Anatolia: its causes and mantle sources in the absence of active subduction. *International Geology Review*, *55:13*, 1641-1659

Altunkaynak, Ş., Dilek, Y., Genç, C. Ş., Sunal, G., Gertisser, R., Furnes, H., Yang, J. (2012a). *Spatial, temporal and geochemical evolution of Oligo-Miocene granitoid magmatism in western Anatolia, Turkey*. Gondwana Research.

Altunkaynak, Ş., Sunal, G., Aldanmaz, E., Genç, C. Ş., Dilek, Y., Furnes, H., ... & Yıldız, M. (2012). (2012b). Eocene Granitic Magmatism in NW Anatolia (Turkey) revisited: New implications from comparative zircon SHRIMP U–Pb and 40Ar–39Ar geochronology and isotope geochemistry on magma genesis and emplacement. *Lithos*, *155*, 289–309.

Altunkaynak, Ş., Genç, Ş.C. (2008). Petrogenesis and time-progressive evolution of the Cenozoic continental volcanism in the Biga Peninsula, NW Anatolia (Turkey). *Lithos*, *102*, 316–340.

Altunkaynak, Ş., Rogers, N.W., Kelley, S.P. (2010). Causes and effects of geochemical variations in late Cenozoic volcanism of the Foça volcanic centre, NW Anatolia, Turkey. *International Geology Review*, *52*, 579–607.

Altunkaynak, Ş., Ünal, A., Sunal, G., Kamacı, Ö., & Dunkl, I. (2021). Miocene uplift and exhumation history of northwestern Anatolia (Turkey): Implications from apatite (U-Th)/He thermochronology of syn-extensional plutons. *Journal of Asian Earth Sciences*, *213*, 104770.

Altunkaynak, Ş., & Yılmaz, Y. (1998). The mount Kozak magmatic complex, western Anatolia. *Journal of Volcanology and Geothermal Research*, *85*(1-4), 211-231.

Altunkaynak, Ş., & Yılmaz, Y. (1999). The Kozak Pluton and its emplacement. *Geological Journal*, *34*(3), 257-274.

Armstrong, R.L. (1972). Low-angle (denudation) faults, hinterland of the Sevier orogenic belt, eastern Nevada and western Utah. *Geological Society of America Bulletin*, *83*(6), 1729-1754.

Avigad, D., & Garfunkel, Z. (1991). Uplift and exhumation of high-pressure metamorphic terrains: the example of the Cycladic blueschist belt (Aegean Sea). *Tectonophysics*, *188*(3-4), 357-372.

Baran, Z. O., Dilek, Y., & Stockli, D. (2017). Diachronous uplift and cooling history of the Menderes core complex, western Anatolia (Turkey), based on new Zircon (U-Th)/He ages. *Tectonophysics*, *694*, 181-196.

Barbarin, B. (1999). A review of the relationships between granitoid types, their origins and their geodynamic environments. *Lithos*, *46*(3), 605-626.

Barth, T. F. (1951). The feldspar geologic thermometers. *Neues Jahrbuch für Mineralogie*, *82*, 143-154.

Barth, T. F. (1968). Additional data for the two-feldspar geothermometer. *Lithos; (Netherlands)*, *1*(4).

Bell, T. H., & Johnson, S. E. (1989). The role of deformation partitioning in the deformation and recrystallization of plagioclase and K-feldspar in the Woodroffe Thrust mylonite zone, central Australia. *Journal of Metamorphic Geology*, *7*(2), 151-168.

Benisek, A., Kroll, H., & Cemic, L. (2004). New developments in two-feldspar thermometry. *American Mineralogist*, *89*(10), 1496-1504.

Berthé, D., Choukroune, P., & Jégouzo, P. (1979). Orthogneiss, mylonite and non coaxial deformation of granites: the example of the South Armorican Shear Zone. *Journal of Structural Geology*, *1*(1), 31-42.

Singh, R. B., & Gururajan, N. S. (2011). Microstructures in quartz and feldspars of the Bomdila Gneiss from western Arunachal Himalaya, Northeast India: Implications for the geotectonic evolution of the Bomdila mylonitic zone. *Journal of Asian Earth Sciences*, *42*(6), 1163-1178.

Black, K. N., Catlos, E. J., Oyman, T., & Demirbilek, M. (2013). Timing Aegean extension: evidence from in situ U–Pb geochronology and cathodoluminescence imaging of granitoids from NW Turkey. *Lithos*, *180*, 92-108.

Blumenfeld, P., Mainprice, D., & Bouchez, J. L. (1986). C-slip in quartz from subsolidus deformed granite. *Tectonophysics*, *127*(1-2), 97-115.

Bonev, N., Beccaletto, L., Robyr, M., & Monié, P. (2009). Metamorphic and age constraints on the Alakeçi shear zone: Implications for the extensional exhumation history of the northern Kazdağ Massif, NW Turkey. *Lithos*, *113*(1-2), 331-345.

Bozkurt, E. (2000). Timing of extension on the Büyük Menderes Graben, western Turkey, and its tectonic implications. *Geological Society, London, Special Publications*, *173*(1), 385-403.

Bozkurt, E. (2007). Extensional v. contractional origin for the southern Menderes shear zone, SW Turkey: tectonic and metamorphic implications. *Geological Magazine*, *144*(1), 191-210.

Bozkurt, E., & Satir, M. (2000). The southern Menderes Massif (western Turkey): geochronology and exhumation history. *Geological Journal*, *35*(3-4), 285-296.

Bozkurt, E., Satır, M., & Buğdaycıoğlu, Ç. (2011). Surprisingly young Rb/Sr ages from the Simav extensional detachment fault zone, northern Menderes Massif, Turkey. *Journal of geodynamics*, *52*(5), 406-431.

Bozkurt, E., & Mittwede, S. K. (2005). Introduction: Evolution of continental extensional tectonics of western Turkey. *Geodinamica Acta*, *18*(3-4), 153-165.

Bozkurt, E., & Park, L. R. (1994). Southern Menderes Massif: an incipient metamorphic core complex in western Anatolia, Turkey. *Journal of the Geological Society*, *151*(2), 213-216.

Bozkurt, E., Satır, M., & Buğdaycıoğlu, Ç. (2010). Timing of post-orogenic extension in the Gördes migmatite dome, Western Turkey: insights from U–Pb and Rb-Sr chronology. *Tectonic Crossroads: Evolving Orogens of Eurasia-Africa-Arabia, Ankara, Turkey*.

Boztuğ, D., Harlavan, Y., Jonckheere, R., Can, I., & Sarı, R. (2009). Geochemistry and K-Ar cooling ages of the Ilıca, Çataldağ (Balıkesir) and Kozak (İzmir) granitoids, west Anatolia, Turkey. *Geological Journal*, *44*(1), 79-103.

Brown, M. (2001). Orogeny, migmatites and leucogranites: a review. *Journal of Earth System Science*, *110*(4), 313-336.

Brown, M. (1973). The definition of metatexis, diatexis and migmatite. *Proceedings of the Geologists' Association*, *84*, 371-IN2.

Brun, J. P. (1999). Narrow rifts versus wide rifts: inferences for the mechanics of rifting from laboratory experiments. *Philosophical Transactions of the Royal Society of London. Series A: Mathematical, Physical and Engineering Sciences*, *357*(1753), 695-712.

Buck, W. R., Martinez, F., Steckler, M. S., & Cochran, J. R. (1988). Thermal consequences of lithospheric extension: pure and simple. *Tectonics*, *7* (2), 213-234.

Buick, I. S. (1991). Mylonite fabric development on Naxos, Greece. *Journal of Structural Geology*, *13*(6), 643-655.

Buick, I. S., & Holland, T. J. B. (1989). The PTt path associated with crustal extension, Naxos, Cyclades, Greece. *Geological Society, London, Special Publications*, *43*(1), 365-369.

Burg, J. P., & Chen, G. M. (1984). Tectonics and structural zonation of southern Tibet, China. *Nature*, *311*(5983), 219-223.

Candan, O., Dora, O., Oberhänsli, R., Çetinkaplan, M., Partzsch, J., Warkus, F., & Dürr, S. (2001). Pan-African high-pressure metamorphism in the

Precambrian basement of the Menderes Massif, western Anatolia, Turkey. *International Journal of Earth Sciences*, *89*(4), 793-811.

Castelli, D., & Lombardo, B. (1988). The Gophu La and western Lunana granites: Miocene muscovite leucogranites of the Bhutan Himalaya. *Lithos*, *21*(3), 211-225.

Catlos, E. J., Baker, C., Sorensen, S. S., Çemen, I., & Hançer, M. (2010). Geochemistry, geochronology, and cathodoluminescence imagery of the Salihli and Turgutlu granites (central Menderes Massif, western Turkey): Implications for Aegean tectonics. *Tectonophysics*, *488* (1-4), 110-130.

Catlos, E. J., & Cemen, I. (2005). Monazite ages and the evolution of the Menderes Massif, western Turkey. *International Journal of Earth Sciences*, *94*(2), 204-217.

Catlos, E., Jacob, L., Oyman, T., & Sorensen, S. (2012). Long-term exhumation of an Aegean metamorphic core complex granitoids in the Northern Menderes Massif, western Turkey. *American Journal of Science*, *312*(5), 534-571.

Cavazza, W., Okay, A. I., & Zattin, M. (2009). Rapid early-middle Miocene exhumation of the Kazdağ Massif (western Anatolia). *International Journal of Earth Sciences*, *98*(8), 1935-1947.

Cenki-Tok, B., Expert, M., Işık, V., Candan, O., Monié, P., & Bruguier, O. (2016). Complete Alpine reworking of the northern Menderes Massif, western Turkey. *International Journal of Earth Sciences*, *105*(5), 1507-1524.

Chappell, B. W. (1974). Two contrasting granite types. *Pacif. Geol.*, *8*, 173-174.

Charles, N., Gumiaux, C., Augier, R., Chen, Y., Zhu, R., & Lin, W. (2011). Metamorphic core complexes vs. synkinematic plutons in continental extension setting: Insights from key structures (Shandong Province, eastern China). *Journal of Asian Earth Sciences*, *40*(1), 261-278.

Claiborne, L. L., Miller, C. F., Flanagan, D. M., Clynne, M. A., & Wooden, J. L. (2010). Zircon reveals protracted magma storage and recycling beneath Mount St. Helens. *Geology*, *38*(11), 1011-1014.

Claiborne, L. L., Miller, C. F., Walker, B. A., Wooden, J. L., Mazdab, F. K., & Bea, F. (2006). Tracking magmatic processes through Zr/Hf ratios in rocks and Hf and Ti zoning in zircons: an example from the Spirit Mountain batholith, Nevada. *Mineralogical Magazine*, *70*(5), 517-543.

Clemens, J. D. (1998). Observations on the origins and ascent mechanisms of granitic magmas. *Journal of the Geological Society*, *155*(5), 843-851.

Collins, W. J. (1996). Lachlan Fold Belt granitoids: products of three-component mixing. *Earth and Environmental Science Transactions of the Royal Society of Edinburgh*, *87* (1-2), 171-181.

Coney, P. J. (1973). Plate tectonics of marginal foreland thrust-fold belts. *Geology*, *1*(3), 131-134.

Coney, P. J., & Crittenden, M. D. (1980). Cordilleran metamorphic core complexes: An overview. *Cordilleran metamorphic core complexes: Geological Society of America Memoir*, *153*, 7-31.

Corti, G., Bonini, M., Conticelli, S., Innocenti, F., Manetti, P., & Sokoutis, D. (2003). Analogue modelling of continental extension: a review focused on the relations between the patterns of deformation and the presence of magma. *Earth-Science Reviews*, *63*(3-4), 169-247.

Cottle, J. M., Jessup, M. J., Newell, D. L., Horstwood, M. S., Noble, S. R., Parrish, R. R., ... & Searle, M. P. (2009). Geochronology of granulitized eclogite from the Ama Drime Massif: Implications for the tectonic evolution of the South Tibetan Himalaya. *Tectonics*, *28*(1).

Cox, K. G., Bell, J. D., & Pankhurst, R. J. (1979). The Interpretation of Igneous Rocks. Allen and Unwine, London, 450 p.

Crittenden, M. D., Coney, P. J., Davis, G. H., & Davis, G. H. (Eds.). (1980). *Cordilleran metamorphic core complexes* (Vol. 153). Geological Society of America.

Çemen, I., Catlos, E. J., Gogus, O., Ozerdem, C., Dilek, Y., & Pavlides, S. (2006). Postcollisional extensional tectonics and exhumation of the Menderes massif in the Western Anatolia extended terrane, Turkey. *Special Papers-Geological Society of America*, *409*, 353.

Davis, G. H. (1983). Shear-zone model for the origin of metamorphic core complexes. *Geology*, *11*(6), 342-347.

Davis, G. A. (1980). Mylonitization and detachment faulting in the Whipple-Buckskin-Rawhide Mountains. *Cordilleran metamorphic core complexes*, *153*, 79.

Davis, G. H., & Coney, P. J. (1979). Geologic development of the Cordilleran metamorphic core complexes. *Geology*, *7*(3), 120-124.

de Saint Blanquat, M., Horsman, E., Habert, G., Morgan, S., Vanderhaeghe, O., Law, R., & Tikoff, B. (2011). Multiscale magmatic cyclicity, duration of pluton construction, and the paradoxical relationship between tectonism and plutonism in continental arcs. *Tectonophysics*, *500*(1-4), 20-33.

Delaloye, M., & Bingol, E. (2000). Granitoids from western and northwestern Anatolia: geochemistry and modeling of geodynamic evolution. *International Geology Review*, *42*(3), 241-268.

Denèle, Y., Lecomte, E., Jolivet, L., Lacombe, O., Labrousse, L., Huet, B., & Le Pourhiet, L. (2011). Granite intrusion in a metamorphic core complex: the example of the Mykonos laccolith (Cyclades, Greece). *Tectonophysics*, *501*(1-4), 52-70.

Deschamps, F., Duchêne, S., de Sigoyer, J., Bosse, V., Benoit, M., & Vanderhaeghe, O. (2017). Coeval mantle-derived and crust-derived magmas forming two neighbouring plutons in the Songpan Ganze accretionary orogenic wedge (SW China). *Journal of Petrology*, *58*(11), 2221-2256.

Dilek, Y., & Altunkaynak, Ş. (2007). Cenozoic crustal evolution and mantle dynamics of post-collisional magmatism in western Anatolia. *International Geology Review*, *49*(5), 431-453.

Dilek, Y., & Altunkaynak, Ş. (2010). Geochemistry of Neogene–Quaternary alkaline volcanism in western Anatolia, Turkey, and implications for the Aegean mantle. *International Geology Review*, *52*(4-6), 631-655.

Dilek, Y., Altunkaynak, S., Oner, Z., Ring, U., & Wernicke, B. (2009). Syn-extensional Miocene granitoids in the Menderes core complex (Western Anatolia), and their role in the late Cenozoic extensional tectonics of the Aegean province. *Continental Extensional Tectonics. Geol. Soc. London, Spec. Publ*, *321*, 197-223.

Dilek, Y., Whitney, D. L., Panayides, I., Xenophontos, C., & Malpas, J. (2000). Cenozoic crustal evolution in central Anatolia: Extension, magmatism and landscape development. In *Proceedings of the Third International Conference on the Geology of the Eastern Mediterranean. Geological Survey Department, Nicosia* (Vol. 183, p. 192).

Dinter, D. A. (1998). Late Cenozoic extension of the Alpine collisional orogen, northeastern Greece: Origin of the north Aegean basin. *Geological society of America bulletin*, *110*(9), 1208-1230.

Dinter, D. A., & Royden, L. (1993). Late Cenozoic extension in northeastern Greece: Strymon Valley detachment system and Rhodope metamorphic core complex. *Geology*, *21*(1), 45-48.

Duchêne, S., Aissa, R., & Vanderhaeghe, O. (2006). Pressure-temperature-time evolution of metamorphic rocks from Naxos (Cyclades, Greece): Constraints from thermobarometry and Rb/Sr dating. *Geodinamica Acta*, *19*(5), 301-321.

Eggleton, R. A. (1979). The ordering path for igneous K-feldspar megacrysts. *American Mineralogist*, *64*(7-8), 906-911.

Eggleton, R. A., & Buseck, P. R. (1980). The orthoclase-microcline inversion: a high-resolution transmission electron microscope study and strain analysis. *Contributions to Mineralogy and Petrology*, *74*(2), 123-133.

Elkins, L. T., & Grove, T. L. (1990). Ternary feldspar experiments and thermodynamic models. *American Mineralogist*, *75*(5-6), 544-559.

England, P., & Molnar, P. (1990). Surface uplift, uplift of rocks, and exhumation of rocks. *Geology*, *18*(12), 1173-1177.

Erkül, F. (2010). Tectonic significance of synextensional ductile shear zones within the Early Miocene Alaçamdağ granites, northwestern Turkey. *Geological Magazine*, *147*(4), 611-637.

Erkül, F., Erkül, S. T., Ersoy, Y., Uysal, İ., & Klötzli, U. (2013). Petrology, mineral chemistry and Sr–Nd–Pb isotopic compositions of granitoids in the central Menderes metamorphic core complex: Constraints on the evolution of Aegean lithosphere slab. *Lithos*, *180*, 74-91.

Erkül, F., Tatar Erkül, S., Manap, H. S., & Çolak, C. (2017). An extensional and transtensional origin of elongated magmatic domes and localised transfer faults in the northern Menderes metamorphic core complex, western Turkey. *Geodinamica acta*, *29*(1), 139-159.

Erkül, S. T., & Erkül, F. (2012). Magma interaction processes in syn-extensional granitoids: the Tertiary Menderes Metamorphic Core Complex, western Turkey. *Lithos*, *142*, 16-33.

Ersoy, E. Y., Palmer, M. R., Genç, Ş. C., Prelević, D., Akal, C., & Uysal, İ. (2017). Chemo-probe into the mantle origin of the NW Anatolia Eocene to Miocene volcanic rocks: Implications for the role of, crustal accretion, subduction, slab roll-back and slab break-off processes in genesis of post-collisional magmatism. *Lithos*, *288*, 55-71.

Ersoy, Y. E., Helvacı, C., & Palmer, M. R. (2011). Stratigraphic, structural and geochemical features of the NE–SW trending Neogene volcano-sedimentary basins in western Anatolia: implications for associations of supra-detachment and transtensional strike-slip basin formation in extensional tectonic setting. *Journal of Asian Earth Sciences*, *41*(2), 159-183.

Ersoy, E. Y., Çemen, İ., Helvacı, C., & Billor, Z. (2014). Tectono-stratigraphy of the Neogene basins in Western Turkey: Implications for tectonic evolution of the Aegean Extended Region. *Tectonophysics*, *635*, 33-58.

Ersoy, Y. E., Helvacı, C., & Palmer, M. R. (2012). Petrogenesis of the Neogene volcanic units in the NE–SW-trending basins in western Anatolia, Turkey. *Contributions to Mineralogy and Petrology*, *163*(3), 379-401.

Faure, Michel., Bonneau, Michel., & Pons, J. (1991). Ductile deformation and syntectonic granite emplacement during the late Miocene extension of the Aegea (Greece). *Bulletin de la Societé géologique de France*, *162*(1), 3-11.

Ferry, J. M., & Watson, E. B. (2007). New thermodynamic models and revised calibrations for the Ti-in-zircon and Zr-in-rutile thermometers. *Contributions to Mineralogy and Petrology*, *154*(4), 429-437.

Fletcher, R. C., & Hallet, B. (1983). Unstable extension of the lithosphere: A mechanical model for basin-and-range structure. *Journal of Geophysical Research: Solid Earth*, *88*(B9), 7457-7466.

Foster, D. A., & Mark Fanning, C. (1997). Geochronology of the northern Idaho batholith and the Bitterroot metamorphic core complex: Magmatism preceding and contemporaneous with extension. *Geological Society of America Bulletin*, *109*(4), 379-394.

Fuhrman, M. L., & Lindsley, D. H. (1988). Ternary-feldspar modeling and thermometry. *American mineralogist*, *73*(3-4), 201-215.

Gans, P. B. (1989). *Synextensional magmatism in the Basin and Range province: A case study from the eastern Great Basin* (Vol. 233). Geological Society of America.

Gapais, D. (1989). Shear structures within deformed granites: mechanical and thermal indicators. *Geology*, *17*(12), 1144-1147.

Gautier, P., & Brun, J. P. (1994). Ductile crust exhumation and extensional detachments in the central Aegean (Cyclades and Evvia Islands). *Geodinamica Acta*, *7*(2), 57-85.

Gautier, P., Brun, J. P., & Jolivet, L. (1993). Structure and kinematics of upper Cenozoic extensional detachment on Naxos and Paros (Cyclades Islands, Greece). *Tectonics*, *12*(5), 1180-1194.

Gautier, P., Brun, J. P., Moriceau, R., Sokoutis, D., Martinod, J., & Jolivet, L. (1999). Timing, kinematics and cause of Aegean extension: a scenario based on a comparison with simple analogue experiments. *Tectonophysics*, *315* (1-4), 31-72.

Genç, S. C., & Altunkaynak, S. (2007). On the Eybek granite (Biga Peninsula, NW Anatolia): a new evaluation in the light of new geochemical data. *Journal of the Earth Sciences Application and Research Centre of Hacettepe University*, *28*, 75-98.

Geoffroy, L., Huchon, P., & Khanbari, K. (1998). Did Yemeni Tertiary granites intrude neck zones of a stretched continental upper crust? *Terra Nova*, *10*(4), 196-200.

Gerald, J. F., & McLaren, A. C. (1982). The microstructures of microcline from some granitic rocks and pegmatites. *Contributions to Mineralogy and Petrology*, *80*(3), 219-229.

Gessner, K., Collins, A. S., Ring, U., & Güngör, T. (2004). Structural and thermal history of poly-orogenic basement: U–Pb geochronology of granitoid rocks in the southern Menderes Massif, Western Turkey. *Journal of the Geological Society*, *161*(1), 93-101.

Gessner, K., Piazolo, S., Güngör, T., Ring, U., Kröner, A., & Passchier, C. W. (2001). Tectonic significance of deformation patterns in granitoid rocks of the Menderes nappes, Anatolide belt, southwest Turkey. *International Journal of Earth Sciences*, *89*(4), 766-780.

Gessner, K., Ring, U., Johnson, C., Hetzel, R., Passchier, C. W., & Güngör, T. (2001). An active bivergent rolling-hinge detachment system: Central Menderes metamorphic core complex in western Turkey. *Geology*, *29*(7), 611-614.

Ghiorso, M. S., & Sack, R. O. (1995). Chemical mass transfer in magmatic processes IV. A revised and internally consistent thermodynamic model for the interpolation and extrapolation of liquid-solid equilibria in magmatic systems at elevated temperatures and pressures. *Contributions to Mineralogy and Petrology*, *119*(2), 197-212.

Glodny, J., & Hetzel, R. (2007). Precise U–Pb ages of syn-extensional Miocene intrusions in the central Menderes Massif, western Turkey. *Geological Magazine*, *144*(2), 235-246.

Godin, L., Grujic, D., Law, R. D., & Searle, M. P. (2006). Channel flow, ductile extrusion and exhumation in continental collision zones: an introduction. *Geological Society, London, Special Publications*, *268*(1), 1-23.

Goldstein, S. J., & Jacobsen, S. B. (1988). Nd and Sr isotopic systematics of river water suspended material: implications for crustal evolution. *Earth and Planetary Science Letters*, *87*(3), 249-265.

Güraslan, I. N., & Altunkaynak, Ş. (2019). Role of mantle and lower continental crust in the genesis of Eocene post-collisional granitoids: Insights from the Topuk pluton (NW Turkey). *Journal of Asian Earth Sciences*, *179*, 365-384.

Harris, N. B. W., & Inger, S. (1992). Trace element modelling of pelite-derived granites. *Contributions to Mineralogy and Petrology*, *110*(1), 46-56.

Harris, N., Ayres, M., & Massey, J. (1995). Geochemistry of granitic melts produced during the incongruent melting of muscovite: implications for the extraction of Himalayan leucogranite magmas. *Journal of Geophysical Research: Solid Earth*, *100*(B8), 15767-15777.

Harris, N., & Massey, J. (1994). Decompression and anatexis of Himalayan metapelites. *Tectonics*, *13*(6), 1537-1546.

Harrison, T. M., Célérier, J., Aikman, A. B., Hermann, J., & Heizler, M. T. (2009). Diffusion of ^{40}Ar in muscovite. *Geochimica et Cosmochimica Acta*, *73*(4), 1039-1051.

Harrison, T. M., Duncan, I. A. N., & Mcdougall, I. A. N. (1985). Diffusion of 40Ar in biotite: temperature, pressure and compositional effects. *Geochimica et Cosmochimica Acta*, *49*(11), 2461-2468.

Hasözbek, A., Akay, E., Erdoğan, B., Satır, M., & Siebel, W. (2010). Early Miocene granite formation by detachment tectonics or not? A case study from the northern Menderes Massif (Western Turkey). *Journal of Geodynamics*, *50*(2), 67-80.

Helvacı, C., Ersoy, E. Y., Sözbilir, H., Erkül, F., Sümer, Ö., & Uzel, B. (2009). Geochemistry and 40Ar/39Ar geochronology of Miocene volcanic rocks from the Karaburun Peninsula: implications for amphibole-bearing lithospheric mantle source, Western Anatolia. *Journal of Volcanology and Geothermal Research*, *185*(3), 181-202.

Hetzel, R., Passchier, C. W., Ring, U., & Dora, O. O. (1995). Bivergent extension in orogenic belts: the Menderes massif (southwestern Turkey). *Geology*, *23*(5), 455-458.

Hetzel, R., Ring, U., Akal, C., & Troesch, M. (1995). Miocene NNE-directed extensional unroofing in the Menderes Massif, southwestern Turkey. *Journal of the Geological Society*, *152*(4), 639-654.

Hill, E. J., Baldwin, S. L., & Lister, G. S. (1995). Magmatism as an essential driving force for formation of active metamorphic core complexes in eastern Papua New Guinea. *Journal of Geophysical Research: Solid Earth*, *100*(B6), 10441-10451.

Hopkinson, T. N., Harris, N. B., Warren, C. J., Spencer, C. J., Roberts, N. M., Horstwood, M. S., & Parrish, R. R. (2017). The identification and significance of pure sediment-derived granites. *Earth and Planetary Science Letters*, *467*, 57-63.

Huet, B., Le Pourhiet, L., Labrousse, L., Burov, E., & Jolivet, L. (2011). Post-orogenic extension and metamorphic core complexes in a heterogeneous crust: the role of crustal layering inherited from collision. Application to the Cyclades (Aegean domain). *Geophysical Journal International*, *184*(2), 611-625.

Hutton, D. H. (1988). Granite emplacement mechanisms and tectonic controls: inferences from deformation studies. *Earth and Environmental Science Transactions of the Royal Society of Edinburgh*, *79*(2-3), 245-255.

Hutton, D. H. W., Dempster, T. J., Brown, P. E., & Becker, S. D. (1990). A new mechanism of granite emplacement: intrusion in active extensional shear zones. *Nature*, *343*(6257), 452-455.

Inger, S., & Harris, N. (1993). Geochemical constraints on leucogranite magmatism in the Langtang Valley, Nepal Himalaya. *Journal of Petrology*, *34*(2), 345-368.

Işik, V., & Tekeli, O. (2001). Late orogenic crustal extension in the northern Menderes massif (western Turkey): evidence for metamorphic core complex formation. *International Journal of Earth Sciences*, *89*(4), 757-765.

Işık, V., Seyitoğlu, G., & Cemen, I. (2003). Ductile–brittle transition along the Alaşehir detachment fault and its structural relationship with the Simav detachment fault, Menderes massif, western Turkey. *Tectonophysics*, *374*(1-2), 1-18.

Isik, V., Tekeli, O., & Seyitoglu, G. (2004). The 40Ar/39Ar age of extensional ductile deformation and granitoid intrusion in the northern Menderes core complex: implications for the initiation of extensional tectonics in western Turkey. *Journal of Asian Earth Sciences*, *23*(4), 555-566.

Jackson, J. (1994). Active tectonics of the Aegean region. *Annual Review of Earth and Planetary Sciences*, *22*(1), 239-271.

Janoušek, V., Farrow, C. M., & Erban, V. (2006). Interpretation of whole-rock geochemical data in igneous geochemistry: introducing Geochemical Data Toolkit (GCDkit). *Journal of Petrology*, *47*(6), 1255-1259.

Jessell, M. W. (1987). Grain-boundary migration microstructures in a naturally deformed quartzite. *Journal of Structural Geology*, *9*(8), 1007-1014.

Jolivet, L., Faccenna, C., Goffé, B., Mattei, M., Rossetti, F., Brunet, C., ... & Parra, T. (1998). Midcrustal shear zones in postorogenic extension: example from the northern Tyrrhenian Sea. *Journal of Geophysical Research: Solid Earth*, *103*(B6), 12123-12160.

Jolivet, L., Faccenna, C., Huet, B., Labrousse, L., Le Pourhiet, L., Lacombe, O., ... & Driussi, O. (2013). Aegean tectonics: Strain localisation, slab tearing and trench retreat. *Tectonophysics*, *597*, 1-33.

Jolivet, L., Daniel, J. M., Truffert, C., & Goffé, B. (1994). Exhumation of deep crustal metamorphic rocks and crustal extension in arc and back-arc regions. *Lithos*, *33*(1-3), 3-30.

Jolivet, L., & Faccenna, C. (2000). Mediterranean extension and the Africa-Eurasia collision. *Tectonics*, *19*(6), 1095-1106.

Jolivet, L., Faccenna, C., & Piromallo, C. (2009). From mantle to crust: Stretching the Mediterranean. *Earth and Planetary Science Letters*, *285*(1-2), 198-209.

Jung, S., & Pfänder, J. A. (2007). Source composition and melting temperatures of orogenic granitoids: constraints from CaO/Na2O, Al2O3/TiO2 and accessory mineral saturation thermometry. *European Journal of Mineralogy*, *19*(6), 859-870.

Kamacı, Ö., & Altunkaynak, S. (2011). Petrogenetic implications of two contrasting granite types in the çataldag plutonic complex, NW Turkey. *Mineral. Mag*, *1138*.

Kamacı, Ö., & Altunkaynak, S. (2011). Çataldağ Plütonik Kompleksi: Sıyrılma Fayları Ve İlişkili Makaslama Zonlarının Granit Yerleşimi Üzerindeki Rolü. *Türkiye Jeoloji Kurultayı*.

Kamaci, Ö., & Altunkaynak, S. (2010). Mineral Chemistry and Petrography of Lava Successions From Kepsut-Dursunbey Volcanic Field, NW Turkey: Implications For Magmatic Processes and Crystallization Conditions. *International Journal of Geological and Environmental Engineering*, *4*(11), 594-598.

Kamacı, Ö., & Altunkaynak, Ş. (2019a). Cooling and deformation history of the Çataldağ metamorphic core complex (NW Turkey). *Journal of Asian Earth Sciences*, *172*, 279-291.

Kamacı, Ö., & Altunkaynak, Ş. (2019). Magma chamber processes and dynamics beneath northwestern Anatolia: Insights from mineral chemistry and crystal size distributions (CSDs) of the Kepsut volcanic complex (NW Turkey). *Journal of Asian Earth Sciences*, *181*, 103889.

Kamacı, Ö., Ünal, A., Altunkaynak, S., Georgiev, S., & Billor, Z. M. (2017). The Çataldag Plutonic Complex in Western Anatolia: roles of different granites on the crustal buildup in connection with the core complex development. *Active Global Seismology: Neotectonics and Earthquake Potential of the Eastern Mediterranean Region*, *225*, 189.

Kamacı, Ö., Unal, A., Altunkaynak, S., Billor, M. Z., Georgiev, S., & Marchev, P. (2013). Emplacement, Deformation and Exhumation of the Çataldağ Plutonic Complex: Implications for Neotectonic Evolution of NW Anatolia (Turkey). In *American Geophysical Union, Fall Meeting, Abstract# T31E-2568*.

Keskin, M., Genç, Ş. C., & Tüysüz, O. (2008). Petrology and geochemistry of post-collisional Middle Eocene volcanic units in North-Central Turkey: evidence for magma generation by slab breakoff following the closure of the Northern Neotethys Ocean. *Lithos*, *104*(1-4), 267-305.

Kilias, A., Fassoulas, C., & Mountrakis, D. (1994). Tertiary extension of continental crust and uplift of Psiloritis metamorphic core complex in the central part of the Hellenic Arc (Crete, Greece). In *Active Continental Margins—Present and Past* (pp. 417-430). Springer, Berlin, Heidelberg.

Koprubasi, N., & Aldanmaz, E. (2004). Geochemical constraints on the petrogenesis of Cenozoic I-type granitoids in Northwest Anatolia, Turkey: evidence for magma generation by lithospheric delamination in a post-collisional setting. *International Geology Review*, *46*(8), 705-729.

Kruhl, J. H., & Peternell, M. (2002). The equilibration of high-angle grain boundaries in dynamically recrystallized quartz: the effect of crystallography and temperature. *Journal of Structural geology*, *24*(6-7), 1125-1137.

Lamont, T. N., Searle, M. P., Waters, D. J., Roberts, N. M., Palin, R. M., Smye, A., ... & St-Onge, M. R. (2020). Compressional origin of the Naxos metamorphic core complex, Greece: Structure, petrography, and thermobarometry. *GSA Bulletin*, *132*(1-2), 149-197.

Langille, J. M., Jessup, M. J., Cottle, J. M., Newell, D., & Seward, G. (2010). Kinematic evolution of the Ama Drime detachment: Insights into orogen-parallel extension and exhumation of the Ama Drime Massif, Tibet–Nepal. *Journal of Structural Geology*, *32*(7), 900-919.

Lee, J., Hacker, B., & Wang, Y. (2004). Evolution of North Himalayan gneiss domes: structural and metamorphic studies in Mabja Dome, southern Tibet. *Journal of Structural Geology*, *26*(12), 2297-2316.

Le Fort, P., Cuney, M., Deniel, C., France-Lanord, C., Sheppard, S. M. F., Upreti, B. N., & Vidal, P. (1987). Crustal generation of the Himalayan leucogranites. *Tectonophysics*, *134*(1-3), 39-57.

Lister, G. S., Banga, G., & Feenstra, A. (1984). Metamorphic core complexes of Cordilleran type in the Cyclades, Aegean Sea, Greece. *Geology*, *12*(4), 221-225.

Lister, G. S., & Baldwin, S. L. (1993). Plutonism and the origin of metamorphic core complexes. *Geology*, *21*(7), 607-610.

Lister, G. S., & Davis, G. A. (1989). The origin of metamorphic core complexes and detachment faults formed during Tertiary continental extension in the northern Colorado River region, USA. *Journal of Structural Geology*, *11*(1-2), 65-94.

Lister, G. S., & Dornsiepen, U. F. (1982). Fabric transitions in the Saxony granulite terrain. *Journal of Structural Geology*, *4*(1), 81-92.

Loos, S., & Reischmann, T. (1999). The evolution of the southern Menderes Massif in SW Turkey as revealed by zircon dating. *Journal of the Geological Society*, *156*(5), 1021-1030.

Lovera, O. M., Richter, F. M., & Harrison, T. M. (1989). The 40Ar/39Ar thermochronometry for slowly cooled samples having a distribution of diffusion domain sizes. *Journal of Geophysical Research: Solid Earth*, *94*(B12), 17917-17935.

Ludwig, K. R. (2003). User's Manual for Isoplot 3.00. Berkeley Geochronology Center Special Publication No. 4. *Berkeley, CA*.

Mainprice, D., Bouchez, J. L., Blumenfeld, P., & Tubià, J. M. (1986). Dominant c slip in naturally deformed quartz: Implications for dramatic plastic softening at high temperature. *Geology*, *14*(10), 819-822.

Matte, P. (2007). Variscan thrust nappes, detachments, and strike-slip faults in the French Massif Central: Interpretation of the lineations. *Geological Society of America Memoirs*, *200*, 391-402.

McClusky, S., Balassanian, S., Barka, A., Demir, C., Ergintav, S., Georgiev, I., ... & Veis, G. (2000). Global Positioning System constraints on plate kinematics and dynamics in the eastern Mediterranean and Caucasus. *Journal of Geophysical Research: Solid Earth*, *105*(B3), 5695-5719.

McDonough, W. S. (1990). Constraints on the composition of the continental lithospheric mantle. *Earth and Planetary Science Letters*, *101*(1), 1-18.

McFadden, R. R., Teyssier, C., Siddoway, C. S., Whitney, D. L., & Fanning, C. M. (2010). Oblique dilation, melt transfer, and gneiss dome emplacement. *Geology*, *38*(4), 375-378.

McKenzie, D. (1972). Active tectonics of the Mediterranean region. *Geophysical Journal International*, *30*(2), 109-185.

McKenzie, D. (1978). Active tectonics of the Alpine—Himalayan belt: the Aegean Sea and surrounding regions. *Geophysical Journal International*, *55*(1), 217-254.

Mehnert, K. R. (1968). Migmatites and the origin of granitic rocks. *Megascopic structures of migmatite*, 7-42. Elsevier, Amsterdam, London.

Montel, J. M. (1993). A model for monazite/melt equilibrium and application to the generation of granitic magmas. *Chemical Geology*, *110*(1-3), 127-146.

Murakami, H., Watanabe, Y., & Stein, H. (2005). Re-Os ages for molybdenite from the Tepeoba breccia-centered Cu-Mo-Au deposit, western Turkey: Brecciation-triggered mineralization. In *Mineral Deposit Research: Meeting the Global Challenge* (pp. 805-808). Springer, Berlin, Heidelberg.

Neves, S. P., Vauchez, A., & Archanjo, C. J. (1996). Shear zone-controlled magma emplacement or magma-assisted nucleation of shear zones? Insights from northeast Brazil. *Tectonophysics*, *262*(1-4), 349-364.

Okay, A. I., & Satir, M. (2000). Coeval plutonism and metamorphism in a latest Oligocene metamorphic core complex in northwest Turkey. *Geological Magazine*, *137*(5), 495-516.

Okay, A. I., Satir, M., Zattin, M., Cavazza, W., & Topuz, G. (2008). An Oligocene ductile strike-slip shear zone: The Uludağ Massif, northwest Turkey—Implications for the westward translation of Anatolia. *Geological Society of America Bulletin*, *120*(7-8), 893-911.

Okay, A. I., Tansel, I., & Tüysüz, O. (2001). Obduction, subduction and collision as reflected in the Upper Cretaceous–Lower Eocene sedimentary record of western Turkey. *Geological Magazine*, *138*(2), 117-142.

Okay, A. I., & Tüysüz, O. (1999). Tethyan sutures of northern Turkey. *Geological Society, London, Special Publications*, *156*(1), 475-515.

Okay, A., I. (1984). The geology of the Ağvanis metamorphic rocks and neighbouring formations. *Bulletin of the Mineral Research and Exploration Institute of Turkey, 99/100*, 16-36.

Oner, Z., & Dilek, Y. (2011). Supradetachment basin evolution during continental extension: The Aegean province of western Anatolia, Turkey. *Bulletin*, *123*(11-12), 2115-2141.

Oner, Z., & Dilek, Y. (2013). Fault kinematics in supradetachment basin formation, Menderes core complex of western Turkey. *Tectonophysics*, *608*, 1394-1412.

Önen, A. P., & Hall, R. (1993). Ophiolites and related metamorphic rocks from the Kütahya region, north-west Turkey. *Geological Journal*, *28*(3-4), 399-412.

Passchier, C. W., & Trouw, R. A. J. (1996). *Microtectonics*, Springer-Verlag, Heidelberg. 289 p.

Passchier, C. W., & Trouw, R. A. J. (2005). *Microtectonics*, Berlin; New York, Springer, xvi, 366 p. p.

Paterson, S. R., & Tobisch, O. T. (1992). Rates of processes in magmatic arcs: implications for the timing and nature of pluton emplacement and wall rock deformation. *Journal of Structural Geology*, *14*(3), 291-300.

Patiño Douce, A. E. (1995). Experimental generation of hybrid silicic melts by reaction of high-Al basalt with metamorphic rocks. *Journal of Geophysical Research: Solid Earth*, *100*(B8), 15623-15639.

Patiño Douce, A. E. (1996). Effects of pressure and H2O content on the compositions of primary crustal melts. *Earth and Environmental Science Transactions of the Royal Society of Edinburgh*, *87*(1-2), 11-21.

Patiño Douce, A. E., & Harris, N. (1998). Experimental constraints on Himalayan anatexis. *Journal of Petrology*, *39*(4), 689-710.

Peccerillo, A., & Taylor, S. R. (1976). Geochemistry of Eocene calc-alkaline volcanic rocks from the Kastamonu area, northern Turkey. *Contributions to mineralogy and petrology*, *58*(1), 63-81.

Pe-Piper, G. (2000). Origin of S-type granites coeval with I-type granites in the Hellenic subduction system, Miocene of Naxos, Greece. *European Journal of Mineralogy*, *12*(4), 859-875.

Pe-Piper, G., & Piper, D. J. (2007). Neogene backarc volcanism of the Aegean: new insights into the relationship between magmatism and tectonics. *Special Papers-Geological Society of America*, *418*, 17.

Le Pichon, X., & Angelier, J. (1979). The Hellenic arc and trench system: a key to the neotectonic evolution of the eastern Mediterranean area. *Tectonophysics*, *60*(1-2), 1-42.

Plissart, G., Diot, H., Monnier, C., Mărunţiu, M., & Berger, J. (2012). Relationship between a syntectonic granitic intrusion and a shear zone in the Southern Carpathian-Balkan area (Almăj Mountains, Romania): implications for late Variscan kinematics and Cherbelezu granitoid emplacement. *Journal of structural geology*, *39*, 83-102.

Plunder, A., Agard, P., Chopin, C., Pourteau, A., & Okay, A. I. (2015). Accretion, underplating and exhumation along a subduction interface: From subduction initiation to continental subduction (Tavşanlı zone, W. Turkey). *Lithos*, *226*, 233-254.

Pourteau, A., Candan, O., & Oberhänsli, R. (2010). High‐pressure metasediments in central Turkey: Constraints on the Neotethyan closure history. *Tectonics*, *29*(5).

Powell, M., & Powell, R. (1977). Plagioclase-alkali-feldspar geothermometry revisited. *Mineralogical Magazine*, *41*(318), 253-256.

Pryer, L. L. (1993). Microstructures in feldspars from a major crustal thrust zone: the Grenville Front, Ontario, Canada. *Journal of structural Geology*, *15*(1), 21-36.

Pryer, L. L., & Robin, P. Y. (1996). Differential stress control on the growth and orientation of flame perthite: a palaeostress-direction indicator. *Journal of Structural Geology*, *18*(9), 1151-1166.

Putirka, K. D. (2008). Thermometers and barometers for volcanic systems. *Reviews in mineralogy and geochemistry*, *69*(1), 61-120.

Rabillard, A., Jolivet, L., Arbaret, L., Bessière, E., Laurent, V., Menant, A., ... & Beaudoin, A. (2018). Synextensional granitoids and detachment systems within Cycladic metamorphic core complexes (Aegean Sea, Greece): Toward a regional tectonomagmatic model. *Tectonics*, *37*(8), 2328-2362.

Ramberg, H. (1981). *Gravity, deformation, and the earth's crust: In theory, experiments, and geological application*. Academic press, New York, 452 pp.

Ramsay, J. G. (1989). Emplacement kinematics of a granite diapir: the Chindamora batholith, Zimbabwe. *Journal of Structural Geology*, *11*(1-2), 191-209.

Renne, P. R., Swisher, C. C., Deino, A. L., Karner, D. B., Owens, T. L., & DePaolo, D. J. (1998). Intercalibration of standards, absolute ages and uncertainties in 40Ar/39Ar dating. *Chemical Geology*, *145*(1-2), 117-152.

Rey, P. F., Teyssier, C., Kruckenberg, S. C., & Whitney, D. L. (2011). Viscous collision in channel explains double domes in metamorphic core complexes. *Geology*, *39*(4), 387-390.

Rey, P. F., Teyssier, C., & Whitney, D. L. (2009). Extension rates, crustal melting, and core complex dynamics. *Geology*, *37*(5), 391-394.

Rey, P., Vanderhaeghe, O., & Teyssier, C. (2001). Gravitational collapse of the continental crust: definition, regimes and modes. *Tectonophysics*, *342*(3-4), 435-449.

Ring, U., & Collins, A. S. (2005). U–Pb SIMS dating of synkinematic granites: timing of core-complex formation in the northern Anatolide belt of western Turkey. *Journal of the Geological Society*, *162*(2), 289-298.

Ring, U. W. E., Johnson, C., Hetzel, R., & Gessner, K. (2003). Tectonic denudation of a Late Cretaceous–Tertiary collisional belt: regionally symmetric cooling patterns and their relation to extensional faults in the Anatolide belt of western Turkey. *Geological Magazine*, *140*(4), 421-441.

Rudnick, R. L., & Gao, S. (2003). Composition of the Continental Crust. *In Treatise on Geochemistry*: *Second Edition*.

Sawyer, E. W. (2010). Migmatites formed by water-fluxed partial melting of a leucogranodiorite protolith: Microstructures in the residual rocks and source of the fluid. *Lithos*, *116*(3-4), 273-286.

Searle, M. P., & Fryer, B. J. (1986). Garnet, tourmaline and muscovite-bearing leucogranites, gneisses and migmatites of the Higher Himalayas from Zanskar, Kulu, Lahoul and Kashmir. *Geological Society, London, Special Publications*, *19*(1), 185-201.

Searle, M. P., & Lamont, T. N. (2020). Compressional metamorphic core complexes, low-angle normal faults and extensional fabrics in compressional tectonic settings. *Geological Magazine*, *157*(1), 101-118.

Searle, M. P., Law, R. D., & Jessup, M. J. (2006). Crustal structure, restoration and evolution of the Greater Himalaya in Nepal-South Tibet: implications for channel flow and ductile extrusion of the middle crust. *Geological Society, London, Special Publications*, *268*(1), 355-378.

Seyítoğlu, G., & Scott, B. C. (1996). The cause of NS extensional tectonics in western Turkey: tectonic escape vs back-arc spreading vs orogenic collapse. *Journal of Geodynamics*, *22*(1-2), 145-153.

Seyitoğlu, G., & Scott, B. (1991). Late Cenozoic crustal extension and basin formation in west Turkey. *Geological Magazine*, *128*(2), 155-166.

Sherlock, S., Kelley, S., Inger, S., Harris, N., & Okay, A. (1999). 40 Ar-39 Ar and Rb-Sr geochronology of high-pressure metamorphism and exhumation history of the Tavsanli Zone, NW Turkey. *Contributions to Mineralogy and Petrology*, *137*(1), 46-58.

Simpson, C. (1985). Deformation of granitic rocks across the brittle-ductile transition. *Journal of structural geology*, *7*(5), 503-511.

Simpson, C., & Wintsch, R. P. (1989). Evidence for deformation-induced K-feldspar replacement by myrmekite. *Journal of Metamorphic Geology*, *7*(2), 261-275.

Sokoutis, D., Brun, J. P., Van Den Driessche, J., & Pavlides, S. (1993). A major Oligo-Miocene detachment in southern Rhodope controlling north Aegean extension. *Journal of the Geological Society*, *150*(2), 243-246.

Stipp, M., Stuènitz, H., Heilbronner, R., & Schmid, S. M. (2002). The eastern Tonale fault zone: a 'natural laboratory'for crystal plastic deformation of quartz over a temperature range from 250 to 700 C. *Journal of structural geology*, *24*(12), 1861-1884.

Stormer Jr, J. C. (1975). A practical two-feldspar geothermometer. *American Mineralogist: Journal of Earth and Planetary Materials*, *60*(7-8), 667-674.

Strachan, R. A., Martin, M. W., & Friderichsen, J. D. (2001). Evidence for contemporaneous yet contrasting styles of granite magmatism during extensional collapse of the northeast Greenland Caledonides. *Tectonics*, *20*(4), 458-473.

Sylvester, P. J. (1998). Post-collisional strongly peraluminous granites. *Lithos*, *45*(1-4), 29-44.

Şengör, A. M. C., Satir, M., & Akkök, R. (1984). Timing of tectonic events in the Menderes Massif, western Turkey: Implications for tectonic evolution and evidence for Pan-African basement in Turkey. *Tectonics*, *3*(7), 693-707.

Şengör, A. M. C., & Yilmaz, Y. (1981). Tethyan evolution of Turkey: a plate tectonic approach. *Tectonophysics*, *75*(3-4), 181-241.

Taymaz, T., Jackson, J., & McKenzie, D. (1991). Active tectonics of the north and central Aegean Sea. *Geophysical Journal International*, *106*(2), 433-490.

Tekeli, O., Işık, V., Seyitoglu, G., & Çemen, I. (2001). The 40Ar/Ar39 age of ductile extension and granitoid intrusions in the northern Menderes massif, western Turkey. 4th Int. *Turkish Geology Sym. Abstract*, *226*.

Teyssier, C., & Whitney, D. L. (2002). Gneiss domes and orogeny. *Geology*, *30*(12), 1139-1142.

Thomson, S. N., & Ring, U. (2006). Thermochronologic evaluation of postcollision extension in the Anatolide orogen, western Turkey. *Tectonics*, *25*(3).

Tirel, C., Brun, J. P., & Burov, E. (2004). Thermomechanical modeling of extensional gneiss domes. *Geologıcal Socıety Of Amerıca Special Papers*, 67-78.

Tirel, C., Brun, J. P., & Burov, E. (2008). Dynamics and structural development of metamorphic core complexes. *Journal of Geophysical Research: Solid Earth*, *113*(B4).

Tirel, C., Brun, J. P., & Sokoutis, D. (2006). Extension of thickened and hot lithospheres: Inferences from laboratory modeling. *Tectonics*, *25*(1).

Tobisch, O. T., Renne, P. R., & Saleeby, J. B. (1993). Deformation resulting from regional extension during pluton ascent and emplacement, central Sierra Nevada, California. *Journal of Structural Geology*, *15*(3-5), 609-628.

Topuz, G., Altherr, R., Siebel, W., Schwarz, W. H., Zack, T., Hasözbek, A., ... & Şen, C. (2010). Carboniferous high-potassium I-type granitoid magmatism in the Eastern Pontides: the Gümüşhane pluton (NE Turkey). *Lithos*, *116*(1-2), 92-110.

Topuz, G., & Okay, A. I. (2017). Late Eocene–Early Oligocene two-mica granites in NW Turkey (the Uludağ Massif): water-fluxed melting products of a mafic metagreywacke. *Lithos*, *268*, 334-350.

Ünal, A., Kamaci, Ö., Yildiz, M., Atabek, G., & Altunkaynak, Ş. (2012). Volcanic stratigraphy and petrology of Susurluk Volcanites (NW Turkey). *International Multidisciplinary Scientific GeoConference: SGEM*, *1*, 391.

Ünal, A., & Altunkaynak, Ş. (2018). Nature and genesis of potassic high BaSr granitoids associated with syn-convergent extension in NW Turkey. *Lithos*, *316*, 261-277.

van Hinsbergen, D. J. (2010). A key extensional metamorphic complex reviewed and restored: the Menderes Massif of western Turkey. *Earth-Science Reviews*, *102*(1-2), 60-76.

Vandenberg, L. C., & Lister, G. S. (1996). Structural analysis of basement tectonites from the Aegean metamorphic core complex of Ios, Cyclades, Greece. *Journal of Structural Geology*, *18*(12), 1437-1454.

Vanderhaeghe, O. (1999). Pervasive melt migration from migmatites to leucogranite in the Shuswap metamorphic core complex, Canada: control of regional deformation. *Tectonophysics*, *312*(1), 35-55.

Vanderhaeghe, O. (2009). Migmatites, granites and orogeny: Flow modes of partially-molten rocks and magmas associated with melt/solid segregation in orogenic belts. *Tectonophysics*, *477*(3-4), 119-134.

Vanderhaeghe, O., Kruckenberg, S. C., Gerbault, M., Martin, L., Duchêne, S., & Deloule, E. (2018). Crustal-scale convection and diapiric upwelling of a partially molten orogenic root (Naxos dome, Greece). *Tectonophysics*, *746*, 459-469.

Vanderhaeghe, O., Teyssier, C., & Wysoczanski, R. (1999). Structural and geochronological constraints on the role of partial melting during the formation of the Shuswap metamorphic core complex at the latitude of the Thor-Odin dome, British Columbia. *Canadian Journal of Earth Sciences*, *36*(6), 917-943.

Vanderhaeghe, O. (2001). Melt segragation, pervasive melt migration and magma mobility in the continental crust: the structural record from pores to orogens. *Physics and Chemistry of the Earth, Part A: Solid Earth and Geodesy*, *26*(4-5), 213-223.

Vanderhaeghe, O., & Teyssier, C. (2001). Crustal-scale rheological transitions during late-orogenic collapse. *Tectonophysics*, *335*(1-2), 211-228.

Vanderhaeghe, O., Whitney, D. L., Teyssier, C., & Siddoway, C. S. (2004). Structural development of the Naxos migmatite dome. *Special Papers-Geological Society Of America*, 211-228.

Vanderhaeghe, O., & Duchêne, S. (2010). Crustal-scale mass transfer, geotherm and topography at convergent plate boundaries. *Terra Nova*, *22*(5), 315-323.

Vernon, R. H. (1991). Questions about myrmekite in deformed rocks. *Journal of Structural Geology*, *13*(9), 979-985.

Vernon, R.H. (2004). *A practical guide to rock microstructure*. Cambridge university press.

Vernon, R. H., Williams, V. A., & D'arcy, W. F. (1983). Grain-size reduction and foliation development in a deformed granitoid batholith. *Tectonophysics*, *92*(1-3), 123-145.

Villaseca, C., Barbero, L., & Herreros, V. (1998). A re-examination of the typology of peraluminous granite types in intracontinental orogenic belts. *Earth and Environmental Science Transactions of The Royal Society of Edinburgh*, *89*(2), 113-119.

Weinberg, R. F., & Hasalová, P. (2015). Water-fluxed melting of the continental crust: A review. *Lithos*, *212*, 158-188.

Wernicke, B. (1981). Low-angle normal faults in the Basin and Range Province: nappe tectonics in an extending orogen. *Nature*, *291*(5817), 645-648.

Wernicke, B. (1985). Uniform-sense normal simple shear of the continental lithosphere. *Canadian Journal of earth sciences*, *22*(1), 108-125.

Wernicke, B., & Axen, G. J. (1988). On the role of isostasy in the evolution of normal fault systems. *Geology*, *16*(9), 848-851.

Whitney, D. L., Teyssier, C., & Heizler, M. T. (2007). Gneiss domes, metamorphic core complexes, and wrench zones: Thermal and structural evolution of the Niğde Massif, central Anatolia. *Tectonics*, *26*(5).

Whitney, D. L., Teyssier, C., Rey, P., & Buck, W. R. (2013). Continental and oceanic core complexes. *Bulletin*, *125*(3-4), 273-298.

Whitney, D. L., Teyssier, C., & Vanderhaeghe, O. (2004). Gneiss domes and crustalflow. *Gneiss domes in orogeny*, *380*, 15.

Whitney, J. A., & Stormer, J. C. (1977). Two-feldspar geothermometry, geobarometry in mesozonal granitic intrusions: three examples from the Piedmont of Georgia. *Contributions to Mineralogy and Petrology*, *63*(1), 51-64.

Yang, J. H., Chung, S. L., Zhai, M. G., & Zhou, X. H. (2004). Geochemical and Sr–Nd–Pb isotopic compositions of mafic dikes from the Jiaodong Peninsula, China: evidence for vein-plus-peridotite melting in the lithospheric mantle. *Lithos*, *73*(3-4), 145-160.

Yılmaz, Y. (1997). Geology of Western Anatolia. Active tectonic of northwestern Anatolia. *The Marmara Poly-Project, a Multidisciplinary Approach by Space-Geodesy, Geology, Hydrogeology, Geothermics and Seismology*, 31-35.

Yılmaz, Y. (1989). An approach to the origin of young volcanic rocks of western Turkey. In *Tectonic evolution of the Tethyan region* (pp. 159-189). Springer, Dordrecht.

Yılmaz, Y. (1990). Comparison of young volcanic associations of western and eastern Anatolia formed under a compressional regime: a review. *Journal of Volcanology and Geothermal Research*, *44*(1-2), 69-87.

Yılmaz, Y., Genç, Ş. C., Gürer, F., Bozcu, M., Yilmaz, K., Karacik, Z., ... & Elmas, A. (2000). When did the western Anatolian grabens begin to develop? *Geological Society, London, Special Publications*, *173*(1), 353-384.

Yılmaz, Y. (2017). Major Problems of Western Anatolian Geology. *Active Global Seismology*, 141-187.

Yin, A. (1991). Mechanisms for the formation of domal and basinal detachment faults: A three-dimensional analysis. *Journal of Geophysical Research: Solid Earth*, *96*(B9), 14577-14594.

Yurdagül, A. (2004). Lithogeochemical Investigation of the Uludağ Granitoide. *Unpublished MSc thesis. Istanbul University, Institute of Science. 140p*.

Zhu Yuan-Qing, & Shi Yao-Lin (1990). Shear heating and partial melting of granite - thermal structure at overthrusted terrains in the Greater Himalaya. *Chinese Journal of Geophysics*, 04.

Zlatkin, O., Avigad, D., & Gerdes, A. (2013). Evolution and provenance of Neoproterozoic basement and Lower Paleozoic siliciclastic cover of the Menderes Massif (western Taurides): coupled U–Pb–Hf zircon isotope geochemistry. *Gondwana Research*, *23*(2), 682-700.

APPENDICES

Table A.1 : U/Pb LAICPMS age data of the CPC.
Table A.2 : $^{40}Ar/^{39}Ar$ ages obtained from the CPC.

Table A.1 : U/Pb LAICPMS age data of the CPC.

LA–ICP–MS zircon radiometric age determination of sample SA1

Spot	$^{206}Pb/^{238}U$	1 Sigma	$^{207}Pb/^{235}U$	1 Sigma	$^{208}Pb/^{232}Th$	1 Sigma	$^{207}Pb/^{206}Pb$	1 Sigma	Age, Ma $^{206}Pb/^{238}U$	1 Sigma
1r	0.00499	0.0001	0.0322	0.0029	0.00214	0.0003	0.04677	0.0043	32.1	0.66
1c	0.15479	0.0019	1.50848	0.0406	0.0469	0.0028	0.07068	0.0019	927.8	10.51
2r	0.00499	0.0001	0.04281	0.0033	0.02299	0.0033	0.06216	0.0049	32.1	0.66
2c	0.04815	0.0008	0.39383	0.0236	0.02249	0.0018	0.05932	0.0036	303.1	4.99
3r	0.005	6E-05	0.03231	0.0012	0.00235	0.0002	0.04686	0.0017	32.2	0.4
3c	0.08722	0.001	0.72829	0.0187	0.02945	0.0019	0.06055	0.0016	539.1	6.09
4	0.00508	6E-05	0.04182	0.0013	0.00426	0.0003	0.05971	0.002	32.7	0.41
5r	0.00496	6E-05	0.03224	0.0012	0.00207	0.0002	0.04716	0.0019	31.9	0.41
5c	0.00507	0.0001	0.04281	0.0036	0.0023	0.0003	0.06125	0.0053	32.6	0.72
6r	0.00502	7E-05	0.03883	0.0014	0.01297	0.0013	0.05612	0.0021	32.3	0.42
7r	0.00512	9E-05	0.03497	0.0022	0.00294	0.0004	0.04955	0.0031	32.9	0.56
7c	0.04966	0.0011	0.3611	0.0352	0.02781	0.003	0.05273	0.0052	312.4	6.84
8c	0.07113	0.0011	0.53793	0.0292	0.02986	0.003	0.05485	0.003	443	6.76
8r	0.00506	7E-05	0.03842	0.0014	0.00742	0.0008	0.05511	0.0021	32.5	0.43
9r	0.0051	8E-05	0.04661	0.0021	0.02196	0.0025	0.06623	0.003	32.8	0.49
10r	0.00799	0.0001	0.05664	0.0027	0.00533	0.0006	0.05144	0.0025	51.3	0.76
11r	0.00486	7E-05	0.03822	0.0018	0.01018	0.0009	0.05704	0.0028	31.3	0.46
11c	0.04475	0.0005	0.37014	0.0095	0.01839	0.0014	0.05999	0.0016	282.2	3.23
12c	0.08576	0.0012	0.89753	0.0309	0.05189	0.0037	0.07591	0.0027	530.4	6.87
13r	0.0234	0.0003	0.15997	0.0044	0.01139	0.0012	0.04959	0.0014	149.1	1.73
14r	0.00597	9E-05	0.16259	0.0053	0.04987	0.0036	0.19757	0.0068	38.4	0.6
14c	0.01295	0.0003	0.6599	0.0279	0.01999	0.0015	0.36956	0.0173	83	1.86
15r	0.00494	7E-05	0.03271	0.0014	0.00171	0.0003	0.04802	0.0022	31.8	0.44

Table A.1 (continued) : U/Pb LAICPMS age data of the CPC.

Spot	$^{206}Pb/^{238}U$	1 Sigma	$^{207}Pb/^{235}U$	1 Sigma	$^{208}Pb/^{232}Th$	1 Sigma	$^{207}Pb/^{206}Pb$	1 Sigma	Age, Ma $^{206}Pb/^{238}U$	1 Sigma
15c	0.00505	0.0001	0.04572	0.0047	0.00449	0.0007	0.06561	0.0069	32.5	0.86
16r	0.00495	7E-05	0.0329	0.0015	0.00839	0.001	0.04821	0.0023	31.8	0.45
17r	0.00473	8E-05	0.03483	0.0023	0.00914	0.0014	0.05338	0.0036	30.4	0.54
18c	0.30158	0.0036	6.72922	0.1706	0.09812	0.0082	0.16184	0.0042	1699.1	17.63
18r	0.00583	0.0001	0.05297	0.0033	0.00365	0.0006	0.06584	0.0042	37.5	0.67
19c	0.08576	0.0012	0.93112	0.0348	0.03967	0.004	0.07875	0.003	530.4	7.18
19r	0.00511	9E-05	0.04529	0.0026	0.00573	0.0007	0.06432	0.0038	32.8	0.57
21r1	0.00518	7E-05	0.03326	0.0013	0.00221	0.0003	0.04655	0.0019	33.3	0.45
21r2	0.11821	0.0017	1.15861	0.0453	0.04989	0.0054	0.07109	0.0028	720.2	9.71
21c	0.14077	0.0018	1.4072	0.0441	0.04836	0.0048	0.07251	0.0023	849	10.09
20r	0.00504	6E-05	0.03675	0.0011	0.00578	0.0005	0.05288	0.0016	32.4	0.39
23r	0.00523	8E-05	0.03892	0.0018	0.0148	0.0015	0.05399	0.0026	33.6	0.49
24r	0.00497	7E-05	0.03281	0.0015	0.00462	0.0007	0.04785	0.0023	32	0.45
25c	0.12022	0.002	1.05509	0.0551	0.04347	0.0031	0.06365	0.0034	731.8	11.44
25r	0.00782	0.0002	0.05993	0.0043	0.00067	0.002	0.0556	0.0041	50.2	0.93
26r	0.00503	9E-05	0.03251	0.0023	0.00698	0.0016	0.04686	0.0033	32.4	0.57
26c	0.00499	7E-05	0.03291	0.0013	0.00318	0.0003	0.04788	0.002	32.1	0.43
28r	0.00507	8E-05	0.03257	0.0017	0.00194	0.0002	0.04657	0.0025	32.6	0.48
29r	0.00493	8E-05	0.03153	0.0017	0.0021	0.0009	0.04643	0.0026	31.7	0.48
29c	0.00503	9E-05	0.05197	0.0033	0.00494	0.0005	0.07489	0.0049	32.4	0.6
30c	0.11992	0.0021	1.07056	0.0609	0.0414	0.0037	0.06475	0.0038	730.1	11.92
30r	0.0072	0.0001	0.04652	0.0033	0.00126	0.0006	0.04689	0.0034	46.2	0.81

Table A.1 (continued) : U/Pb LAICPMS age data of the CPC.

LA–ICP–MS zircon radiometric age determination of sample SA2

Spot	$^{206}Pb/^{238}U$	1 Sigma	$^{207}Pb/^{235}U$	1 Sigma	$^{208}Pb/^{232}Th$	1 Sigma	$^{207}Pb/^{206}Pb$	1 Sigma	Age, Ma $^{206}Pb/^{238}U$	1 Sigma
1r	0.00538	0.00006	0.03654	0.00107	0.00206	0.00013	0.04924	0.00147	34.6	0.41
2r	0.06663	0.00086	0.59767	0.01985	0.02428	0.0013	0.06506	0.00221	415.8	5.21
2c	0.0053	0.00007	0.03773	0.00129	0.00281	0.0004	0.0516	0.0018	34.1	0.42
3	0.0055	0.00012	0.03554	0.00332	0.00156	0.00062	0.04684	0.00446	35.4	0.75
4r	0.00549	0.00013	0.03603	0.00433	0.00231	0.00033	0.04756	0.0058	35.3	0.85
4r	0.00531	0.00006	0.06376	0.00167	0.009	0.0005	0.08705	0.00233	34.2	0.41
4c	0.24849	0.00281	5.67676	0.1167	0.07505	0.00418	0.16567	0.00346	1430.7	14.51
5c	0.07338	0.00085	0.5959	0.01463	0.02339	0.00161	0.05889	0.00147	456.5	5.11
6r	0.00535	0.00007	0.0422	0.00168	0.00699	0.00058	0.05724	0.00233	34.4	0.47
6c	0.00636	0.00015	0.05865	0.00562	0.00298	0.00155	0.06682	0.00656	40.9	0.98
7r	0.00535	0.00008	0.03927	0.00192	0.00888	0.00101	0.05322	0.00265	34.4	0.51
7c	0.07421	0.00098	0.5976	0.02142	0.02337	0.00175	0.0584	0.00213	461.5	5.88
8	0.04877	0.00066	0.39024	0.015	0.0237	0.00263	0.05802	0.00227	307	4.08
9c	0.31196	0.00397	5.48444	0.15315	0.08643	0.00649	0.12749	0.00361	1750.3	19.5
9r	0.00536	0.00008	0.03469	0.00199	0.0036	0.00059	0.04694	0.00275	34.5	0.54
10	0.0054	0.00014	0.03622	0.00518	0.00165	0.00038	0.04867	0.00706	34.7	0.93
11r	0.00498	0.00008	0.03387	0.00176	0.0043	0.00053	0.0493	0.00262	32	0.49
11c	0.00529	0.00009	0.03433	0.00272	0.00184	0.00022	0.04707	0.00378	34	0.6
13r	0.00506	0.00006	0.03446	0.00107	0.00259	0.00023	0.04938	0.00156	32.5	0.4
13c	0.03814	0.00064	0.29061	0.01724	0.0214	0.00168	0.05526	0.00336	241.3	3.99
14r	0.00515	0.00008	0.03772	0.0018	0.00517	0.00074	0.05314	0.00261	33.1	0.49
14c	0.01641	0.00041	0.10631	0.0134	0.00057	0.00086	0.04699	0.00602	104.9	2.59

Table A.1 (continued) : U/Pb LAICPMS age data of the CPC.

Spot	$^{206}Pb/^{238}U$	1 Sigma	$^{207}Pb/^{235}U$	1 Sigma	$^{208}Pb/^{232}Th$	1 Sigma	$^{207}Pb/^{206}Pb$	1 Sigma	Age, Ma $^{206}Pb/^{238}U$	1 Sigma
17r	0.00518	0.00008	0.03373	0.00179	0.00209	0.00039	0.04721	0.00255	33.3	0.51
17c	0.00521	0.0001	0.03349	0.00314	0.00138	0.00051	0.04666	0.00445	33.5	0.66
16r	0.00522	0.00009	0.03995	0.00242	0.01045	0.00128	0.05554	0.00345	33.5	0.58
16c	0.0069	0.0002	0.04507	0.00624	0.00154	0.00067	0.04737	0.00668	44.3	1.27
15	0.04989	0.00068	0.45205	0.01615	0.02239	0.00128	0.06571	0.0024	313.9	4.16
18r	0.00514	0.00007	0.03337	0.00153	0.00244	0.00039	0.0471	0.0022	33	0.46
18c	0.01711	0.00033	0.13989	0.01018	0.01656	0.00138	0.05928	0.00441	109.4	2.09
19r	0.00518	0.00008	0.04499	0.0022	0.0048	0.00058	0.06293	0.00316	33.3	0.52
19c	0.39834	0.0046	8.99838	0.20809	0.10398	0.00713	0.16382	0.00385	2161.4	21.21
19c2	0.00733	0.00025	0.07591	0.01031	0.00257	0.00418	0.07515	0.01048	47.1	1.6
20c	0.00664	0.00019	0.06211	0.00792	0.00381	0.00138	0.06787	0.00883	42.6	1.2
21r	0.00523	0.00008	0.05561	0.00253	0.01686	0.00161	0.07705	0.00362	33.7	0.53
21c	0.00515	0.0001	0.03326	0.00277	0.00149	0.00017	0.04685	0.00396	33.1	0.62
22c	0.09822	0.00161	0.81209	0.04568	0.03081	0.00279	0.05996	0.00344	604	9.45
23r	0.00512	0.00009	0.03352	0.00225	0.00197	0.00064	0.04751	0.00327	32.9	0.58
23c	0.02898	0.0004	0.24435	0.00989	0.01276	0.00124	0.06116	0.00254	184.1	2.53
24r	0.00519	0.00007	0.0349	0.00158	0.00229	0.00035	0.0488	0.00225	33.3	0.47
24c	0.00533	0.00016	0.03569	0.0052	0.00147	0.00048	0.04855	0.0072	34.3	1
25c	0.01285	0.00024	0.12391	0.0079	0.02622	0.00239	0.06996	0.00458	82.3	1.51
26c	0.00514	0.00013	0.03305	0.00431	0.0016	0.00036	0.04665	0.00618	33	0.84
27c	0.11215	0.00154	1.01843	0.03738	0.0383	0.0033	0.06585	0.00246	685.2	8.9
27r	0.00802	0.00012	0.06377	0.00298	0.00567	0.00062	0.05764	0.00275	51.5	0.77
25r	0.0053	0.00008	0.03473	0.00186	0.00304	0.00068	0.0475	0.00259	34.1	0.52

Table A.1 (continued) : U/Pb LAICPMS age data of the CPC.

LA–ICP–MS zircon radiometric age determination of sample SA3

Spot	$^{206}Pb/^{238}U$	1 Sigma	$^{207}Pb/^{235}U$	1 Sigma	$^{208}Pb/^{232}Th$	1 Sigma	$^{207}Pb/^{206}Pb$	1 Sigma	Age, Ma $^{206}Pb/^{238}U$	1 Sigma
1r	0.00399	0.00007	0.02804	0.00195	0.00753	0.00171	0.05099	0.00363	25.7	0.46
2r	0.00467	0.00006	0.03745	0.00133	0.00603	0.00045	0.05817	0.00211	30	0.4
2c	0.01009	0.00017	0.06978	0.00447	0.00495	0.00116	0.05016	0.00327	64.7	1.07
3	0.00524	0.00012	0.03759	0.00433	0.00149	0.00037	0.05203	0.00609	33.7	0.79
4r	0.0044	0.00006	0.02945	0.00109	0.00334	0.00065	0.04855	0.00182	28.3	0.37
5	0.00498	0.00008	0.0351	0.00191	0.00172	0.00014	0.05111	0.00284	32	0.52
6	0.00877	0.00238	1.71385	0.3177	0.05345	0.01196	1.41638	0.46489	56.3	15.23
7r	0.00523	0.00007	0.03384	0.00152	0.00197	0.00022	0.04692	0.00214	33.6	0.47
7c	0.0052	0.00009	0.03694	0.00236	0.00177	0.00014	0.0515	0.00336	33.4	0.59
8c	0.0053	0.00014	0.03353	0.00417	0.00157	0.00029	0.04585	0.0058	34.1	0.87
9r	0.00524	0.00007	0.03909	0.00129	0.00528	0.00041	0.0541	0.00183	33.7	0.43
9c	0.08745	0.00113	0.70524	0.02266	0.02735	0.0016	0.05846	0.00192	540.5	6.69
10r	0.00532	0.00009	0.03475	0.00223	0.00634	0.00104	0.04735	0.0031	34.2	0.56
10c	0.04819	0.00087	0.39332	0.02527	0.01945	0.0013	0.05917	0.00389	303.4	5.36
11r	0.00505	0.00007	0.03256	0.00129	0.00223	0.00037	0.04673	0.00189	32.5	0.43
11c1	0.00546	0.0001	0.03534	0.00282	0.00291	0.00037	0.04692	0.00382	35.1	0.66
11c2	0.00535	0.00009	0.0426	0.00253	0.00222	0.00034	0.05771	0.00352	34.4	0.59
12r	0.0052	0.00007	0.0688	0.00245	0.02809	0.00209	0.09597	0.00356	33.4	0.47
13r	0.00524	0.00011	0.04296	0.00334	0.01023	0.00159	0.05944	0.00474	33.7	0.68
14r	0.00522	0.00009	0.11605	0.00469	0.12272	0.0097	0.16111	0.00692	33.6	0.58
13c	0.38923	0.00482	8.91671	0.24045	0.10498	0.0079	0.16612	0.00467	2119.2	22.35
14c	0.069	0.00124	0.57502	0.03834	0.03841	0.00326	0.06044	0.00413	430.1	7.51

Table A.1 (continued) : U/Pb LAICPMS age data of the CPC.

LA–ICP–MS monazite radiometric age determination of sample SA3

Spot	$^{206}Pb/^{238}U$	1 Sigma	$^{207}Pb/^{235}U$	1 Sigma	$^{208}Pb/^{232}Th$	1 Sigma	$^{207}Pb/^{206}Pb$	1 Sigma	Age, Ma $^{206}Pb/^{238}U$	1 Sigma
mz1	0.00467	0.00006	0.0387	0.00101	0.00119	0.00006	0.06015	0.0016	30	0.36
mz2	0.0047	0.00007	0.05514	0.00204	0.00114	0.00006	0.08514	0.00324	30.2	0.44
mz3	0.0047	0.00006	0.03528	0.00096	0.00123	0.00008	0.05449	0.0015	30.2	0.37
mz4	0.00471	0.00006	0.04193	0.00132	0.00126	0.00008	0.0646	0.00207	30.3	0.39
mz6	0.00467	0.00006	0.03588	0.00108	0.00125	0.00008	0.05571	0.0017	30	0.38
mz7	0.0047	0.00006	0.03383	0.00092	0.00126	0.00009	0.05222	0.00144	30.2	0.37
mz11	0.00473	0.00008	0.06512	0.0027	0.00123	0.00009	0.09992	0.00429	30.4	0.49
mz12	0.00468	0.00006	0.03234	0.00121	0.00127	0.00009	0.05014	0.0019	30.1	0.41
mz13	0.00468	0.00006	0.04881	0.00154	0.00124	0.0001	0.07566	0.00243	30.1	0.39
mz16	0.00467	0.00006	0.0362	0.00115	0.00126	0.0001	0.05624	0.0018	30	0.38
mz18	0.00468	0.00006	0.03616	0.00112	0.00118	0.0001	0.05607	0.00176	30.1	0.38

Table A.2 : $^{40}Ar/^{39}Ar$ ages obtained from the CPC.

Single crystal Total Fusion Ar/Ar dating of the sample OS-55 of ÇG (mineral: biotite; N: 18).

Sample	P	t	40 V		39 V		38 V		37 V		36 V		Moles 40Ar*	%Rad	R	Age (Ma)		%-sd
a	1.8	15	2.907	± 0.00176	1.524	± 0.00148	0.02027	± 0.00022	0.03442	± 0.00026	0.000616	± 0.00002	2.04E-14	93.84%	1.7892	20.82	± 0.05	0.22%
b	1.8	15	1.817	± 0.00106	0.953	± 0.00105	0.01234	± 0.00014	0.01813	± 0.00031	0.000395	± 0.00002	1.27E-14	93.65%	1.7847	20.77	± 0.07	0.34%
c	1.8	15	2.145	± 0.00206	1.094	± 0.00152	0.01432	± 0.00016	0.04295	± 0.00055	0.000611	± 0.00002	1.50E-14	91.74%	1.7987	20.93	± 0.06	0.29%
d	1.8	15	1.027	± 0.00108	0.537	± 0.00053	0.00680	± 0.00009	0.00589	± 0.00016	0.000225	± 0.00002	7.19E-15	93.59%	1.7907	20.84	± 0.13	0.62%
e	1.8	15	2.533	± 0.00203	1.322	± 0.00143	0.01710	± 0.00021	0.04361	± 0.00045	0.000597	± 0.00002	1.77E-14	93.18%	1.7856	20.78	± 0.06	0.30%
f	1.8	15	1.560	± 0.00190	0.815	± 0.00093	0.01064	± 0.00013	0.01106	± 0.00019	0.000364	± 0.00002	1.09E-14	93.17%	1.7842	20.76	± 0.08	0.37%
g	1.8	15	1.653	± 0.00139	0.869	± 0.00148	0.01133	± 0.00013	0.01223	± 0.00032	0.000360	± 0.00002	1.16E-14	93.63%	1.7807	20.72	± 0.09	0.46%
h	1.8	15	2.552	± 0.00170	1.347	± 0.00099	0.01740	± 0.00018	0.04497	± 0.00030	0.000444	± 0.00002	1.79E-14	95.01%	1.8001	20.94	± 0.05	0.26%
i	1.8	15	1.727	± 0.00269	0.907	± 0.00143	0.01181	± 0.00016	0.04430	± 0.00077	0.000350	± 0.00002	1.21E-14	94.22%	1.7943	20.88	± 0.09	0.43%
j	1.8	15	1.206	± 0.00121	0.620	± 0.00083	0.00778	± 0.00008	0.00566	± 0.00018	0.000320	± 0.00002	8.45E-15	92.21%	1.7935	20.87	± 0.11	0.52%
k	1.8	15	1.808	± 0.00184	0.925	± 0.00083	0.01199	± 0.00015	0.01750	± 0.00024	0.000551	± 0.00002	1.27E-14	91.07%	1.7800	20.71	± 0.08	0.36%
l	1.8	15	1.212	± 0.00133	0.638	± 0.00077	0.00841	± 0.00014	0.00590	± 0.00020	0.000272	± 0.00002	8.49E-15	93.42%	1.7731	20.63	± 0.10	0.49%
m	1.8	15	0.806	± 0.00084	0.403	± 0.00101	0.00514	± 0.00005	0.01672	± 0.00025	0.000296	± 0.00002	5.65E-15	89.30%	1.7853	20.77	± 0.16	0.79%
n	1.8	15	2.503	± 0.00163	1.319	± 0.00111	0.01700	± 0.00010	0.03304	± 0.00023	0.000457	± 0.00002	1.75E-14	94.71%	1.7977	20.92	± 0.06	0.29%
o	1.8	15	1.974	± 0.00211	1.023	± 0.00101	0.01323	± 0.00015	0.00450	± 0.00014	0.000484	± 0.00002	1.38E-14	92.77%	1.7896	20.82	± 0.08	0.40%
p	1.8	15	0.602	± 0.00122	0.309	± 0.00046	0.00392	± 0.00010	0.00295	± 0.00011	0.000164	± 0.00003	4.21E-15	91.98%	1.7919	20.85	± 0.34	1.63%
q	1.8	15	5.176	± 0.00208	2.720	± 0.00139	0.03543	± 0.00017	0.02401	± 0.00029	0.001052	± 0.00002	3.63E-14	94.03%	1.7899	20.83	± 0.03	0.14%
r	1.8	15	3.616	± 0.00451	1.809	± 0.00227	0.02394	± 0.00018	0.12579	± 0.00135	0.001250	± 0.00002	2.53E-14	90.07%	1.8008	20.95	± 0.06	0.28%

Table A.2 (continued) : $^{40}Ar/^{39}Ar$ ages obtained from the CPC.

Single crystal incremental heating Ar/Ar dating of the sample OS-55 of ÇG (mineral: biotite).

Steps	P	t	40 V		39 V		38 V		37 V		36 V		Moles 40Ar*	%Rad	R	Age (Ma)		%-sd
1	0.48	20	0.144	± 0.00048	0.016	± 0.00015	0.00028	± 0.00005	0.00057	± 0.00016	0.000363	± 0.00002	1.01E-15	25.85%	2.3617	27.43	± 3.86	14.06%
2	0.52	15	0.160	± 0.00047	0.034	± 0.00016	0.00046	± 0.00004	0.00106	± 0.00017	0.000343	± 0.00002	1.12E-15	36.54%	1.7151	19.96	± 1.96	9.81%
3	0.56	15	0.096	± 0.00055	0.035	± 0.00014	0.00044	± 0.00006	0.00037	± 0.00020	0.000109	± 0.00002	6.69E-16	66.29%	1.7916	20.85	± 1.78	8.53%
4	0.6	15	0.797	± 0.00099	0.394	± 0.00043	0.00517	± 0.00010	0.00799	± 0.00017	0.000334	± 0.00002	5.58E-15	87.70%	1.7746	20.65	± 0.15	0.71%
5	0.65	15	0.615	± 0.00072	0.336	± 0.00080	0.00408	± 0.00005	0.02148	± 0.00043	0.000070	± 0.00002	4.31E-15	96.94%	1.7768	20.67	± 0.18	0.88%
6	0.72	15	0.595	± 0.00058	0.319	± 0.00075	0.00401	± 0.00006	0.09705	± 0.00092	0.000106	± 0.00002	4.17E-15	96.08%	1.7943	20.88	± 0.20	0.97%
7	0.8	15	0.700	± 0.00117	0.384	± 0.00115	0.00488	± 0.00008	0.03498	± 0.00028	0.000038	± 0.00002	4.90E-15	98.79%	1.8026	20.97	± 0.16	0.74%
8	0.9	15	0.727	± 0.00113	0.397	± 0.00066	0.00522	± 0.00014	0.00784	± 0.00026	0.000043	± 0.00001	5.09E-15	98.34%	1.7984	20.92	± 0.13	0.64%
9	1	15	0.631	± 0.00073	0.347	± 0.00092	0.00437	± 0.00006	0.00948	± 0.00011	0.000022	± 0.00002	4.42E-15	99.08%	1.8011	20.96	± 0.20	0.95%
10	1.1	15	0.615	± 0.00104	0.337	± 0.00035	0.00419	± 0.00005	0.03509	± 0.00061	0.000054	± 0.00002	4.30E-15	97.89%	1.7870	20.79	± 0.19	0.90%
11	1.2	15	0.094	± 0.00039	0.050	± 0.00015	0.00059	± 0.00004	0.03005	± 0.00048	0.000015	± 0.00002	6.60E-16	97.99%	1.8420	21.43	± 1.20	5.61%

P: % power of 60 W (60 W *(P/10) Synrad CO2 laser); t: laser duration time; V: volt; %Rad: % radiogenic argon; R: 40Ar*/39Ar (Ar*: radiogenic argon); J value: 0.0064870 ± 0.000011 (1σ).

Table A.2 (continued) : $^{40}Ar/^{39}Ar$ ages obtained from the CPC.

Single crystal Total Fusion Ar/Ar dating of the sample OS-72 of ÇG (mineral: biotite; N: 17).

Mineral	P	t	40 V		39 V		38 V		37 V		36 V		Moles 40Ar*	%Rad	R	Age (Ma)		%-sd
a	1.6	10	6.948	± 0.00416	3.504	± 0.00288	0.05058	± 0.00021	0.08009	± 0.00092	0.000368	± 0.00003	4.87E-14	98.54%	1.9536	21.09	± 0.03	0.16%
b	1.6	10	3.677	± 0.00178	1.820	± 0.00161	0.02675	± 0.00016	0.09655	± 0.00061	0.000509	± 0.00002	2.57E-14	96.14%	1.9420	20.97	± 0.05	0.22%
c	1.6	10	6.125	± 0.00465	2.995	± 0.00306	0.04404	± 0.00027	0.19326	± 0.00061	0.000943	± 0.00003	4.29E-14	95.73%	1.9580	21.14	± 0.04	0.20%
d	1.6	10	3.265	± 0.00366	1.635	± 0.00278	0.02354	± 0.00015	0.08350	± 0.00054	0.000282	± 0.00003	2.29E-14	97.67%	1.9506	21.06	± 0.07	0.35%
e	1.6	10	6.215	± 0.00400	3.075	± 0.00241	0.04318	± 0.00023	0.15627	± 0.00104	0.000793	± 0.00003	4.35E-14	96.45%	1.9495	21.05	± 0.04	0.18%
f	1.6	10	3.934	± 0.00372	1.942	± 0.00266	0.02770	± 0.00021	0.06673	± 0.00046	0.000473	± 0.00003	2.76E-14	96.60%	1.9567	21.12	± 0.06	0.28%
g	1.6	10	7.060	± 0.00593	3.556	± 0.00373	0.05115	± 0.00037	0.19785	± 0.00084	0.000531	± 0.00003	4.94E-14	98.03%	1.9462	21.01	± 0.04	0.18%
h	1.6	10	5.727	± 0.00219	2.865	± 0.00195	0.04135	± 0.00029	0.13743	± 0.00087	0.000493	± 0.00003	4.01E-14	97.67%	1.9525	21.08	± 0.03	0.17%
i	1.6	10	3.341	± 0.00415	1.667	± 0.00196	0.02403	± 0.00012	0.04989	± 0.00021	0.000293	± 0.00002	2.34E-14	97.54%	1.9553	21.11	± 0.06	0.28%
j	1.6	10	6.757	± 0.00247	3.350	± 0.00213	0.04912	± 0.00015	0.10587	± 0.00062	0.000748	± 0.00003	4.73E-14	96.87%	1.9540	21.09	± 0.03	0.16%
k	1.6	10	3.460	± 0.00211	1.679	± 0.00291	0.02480	± 0.00010	0.14964	± 0.00068	0.000681	± 0.00003	2.42E-14	94.56%	1.9491	21.04	± 0.07	0.31%
l	1.6	10	5.487	± 0.00437	2.704	± 0.01173	0.03996	± 0.00026	0.14656	± 0.00145	0.000794	± 0.00003	3.84E-14	95.96%	1.9475	21.02	± 0.10	0.49%
m	1.6	10	6.275	± 0.00597	3.160	± 0.00178	0.04495	± 0.00029	0.15755	± 0.00135	0.000375	± 0.00002	4.39E-14	98.46%	1.9551	21.11	± 0.03	0.16%
n	1.6	10	5.605	± 0.00537	2.829	± 0.00223	0.04173	± 0.00031	0.17391	± 0.00133	0.000339	± 0.00003	3.93E-14	98.49%	1.9511	21.06	± 0.04	0.19%
o	1.6	10	2.628	± 0.00294	1.326	± 0.00107	0.01852	± 0.00015	0.02145	± 0.00022	0.000110	± 0.00002	1.84E-14	98.83%	1.9589	21.15	± 0.06	0.30%
p	1.6	10	8.174	0.00429	4.103	± 0.00464	0.05929	± 0.00041	0.18749	± 0.00150	0.000701	± 0.00003	5.72E-14	97.67%	1.9460	21.01	± 0.03	0.16%
q	1.6	10	5.824	0.00319	2.910	± 0.00191	0.04269	± 0.00034	0.12330	± 0.00093	0.000543	± 0.00003	4.08E-14	97.43%	1.9500	21.05	± 0.04	0.18%
r	1.6	10	6.356	0.00536	3.139	± 0.00296	0.04467	± 0.00018	0.09767	± 0.00082	0.000810	± 0.00003	4.45E-14	96.37%	1.9512	21.06	± 0.04	0.19%

Table A.2 (continued) : ^{40}Ar/^{39}Ar ages obtained from the CPC.

Single crystal incremental heating Ar/Ar dating of the sample OS-72 of ÇG (mineral: biotite)

Steps	P	t	40 V		39 V		38 V		37 V		36 V		Moles 40Ar*	%Rad	R	Age (Ma)		%-sd
1	0.35	20	0.294	± 0.00061	0.117	± 0.00046	0.00173	± 0.00005	0.00332	± 0.00017	0.000189	± 0.00003	2.06E-15	81.12%	2.0455	22.08	± 0.75	3.40%
2	0.4	15	0.299	± 0.00036	0.133	± 0.00035	0.00197	± 0.00008	0.00253	± 0.00015	0.000132	± 0.00003	2.09E-15	87.01%	1.9567	21.12	± 0.63	3.00%
3	0.44	10	0.248	± 0.00044	0.119	± 0.00046	0.00183	± 0.00005	0.00195	± 0.00023	0.000021	± 0.00003	1.74E-15	97.62%	2.0279	21.89	± 0.76	3.47%
4	0.48	10	0.373	± 0.00066	0.185	± 0.00073	0.00274	± 0.00005	0.00193	± 0.00017	0.000032	± 0.00003	2.61E-15	97.55%	1.9687	21.25	± 0.45	2.11%
5	0.52	10	0.393	± 0.00048	0.197	± 0.00048	0.00283	± 0.00007	0.00195	± 0.00015	0.000026	± 0.00002	2.76E-15	98.09%	1.9588	21.15	± 0.39	1.84%
6	0.56	10	0.556	± 0.00095	0.282	± 0.00069	0.00406	± 0.00007	0.00264	± 0.00012	-0.000001	± 0.00003	3.89E-15	100.10%	1.9743	21.31	± 0.32	1.49%
7	0.6	10	0.763	± 0.00140	0.385	± 0.00080	0.00544	± 0.00009	0.00361	± 0.00016	0.000025	± 0.00002	5.35E-15	99.08%	1.9623	21.18	± 0.21	1.01%
8	0.65	10	1.050	± 0.00221	0.530	± 0.00073	0.00767	± 0.00007	0.00517	± 0.00027	0.000032	± 0.00002	7.35E-15	99.13%	1.9643	21.20	± 0.15	0.73%
9	0.72	10	1.319	± 0.00164	0.670	± 0.00091	0.00955	± 0.00010	0.00867	± 0.00015	0.000023	± 0.00002	9.24E-15	99.54%	1.9609	21.17	± 0.12	0.59%
10	0.8	10	1.847	± 0.00168	0.936	± 0.00160	0.01346	± 0.00008	0.02261	± 0.00039	0.000040	± 0.00003	1.29E-14	99.47%	1.9639	21.20	± 0.11	0.51%
11	0.95	10	2.776	± 0.00263	1.409	± 0.00195	0.02070	± 0.00020	0.08949	± 0.00039	0.000080	± 0.00003	1.94E-14	99.43%	1.9600	21.16	± 0.07	0.35%
12	1.1	10	2.038	± 0.00243	1.030	± 0.00164	0.01521	± 0.00020	0.11136	± 0.00121	0.000118	± 0.00003	1.43E-14	98.78%	1.9551	21.11	± 0.09	0.45%
13	1.3	10	1.325	± 0.00199	0.668	± 0.00121	0.00969	± 0.00008	0.10050	± 0.00057	0.000095	± 0.00003	9.28E-15	98.55%	1.9534	21.09	± 0.15	0.70%
14	1.6	10	0.012	± 0.00024	0.006	± 0.00022	0.00005	± 0.00006	0.00165	± 0.00021	-0.000039	± 0.00002	8.38E-17	198.05%	2.1860	23.58	± 14.1	59.66%
15	1.8	10	0.031	± 0.00027	0.015	± 0.00013	0.00017	± 0.00005	0.00712	± 0.00023	0.000003	± 0.00002	2.17E-16	98.88%	2.0968	22.63	± 5.17	22.86%

P: % power of 60 W (60 W *(P/10) Synrad CO2 laser); t: laser duration time; V: volt; %Rad: % radiogenic argon; R: 40Ar*/39Ar (Ar*: radiogenic argon); J value: 0.0064870 ± 0.000011 (1σ).

Table A.2 (continued) : $^{40}Ar/^{39}Ar$ ages obtained from the CPC.

Single crystal Total Fusion Ar/Ar dating of the sample OS-150 of GGMC (mineral: biotite; N: 18).

Mineral	P	t	40 V		39 V		38 V		37 V		36 V		Moles 40Ar*	%Rad	R	Age (Ma)		%-sd
a	1.6	10	9.014	± 0.00595	4.297	± 0.00617	0.06203	± 0.00047	0.04541	± 0.00056	0.002109	± 0.00003	6.31E-14	93.13%	1.9537	20.72	± 0.04	0.20%
b	1.6	10	5.455	± 0.00537	2.521	± 0.00297	0.03684	± 0.00036	0.11439	± 0.00075	0.001899	± 0.00003	3.82E-14	89.90%	1.9452	20.63	± 0.05	0.25%
c	1.6	10	5.107	± 0.00548	2.472	± 0.00252	0.03540	± 0.00023	0.03973	± 0.00041	0.000871	± 0.00003	3.58E-14	95.03%	1.9632	20.82	± 0.05	0.23%
d	1.6	10	3.847	± 0.00211	1.802	± 0.00274	0.02640	± 0.00033	0.06079	± 0.00095	0.001113	± 0.00003	2.69E-14	91.59%	1.9551	20.73	± 0.06	0.29%
e	1.6	10	3.103	± 0.00347	1.465	± 0.00117	0.02088	± 0.00011	0.05599	± 0.00099	0.000853	± 0.00003	2.17E-14	92.04%	1.9493	20.67	± 0.07	0.34%
f	1.6	10	5.069	± 0.00326	2.293	± 0.00216	0.03359	± 0.00020	0.02200	± 0.00025	0.001968	± 0.00003	3.55E-14	88.57%	1.9577	20.76	± 0.05	0.26%
g	1.6	10	5.727	± 0.00310	2.577	± 0.00232	0.03789	± 0.00027	0.01539	± 0.00049	0.002298	± 0.00003	4.01E-14	88.17%	1.9593	20.78	± 0.04	0.20%
h	1.6	10	3.562	± 0.00454	1.662	± 0.00232	0.02399	± 0.00017	0.03326	± 0.00029	0.001009	± 0.00002	2.49E-14	91.71%	1.9659	20.85	± 0.06	0.30%
i	1.6	10	2.465	± 0.00311	1.090	± 0.00145	0.01569	± 0.00012	0.02244	± 0.00020	0.001137	± 0.00003	1.73E-14	86.45%	1.9554	20.74	± 0.09	0.44%
j	1.6	10	3.694	± 0.00361	1.784	± 0.00164	0.02495	± 0.00017	0.02889	± 0.00032	0.000692	± 0.00003	2.59E-14	94.54%	1.9573	20.76	± 0.05	0.26%
k	1.6	10	2.820	± 0.00253	1.323	± 0.00184	0.01859	± 0.00011	0.00179	± 0.00023	0.000823	± 0.00003	1.97E-14	91.38%	1.9474	20.65	± 0.08	0.36%
l	1.6	10	3.501	± 0.00304	1.689	± 0.00106	0.02385	± 0.00011	0.02131	± 0.00053	0.000750	± 0.00003	2.45E-14	93.73%	1.9434	20.61	± 0.06	0.28%
m	1.6	10	2.969	± 0.00160	1.434	± 0.00154	0.02000	± 0.00013	0.01469	± 0.00029	0.000542	± 0.00003	2.08E-14	94.65%	1.9592	20.78	± 0.07	0.35%
n	1.6	10	4.038	± 0.00303	1.959	± 0.00248	0.02802	± 0.00029	0.01055	± 0.00020	0.000696	± 0.00002	2.83E-14	94.93%	1.9563	20.75	± 0.05	0.23%
o	1.6	10	3.566	± 0.00316	1.531	± 0.00256	0.02178	± 0.00009	0.04261	± 0.00027	0.001945	± 0.00003	2.50E-14	83.99%	1.9558	20.74	± 0.08	0.39%
p	1.6	10	3.774	0.00540	1.726	± 0.00112	0.02466	± 0.00015	0.01608	± 0.00025	0.001329	± 0.00003	2.64E-14	89.63%	1.9596	20.78	± 0.07	0.33%
q	1.6	10	6.092	0.00972	2.690	± 0.00263	0.03809	± 0.00020	0.05360	± 0.00038	0.002818	± 0.00003	4.27E-14	86.41%	1.9565	20.75	± 0.06	0.28%
r	1.6	10	6.561	0.00718	3.155	± 0.00264	0.04518	± 0.00034	0.03909	± 0.00044	0.001310	± 0.00003	4.59E-14	94.15%	1.9578	20.76	± 0.04	0.21%

Table A.2 (continued) : $^{40}Ar/^{39}Ar$ ages obtained from the CPC.

Single crystal incremental heating Ar/Ar dating of the sample OS-150 of GGMC (mineral: biotite)

Steps	P	t	40 V		39 V		38 V		37 V		36 V		Moles 40Ar*	%Rad	R	Age (Ma)		%-sd
1	0.35	20	1.497	± 0.00133	0.556	± 0.00134	0.00806	± 0.00008	0.00086	± 0.00016	0.001390	± 0.00003	1.05E-14	72.56%	1.9537	20.72	± 0.19	0.92%
2	0.4	15	1.307	± 0.00104	0.662	± 0.00110	0.00931	± 0.00009	0.00027	± 0.00020	0.000019	± 0.00004	9.16E-15	99.57%	1.9669	20.86	± 0.21	0.99%
3	0.44	10	0.780	± 0.00160	0.396	± 0.00067	0.00561	± 0.00006	0.00020	± 0.00012	0.000051	± 0.00003	5.46E-15	98.06%	1.9301	20.47	± 0.24	1.16%
4	0.48	10	0.757	± 0.00108	0.379	± 0.00081	0.00537	± 0.00009	0.00005	± 0.00021	0.000031	± 0.00003	5.30E-15	98.80%	1.9716	20.91	± 0.22	1.05%
5	0.52	10	0.917	± 0.00161	0.460	± 0.00068	0.00656	± 0.00009	0.00094	± 0.00020	0.000063	± 0.00003	6.42E-15	97.98%	1.9538	20.72	± 0.18	0.88%
6	0.56	10	1.142	± 0.00075	0.574	± 0.00085	0.00841	± 0.00014	0.00492	± 0.00026	0.000039	± 0.00003	8.00E-15	99.02%	1.9711	20.90	± 0.16	0.75%
7	0.6	10	0.550	± 0.00098	0.275	± 0.00045	0.00383	± 0.00009	0.02122	± 0.00030	0.000025	± 0.00002	3.85E-15	99.01%	1.9819	21.02	± 0.26	1.22%
8	0.72	10	0.043	± 0.00050	0.022	± 0.00010	0.00035	± 0.00005	0.01003	± 0.00024	-0.000003	± 0.00003	3.00E-16	104.30%	1.9755	20.95	± 3.62	17.30%
9	0.8	10	0.044	± 0.00051	0.021	± 0.00015	0.00032	± 0.00004	0.01094	± 0.00034	0.000025	± 0.00002	3.11E-16	85.74%	1.8086	19.19	± 3.48	18.13%
10	0.9	10	0.044	± 0.00030	0.023	± 0.00011	0.00029	± 0.00006	0.00572	± 0.00010	-0.000056	± 0.00003	3.07E-16	139.20%	1.9406	20.58	± 3.44	16.70%
11	1	10	0.082	± 0.00041	0.040	± 0.00031	0.00057	± 0.00005	0.02165	± 0.00022	-0.000068	± 0.00004	5.77E-16	126.86%	2.0915	22.17	± 3.37	15.20%
12	1.3	10	0.011	± 0.00026	0.004	± 0.00014	0.00002	± 0.00005	0.00514	± 0.00017	-0.000120	± 0.00005	7.76E-17	425.47%	2.6226	27.76	± 33.1	119.31%
13	1.6	10	0.002	± 0.00021	0.001	± 0.00012	-0.00012	± 0.00004	0.00104	± 0.00022	-0.000066	± 0.00002	1.52E-17	998.47%	3.4126	36.04	± 125	347.01%

P: % power of 60 W (60 W *(P/10) Synrad CO_2 laser); t: laser duration time; V: volt; %Rad: % radiogenic argon; R: 40Ar*/39Ar (Ar*: radiogenic argon); J value: 0.0064870 ± 0.000011 (1σ).

Table A.2 (continued) : $^{40}Ar/^{39}Ar$ ages obtained from the CPC.

Single crystal Total Fusion Ar/Ar dating of the sample OS-150 of GMMC (mineral: K-feldspar; N: 15).

Mineral	P	t	40 V		39 V		38 V		37 V		36 V		Moles 40Ar*	%Rad	R	Age (Ma)		%-sd
a	1.6	10	20.445	± 0.03561	9.295	± 0.02260	0.12567	± 0.00057	0.04966	± 0.00028	0.004836	± 0.00016	1.43E-13	93.03%	2.0463	21.69	± 0.09	0.41%
b	1.6	10	9.148	± 0.00570	4.467	± 0.00684	0.06008	± 0.00025	0.05580	± 0.00027	0.000970	± 0.00007	6.41E-14	96.92%	1.9846	21.04	± 0.06	0.28%
c	1.6	10	17.074	± 0.01162	7.872	± 0.00842	0.10578	± 0.00045	0.03420	± 0.00020	0.004237	± 0.00016	1.20E-13	92.69%	2.0101	21.31	± 0.07	0.32%
d*	1.6	10	19.979	± 0.01854	8.289	± 0.00784	0.11244	± 0.00058	0.08412	± 0.00036	0.007757	± 0.00018	1.40E-13	88.56%	2.1347	22.63	± 0.07	0.33%
e	1.6	10	5.321	± 0.00482	2.411	± 0.00263	0.03265	± 0.00021	0.40278	± 0.00142	0.001722	± 0.00012	3.73E-14	91.11%	2.0110	21.32	± 0.15	0.72%
f	1.6	10	12.913	± 0.00943	6.109	± 0.00492	0.08110	± 0.00033	0.04161	± 0.00031	0.001224	± 0.00014	9.04E-14	97.23%	2.0553	21.79	± 0.08	0.35%
g	1.6	10	13.874	± 0.00832	6.322	± 0.00718	0.08575	± 0.00051	0.08086	± 0.00030	0.003845	± 0.00016	9.72E-14	91.86%	2.0160	21.37	± 0.08	0.39%
h	1.6	10	13.619	± 0.01158	5.397	± 0.00414	0.07212	± 0.00022	0.13657	± 0.00032	0.008089	± 0.00038	9.54E-14	82.54%	2.0827	22.08	± 0.22	1.01%
i	1.6	10	14.126	± 0.01164	6.860	± 0.00622	0.09143	± 0.00035	0.02996	± 0.00011	0.002112	± 0.00027	9.89E-14	95.60%	1.9687	20.88	± 0.13	0.61%
j	1.6	10	13.774	± 0.00695	6.111	± 0.00403	0.08188	± 0.00019	0.37241	± 0.00103	0.004662	± 0.00021	9.65E-14	90.24%	2.0341	21.57	± 0.11	0.50%
k	1.6	10	14.528	± 0.00881	6.987	± 0.00664	0.09400	± 0.00069	0.04211	± 0.00016	0.001485	± 0.00010	1.02E-13	97.00%	2.0171	21.39	± 0.05	0.24%
l	1.6	10	12.598	± 0.00706	5.847	± 0.00619	0.07892	± 0.00029	0.04478	± 0.00027	0.002990	± 0.00018	8.82E-14	93.02%	2.0041	21.25	± 0.10	0.48%
n	1.6	10	10.410	± 0.00570	4.950	± 0.00426	0.06703	± 0.00056	0.03162	± 0.00025	0.001600	± 0.00012	7.29E-14	95.49%	2.0082	21.29	± 0.08	0.38%
o	1.6	10	12.206	± 0.01333	5.924	± 0.00389	0.07954	± 0.00037	0.03953	± 0.00047	0.001394	± 0.00010	8.55E-14	96.65%	1.9913	21.11	± 0.06	0.29%
p*	1.6	10	3.712	± 0.00276	1.533	± 0.00197	0.02077	± 0.00023	0.26772	± 0.00138	0.001168	± 0.00010	2.60E-14	91.34%	2.2117	23.44	± 0.20	0.87%

* Rejected data

Table A.2 (continued) : $^{40}Ar/^{39}Ar$ ages obtained from the CPC.

Single crystal incremental heating Ar/Ar dating of the sample OS-150 of GGMC (mineral: K-feldspar)

Steps	P	t	40 V		39 V		38 V		37 V		36 V		Moles 40Ar*	%Rad	R	Age (Ma)		%-sd
1	0.35	20	0.395	± 0.00052	0.108	± 0.00037	0.00156	± 0.00007	0.00115	± 0.00014	0.000433	± 0.00008	2.77E-15	67.64%	2.4873	26.34	± 2.45	9.31%
2	0.4	20	1.186	± 0.00164	0.460	± 0.00085	0.00612	± 0.00008	0.00310	± 0.00017	0.000607	± 0.00008	8.31E-15	84.91%	2.1906	23.21	± 0.56	2.40%
3	0.45	20	3.235	± 0.00213	1.583	± 0.00185	0.02166	± 0.00020	0.00617	± 0.00014	0.000367	± 0.00008	2.27E-14	96.67%	1.9749	20.94	± 0.16	0.77%
4	0.475	20	4.365	± 0.00295	2.111	± 0.00163	0.02794	± 0.00015	0.00648	± 0.00020	0.000446	± 0.00009	3.06E-14	96.99%	2.0059	21.27	± 0.14	0.64%
5	0.5	20	5.250	± 0.00287	2.545	± 0.00240	0.03416	± 0.00035	0.00554	± 0.00015	0.000554	± 0.00007	3.68E-14	96.89%	1.9987	21.19	± 0.09	0.42%
6	0.55	20	0.732	± 0.00142	0.364	± 0.00064	0.00497	± 0.00008	0.00050	± 0.00008	0.000036	± 0.00006	5.12E-15	98.56%	1.9802	21.00	± 0.55	2.63%
7	0.6	20	1.771	± 0.00164	0.888	± 0.00166	0.01188	± 0.00010	0.00092	± 0.00019	0.000090	± 0.00007		98.50%	1.9651	20.84	± 0.25	1.19%
8	0.7	20	3.065	± 0.00184	1.538	± 0.00188	0.02007	± 0.00011	0.00219	± 0.00011	0.000129	± 0.00018	2.15E-14	98.76%	1.9676	20.86	± 0.37	1.78%
9	0.8	20	1.285	± 0.00151	0.644	± 0.00178	0.00839	± 0.00007	0.00074	± 0.00007	0.000053	± 0.00006	9.00E-15	98.79%	1.9700	20.89	± 0.32	1.54%
10	0.9	20	0.446	± 0.00068	0.225	± 0.00064	0.00295	± 0.00007	-0.00017	± 0.00017	-0.000027	± 0.00008	3.13E-15	101.77%	1.9828	21.02	± 1.09	5.20%
11	1.1	20	0.065	± 0.00039	0.031	± 0.00014	0.00031	± 0.00004	-0.00062	± 0.00013	-0.000013	± 0.00009	4.56E-16	106.07%	2.0784	22.03	± 9.27	42.08%
12	1.3	20	0.040	± 0.00039	0.020	± 0.00017	0.00017	± 0.00005	-0.00041	± 0.00011	-0.000036	± 0.00008	2.80E-16	126.56%	1.9797	20.99	± 11.8	56.28%

P: % power of 60 W (60 W *(P/10) Synrad CO2 laser); t: laser duration time; V: volt; %Rad: % radiogenic argon; R: 40Ar*/39Ar (Ar*: radiogenic argon); J value: 0.0064870 ± 0.000011 (1σ).

Table A.2 (continued) : $^{40}Ar/^{39}Ar$ ages obtained from the CPC.

Single crystal Total Fusion Ar/Ar dating of the sample OS-77 of GGMC (mineral: muscovite; N: 18).

Mineral	P	t	40 V		39 V		38 V		37 V		36 V		Moles 40Ar*	%Rad	R	Age (Ma)		%-sd
a	1.6	10	4.283	± 0.00569	2.053	± 0.00327	0.02700	± 0.00017	0.00239	± 0.00029	0.000720	± 0.00003	3.00E-14	95.04%	1.9832	21.03	± 0.06	0.30%
b	1.6	10	1.104	± 0.00093	0.527	± 0.00063	0.00680	± 0.00011	0.00097	± 0.00020	0.000178	± 0.00003	7.73E-15	95.25%	1.9942	21.14	± 0.17	0.79%
c	1.6	10	2.494	± 0.00251	1.164	± 0.00132	0.01525	± 0.00012	0.00132	± 0.00023	0.000584	± 0.00003	1.75E-14	93.09%	1.9945	21.15	± 0.08	0.40%
d	1.6	10	1.006	± 0.00112	0.475	± 0.00113	0.00617	± 0.00004	0.00066	± 0.00015	0.000201	± 0.00002	7.04E-15	94.09%	1.9915	21.12	± 0.17	0.81%
e	1.6	10	1.578	± 0.00266	0.660	± 0.00129	0.00880	± 0.00008	0.00341	± 0.00012	0.000890	± 0.00002	1.10E-14	83.35%	1.9926	21.13	± 0.13	0.64%
f	1.6	10	2.944	± 0.00282	1.266	± 0.00159	0.01679	± 0.00009	0.00390	± 0.00017	0.001451	± 0.00003	2.06E-14	85.45%	1.9878	21.08	± 0.08	0.39%
g	1.6	10	2.755	± 0.00227	1.341	± 0.00189	0.01821	± 0.00018	0.00286	± 0.00018	0.000317	± 0.00002	1.93E-14	96.61%	1.9853	21.05	± 0.07	0.32%
h	1.6	10	1.488	± 0.00084	0.697	± 0.00095	0.00900	± 0.00009	0.00043	± 0.00012	0.000339	± 0.00002	1.04E-14	93.28%	1.9912	21.11	± 0.11	0.53%
i	1.6	10	2.093	± 0.00245	0.996	± 0.00134	0.01298	± 0.00011	0.00249	± 0.00015	0.000366	± 0.00002	1.47E-14	94.84%	1.9922	21.12	± 0.08	0.39%
j	1.6	10	1.273	± 0.00103	0.600	± 0.00104	0.00827	± 0.00011	0.00070	± 0.00015	0.000224	± 0.00002	8.92E-15	94.82%	2.0138	21.35	± 0.14	0.64%
k	1.6	10	1.191	± 0.00151	0.557	± 0.00122	0.00740	± 0.00006	0.00054	± 0.00015	0.000266	± 0.00003	8.34E-15	93.41%	1.9966	21.17	± 0.16	0.77%
l	1.6	10	1.077	± 0.00153	0.515	± 0.00091	0.00678	± 0.00003	0.00097	± 0.00013	0.000200	± 0.00002	7.55E-15	94.53%	1.9760	20.95	± 0.16	0.76%
m	1.6	10	1.888	± 0.00305	0.874	± 0.00093	0.01188	± 0.00017	0.00665	± 0.00012	0.000493	± 0.00003	1.32E-14	92.32%	1.9935	21.14	± 0.11	0.50%
n	1.6	10	1.944	± 0.00148	0.901	± 0.00156	0.01183	± 0.00007	0.00175	± 0.00015	0.000516	± 0.00003	1.36E-14	92.16%	1.9887	21.09	± 0.10	0.49%
o	1.6	10	2.710	± 0.00216	1.239	± 0.00128	0.01636	± 0.00010	0.00169	± 0.00015	0.000910	± 0.00003	1.90E-14	90.08%	1.9704	20.89	± 0.08	0.38%
p	1.6	10	1.525	0.00156	0.668	± 0.00144	0.00914	± 0.00014	0.00061	± 0.00019	0.000616	± 0.00003	1.07E-14	88.06%	2.0120	21.33	± 0.14	0.64%
q	1.6	10	1.246	0.00171	0.568	± 0.00085	0.00748	± 0.00006	0.00025	± 0.00022	0.000372	± 0.00002	8.72E-15	91.17%	1.9995	21.20	± 0.13	0.63%
r	1.6	10	0.866	0.00125	0.390	± 0.00103	0.00527	± 0.00008	0.00110	± 0.00010	0.000346	± 0.00002	6.06E-15	88.20%	1.9561	20.74	± 0.19	0.93%

Table A.2 (continued) : ^{40}Ar/^{39}Ar ages obtained from the CPC.

Single crystal incremental heating Ar/Ar dating of the sample OS-77 of GGMC (mineral: muscovite)

Steps	P	t	40 V		39 V		38 V		37 V		36 V		Moles 40Ar*	%Rad	R	Age (Ma)		%-sd
1	0.35	15	0.037	± 0.00038	0.005	± 0.00013	0.00006	± 0.00004	0.00448	± 0.00022	0.000046	± 0.00003	2.59E-16	64.64%	4.5176	47.55	± 16.6	34.84%
2	0.4	15	0.288	± 0.00035	0.052	± 0.00029	0.00073	± 0.00005	0.00346	± 0.00021	0.000529	± 0.00003	2.01E-15	45.77%	2.5408	26.90	± 1.81	6.74%
3	0.44	10	0.256	± 0.00049	0.118	± 0.00048	0.00145	± 0.00005	0.00091	± 0.00014	0.000009	± 0.00003	1.79E-15	98.98%	2.1365	22.64	± 0.67	2.96%
4	0.48	10	0.614	± 0.00109	0.302	± 0.00055	0.00394	± 0.00008	0.00140	± 0.00016	0.000010	± 0.00003	4.30E-15	99.56%	2.0215	21.43	± 0.29	1.36%
5	0.52	10	0.924	± 0.00064	0.455	± 0.00068	0.00592	± 0.00008	0.00170	± 0.00019	0.000006	± 0.00003	6.47E-15	99.83%	2.0254	21.47	± 0.20	0.94%
6	0.56	10	1.035	± 0.00217	0.516	± 0.00096	0.00667	± 0.00010	0.00132	± 0.00016	-0.000040	± 0.00003	7.25E-15	101.16%	2.0036	21.24	± 0.18	0.82%
7	0.6	10	1.268	± 0.00212	0.626	± 0.00120	0.00814	± 0.00007	0.00209	± 0.00017	0.000055	± 0.00003	8.88E-15	98.74%	2.0007	21.21	± 0.14	0.67%
8	0.72	10	0.400	± 0.00053	0.204	± 0.00064	0.00259	± 0.00007	0.00033	± 0.00019	-0.000040	± 0.00003	2.80E-15	102.93%	1.9643	20.83	± 0.42	2.03%
9	0.8	10	0.076	± 0.00064	0.038	± 0.00014	0.00049	± 0.00004	0.00084	± 0.00032	-0.000035	± 0.00003	5.30E-16	113.60%	1.9796	20.99	± 2.40	11.44%
10	0.95	10	0.023	± 0.00036	0.012	± 0.00019	0.00010	± 0.00004	0.00020	± 0.00014	-0.000046	± 0.00003	1.60E-16	160.15%	1.8778	19.92	± 6.77	33.98%
11	1.1	10	-0.002	± 0.00026	0.000	± 0.00009	-0.00007	± 0.00005	0.00007	± 0.00016	-0.000052	± 0.00003	-1.49E-17	-620.22%	-14.8078	-165.28	-± 959	580.03%
12	1.3	10	0.003	± 0.00026	0.001	± 0.00010	-0.00007	± 0.00005	0.00020	± 0.00013	-0.000122	± 0.00004	2.07E-17	1321.87%	4.5901	48.30	± 220	455.57%

P: % power of 60 W (60 W *(P/10) Synrad CO2 laser); t: laser duration time; V: volt; %Rad: % radiogenic argon; R: 40Ar*/39Ar (Ar*: radiogenic argon); J value: 0.0064870 ± 0.000011 (1σ).

Table A.2 (continued) : $^{40}Ar/^{39}Ar$ ages obtained from the CPC.

Mineral	P	t	40 V		39 V		38 V		37 V		36 V		Moles 40Ar*	%Rad	R	Age (Ma)		%-sd
a	1.6	10	1.397	± 0.00184	0.674	± 0.0017	0.0091	± 0.0001	0.0004	± 0.00011	0.000217	± 0.00002	9.78E-15	95.42%	1.9784	21.36	± 0.11	0.52%
b	1.6	10	2.681	± 0.00488	1.198	± 0.0028	0.0165	± 0.0001	0.0010	± 0.00015	0.001101	± 0.00003	1.88E-14	87.88%	1.9661	21.22	± 0.10	0.48%
c	1.6	10	1.997	± 0.00226	0.911	± 0.0015	0.0123	± 0.0001	0.0005	± 0.00008	0.000661	± 0.00002	1.40E-14	90.22%	1.9775	21.35	± 0.09	0.43%
d	1.6	10	2.584	± 0.00282	1.268	± 0.0018	0.0175	± 0.0001	0.0011	± 0.00007	0.000313	± 0.00002	1.81E-14	96.42%	1.9646	21.21	± 0.07	0.33%
e	1.6	10	1.922	± 0.00269	0.889	± 0.0012	0.0120	± 0.0001	0.0018	± 0.00009	0.000538	± 0.00002	1.35E-14	91.73%	1.9834	21.41	± 0.09	0.43%
f	1.6	10	1.635	± 0.00189	0.733	± 0.0012	0.0100	± 0.0001	0.0015	± 0.00011	0.000659	± 0.00002	1.14E-14	88.10%	1.9657	21.22	± 0.11	0.54%
g	1.6	10	1.887	± 0.00145	0.921	± 0.0019	0.0123	± 0.0001	0.0004	± 0.00010	0.000219	± 0.00002	1.32E-14	96.58%	1.9783	21.36	± 0.09	0.43%
h	1.6	10	2.633	± 0.00716	1.123	± 0.0030	0.0142	± 0.0013	0.0315	± 0.00104	0.001412	± 0.00003	1.84E-14	84.26%	1.9765	21.34	± 0.13	0.60%
i	1.6	10	2.620	± 0.00339	1.059	± 0.0013	0.0144	± 0.0001	0.0013	± 0.00011	0.001817	± 0.00003	1.83E-14	79.52%	1.9682	21.25	± 0.09	0.45%
j	1.6	10	3.027	± 0.00288	1.314	± 0.0013	0.0181	± 0.0001	0.0011	± 0.00011	0.001463	± 0.00003	2.12E-14	85.72%	1.9739	21.31	± 0.07	0.34%
k	1.6	10	1.621	± 0.00135	0.787	± 0.0013	0.0105	± 0.0001	0.0015	± 0.00007	0.000255	± 0.00002	1.14E-14	95.36%	1.9646	21.21	± 0.09	0.44%
l	1.6	10	1.048	± 0.00181	0.485	± 0.0007	0.0066	± 0.0001	0.0004	± 0.00010	0.000302	± 0.00002	7.34E-15	91.49%	1.9749	21.32	± 0.15	0.70%
m	1.6	10	1.883	± 0.00173	0.924	± 0.0014	0.0125	± 0.0001	0.0008	± 0.00013	0.000217	± 0.00002	1.32E-14	96.60%	1.9681	21.25	± 0.09	0.42%
n	1.6	10	2.149	± 0.00097	0.876	± 0.0019	0.0119	± 0.0001	0.0005	± 0.00010	0.001444	± 0.00003	1.51E-14	80.15%	1.9675	21.24	± 0.11	0.53%
o	1.6	10	2.382	± 0.00154	1.118	± 0.0015	0.0150	± 0.0001	0.0014	± 0.00012	0.000634	± 0.00002	1.67E-14	92.14%	1.9638	21.20	± 0.08	0.36%
p	1.6	10	0.798	0.00069	0.382	± 0.0011	0.0053	± 0.0001	0.0005	± 0.00005	0.000140	± 0.00002	5.59E-15	94.82%	1.9828	21.40	± 0.18	0.86%
q	1.6	10	2.146	0.00311	1.020	± 0.0012	0.0136	± 0.0001	0.0014	± 0.00010	0.000443	± 0.00002	1.50E-14	93.91%	1.9754	21.32	± 0.08	0.36%
r	1.6	10	4.874	0.00350	2.459	± 0.0020	0.0329	± 0.0002	0.0068	± 0.00019	0.000116	± 0.00003	3.41E-14	99.31%	1.9688	21.25	± 0.04	0.20%

Table A.2 (continued) : $^{40}Ar/^{39}Ar$ ages obtained from the CPC.

Single crystal incremental heating Ar/Ar dating of the sample OS-75 of GMMC (mineral: muscovite)

Steps	P	t	40 V		39 V		38 V		37 V		36 V		Moles 40Ar*	%Rad	R	Age (Ma)		%-sd
1	0.35	10	0.008	± 0.00032	0.003	± 0.00009	0.00014	± 0.00005	0.00036	± 0.00009	-0.000007	± 0.00002	5.49E-17	126.40%	2.6059	28.08	± 23.2	82.61%
2	0.4	10	0.159	± 0.00066	0.060	± 0.00032	0.00091	± 0.00004	0.00045	± 0.00010	0.000091	± 0.00002	1.11E-15	83.03%	2.1851	23.57	± 1.20	5.07%
3	0.44	10	0.364	± 0.00070	0.171	± 0.00075	0.00226	± 0.00004	0.00039	± 0.00015	0.000059	± 0.00002	2.55E-15	95.19%	2.0268	21.88	± 0.45	2.06%
4	0.48	10	0.585	± 0.00075	0.287	± 0.00052	0.00385	± 0.00005	0.00047	± 0.00009	0.000058	± 0.00003	4.10E-15	97.08%	1.9832	21.41	± 0.28	1.33%
5	0.52	10	0.820	± 0.00138	0.404	± 0.00079	0.00528	± 0.00004	0.00031	± 0.00011	0.000028	± 0.00002	5.74E-15	99.00%	2.0072	21.67	± 0.20	0.93%
6	0.56	10	0.939	± 0.00160	0.467	± 0.00102	0.00586	± 0.00011	-0.00008	± 0.00016	-0.000004	± 0.00002	6.58E-15	100.12%	2.0093	21.69	± 0.16	0.75%
7	0.6	10	1.165	± 0.00167	0.580	± 0.00112	0.00767	± 0.00008	0.00009	± 0.00010	0.000071	± 0.00002	8.16E-15	98.21%	1.9722	21.29	± 0.14	0.67%
8	0.65	10	1.546	± 0.00190	0.767	± 0.00165	0.01019	± 0.00009	0.00007	± 0.00007	0.000126	± 0.00002	1.08E-14	97.59%	1.9680	21.24	± 0.10	0.48%
9	0.72	10	1.653	± 0.00246	0.823	± 0.00129	0.01132	± 0.00014	0.00107	± 0.00011	0.000079	± 0.00002	1.16E-14	98.60%	1.9804	21.38	± 0.09	0.43%
10	0.8	10	0.579	± 0.00089	0.291	± 0.00049	0.00377	± 0.00008	0.00018	± 0.00009	-0.000003	± 0.00003	4.05E-15	100.16%	1.9894	21.47	± 0.38	1.75%
11	0.9	10	0.516	± 0.00101	0.261	± 0.00090	0.00363	± 0.00008	-0.00027	± 0.00011	-0.000011	± 0.00002	3.61E-15	100.65%	1.9736	21.30	± 0.30	1.40%
12	1	10	0.636	± 0.00113	0.324	± 0.00051	0.00427	± 0.00009	-0.00023	± 0.00012	-0.000023	± 0.00002	4.45E-15	101.06%	1.9602	21.16	± 0.22	1.03%
13	1.15	10	0.220	± 0.00038	0.112	± 0.00055	0.00163	± 0.00008	-0.00032	± 0.00012	-0.000019	± 0.00002	1.54E-15	102.57%	1.9610	21.17	± 0.66	3.13%
14	1.3	10	0.164	± 0.00073	0.083	± 0.00033	0.00113	± 0.00006	-0.00026	± 0.00011	-0.000028	± 0.00002	1.15E-15	105.08%	1.9744	21.31	± 0.86	4.06%
15	1.6	10	0.089	± 0.00036	0.046	± 0.00019	0.00056	± 0.00005	-0.00008	± 0.00007	-0.000015	± 0.00002	6.23E-16	104.96%	1.9383	20.93	± 1.44	6.90%
16	1.7	10	0.002	± 0.00026	0.003	± 0.00015	0.00001	± 0.00004	-0.00011	± 0.00012	0.000002	± 0.00002	1.20E-17	60.70%	0.3521	3.82	± 22.6	591.92%

P: % power of 60 W (60 W *(P/10) Synrad CO2 laser); t: laser duration time; V: volt; %Rad: % radiogenic argon; R: 40Ar*/39Ar (Ar*: radiogenic argon); J value: 0.0064870 ± 0.000011 (1σ).

Table A.2 (continued) : $^{40}Ar/^{39}Ar$ ages obtained from the CPC.

Single crystal Total Fusion Ar/Ar dating of the sample OS-111 of GGMC (mineral: biotite; N: 17).

Mineral	P	t	40 V		39 V		38 V		37 V		36 V		Moles 40Ar*	%Rad	R	Age (Ma)		%-sd
a	1.6	10	0.778	± 0.00126	0.384	± 0.00092	0.00561	± 0.00009	0.00062	± 0.00010	0.000088	± 0.00002	5.45E-15	96.66%	1.9582	21.14	± 0.19	0.91%
b	1.6	10	2.372	± 0.00274	1.165	± 0.00185	0.01685	± 0.00015	0.00064	± 0.00009	0.000318	± 0.00002	1.66E-14	96.04%	1.9546	21.10	± 0.07	0.35%
c	1.6	10	1.476	± 0.00173	0.729	± 0.00081	0.01019	± 0.00009	0.00041	± 0.00008	0.000220	± 0.00002	1.03E-14	95.61%	1.9361	20.90	± 0.10	0.47%
d	1.6	10	1.090	± 0.00122	0.489	± 0.00113	0.00714	± 0.00012	0.00103	± 0.00013	0.000336	± 0.00002	7.63E-15	90.90%	2.0268	21.88	± 0.15	0.71%
e	1.6	10	2.103	± 0.00228	1.009	± 0.00176	0.01464	± 0.00015	0.00107	± 0.00013	0.000489	± 0.00002	1.47E-14	93.14%	1.9418	20.96	± 0.09	0.42%
f	1.8	10	1.618	± 0.00118	0.781	± 0.00142	0.01131	± 0.00017	0.00074	± 0.00014	0.000369	± 0.00002	1.13E-14	93.27%	1.9316	20.85	± 0.10	0.49%
g	1.8	10	1.112	± 0.00170	0.513	± 0.00103	0.00767	± 0.00014	0.00072	± 0.00011	0.000200	± 0.00002	7.79E-15	94.69%	2.0528	22.15	± 0.13	0.61%
h	1.8	10	0.982	± 0.00157	0.404	± 0.00076	0.00577	± 0.00003	0.00050	± 0.00010	0.000744	± 0.00002	6.88E-15	77.63%	1.8887	20.39	± 0.17	0.85%
i	1.8	10	3.314	± 0.00349	1.591	± 0.00099	0.02235	± 0.00012	0.00126	± 0.00016	0.000769	± 0.00002	2.32E-14	93.15%	1.9402	20.95	± 0.05	0.24%
j	1.8	10	3.980	± 0.00273	1.795	± 0.00092	0.02544	± 0.00014	0.00419	± 0.00007	0.001566	± 0.00002	2.79E-14	88.38%	1.9593	21.15	± 0.04	0.21%
k	1.8	10	2.118	± 0.00213	0.973	± 0.00163	0.01369	± 0.00009	0.00079	± 0.00013	0.000719	± 0.00002	1.48E-14	89.97%	1.9578	21.13	± 0.09	0.44%
l	1.8	10	0.793	± 0.00119	0.397	± 0.00121	0.00548	± 0.00007	0.00071	± 0.00011	0.000109	± 0.00002	5.55E-15	95.96%	1.9183	20.71	± 0.18	0.89%
m	1.8	10	1.761	± 0.00219	0.772	± 0.00070	0.01153	± 0.00016	0.00211	± 0.00013	0.000572	± 0.00002	1.23E-14	90.41%	2.0614	22.25	± 0.09	0.42%
n	1.8	10	1.567	± 0.00260	0.464	± 0.00083	0.00692	± 0.00007	0.00115	± 0.00015	0.002204	± 0.00003	1.10E-14	58.43%	1.9727	21.30	± 0.23	1.09%
o	1.8	10	1.405	± 0.00148	0.641	± 0.00109	0.00915	± 0.00008	0.00072	± 0.00010	0.000560	± 0.00002	9.84E-15	88.22%	1.9347	20.89	± 0.10	0.49%
p	1.8	10	1.240	0.00168	0.530	± 0.00095	0.00762	± 0.00007	0.00059	± 0.00012	0.000424	± 0.00002	8.68E-15	89.91%	2.1025	22.69	± 0.14	0.64%
q	1.8	10	2.239	0.00119	1.117	± 0.00163	0.01601	± 0.00017	0.00094	± 0.00014	0.000305	± 0.00002	1.57E-14	95.98%	1.9233	20.76	± 0.07	0.33%

Table A.2 (continued) : $^{40}Ar/^{39}Ar$ ages obtained from the CPC.

Single crystal incremental heating Ar/Ar dating of the sample OS-111 of GMMC (mineral: biotite)

Steps	P	t	40 V	±	39 V	±	38 V	±	37 V	±	36 V	±	Moles 40Ar*	%Rad	R	Age (Ma)	±	%-sd
1	0.35	15	0.054	± 0.00036	0.024	± 0.00014	0.00032	± 0.00005	0.00083	± 0.00047	0.000044	± 0.00002	3.79E-16	76.24%	1.7373	18.77	± 3.12	16.62%
2	0.4	15	0.545	± 0.00071	0.260	± 0.00061	0.00361	± 0.00005	0.00102	± 0.00025	0.000152	± 0.00002	3.82E-15	91.79%	1.9227	20.76	± 0.27	1.28%
3	0.44	10	0.570	± 0.00085	0.278	± 0.00061	0.00386	± 0.00006	0.00095	± 0.00022	0.000059	± 0.00004	3.99E-15	96.97%	1.9910	21.49	± 0.42	1.93%
4	0.48	10	0.596	± 0.00100	0.291	± 0.00068	0.00416	± 0.00008	0.00099	± 0.00015	0.000057	± 0.00002	4.18E-15	97.18%	1.9890	21.47	± 0.23	1.05%
5	0.52	10	0.576	± 0.00124	0.284	± 0.00057	0.00391	± 0.00006	0.00097	± 0.00032	0.000057	± 0.00002	4.03E-15	97.07%	1.9670	21.23	± 0.26	1.21%
6	0.56	10	0.844	± 0.00106	0.419	± 0.00098	0.00583	± 0.00009	0.00100	± 0.00018	0.000049	± 0.00002	5.91E-15	98.29%	1.9780	21.35	± 0.18	0.86%
7	0.6	10	1.041	± 0.00143	0.521	± 0.00053	0.00714	± 0.00011	0.00104	± 0.00021	0.000071	± 0.00003	7.29E-15	97.99%	1.9587	21.14	± 0.21	0.99%
8	0.65	10	1.200	± 0.00127	0.613	± 0.00069	0.00843	± 0.00006	0.00046	± 0.00032	0.000023	± 0.00003	8.41E-15	99.44%	1.9479	21.03	± 0.14	0.66%
9	0.72	10	1.376	± 0.00193	0.702	± 0.00132	0.00967	± 0.00013	0.00047	± 0.00017	-0.000034	± 0.00002	9.64E-15	100.73%	1.9617	21.18	± 0.12	0.57%
10	0.8	10	0.418	± 0.00085	0.212	± 0.00057	0.00321	± 0.00008	0.00029	± 0.00026	-0.000024	± 0.00003	2.92E-15	101.71%	1.9662	21.22	± 0.40	1.87%
11	0.9	10	0.038	± 0.00030	0.019	± 0.00014	0.00031	± 0.00005	-0.00051	± 0.00016	-0.000035	± 0.00002	2.69E-16	126.99%	1.9821	21.40	± 4.08	19.07%
12	1	10	0.026	± 0.00031	0.013	± 0.00012	0.00021	± 0.00004	-0.00057	± 0.00031	-0.000038	± 0.00002	1.82E-16	143.60%	2.0082	21.68	± 5.42	25.02%
13	1.2	10	0.052	± 0.00027	0.026	± 0.00013	0.00034	± 0.00005	0.00159	± 0.00021	-0.000033	± 0.00002	3.66E-16	119.14%	2.0010	21.60	± 2.67	12.38%
14	1.5	10	0.270	± 0.00034	0.137	± 0.00048	0.00186	± 0.00004	0.00010	± 0.00023	-0.000028	± 0.00002	1.89E-15	103.06%	1.9705	21.27	± 0.54	2.54%

P: % power of 60 W (60 W *(P/10) Synrad CO2 laser); t: laser duration time; V: volt; %Rad: % radiogenic argon; R: 40Ar*/39Ar (Ar*: radiogenic argon); J value: 0.0064870 ± 0.000011 (1σ).

Table A.2 (continued) : $^{40}Ar/^{39}Ar$ ages obtained from the CPC.

Single crystal Total Fusion Ar/Ar dating of the sample OS-105 of GGMC (mineral: muscovite; N: 19).

Mineral	P	t	40 V		39 V		38 V		37 V		36 V		Moles 40Ar*	%Rad	R	Age (Ma)		%-sd
a	1.6	10	6.944	± 0.00170	3.247	± 0.00220	0.04407	± 0.00024	0.00836	± 0.00019	0.001924	± 0.00003	4.86E-14	91.82%	1.9637	20.82	± 0.03	0.16%
b	1.6	10	4.517	± 0.00404	2.049	± 0.00183	0.02803	± 0.00022	0.00353	± 0.00027	0.001587	± 0.00005	3.16E-14	89.62%	1.9762	20.96	± 0.08	0.38%
c	1.6	10	4.954	± 0.00359	2.317	± 0.00235	0.03159	± 0.00027	0.01929	± 0.00027	0.001382	± 0.00003	3.47E-14	91.79%	1.9628	20.81	± 0.05	0.24%
d	1.6	10	1.679	± 0.00109	0.809	± 0.00076	0.01067	± 0.00010	0.00005	± 0.00012	0.000358	± 0.00003	1.18E-14	93.69%	1.9443	20.62	± 0.11	0.51%
e	1.6	10	2.527	± 0.00220	1.166	± 0.00184	0.01534	± 0.00008	0.00174	± 0.00018	0.000748	± 0.00003	1.77E-14	91.25%	1.9774	20.97	± 0.09	0.41%
f	1.6	10	2.557	± 0.00162	1.190	± 0.00158	0.01606	± 0.00015	0.00089	± 0.00024	0.000751	± 0.00003	1.79E-14	91.32%	1.9630	20.82	± 0.09	0.41%
g	1.6	10	1.942	± 0.00239	0.885	± 0.00147	0.01164	± 0.00010	0.00062	± 0.00017	0.000712	± 0.00003	1.36E-14	89.16%	1.9565	20.75	± 0.11	0.53%
h	1.6	10	2.466	± 0.00166	1.231	± 0.00172	0.01617	± 0.00010	0.00102	± 0.00017	0.000251	± 0.00003	1.73E-14	97.00%	1.9435	20.61	± 0.08	0.38%
i	1.6	10	2.269	± 0.00122	1.083	± 0.00125	0.01423	± 0.00007	0.00033	± 0.00019	0.000485	± 0.00003	1.59E-14	93.68%	1.9617	20.80	± 0.09	0.42%
j	1.6	10	2.516	± 0.00201	1.110	± 0.00122	0.01452	± 0.00010	0.00268	± 0.00012	0.001151	± 0.00003	1.76E-14	86.50%	1.9599	20.78	± 0.10	0.50%
k	1.6	10	2.317	± 0.00211	1.055	± 0.00106	0.01421	± 0.00020	0.00090	± 0.00019	0.000844	± 0.00003	1.62E-14	89.24%	1.9610	20.80	± 0.10	0.49%
l	1.6	10	2.459	± 0.00195	1.185	± 0.00158	0.01548	± 0.00013	0.00048	± 0.00016	0.000471	± 0.00003	1.72E-14	94.34%	1.9575	20.76	± 0.08	0.41%
m	1.6	10	1.710	± 0.00191	0.792	± 0.00156	0.01043	± 0.00011	0.00040	± 0.00016	0.000576	± 0.00003	1.20E-14	90.05%	1.9443	20.62	± 0.13	0.63%
n	1.6	10	1.704	± 0.00175	0.686	± 0.00106	0.00949	± 0.00012	0.00096	± 0.00018	0.001205	± 0.00003	1.19E-14	79.11%	1.9665	20.85	± 0.15	0.73%
o	1.6	10	2.498	± 0.00143	1.114	± 0.00080	0.01466	± 0.00011	0.00103	± 0.00012	0.000997	± 0.00003	1.75E-14	88.21%	1.9770	20.96	± 0.08	0.39%
p	1.6	10	3.009	0.00227	1.457	± 0.00198	0.01899	± 0.00011	0.00124	± 0.00016	0.000520	± 0.00003	2.11E-14	94.90%	1.9599	20.78	± 0.07	0.34%
q	1.6	10	2.438	0.00230	1.193	± 0.00156	0.01536	± 0.00014	0.00178	± 0.00020	0.000353	± 0.00003	1.71E-14	95.73%	1.9562	20.74	± 0.08	0.41%
r	1.6	10	1.732	0.00134	0.778	± 0.00100	0.01036	± 0.00008	0.00063	± 0.00016	0.000732	± 0.00003	1.21E-14	87.52%	1.9481	20.66	± 0.13	0.64%

P: % power of 60 W (60 W *(P/10) Synrad CO2 laser); t: laser duration time; V: volt; %Rad: % radiogenic argon; R: 40Ar*/39Ar (Ar*: radiogenic argon); J value: 0.0064870 ± 0.000011 (1σ).

CURRICULUM VITAE

Name-Surname: Ömer KAMACI

EDUCATION:

- **B.Sc. :** 2006, Kocaeli University, Geological Engineering Department.
- **M.Sc. :** 2008, Kocaeli University, Institute of Science.

PROFESSIONAL EXPERIENCE AND REWARDS:

- Istanbul Technical University Faculty of Mines Research Assistant (2010-2015)
- TUBİTAK BİDEB 2214A Visiting Research Scholarship Program (2013-2014)
- Honor Student (Five consecutive years) at Kocaeli University (2001-2006)

PUBLICATIONS, PRESENTATIONS AND PATENTS ON THE THESIS:

- **Kamacı, Ö.,** Altunkaynak, Ş., (2020). The role of accreted continental crust in the formation of granites within the Alpine-style continental collision zone: Geochemical and geochronological constraints from leucogranites in the Çataldağ Metamorphic Core Complex (NW Turkey), *Lithos, 354,* 105347.
- **Kamacı, Ö.,** Altunkaynak, Ş., (2019a). Cooling and deformation history of the Çataldağ Metamorphic Core Complex (NW Turkey). *Journal of Asian Earth Sciences*, *172*, 279-291.
- **Kamaci, Ö.,** Altunkaynak, Ş., (2018). Çataldağ Granit-Gnays-Migmatit Kompleksi'nin (KB Türkiye) Soğuma, Deformasyon Ve Yükseliş Tarihçesi, *71. Jeoloji Kurultayı Bildiri Özleri*, 45-46.
- **Kamacı, Ö.,** Ünal, A., Altunkaynak, Ş., Georgiev, S., Billor, Z. M., (2017), The Çataldağ Plutonic Complex in Western Anatolia: Roles of Different Granites on the Crustal Buildup in Connection With the Core Complex Development In: Çemen, İ. & Yılmaz, Y. (eds) *Active Global Seismology*: Neotectonics and Earthquake Potential of the Eastern Mediterranean Region, 189-222.
- **Kamacı, Ö.,** Altunkaynak, S., (2017). An integrated study on microtectonics, geothermometry and thermochronology of the Çataldağ Core Complex (NW Turkey): Implications for cooling, deformation and uplift history, *Geophysical Research Abstracts, Vol. 19*, EGU2017-13049.

- **Kamacı, Ö.,** Altunkaynak, S., (2016). Two-stage Uplift of Granite-Gneiss-Migmatite Complex (GGMC) of Çataldağ Core Complex (Western Anatolia, Turkey): the role of detachment faults on uplift processes, *Geophysical Research Abstracts, Vol. 18,* EGU2016-10086, 2016**.**

- Ünal A., **Kamacı Ö.,** Altunkaynak Ş., Sunal G., Billor M.Z. (2013). "Origin of The Ductile and Overlaying Brittle Deformation in Çataldağ Plutonic Complex (Nw Anatolia)", *66. Geological Congress of Turkey*, p. 104.

- **Kamacı Ö.,** Ünal A., Altunkaynak Ş., Billor M.Z, Georgiev S., Marchev P. (2013). "Emplacement, Deformation and Exhumation of the Çataldag Plutonic Complex: Implications for Neotectonic Evolution of NW Anatolia (Turkey)", *American Geophysical Union Abstracts*, Fall Meeting, 2013.
- **Kamacı, Ö.** and Altunkaynak, S., (2011). Petrogenetic Implications of Two Contrasting Granite Types in The Çataldag Plutonic Complex, NW Turkey, *Mineralogical Magazine*, 1138.

OTHER PUBLICATIONS, PRESENTATIONS AND PATENTS:

- Altunkaynak, Ş., Ünal, A., Sunal, G., **Kamacı, Ö.,** Dunkl, I., (2021). Miocene uplift and exhumation history of northwestern Anatolia (Turkey): Implications from apatite (U-Th)/He thermochronology of syn-extensional plutons. *J. Asian Earth Sci*.
- **Kamacı, Ö.,** Ünlüer, A. T., Ünal, A., Doner, Z., Altunkaynak, Ş., Kumral, M. (2021). The first finding of Th-rich peraluminous alaskitic granite in Western Anatolia, EGU General Assembly 2021, online, 19–30 Apr 2021, EGU21-9963,.
- Arık, T., **Kamacı, Ö.,** Güraslan, I. N., and Altunkaynak, Ş. (2021). The role of shallow open system processes in the evolution of South Tepeldag Pluton (NW Turkey): insights and constraints from thermodynamic modelling, EGU General Assembly 2021, online, 19–30 Apr 2021, EGU21-13662,
- Bayrak, S. B., Ünal, A., Güraslan, I. N., **Kamacı, Ö.,** Yiğitbaş, E., and Altunkaynak, Ş. (2021). Insights into a dextral transtensional shear zone in NW Anatolia, Turkey: Preliminary results from the three dimensional strain and kinematic analyses of the Marmara Granitoid. EGU General Assembly 2021, online, 19–30 Apr 2021, EGU21-12884.
- Bayrak, S. B., Güraslan, I. N., Ünal, A., **Kamacı, Ö.,** Altunkaynak, Ş., and Yiğitbaş, E. (2020). Deformation history of the Marmara Granitoid and implications for a dextral shear zone in NW Anatolia, EGU General Assembly 2020.

- **Kamacı, Ö.,** & Altunkaynak, Ş. (2019). Magma chamber processes and dynamics beneath northwestern Anatolia: Insights from mineral chemistry and crystal size distributions (CSDs) of the Kepsut volcanic complex (NW Turkey). *Journal of Asian Earth Sciences*, *181*, 103889.

- Papadopoulos, A., Altunkaynak, Ş., Koroneos, A., Ünal, A., & **Kamacı, Ö.** (2017). Geochemistry of uranium and thorium and natural radioactivity levels of the western Anatolian plutons, Turkey. *Mineralogy and Petrology, 111*: 677-691.

- Çaliskanoglu, A.Z., Ünal, A., **Kamacı, Ö.,** Altunkaynak, Ş. (2017). "The Origin and Petrogenesis of Mount Hasan (Small Mt. Hasan) and Keçiboyduran Stratovolcanoes". *EGU General Assembly Conference Abstracts, Vol. 19,* p. 849.

- Papadopoulos, A., Altunkaynak, Ş., Koroneos, A., Ünal, A., & **Kamacı, Ö.** (2016). Distribution of natural radioactivity and assessment of radioactive dose of Western Anatolian plutons, Turkey. *Turkish Journal of Earth Sciences, 25*: 434-455.

- Papadopoulos, A., Altunkaynak, S., Koroneos, A., Ünal, A., **Kamacı, Ö.** (2016). "Natural Radioactivity Of Western Anatolian Plutons, Turkey". *Bulletin of the Geological Society of Greece, 50*(4), 2332-2341.

- Ünal A., **Kamacı Ö.,** Altunkaynak Ş. (2015). "Petrogenesis of Post-collisional high Ba-Sr granitoids: the Solarya Pluton, NW Turkey." *Geophysical Research Abstracts, Vol. 17,* p. 7014.

- Ünal A., **Kamacı Ö.,** Altunkaynak Ş. (2014). "Solarya Pluton (Balıkesir): An example to the epizonal plutons of NW Anatolia", 67. Geological Congress of Turkey, p. 498-499.

- Ünal A., **Kamacı Ö.,** Altunkaynak Ş. (2014). "The Solarya Volcano-Plutonic Complex (NW Turkey): Petrography, Petrogenesis and Tectonic Implications", *EGU General Assembly Conference Abstracts, Vol. 16,* p. 9096.

- Ünal A., **Kamacı Ö.,** Yildiz M., Atabek G., Yarar S., Altunkaynak Ş. (2012). "Volcanic Stratigraphy and Petrology of Susurluk Volcanites (NW Turkey), *12th Multidisciplinary Scientific GeoConference*, pp 391-398,

- **Kamacı, Ö.,** Altunkaynak, S. (2012), The Role of Episodic Basaltic Input in The Generation of Early Miocene Volcanic Suites of NW Anatolia: Evidence From petrography and mineral chemistry of Kepsut-Dursunbey volcanites, *International Earth Science Colloquium on the Aegean Region*.

- Unal, A., **Kamacı, Ö.,** Altunkaynak, S. (2012), Unal A Petrographic and petrochemical evolution of calc-alkaline volcanic associations of western Turkey: Susurluk volcanites, *International Earth Science Colloquium on the Aegean Region.*

- Unal, A., **Kamacı,** Ö., Yıldız, M., Atabek, G., Yarar, S., Altunkaynak, S. (2012), Volcanic Stratigraphy and Petrology of Susurluk Volcanites (NW Turkey), *SGEM2012 Conference Proceedings*/ ISSN 1314-2704, Vol. 1, 391 - 398 pp.

- **Kamacı, Ö.,** Altunkaynak, Ş. (2012), Geothermometry and Geobarometry of Kepsut-Dursunbey Volcanites (NW Anatolia, Turkey): Implications for Magma Chamber Depth and Crystallization Conditions, *Geophysical Research Abstracts, Vol. 14,* p. 7678.

- Unal, A., **Kamacı, Ö.,** Altunkaynak, S. (2012). Geochemistry and Sr-Nd-Pb Isotopic Characteristics of The Oligo-miocene Volcanism in NW Turkey: Susurluk Volcanites, *Geophysical Research Abstracts*, *Vol. 14*, p. 7478.

- Unal, A., **Kamacı, Ö.,** Altunkaynak, S. (2012). Susurluk Volkanitlerinin Jeolojisi ve Petrojenezi (KB Anadolu), *65. Türkiye Jeoloji Kurultayı*, 396-397.

- **Kamacı, Ö.,** Altunkaynak, Ş. (2011). Petrogenetic Implications of Two Contrasting Granite Types in the Çataldag Plutonic Complex, NW Turkey, *Mineralogical Magazine*, 1138.

- Yarar, O.S., **Kamacı, Ö.,** Altunkaynak, Ş. (2011). New Geochemical and Geochronological Constraints for The Origin of Orhaneli-Dursunbey Volcanic Rocks, NW Anatolia (Turkey), *Mineralogical Magazine*, 2216.

- Yarar, O.S., **Kamacı, Ö.,** Altunkaynak, Ş. (2011). Orhaneli-Dursunbey Volkaniklerinin Jeolojisi, Petrolojisi Ve Jeokronolojisi, KB Anadolu 64. *Türkiye Jeoloji Kurultayi Bildirileri*, 2011.

- **Kamacı, Ö.,** Altunkaynak, Ş. (2010). Mineral Chemistry and Petrography of Lava Successions from Kepsut-Dursunbey Volcanic Field, NW Turkey: Implications for Magmatic Processes and Crystallization Conditions, *International Journal of Environmental and Earth Sciences* 1:3.

- **Kamacı, Ö.,** Köprübaşı, N. (2008). Armutlu Yarımadası'nda Yüzeylenen Fıstıklı Granitoyidi İçerisinde Yer Alan Mafik Magmatik Anklavların (Mme) Jeokimyası Ve Dokusal Etkileşimler, 11/2008, s. 74-75, 3. Ulusal Jeokimya Sempozyumu, TÜBİTAK-BUTAL Bursa, Turkey